http://researchcommons.waikato.ac.nz/

Research Commons at the University of Waikato

Copyright Statement:

The digital copy of this thesis is protected by the Copyright Act 1994 (New Zealand).

The thesis may be consulted by you, provided you comply with the provisions of the Act and the following conditions of use:

- Any use you make of these documents or images must be for research or private study purposes only, and you may not make them available to any other person.
- Authors control the copyright of their thesis. You will recognise the author's right to be identified as the author of the thesis, and due acknowledgement will be made to the author where appropriate.
- You will obtain the author's permission before publishing any material from the thesis.

Application of Optical and Infrared Remote Sensing to the Retrieval of Selected Land and Sea Features

A thesis submitted

for the degree of

Doctor of Philosophy in Physics

by

Aleksandar Jelenak

The University of Waikato

Te Whare Wānanga o Waikato

July, 2001

The University of Waikato

Abstract

This thesis discusses two main areas of remote sensing research and thus is divided into two parts. The first part deals with novel methods for sea surface temperature (SST) retrieval using measurements of the Advanced Very High Resolution Radiometer (AVHRR) on-board the National Oceanic and Atmospheric Administration's (NOAA) series of satellites.

The basis for this work is the Dynamic Water Vapour method developed by *Steyn-Ross et al.* [1993], *Smith* [1993]. Two new methods are proposed in this thesis: The Dynamic Water Vapour or Atmospheric Temperature (DWVT) and the Simultaneous Water Vapour and Atmospheric Temperature (SimWVT).

The second part of the thesis is a feasibility study on the potential applicability of airborne multispectral remote sensing technology to pasture biomass prediction in New Zealand. This was a pilot project, done in collaboration with AgResearch Ltd. and Dexcel Ltd. Charles Sturt University's four-band airborne multispectral imaging system was used to acquire images of 65 test pasture plots.

Biomass of the test plots is predicted using a selection of vegetation indices, and multispectral reflectances. The results confirm the widely-held view that vegetation indices are not applicable to New Zealand pastures. Noticeably better results are achieved using the multispectral test plot reflectance in linear multiple regression-type equations.

Acknowledgments

I thank Dr. Moira Steyn-Ross whose supervision has been invaluable in preparing this thesis. I especially appreciate her relaxed approach which have made our collaboration so pleasant.

I also wish to thank Alistair Steyn-Ross for useful discussions regarding my thesis as well as anything related to computing and software, and for sharing his vast experience in these areas with me.

The excellent work of two former M.Sc. students, Peter Smith and Brian Osborne, which formed the basis of the first part of the thesis is greatly appreciated.

A scholarship for the second part of the thesis from the Ellett Trust is gratefully acknowledged.

I thank Dr. David Lamb of Charles Sturt University and Mac Hanna for their advice during the work on the second part of the thesis. I am particularly grateful to Alec M^{c}Gowan (AgResearch Ltd.) and Dr. Peter Schaare (HortResearch Ltd.) for their willingness to help me with the ground-truthing work for the second part of the thesis.

Special thanks go to my family: My loving wife Zorana for being my fervent supporter from the day we met and without whom this would not have happened; my sons Filip and Luka for their unconditional love and for providing me with countless opportunities to think about the thesis during long night hours.

Very special thanks to my parents Miroslava and Dragan Jelenak for their perpetual support throughout my life. My successes are also theirs.

Finally, I extend my deepest gratitude to my parents-in-law, Nada and Milan Vukojević, for accepting me as one of their own and always being available when I needed help and support.

I dedicate this thesis to the memory of my father, Dragan Jelenak.

Contents

List of Figures

List of Tables

Glossary

Acronyms

ABVS	Charles Sturt University's four-band airborne imaging system
DWVT	Dynamic Water Vapour or Atmospheric Temperature
SimWVT	Simultaneous Water Vapour and Atmospheric Temperature
SST	Sea surface Temperature
APT	Automatic Picture Transmission
AVHRR	Advanced Very High Resolution Radiometer
BIP	Band Interleaved by Pixel
BRDF	Bidirectional Reflectance Distribution Function
CCD	Charge Coupled Device
CCIR	Comité Consultatif International des Radiocommunications
CPSST	Cross-product SST
CSIRO	Commonwealth Scientific and Industrial Research Organization
DAT	Dynamic Atmospheric Temperature
DN	Digital number
DWV	Dynamic Water Vapour
ESSA	Environmental Science Services Administration
FIR	Finite Impulse Response

FORTRAN	A high level computer programming language
FPN	Fixed pattern noise (FPN) of the CCD sensor
GEMI	Global Environmental Monitoring Index
GPS	Global Positioning System
GUI	Graphical User Interface
HRPT	High Resolution Picture Transmission
IFUT	A base-36 code developed by CSIRO Hobart, Tasmania, Australia to unambiguously identify each satellite orbit
IPVI	Infrared Percentage Vegetation Index
IR	Infrared
IRIS	Infrared Interferometer Spectrometer
ITOS	Improved TOS
LAI	Leaf Area Index
LOWTRAN-7	Atmospheric radiation transfer model and simulation software
LST	Land surface temperature
MCSST	Multichannel SST
MSAVI2	Second Modified Soil Adjusted Vegetation Index
NASA	National Aeronautic and Space Administration
NDVI	Normalized Difference Vegetation Index
NESDIS	National Environmental Satellite Data Information Service, a part of NOAA
NIR	Near-infrared
NLSST	Nonlinear SST
NOAA	National Oceanic and Atmospheric Administration

PRNU	Pixel response nonuniformity
RMSE	Root mean square error
ROI	Region of interest
RVI	Ratio Vegetation Index
SAVI	Soil Adjusted Vegetation Index
SR	Scanning Radiometer
TIROS	Television Infrared Observation Satellite
TIROS-N	TIROS-NOAA
TOS	TIROS Operational System
TRSST	Transmission Ratio SST
UTC	Universal Time Coordinated
VHF	Very High Frequency
VHRR	Very High Resolution Radiometer
WAK	A BRDF model proposed by *Dymond et al.* [2000]

Chapter 1

Thesis Overview

We begin with an overview of sea surface temperature retrieval theory with special emphasis on the methods involving the AVHRR instrument in Chapter 2. The presentation is governed by the different theoretical approaches used to approximate the radiative transfer equation for a clear-sky plane-parallel atmosphere.

Chapter 3 reviews the Dynamic Water Vapour method developed by *Steyn-Ross et al.* [1993] and *Smith* [1993] that forms the foundation of our work on the novel retrieval algorithms. This method employed a full atmospheric radiation transfer model and simulation software to solve the radiative transfer equation, and dynamically altered a first-guess atmospheric water vapour profile in the search for an optimal sea surface temperature estimate.

We propose two new methods in this thesis: The Dynamic Water Vapour or Atmospheric Temperature (DWVT) and the Simultaneous Water Vapour and Atmospheric Temperature (SimWVT). Both methods also rely on an atmospheric radiation transfer model.

The DWVT is described in Chapter 4. It starts by altering a first-guess atmospheric water vapour profile, as in the DWV. The DWVT, however, features a specially-crafted DWV-failure criterion which addresses the reported DWV method deficiencies [*Osborne*, 1995]. When the criterion is triggered,

the DWVT switches from altering the water vapour profile to the atmospheric temperature profile instead. This algorithm, coined the Dynamic Atmospheric Temperature (DAT), provides much more accurate sea surface temperature estimates than the original DWV in such cases.

The SimWVT marks a completely new approach, and is featured in Chapter 5. Unlike the DWV and DWVT, it alters first-guess atmospheric temperature and water vapour profiles simultaneously—hence its name. The core SimWVT equation is derived by applying the variational calculus to the radiative transfer equation for a clear-sky plane-parallel atmosphere. This equation connects the variation of the satellite-measured radiance with the amount of change of the atmospheric temperature or water vapour profile. By requiring the at-satellite radiance to remain the same, a relationship between the amount of change of the atmospheric temperature and water vapour profiles is obtained, allowing simultaneous alteration and hence a more systematic search for an optimal sea surface estimate.

Both the DWVT and SimWVT are compared with a selection of operational equations for various NOAA satellites (Section 4.8), and a group of transmission-ratio based retrieval methods (Section 4.7) using a data set of 34 coincident NOAA-9 AVHRR channel-4 and -5 radiances, radiosonde-measured atmospheric profiles and buoy-recorded sea surface temperature measurements, collected off the west coast of Tasmania in mid 1987 (Section 3.3). The DWVT and SimWVT compared very well against the most accurate NOAA operational equation for the data set; they exhibited superior performance to the rest of the NOAA equations and the transmission-based retrieval methods.

The second part of the thesis discusses the potential applicability of airborne multispectral remote sensing technology to pasture biomass prediction in New Zealand. The study is done in collaboration with AgResearch Ltd. and Dexcel Ltd. Charles Sturt University's four-band airborne multispectral imaging system was used to acquire images of 65 test pasture plots located near the University of Waikato's campus in Hamilton. The test plots feature

different pasture species, and nutritional and grazing regimes typical of the Waikato farming practice.

Chapter 7 gives a very broad overview of the traditional methods for pasture biomass assessment and the principles of vegetation remote sensing: structure of the leaf, chlorophyll and its role in shaping the spectral properties of the leaf, and the effects of canopy on vegetation reflectance. Also in this chapter, the concept of the vegetation index is introduced and some of the most frequently used indices are presented.

Pasture test plots, measurement methods and instruments are featured in Chapter 8. We design and calibrate an *ad hoc* laboratory reflectance measurement system, and describe the protocol for the reflectance measurement of two $6 \times 6\,\mathrm{m}^2$ canvases used in the study.

We develop an algorithm for post-processing of the acquired images and extraction of top-of-canopy reflectance data, and describe it in Chapter 9. The algorithm compensates for the geometric and radiometric imperfections of the imaging system, as well as the bidirectional reflective character of vegetation by employing the WAK canopy reflectance model of *Dymond et al.* [2000]. The conversion of image pixel values to reflectance is done using the two canvases imaged coincidently with the test plots.

Biomass prediction outcomes using either vegetation indices or multispectral test plot reflectances are presented in Chapter 10. The results affirm the findings of *Hanna et al.* [1999] and *Lin* [1999] that vegetation indices cannot describe the biomass of New Zealand pastures well. Much better results are achieved using the multispectral test plot reflectance in linear multiple regression-type equations. None of the prediction equations was able to produce a root mean square error (RMSE) smaller than 1000 kgDM/ha.

In Chapter 11 we discuss the implications of our findings and identify two deficiencies in the multispectral and biomass data sets which have probably influenced the accuracy of our prediction equations: the plot with the largest biomass reported (an outlier suspect) and the lack of proper radiometric cali-

bration of the imaging system's cameras. We conclude the chapter with suggestions on how to avoid such problems in the future, as well as how to improve the quality of data.

Part I

Novel Methods for SST Retrieval from AVHRR Imagery

Chapter 2

Overview of Sea Surface Temperature Retrieval from AVHRR

As long as we have been receiving satellite imagery, there has been great interest in measuring the sea surface temperature (SST). Oceans cover about 70% of this planet's surface and play a major part in the formation of weather patterns and climatic events. The oceans are also a very important source of food and the most cost-effective route for transport.

As the majority of the Earth's population live in the regions bordering oceans, the economies of many countries are directly linked to the status of nearby oceans. It is therefore very easy to understand why sea surface temperature measurement on the global scale was amongst the first uses of space-borne acquired data. To illustrate this we give a list of applications that rely on the measurements of sea surface temperatures:

- Input to numerical ocean and atmospheric models.
- Support for oceanographic surveys and interpretation of surface oceanographic features in support of fisheries science or physical oceanographic research.

- Support of commercial fishing activities.
- Protection of endangered species.
- Study of red tide outbreaks.
- Derivation of ocean feature charts and ocean surface current measurements in support of ship routing and search-and-rescue activities.
- Analysis of short- and long-term fluctuations in ocean temperature, such as El Niño/Southern Oscillation.
- Climate change studies.
- Environmental impact of sea surface temperature change, such as coral reef bleaching.

We first present the history of weather satellites, followed by the basics of the Advanced Very High Resolution Radiometer (AVHRR). We then continue with the methods developed so far for the retrieval of SST's. Our selection is in no way exhaustive, however we have presented the work that, in our belief, carries the most important and long lasting findings. Naturally, we focus on the techniques developed for the Advanced Very High Resolution Radiometer, onboard the NOAA series of weather satellites.

2.1 History of Weather Satellites

NASA's Television Infrared Observation Satellite (TIROS-1), launched on 1 April 1960, gave the first systematic images of Earth from space. This single television camera was aligned with the axis of this spin-stabilized satellite which meant that it could point at the Earth only for a limited time each orbit. This experimental satellite series eventually carried a variety of sensors, evolving as technology and experience increased. Working together, NASA and the Environmental Science Services Administration (ESSA, merged into

NOAA at the latter's formation in 1970) stimulated improved designs. TIROS-1 through TIROS-X contained simple television cameras, while four of the ten satellites also included infrared sensors.

One interesting development was the change in location of the camera. From the spin axis of the satellite it was turned so that now its side, rather than the central axis, pointed towards the Earth. Called the "wheel" satellite, this new arrangement resulted in the camera collecting a series of circular images of the Earth which, when mosaicked, provided the first global view of the Earth's weather systems from space.

Using this wheel concept, cooperation between NASA and ESSA initiated the TIROS Operational System (TOS) with its first launch in 1966. Odd numbered satellites carried improved vidicon cameras and data storage/replay systems that provided global meteorological data, while even numbered satellites provided direct readout Automatic Picture Transmission (APT) video to low cost VHF receiving stations. APT, now derived from AVHRR imagery, is still provided to thousands of simple stations in schools, on ships, and elsewhere worldwide. Nine wheel satellites, called ESSA-1 through ESSA-9, were launched between 1966 and 1969.

The 1970's saw the Improved TOS (ITOS), which combined APT and global data collection/recording in each satellite. The major improvement was the utilization of guidance systems developed for ballistic missiles that made it possible to stabilize the three axes of the spacecraft. Thus, a single camera could be aimed at the Earth, eliminating the need to assemble a series of circular images to map the world's weather. ITOS also introduced day/night acquisitions and a new series of Scanning Radiometers (SRs), which offered vastly improved data. Later, ITOS carried the Very High Resolution Radiometer (VHRR). As part of international weather data exchange, NOAA introduced the direct reception of VHRR data at no charge to ground stations built by an increasing number of users, beginning in 1972. ITOS-1 and NOAA-1, launched in 1970, were transition satellites of the ITOS series, while NOAA-2 through

NOAA-5, launched in 1972-1976, carried the VHRR instrument.

The latest generation of this series has been operational since 1978. TIROS-N (for TIROS-NOAA) and NOAA-7 through the latest NOAA-16 include the Advanced Very High Resolution Radiometer (AVHRR), discussed in the following section. The major advance introduced by this satellite series was the shift from an analog data relay to a fully digital system, coined High Resolution Picture Transmission (HRPT). The data were thus digitized onboard the spacecraft before being transmitted back to Earth. Also, the size and weight of the satellite increased from under 300 kg with the ESSA series of satellites to over 1200 kg with the TIROS-N satellites.

2.2 The Advanced Very High Resolution Radiometer (AVHRR)

This instrument played a pivotal role in the history of SST retrievals, as it has the longest record of use for this purpose. It was the first multispectral radiometer with on-board calibration and acceptable ground resolution ($\sim$ 1 km), offering for the first time world-wide coverage suitable for operational use. Its arrival stimulated the development of novel methods for SST retrieval and resulted in acceptance of satellite-based SST observations for every day scientific and commercial use.

AVHRR's ancestors were the Scanning Radiometer (SR) and the VHRR. The SR first orbited on ITOS-1 in 1970. These early SRs had a relatively low spatial resolution (8 km) and fairly low radiometric fidelity. The VHRR was the first improvement over the SR and for a while flew simultaneously with the SR. Later, the VHRR was replaced by the AVHRR which combined the high resolution and monitoring functions.

The first AVHRR instrument, a four-channel filter-wheel radiometer, was launched aboard the TIROS-N satellite in October 1978. It was subsequently

improved to become a five channel instrument, designated AVHRR/2, that was initially carried on NOAA-7, launched in June 1981. The latest instrument version is AVHRR/3, with six channels, first carried on NOAA-15 launched in May 1998. AVHRR/3 channel characteristics are given in Table 2.1.

Table 2.1: AVHRR/3 channel characteristics.

Channel	Resol. at Nadir	Wavelength (μm)	Typical Use
1	1.09 km	0.58–0.68	Daytime surface and cloud mapping
2	1.09 km	0.725–1	Land-water boundaries
3A	1.09 km	1.58–1.64	Snow and ice detection
3B	1.09 km	3.55–3.93	Night cloud mapping, sea surface temperature
4	1.09 km	10.3–11.3	Night cloud mapping, sea surface temperature
5	1.09 km	11.5–12.5	Sea surface temperature

Since the format used for transmitting the data to the ground was designed to handle five channels, the newly added channel 3A operates only during the daylight part of the orbit. Channel 3B corresponds to the channel 3 on the AVHRR/2 instrument, and operates during the night portion of the orbit. In this way the five-channel format for transmission is preserved. It is possible to schedule 3A/3B channel switching anytime during an orbit if it is required.

In addition to a new channel, the new AVHRR/3 instrument features also dual gain settings for channels 1, 2 and 3A. The dual gains in effect increase the sensitivity in low light situations. The prime reason for these changes was to improve ice, snow and aerosol information produced from the visible channel data.

AVHRR channels 1 and 2 are designed, and calibrated before launch, to provide direct, quasi-linear conversion between the 10-bit digital numbers and

albedo. The thermal channels are designed and calibrated before launch as well as in space to provide direct nonlinear conversion between digital numbers and temperature.

2.3 A Practical Problem of SST Measurements: The Skin Effect

The skin effect is a water surface phenomenon caused by evaporative cooling. A thin thermal layer on the surface is created with a slightly lower temperature than the bulk of the ocean beneath it. Radiometers sense only the radiation that emanates from this thin layer, whereas ground-truth measurements are recorded at depths ranging anywhere from a few centimeters to few meters. Hence, the temperature derived from radiometer readings, even in the ideal case, will be biased. The absolute error incurred is very difficult to predict due to the high variability of the skin effect.

Hepplewhite [1989] reported a comparison made between SST's derived from a ship-mounted infrared radiometer and a conventional meteorological rubber bucket with a mercury thermometer. His investigation focused on the size and variability of the skin effect from the tropical Atlantic to the waters around Antarctica. On average, the skin temperature recorded by the radiometer was 0.3 K cooler than the temperature measured approximately 10 cm below the surface, with variation ranging from -1.2 K (cooler) to 0.3 K (warmer). *Hepplewhite* noted that the skin effect is less variable in the tropics and of smaller magnitude. This is probably caused by low winds and high humidity over the ocean, forcing evaporation to be low. He also noted the skin effect at night-time was smaller than it was during daytime, a possible effect of the diurnal thermocline.

Schlüessel et al. [1990] conducted a six-week field experiment in the North Atlantic Ocean, collecting coincident measurements of skin and subsurface bulk

temperatures, radiative fluxes and meteorological variables from a research ship. The range of the bulk-skin temperature differences over the entire data set was between -1 and 1 K, with mean values of 0.1–0.2 K depending on wind and surface heat flux conditions. They reported a variation of the skin-bulk differences between night and daytime measurements—average values of 0.11 and 0.3 K respectively—as well as with different cloud conditions.

In an attempt to model the skin-bulk temperature difference, *Schlüessel et al.* [1990] proposed daytime and night-time equations for the bulk-skin temperature difference. The equations are linear combinations of wind speed, surface and air temperatures at 20 m, surface and atmospheric water vapour mixing ratios and the net longwave radiative flux (for the daytime equation). They reported a resulting accuracy of 0.11 K for the night-time and 0.17 K for the daytime equation. Their recommendation was to calibrate satellite-derived SST's during night with buoy measurements and the additional aid of meteorological variables. However, the applicability of such an algorithm is questionable since the meteorological variables used in the paper are not readily available coincidentally with satellite observations.

2.4 The Radiative Transfer Equation

The starting point of all SST retrieval algorithms is the equation of radiative transfer for clear, plane-parallel atmospheres (*Liou* [1980]):

$$I(\infty,\nu,\mu) = I(0,\nu,\mu)\tau(0,\nu,\mu) + \int_{z=0}^{z=\infty} B(\nu,T(z))\frac{\partial\tau(z,\nu,\mu)}{\partial z}\,\mathrm{d}z. \qquad (2.1)$$

Where: ν – wavenumber (usually given in the units of cm^{-1}); μ – cosine of the zenith angle (see Figure 2.1); z – height; $\tau(z,\nu,\mu)$ – atmospheric transmittance from height z to the top of the atmosphere; $T(z)$ – atmospheric temperature profile; $I(\infty,\nu,\theta)$ – upwelling radiance at satellite; $I(0,\nu,\theta)$ – upwelling surface radiance; $B(\nu,T)$ – Planck black body spectral radiance function.

Equation (2.1) describes the amount of radiance reaching the satellite after transversing through an atmosphere that only absorbs and emits radiation, a so-called *clear* atmosphere. The atmosphere is also assumed to consist of stratified infinitesimal layers parallel to the surface, hence the term *plane-parallel.* This assumption reduces the dimensionality of the radiative transfer equation to one dimension normal to the plane of stratification, usually denoted as *height.* The variable $\mu = \cos\theta$, where θ is the zenith angle, accounts for differing paths of radiation. For example, nadir view has $\theta = 0°$, hence $\mu = 1$. Since the atmosphere extends to about 100 km above Earth, and radiation thereafter travels through vacuum—or at least, the influence of the medium can be assumed to be negligible—it is common to describe the satellite location in such equations as $z = \infty$.

The first term on the right-hand side of (2.1) is the surface contribution to the satellite-sensed radiance. The upwelling surface radiance, $I(0, \nu, \mu)$, is attenuated by the atmosphere and this effect is described by the surface-to-satellite transmissivity coefficient $\tau(0, \nu, \mu)$. The second term accounts for the atmospheric contribution to the satellite-sensed radiance. The integral sums up the radiance of every infinitesimal atmospheric layer, attenuated by its own value of transmissivity. As the atmosphere becomes thinner, the value of transmissivity increases. It is important to mention here another assumption in the equation: each atmospheric layer is in local thermodynamic equilibrium, so its emission can be described by Planck's black body spectral function.

It is usual to rewrite (2.1) in a form in which the dependence on ν and μ is assumed and to denote the transmittance of the whole atmosphere, $\tau(0, \nu, \mu)$, simply as τ:

$$I(\infty) = I(0)\tau + \int_{z=0}^{z=\infty} B(T(z))\frac{\partial \tau}{\partial z}\,\mathrm{d}z. \tag{2.2}$$

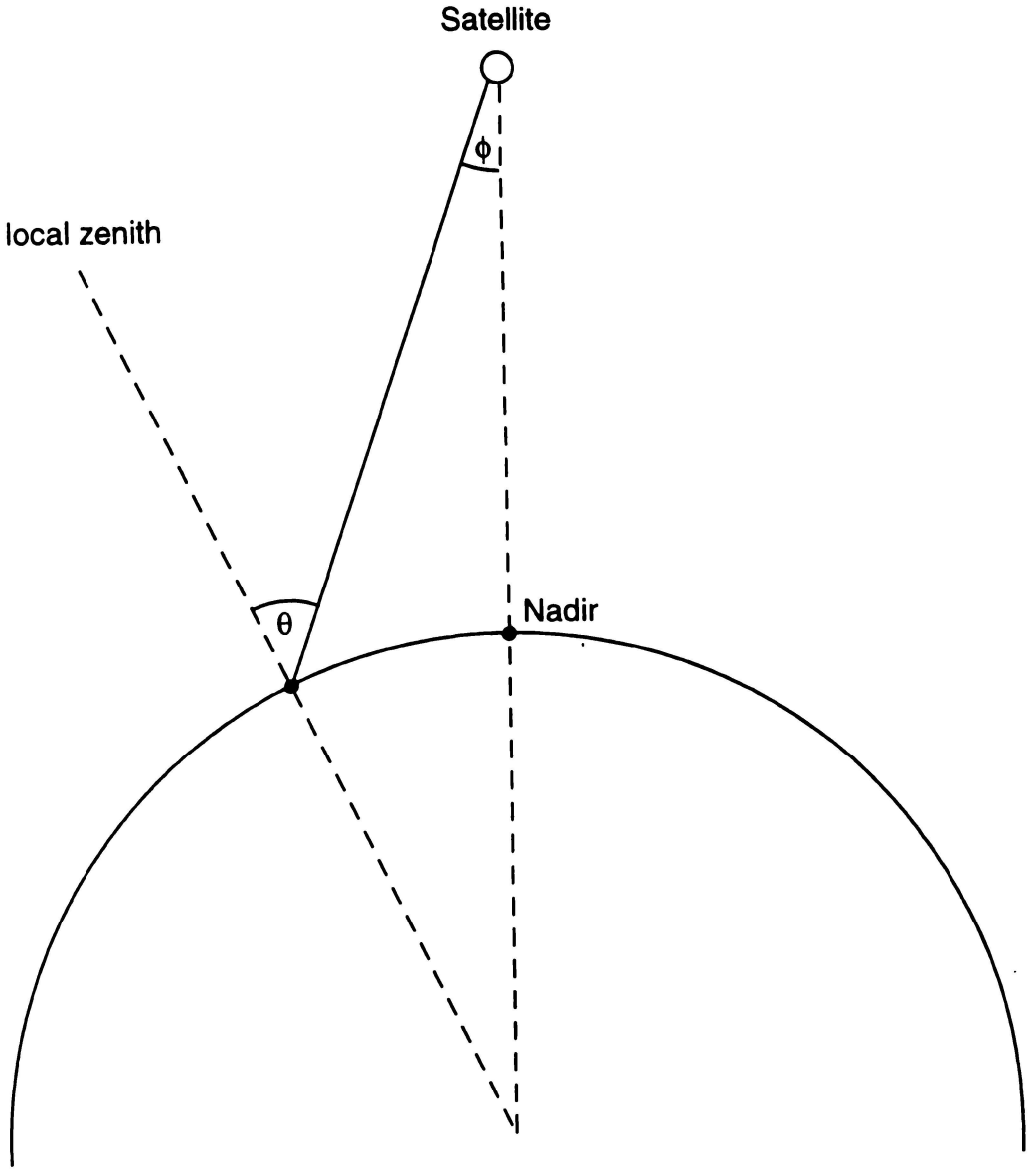

Figure 2.1: Basic satellite scanning geometry: Scan (ϕ) and zenith (θ) angles. (From *Smith* [1993].)

Changing the integration variable from height to transmittance, we find:

$$I(\infty) \;=\; I(0)\tau \;+\; \int_{\tau}^{1} B(T(\tau))\mathrm{d}\tau. \tag{2.3}$$

The integral can be approximated by using the mean-value theorem of calculus:

$$B(\overline{T}_a) \;=\; \frac{\int_{\tau}^{1} B(T)\mathrm{d}\tau}{\int_{\tau}^{1} \mathrm{d}\tau}, \tag{2.4}$$

where $\overline{T}_a$ is interpreted as the equivalent atmospheric temperature. Thus, we arrive at the most compact form of the radiative transfer equation:

$$I(\infty) \;=\; I(0)\tau \;+\; B(\overline{T}_a)(1-\tau). \tag{2.5}$$

The emissivity from the ocean surface can be taken as unity in the infrared region for all practical purposes [*Liou*, 1980]. Thus $I(0) = B(T_s)$, where T_s is the surface temperature. The final form of (2.1) usually used in SST work is:

$$I \;=\; B(T_s)\tau \;+\; B(\overline{T}_a)(1-\tau), \tag{2.6}$$

where we have dropped the ∞ from the left-hand side, indicating that I unambiguously describes satellite-sensed radiance.

Planck's black body spectral radiance function, mentioned in the above equations, is of the form:

$$B(\nu, T) \;=\; \frac{2hc^2\nu^3}{\exp\left(\frac{hc\nu}{kT}\right) \;-\; 1}, \tag{2.7}$$

where: h - Planck's constant; c - speed of light in a vacuum; k - Boltzmann's constant, and T - black body's absolute temperature.

2.5 Overview of Methods for SST Retrieval from AVHRR

The radiation transfer equation (2.6) is very difficult to solve, as it requires precise knowledge of atmospheric constituents and the atmosphere's temperature profile. Many of these variables are not readily available from satellite observations; and even if they were, the solution would necessitate the use of very powerful computers and extensive knowledge of basic interactions of radiation with various gases and particles in the atmosphere. Such hardware and software has only just begun to become available, so the SST methods used in the past had almost exclusively tried to simplify the radiation transfer equation, while retaining its main properties.

In the following sections, we present some of the SST methods developed in the past. It is not possible to present each and every one of them due to their vast number. However, it is possible to gather them into several groups based on their approach in simplifying the transfer equation.

2.6 Multi-Channel SST Method

Multi-Channel SST methods are the most frequently used type of algorithms for SST retrieval. Their widespread application can be ascribed to their very simple form, ideal for operational use as they can be quickly coded and executed even on modest computer hardware. The name reflects the main characteristic of these methods: the utilization of satellite-sensed radiance at more than one channel.

The first to use observations from more than one wavelength were *Anding and Kauth* [1970]. They started from the assumption that only water vapour significantly absorbs and emits radiation in the two wavelength regions, 7–9.5 μm and 10–12 μm. They contended that if two wavelength regions existed with slightly differing absorption, there would be a linear relationship between

the surface temperature and the radiance in the two regions. By numerically simulating radiation transfer using their own spectral radiance model, they managed to find such a pair of wavelengths: 9.19 and 10.96 μm. When *Maul and Sidran* [1972] tested the method with a different spectral model, they found a different pair of wavelengths: 8.60 and 10.96 μm. In their reply to the findings of *Maul and Sidran* [1972], *Anding and Kauth* [1972] confirmed that the choice of wavelengths depended on the employed spectral model by finding a third pair of wavelengths: 8.95 and 11.9 μm. Although there was some discussion on the exact values of the two wavelengths, the initial idea proposed in *Anding and Kauth* [1970] has never been questioned nor found to be invalid.

The theoretical rationale behind the method of *Anding and Kauth* [1970] was given by McMillin [*McMillin*, 1971, 1975]. He showed that a simple linear combination of the radiances measured at two wavelengths can be obtained from the radiative transfer equation. This method gave a good estimate of the radiance leaving the surface and hence the SST value. *McMillin and Crosby* [1984] later also developed a similar relationship between the SST and the satellite-sensed brightness temperatures. These two derivations are given in Section 2.6.1.

Prabhakara et al. [1974] were probably the first to employ successfully the method suggested by *Anding and Kauth* [1970], using IRIS (Infrared Interferometer Spectrometer) data. They used a small sample of 95 km resolution, cloud-free brightness temperature spectra captured in the 11–13 μm region by IRIS (on the Nimbus 4 satellite) to derive SST equation coefficients for the three IRIS channels in the 11–13 μm wavelength region. To check the validity of the proposed model, *Prabhakara et al.* used a sample of 106 Nimbus 3 IRIS measurements with corresponding ship SST measurements within $\pm 1°$ of latitude and longitude, covering the globe from 60° S to 60° N. They reported achieving an rms difference between the ground truth and retrieved SST's of 1.3 °C over a wide SST temperature range of about 4–29 °C. The estimated measurement error of ship SST's was reported to be about 1 °C.

2.6.1 Derivation of the MCSST Method

The main equation of the MCSST method has two different forms; depending on the variables used it can be in either radiance or satellite brightness temperature form. We give the derivation for both of them below.

Temperature-Space Form of the MCSST Equation

The radiative transfer equation (2.6) can be rewritten by introducing the *equivalent satellite brightness temperature* T. It is defined as the temperature of a black body which would give the same amount of radiance as sensed by the satellite. Equation (2.6) becomes:

$$B(T) = B(T_s)\tau + B(\overline{T}_a)(1-\tau). \tag{2.8}$$

A temperature-space expansion of the radiative transfer equation relies on the assumption that the three temperatures in (2.8) are very similar: $T \approx \overline{T}_a \approx T_s$. The rationale is that the majority of atmospheric absorption and emission occurs in the lower part of the atmosphere.

The next step is a Taylor expansion of the terms $B(T)$ and $B(T_s)$ around the average atmospheric temperature $\overline{T}_a$. Ignoring all terms higher than first order, we find:

$$\begin{aligned} B(T) &\approx B(\overline{T}_a) + \left.\frac{\partial B}{\partial T}\right|_{T=\overline{T}_a} (T - \overline{T}_a), \\ B(T_s) &\approx B(\overline{T}_a) + \left.\frac{\partial B}{\partial T}\right|_{T=\overline{T}_a} (T_s - \overline{T}_a). \end{aligned}$$

Introducing these expansions into (2.6) yields:

$$\begin{aligned} B(\overline{T}_a) \;+\; & \left.\frac{\partial B}{\partial T}\right|_{T=\overline{T}_a} (T - \overline{T}_a) \\ = \; & \left[B(\overline{T}_a) + \left.\frac{\partial B}{\partial T}\right|_{T=\overline{T}_a} (T_s - \overline{T}_a)\right] \tau \;+\; B(\overline{T}_a)(1-\tau) \\ = \; & \left.\frac{\partial B}{\partial T}\right|_{T=\overline{T}_a} (T_s - \overline{T}_a)\tau \;+\; B(\overline{T}_a), \end{aligned}$$

resulting in:

$$T \;-\; \overline{T}_a \;=\; (T_s - \overline{T}_a)\tau. \tag{2.9}$$

We now write (2.9) for as many channels used in SST retrieval, which is usually two or three. We shall assume two channels, denoting them by i and j.

$$T_i \;-\; \overline{T}_a \;=\; (T_s - \overline{T}_a)\tau_i \tag{2.10}$$

$$T_j \;-\; \overline{T}_a \;=\; (T_s - \overline{T}_a)\tau_j \tag{2.11}$$

These equations are valid only if the channels i and j are close to each other—as is the case for AVHRR channels 4 and 5. Only then we can assume that $\overline{T}_a$ is the same in all the channels. Eliminating $\overline{T}_a$ and rearranging (2.10–2.11) to solve for T_s, we obtain:

$$T_s \;=\; T_i + \frac{1-\tau_i}{\tau_i - \tau_j}(T_i - T_j). \tag{2.12}$$

If the channels are in the wavelength region of low atmospheric absorption—which, again is true for AVHRR channels 4 and 5—the channel transmittances can be modelled as:

$$\tau \;=\; \exp(-ku) \;\approx\; 1 - ku, \tag{2.13}$$

where: k is the mass absorption coefficient, and u is the mass of the absorbing gas. Equation (2.12) now reads:

$$T_s = T_i + \frac{k_i}{k_j - k_i}(T_i - T_j). \tag{2.14}$$

The fraction occurring in this equation is a constant, hence the surface temperature can be expressed as a linear function of a pair of adjacent channel brightness temperatures.

Radiance-Space form of the MCSST Equation

The derivation of the radiance-space form of the MCSST equation is based on the same premisses utilized during the derivation of its temperature-space counterpart. We start from (2.6) written for two different wavenumbers:

$$I(\nu_i) = B(\nu_i, T_s)\tau_i + B(\nu_i, \overline{T}_a)(1 - \tau_i), \tag{2.15}$$

$$I(\nu_j) = B(\nu_j, T_s)\tau_j + B(\nu_j, \overline{T}_a)(1 - \tau_j), \tag{2.16}$$

where we have adopted $\tau_i \equiv \tau(\nu_i)$ and $\tau_j \equiv \tau(\nu_j)$ for shorter notation. We use the same surface and average atmospheric temperatures in both equations citing the same reasoning as in the previous section.

For small enough ν-differences, we can use a Taylor series expansion of the black body function ignoring terms higher than first-order:

$$B(\nu_r, T) \approx B(\nu, T) + \frac{\partial B(\nu, T)}{\partial \nu}(\nu_r - \nu).$$

Thus, we can approximate the values of black body functions at wavenumber

ν_i with that at the wavenumber ν_j:

$$\begin{aligned} B(\nu_j, T_s) &\approx B(\nu_i, T_s) + \left.\frac{\partial B(\nu, T_s)}{\partial \nu}\right|_{\nu=\nu_i} (\nu_j - \nu_i), \\ B(\nu_j, \overline{T}_a) &\approx B(\nu_i, \overline{T}_a) + \left.\frac{\partial B(\nu, \overline{T}_a)}{\partial \nu}\right|_{\nu=\nu_i} (\nu_j - \nu_i). \end{aligned}$$

Including these approximations into (2.16) yields:

$$I(\nu_i) = B(\nu_j, T_s)\tau_i + B(\nu_j, \overline{T}_a)(1 - \tau_i) - \left.\frac{\partial B(\nu, \overline{T}_a)}{\partial \nu}\right|_{\nu=\nu_i} (\nu_j - \nu_i). \quad (2.17)$$

We can also approximate $I(\nu_i)$ with a Taylor series around ν_j:

$$I(\nu_i) = B(\nu_j, T_i) + \left.\frac{\partial B(\nu, T_i)}{\partial \nu}\right|_{\nu=\nu_i} (\nu_j - \nu_i),$$

where T_i satisfies the condition $I(\nu_i) \equiv B(\nu_i, T_i)$.

The dependence of $\frac{\partial B(\nu,T)}{\partial \nu}$ on the temperature is small in the 10–13 μm region [*McMillin*, 1975]. If ν_i and ν_j are sufficiently close, we can neglect the dependence of $\frac{\partial B(\nu,T)}{\partial \nu}$ on temperature and adopt:

$$\left.\frac{\partial B(\nu, T_i)}{\partial \nu}\right|_{\nu=\nu_i} \approx \left.\frac{\partial B(\nu, \overline{T}_a)}{\partial \nu}\right|_{\nu=\nu_i}.$$

Returning to (2.17), we finally obtain the "ν_j version" of (2.16):

$$\begin{aligned} B(\nu_j, T_i) - \left.\frac{\partial B(\nu, T_i)}{\partial \nu}\right|_{\nu=\nu_i} (\nu_j - \nu_i) = \\ B(\nu_j, T_s)\tau_i + B(\nu_j, \overline{T}_a)(1 - \tau_i) - \left.\frac{\partial B(\nu, \overline{T}_a)}{\partial \nu}\right|_{\nu=\nu_i} (\nu_j - \nu_i), \end{aligned}$$

$$B(\nu_j, T_i) = B(\nu_j, T_s)\tau_i + B(\nu_j, \overline{T}_a)(1 - \tau_i). \quad (2.18)$$

Solving the system of equations (2.16) and (2.18) for $B(\nu_j, T_s)$, we find:

$$B(\nu_j, T_s) = B(\nu_j, T_i) + \frac{1-\tau_i}{\tau_i - \tau_j}\left(B(\nu_j, T_i) - I(\nu_j)\right). \tag{2.19}$$

The equation has been deliberately reorganized to show that the fractional term is the same as in (2.12). Adopting the following notation: $I_s \equiv B(\nu_j, T_s)$ for the surface radiance, $B(\nu_j, T_i) \equiv I_i'$ for wavenumber-j equivalent to the wavenumber-i radiance, and $I_j \equiv I(\nu_j)$ for the wavenumber-j radiance, we obtain the traditional form of the radiance-space MCSST equation:

$$I_s = I_i' + \gamma(I_i' - I_j), \tag{2.20}$$

where $\gamma \equiv \dfrac{1-\tau_i}{\tau_i - \tau_j}$.

Variation of the Angle Form of the MCSST Equation

McMillin [1975] has also proposed another form of the MCSST equation. Instead of using observations at different wavelengths, a similar equation to (2.20) can be derived from observations at two different angles and one wavelength. We will not supply the derivation as it is exactly the same as in the previous section. Recalling that the radiation transfer equation is also dependent on zenith angle θ (2.1), the same principle as in the variation of wavelengths can be utilized in the case of differing zenith angles. The final equation is of the same form as (2.20), but the coefficient γ is now formed from transmittances at different angles:

$$\gamma = \frac{1-\tau(\theta_i)}{\tau(\theta_i) - \tau(\theta_j)}. \tag{2.21}$$

2.6.2 Performance of Different Forms of MCSST

McMillin and Crosby [1984] compared the temperature and radiance MCSST methods and found they produced similar results. The values of the γ co-

efficient on the same data sets were within 1% of each other. The radiance model (2.20) was found to perform just slightly better (0.01 K), but the authors did not indicate whether this difference could be considered statistically significant.

McMillin and Crosby [1984] also reported that the SST error was a highly non-linear (though weak for their test sets) function of the temperature difference between the atmosphere and surface, $\overline{T}_a - T_s$. This small difference was not the norm for the cases near the coast acquired in late spring or late autumn though. They attributed this to possibly the wind which usually blows at those times of the year from the continent, carrying warmer continental air over the water.

Shepherd [1993] tested the radiance MCSST method of *McMillin* [1975] with a group of temperature MCSST methods applicable to a NOAA-9 data set. (We also use the same data set, and the details are given in Section 3.3.) *Shepherd* found that the radiance-based MCSST method outperformed the temperature-based MCSST methods by about 0.5 K. He also confirmed the observation of *McMillin and Crosby* [1984], that the prevailing atmospheric conditions near the coast seem to violate the assumptions of the radiance MCSST method. In general, however, we expect radiance-based MCSST methods to perform better as they do not incorporate such a strong dependence on the $\overline{T}_a \approx T_s$ condition as their temperature-based counterparts.

2.6.3 Multi-Wavelength vs. Multi-Angle MCSST Methods

The first multi-angle SST retrieval algorithm was proposed by *Saunders* [1967] in his pioneering effort to tackle the effect of water vapour absorption on SST. He used an aerial radiometer and made measurements at two different angles: nadir and sixty degrees. The second angle was chosen to roughly double the

atmospheric path[1]. Using measurements at different viewing angles *Saunders* managed to account for some influence of the atmosphere and produce more accurate SST estimates (he reported an absolute accuracy of $\pm 0.2\,^{\circ}\mathrm{C}$). His approach, however, was not directly applicable to satellite observations because of much larger atmospheric paths and difficulties in obtaining truly coincident measurements of the same spot on the ocean surface from satellite observations of that time.

The advantage of the multi-angle method is that the same absorption processes affect all the measurements. The multi-wavelength method, on the other hand, ensures very similar surface emissivities, location on the surface and the state of the instrument during acquisition (e.g. electronic noise, temperature drift, etc.).

Although both methodologies were proposed around the same time—multi-angle in 1967, multi-wavelength in 1970—the latter has had much more use. This was probably due to the dominance of the AVHRR instrument. The AVHRR is a multispectral instrument, not capable of acquiring multi-angle data of high enough quality for SST applications. In addition, much of the SST research has been driven by NOAA, who naturally exploited their own instrument. Also, it was easier to build multispectral instruments, since they have only one optical entrance. Multi-angle observations require along-track radiometers, because across-track observations would not yield temporally coincident data. It typically takes around 100 minutes for one orbit of a sun-synchronous satellite. This is far too long to be able to use observations at different angles and assume the same surface temperature or the state of the atmosphere.

This situation changed in the early 1990's with the launch of the Along-Track Scanning Radiometer (ATSR) onboard the ERS-1 satellite. This instrument is a multiple wavelength dual-angle radiometer (nadir and $52\,^{\circ}$). It

[1]This is true only if we assume the surface is a perfect black body and the amount of radiation leaving it is not a function of the zenith angle.

features three infrared channels very similar to AVHRR channels 3, 4 and 5. The novelty in its design was the tighter integration of a two-channel microwave sounder (MWS) with its optical counterparts. The sounder channels are centered at 23.8 and 36.5 GHz, both with a 200 MHz bandwith. Their role is to provide an estimate of the total water vapour and thus enhance the SST retrieval accuracy.

A recent paper by *Merchant et al.* [1999] reported finding an improved set of coefficients for SST retrieval using the ATSR data from ERS-1. They claim that the new coefficients yield a global data set mean and standard deviation of the order of 0.05 and 0.25 K, respectively, with or without the 3.7 μm channels.

It is to be expected that multi-wavelength and multi-angle methods will start to gain equal attention in the future. The adoption and development of novel multi-angle MCSST algorithms will largely depend on the presence of suitable radiometers and their longevity of service.

2.7 Cross-Product SST Method

The cross-product SST method was developed by *Walton* [1988]. He based this method on the fact that the γ parameter in MCSST equations is not necessarily constant over the wide range of possible atmospheric conditions usually encountered in operational SST retrieval. The simplifying assumption of small differential absorption that allows linearization of the radiative transfer equation in all MCSST methods is not valid in the case of atmospheres with high water vapour loading. *Walton* justified this by computing the value of γ using a set of warm marine atmospheric profiles with a varying amount of water vapour. He reported a noticeable departure from linear behaviour for both low (< 2 cm) and high (> 5 cm) values of the total water vapour column.

The derivation starts from a slightly rearranged (2.9):

$$T = T_s + (1 - \tau)(\overline{T}_a - T_s). \tag{2.22}$$

Using the first-order approximation for transmittance in the low-absorption 11–12 μm spectral region of AVHRR channels 4 and 5:

$$\tau = \exp(-k \cdot u) \approx 1 - k\,u,$$

equation (2.22) can be expanded to a system of equations:

$$\begin{aligned} T_i &= T_s - k_i b_i \\ T_j &= T_s - k_j b_j \end{aligned} \tag{2.23}$$

where: $b_i = u(T_s - \overline{T}_{ai})$ and $b_j = u(T_s - \overline{T}_{aj})$; u is the water vapour path length, k_i and k_j are the water vapour absorption coefficients associated with the channels i and j.

The MCSST solution is obtained from (2.23) under the assumptions that k_i and k_j are known constants and that the channel atmospheric temperatures $\overline{T}_{ai}$ and $\overline{T}_{aj}$ are equal, or alternatively, $b_i = b_j$. An alternative with less restrictive assumptions is to compile a set of satellite observations and sort the data into bins of constant channel temperatures T_i and T_j. Inside each bin we can assume that k_i and k_j are constant with much more certainty. Summing (2.23) over a collection of n measurements inside one bin, we find:

$$\begin{aligned} n\,T_i &= \sum T_s - k_i \sum b_i \\ T_i &= \mathrm{SST}_i - k_i \bar{b}_i \end{aligned} \tag{2.24}$$

where $\mathrm{SST}_i = (\sum T_s)/n$ and $\bar{b}_i = (\sum b_i)/n$. It is important to note that SST_i and $\bar{b}_i$ are dependent on the channel temperature T_i. The SST_i parameter can be construed as a single channel temperature estimate of the actual surface temperature T_s. The same equation as (2.24) can be written for the channel j.

Equation (2.24) defines the absorption coefficient as a function of the chan-

nel brightness temperature T_i:

$$k_i = \frac{\mathrm{SST}_i - T_i}{\bar{b}_i}. \tag{2.25}$$

Substituting (2.25) into (2.23) yields:

$$\begin{aligned} T_i &= T_s - (\mathrm{SST}_i - T_i)\frac{b_i}{\bar{b}_i} \\ T_j &= T_s - (\mathrm{SST}_j - T_j)\frac{b_j}{\bar{b}_j}. \end{aligned} \tag{2.26}$$

Making the assumption that $b_i/\bar{b}_i$ and $b_j/\bar{b}_j$ are approximately equal—which holds true in the 11-12 μm spectral region—and solving the set of linear equations (2.26) for T_s gives the CPSST estimate of SST:

$$\mathrm{CPSST} = T_i + \frac{\mathrm{SST}_i - T_i}{\mathrm{SST}_j - T_j + T_i - \mathrm{SST}_i}. \tag{2.27}$$

Stemming from the derivation, we point out that the CPSST solution (2.27) imposes much less restrictive assumptions than the MCSST. The absorption coefficients are no longer universal constants, and the mean atmospheric temperature $\overline{T}_a$ does not have to be the same in all channels.

The single-channel solutions SST_i must be specified before (2.27) can be utilized. *Walton* [1988] proposed a simple linear expression stating that this would be an adequate approach to correct for absorption of the non-variant uniformly mixed gases (e.g. CO_2, N_2):

$$\mathrm{SST}_i = a_i T_i + c_i, \tag{2.28}$$

where i stands for the AVHRR channels 4 and 5. Coefficients a_i and c_i are determined from a regression fit using a representative range of atmospheres.

A graphical explanation of the CPSST method can also be given using a graph shown in Figure 2.2. We have two points from (2.28) for each channel

on the plot of T_b vs. T_s (T_b is channel brightness temperature; T_s is sea surface temperature): (T_{b4}, T_{s4}) and (T_{b5}, T_{s5}). A line through these two points is extrapolated to the unity line, $T_{si} = T_{bi}$. The unity line can be interpreted as representing a channel free of atmospheric absorption. The intersection point, denoted in the graph as *True SST* , is interpreted as a final and hopefully improved estimate of the true SST.

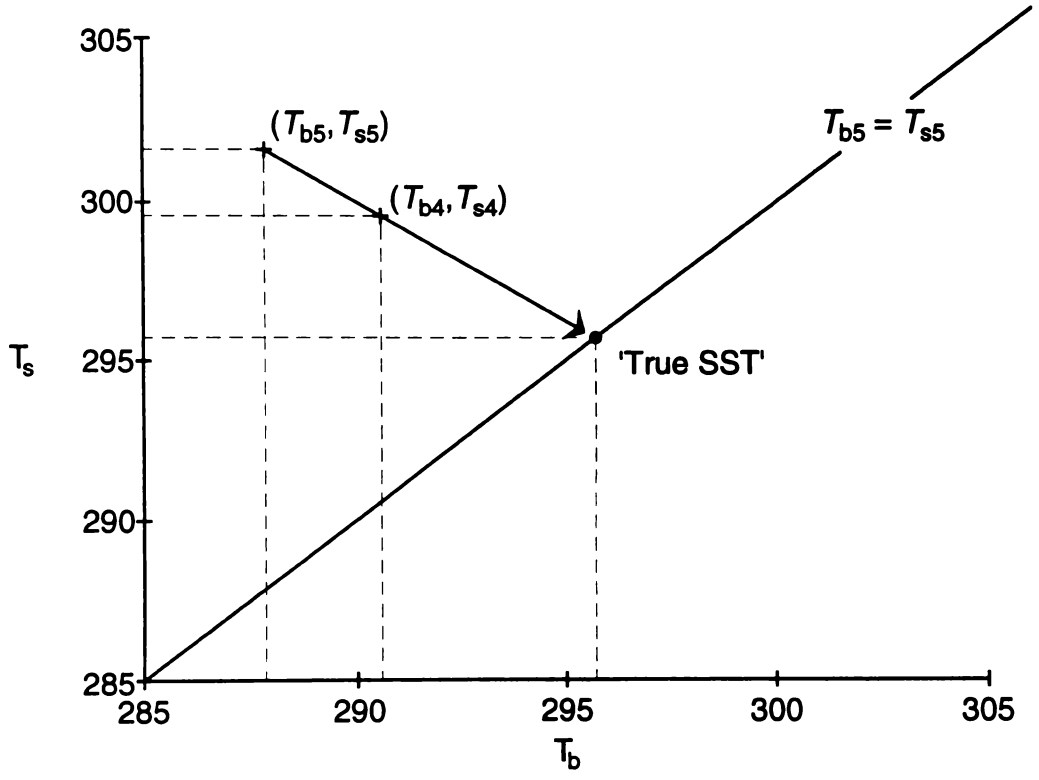

Figure 2.2: Graphical explanation of the CPSST method of *Walton* [1988]. T_b is channel brightness temperature; T_s is sea surface temperature. (From *Smith* [1993].)

Following this graphical explanation, it is straightforward to obtain the equation for the CPSST:

$$\text{CPSST} = \frac{T_{s5} \cdot T_{b4} - T_{b5} \cdot T_{s4}}{T_{b4} - T_{b5} + T_{s5} - T_{s4}}. \tag{2.29}$$

Simulation studies have shown that if the satellite data is error free, MCSST and CPSST methods are equally accurate. In the presence of random

or white noise, however, the CPSST outperforms the MCSST. Tests of the CPSST method using the data in the North Atlantic and North Pacific in 1982 (comparatively noise-free channel 3) and 1983 (much noisier) were reported as successful [*McClain*, 1989].

CPSST equations were used operationally by NOAA-NESDIS during the late 1980's and early 1990's. Their form included an extra term to account for the different path length due to a non-zero zenith angle.

2.8 Nonlinear SST Method

The Nonlinear SST (NLSST) algorithm was first proposed by *Walton et al.* [1990]. The algorithm was undergoing testing at NOAA NESDIS at that time; it has been operational since April 1991 [*Walton et al.*, 1998].

The main difference between the MCSST (Section 2.6) and the CPSST (Section 2.7) methods is in the form of the γ coefficient, which in the case of the latter has a specific two-channel temperature dependence. This can be shown by rearranging (2.29) into the "MCSST" form:

$$\text{CPSST} = T_{b4} + \underbrace{\frac{T_{s4} - T_{b4}}{T_{s5} - T_{b5} + T_{b4} - T_{s4}}}_{\gamma}(T_{b4} - T_{b5}). \tag{2.30}$$

The crux of the NLSST algorithm is in the formulation of the γ coefficient, which becomes a linear function of the surface temperature. The NLSST algorithm assumes this functional relationship:

$$\text{NLSST} = T_{b4} + \gamma(T_{sfc})(T_{b4} - T_{b5}), \tag{2.31}$$

where $\gamma(T_{sfc})$ equals a constant times an external estimate of the ocean surface temperature (T_{sfc}) in units of degrees Celsius. Thus the NLSST can be viewed as an additional simplification of the CPSST.

The first term in (2.31) is a single-channel measurement which is governed

by the thermal structure of the ocean surface. The second term, a function of the temperature difference in two IR channels, measures the effect of atmospheric absorption of the single-channel surface radiance measurement that results from absorption and re-emission by the overlying atmosphere, principally by water vapour. Because the second term is describing the atmospheric effect, which does not have the same horizontal temperature structure as the ocean skin, it is not essential to use a high-resolution surface temperature estimate in the γ coefficient of (2.31). A lower resolution climatological temperature estimate would probably suffice.

Walton et al. [1998] stated that one advantage of this form of γ removes or greatly reduces any dependence of the γ coefficient on satellite measurements. *May* [1993] demonstrated that a typical AVHRR channel-4 and -5 sensor noise value of 0.05 °C results in a 0.33 °C error in the output temperature from the CPSST algorithm, caused partly by the fact that the input error propagates into the γ coefficient. The same level of noise fed into the NLSST produces an error of 0.2 °C.

Since the initial value of the surface temperature is not known *a priori* it must be estimated in some way. *Walton et al.* [1998] compared the effect of initial SST estimates on the NLSST algorithm. The satellite data used was collected over the entire globe in one month, and matched within four hours and 25 km with drifting buoys. He used three different sources for T_{sfc}:

1. A NESDIS analysis compiled from previous orbits of AVHRR SST's. It was maintained on a 1 ° latitude/longitude grid mesh, with a resolution of approximately 100 km for both Northern and Southern hemispheres.

2. An estimate derived from a monthly climatological temperature analysis on a 1 ° latitude/longitude square grid mesh.

3. SST estimates returned from the MCSST algorithm. These estimates were obtained from the same satellite measurement and were of the same resolution as the NLSST (8 km).

Walton et al. reported a somewhat surprising outcome: T_{sfc} derived from the monthly climatology, which had the greatest scatter against the drifting buoys, yielded the most accurate NLSST algorithm. He attributed this result to the sensitivity of the NLSST to any correlation between the errors in the γ coefficient and errors in the satellite measurements. However, because of its low resolution, such a climatology would not be usable near coastlines, nor in areas with anomalous climatological conditions (such as El Niño). Because of this reason, NOAA NESDIS employs their own SST analysis for operational computation of T_{sfc} and its use in their global NLSST model.

A regional user of NLSST who does not have a good *a priori* estimate of T_{sfc} might use the MCSST result. In this case, the user should make a considerable effort to remove error sources from their data since γ is a function of satellite measurements and has strong correlative effect as described above.

2.9 Transmission Ratio SST Methods

The MCSST, CPSST and NLSST methods presented in the previous sections (Section 2.6, 2.7 and 2.8) rely on periodicaly updated coefficients using ocean buoys to provide surface truth, in order to prevent the main source of SST errors—local atmospheric fluctuations. As an alternative to this *in situ* tuning approach, a new generation of atmospherically correcting algorithms has been developed. We refer to them as Transmission Ratio SST methods (TRSST), although they are also called Image Variance techniques [*Barton*, 1995].

The concept of using the variance in brightness temperature images for determination of atmospheric and surface parameters was introduced by *Kleespies and McMillin* [1990] and *Jedlovec* [1990]. The TRSST methods are all based on the notion that the atmosphere is horizontally homogeneous over an area while the surface temperature may change. These methods implement an MCSST-

like equation (2.20), in which the γ coefficient includes a transmittance ratio:

$$R_{54} = \frac{\tau_5}{\tau_4}, \tag{2.32}$$

where 4 and 5 refer to the corresponding AVHRR channels; τ is the surface-to-satellite atmospheric transmittance for a given channel. The effect of including R_{54} in the γ coefficient is to increase the magnitude of the atmospheric correction as the atmosphere becomes optically thicker. We present now the most important TRSST methods.

2.9.1 Method of *Harris and Mason* [1992]

Harris and Mason applied the Závody (Rutherford Appleton Laboratory, U.K.) radiative transfer model to a suite of 56 ocean radiosonde profiles to compute the at-satellite AVHRR brightness temperatures[2] in channels 4 and 5 for nadir viewing. By regressing $(T_s - T_4)$ against $(T_4 - T_5)$, *Harris and Mason* derived a conventional SST algorithm of the form given in (2.12). They then observed that the rms residual error could be significantly improved by arranging that the coefficient which scales the $(T_4 - T_5)$ correction be increased as the atmosphere becomes optically thicker. They found that the ratio of transmittances in channels 5 and 4, (2.32), provided a suitable weighting factor, resulting in a new transmittance-ratio split-window algorithm:

$$T_s = T_4 + \frac{1.755}{R_{54}}(T_4 - T_5) + 0.38, \tag{2.33}$$

whose rms residual for the simulation set was 0.12 K. *Harris and Mason* also developed a 4-coefficient regression fit, but we judged the 0.01 K improvement in rms residual not to be significant, so chose not to implement it for these tests.

[2]They did not identify which AVHRR filter functions were used; from the date of their work it seems likely they used NOAA-11.

2.9.2 Method of *Sobrino, Li and Stoll* [1993]

Sobrino et al. [1993] continued the Harris and Mason philosophy of including explicitly, via the R_{54} transmittance ratio, the effect of variable optical depth on the split-window coefficients. Using a set of 60 radiosoundings which cover the worldwide variability of SST (250 to 315 K) and atmospheric moisture (0.2 to 6.7 g/cm^2), they considered three observation angles (0°, 23°, 46°) and three surface temperatures for a total of 540 simulated geophysical situations. The resulting NOAA-11 AVHRR channel 4 and 5 brightness temperatures were computed with LOWTRAN-7 [*Kneizys et al.*, 1988]. Their simulation study produced the following 4-coefficient split-window SST algorithm:

$$T_s = T_4 + (2.301/R_{54} - 0.16)(T_4 - T_5) - 4.20/R_{54} + 4.61, \qquad (2.34)$$

giving a standard error of 0.27 K for the 540 simulation points. *Sobrino et al.* derived the ratio parameter, R_{54}, from the channel transmittance or total water vapour data, whereas *Harris and Mason* [1992] obtained it from the changes in brightness temperatures observed from space in the two wavebands.

2.9.3 Method of *Sobrino, Li, Stoll and Becker* [1994]

Sobrino et al. [1994] investigated a generalization of the transmittance-ratio split-window technique to the more difficult problem of land surface temperature (LST) determination. Using NOAA-11 filter functions, the same representative set of 60 radiosondes (described in Section 2.9.2), three observation angles, 49 surface emissivity combinations (ε_4, ε_5 ranging from 0.9 to 1.0, with $\Delta\varepsilon$ ranging from -0.02 to 0.02), and five surface temperatures, a total of 44,100 (T_4, T_5) situations were simulated. Their resulting LST algorithm was presented as a radiance formulation:

$$B_4(T_s) = (\alpha_1 + \frac{\alpha_2}{R_{54}})B_4(T_4) + (\alpha_3 + \frac{\alpha_4}{R_{54}})B_4(T_5) + (\alpha_5 + \frac{\alpha_6}{R_{54}}), \qquad (2.35)$$

where $B_4(T)$ is the channel-4 blackbody radiance at temperature T, and the α_i $(i = 1 \ldots 6)$ are functions of channel surface emissivities ε_4 and ε_5. Since for SST studies we can set $\varepsilon_4 = \varepsilon_5 = 1$ [*Liou*, 1980], the emissivity dependence inherent in the α_i coefficients of (2.35) disappears, so that (2.35) becomes equivalent to an SST algorithm stated in radiance space. For this idealized case, the α coefficients simplify to the emissivity-independent constants listed in column 1 of their Table V [*Sobrino et al.*, 1994]: $\alpha_1 = -0.4048$, $\alpha_2 = 3.3074$, $\alpha_3 = 1.4928$, $\alpha_4 = -3.3771$, $\alpha_5 = 0.1416 \times 10^{-6}$, $\alpha_6 = -0.2264 \times 10^{-6}$.

Although not stated in their paper, it is clear that while α_1 through α_4 are dimensionless, coefficients α_5 and α_6 must carry units of radiance. *Sobrino et al.* used LOWTRAN-7 for their radiative transfer calculations, so we presume that (2.35) is written for the default LOWTRAN blackbody radiance unit of W/(cm^2 sr cm^{-1}). Since we choose to work in the standard NOAA/NESDIS radiance units of mW/(m^2 sr cm^{-1}), we scaled the listed values for α_5 and α_6 by a multiplicative factor of 10^7.

2.9.4 Method of *Yu and Barton* [1994]

Yu and Barton [1994] developed their own TRSST formula by expanding the radiative transfer equation in radiance space around the surface temperature. The atmospheric radiation contribution term in their paper was split into the upwelling and surface-reflected downwelling atmospheric radiation parts. The final formula was presented in the well-known MCSST form as:

$$T_s = T_5 + \frac{C_4}{C_4 - R_{54}C_5}(T_4 - T_5), \tag{2.36}$$

where

$$C_i = C(T_i) = \frac{K_i}{T_i^2}\frac{e^{\frac{K_i}{T_i}}}{e^{\frac{K_i}{T_i}} - 1} - \frac{2}{T_i} \quad (i = 4, 5),$$

and K_i $(i = 4, 5)$ are channel-dependent constants.

Yu and Barton used both real and simulated data set to test (2.36). They selected a cloud-free 50 × 50 pixels scene acquired by NOAA-9 and calculated R_{54} statistically:

$$R_{54} = \frac{1}{N} \sum_{n}^{50\times50} \frac{T_5(n) - \overline{T}_5}{T_4(n) - \overline{T}_4}, \tag{2.37}$$

where $\overline{T}_i$ $(i = 4, 5)$ is the average brightness temperature for the channel in the scene. When applied to the test scene using the then current MCSST NOAA-NESDIS equation, (2.36) produced a bias of 0.01 K, rms difference of 0.12 K and standard deviation of 0.12 K.

To test the TRSST formula (2.36) on a simulated set, *Yu and Barton* used an in-house atmospheric transmission model [*Barton*, 1985] coupled with the NOAA-9 AVHRR channel 4 and 5 filter functions to obtain corresponding satellite brightness temperatures for the nadir view. Twenty-five radiosonde profiles were collected together with SST temperatures (using an infrared radiometer from a ship). The profiles were fed into the transmission model with a range of SST (±1 °C from the ground truth) values for each profile. The SST error between the model and the ground truth had a bias of 0.07 K and rms of 0.28 K.

2.9.5 Sensitivity Analysis of TRSST Methods

Yu and Barton [1994] indicated that the TRSST techniques depend heavily on the ability to derive a stable value for the transmittance ratio. To test this, *Barton* [1995] chose a 200 × 200 pixel scene of the same location acquired on consecutive days by the AVHRR on NOAA-11 and the ATSR on ERS-1. He calculated the value of R_{54} in three different ways:

1. As given in (2.37);
2. As average of $\frac{T_5(n)-\overline{T}_5}{T_4(n)-\overline{T}_4}$ for the whole scene;
3. Simply as average of the ratio of the variances in the two channels.

The lack of consistency for the values of R_{54} led *Barton* to conclude that the calculation of the ratio is quite unstable and TRSST methods are difficult to apply on an operational basis. He attributed this to the basic assumption of a uniform atmosphere overlying an ocean surface with variable SST, and/or the data digitization effects dominating the analysis.

2.10 Alternative Approaches to SST Retrieval

We will mention here some of the methods which have attempted to tackle the SST retrieval problem in ways different to the traditional methods featured so far in this chapter.

- The influence of water vapour is included in an MCSST-like equation via the total water vapour column [*Emery et al.*, 1994].
- The channel brightness temperature difference, long recognized as an estimate of the effect of atmospheric moisture, is included in an SST equation up to the second order [*Emery et al.*, 1994].
- Instead of any assumptions regarding the radiative transfer equation, a method proposed by *Steyn-Ross et al.* [1993] uses an iterative procedure with a near-by radiosonde profile and a rigorous atmospheric transmission model.

These methods are briefly described below.

2.10.1 Inclusion of Water Vapour

As the water vapour increases in the atmosphere, i.e. the atmosphere is becoming more *optically thick*, the basic principles underlying the MCSST, CPSST and NLSST methods become less valid. The TRSST methods (see Section 2.9) try to account for the effect of increasing water vapour with the inclusion of a channel-4 and -5 transmittance ratio in their equations.

Emery et al. [1994] expanded the approximation of the channel transmittance given in (2.13) up to second order, namely:

$$\tau = \exp(-ku) \approx 1 - ku + \frac{(ku)^2}{2}. \tag{2.38}$$

Returning to the equation for the γ coefficient (2.20), *Emery et al.* showed it can be written in a simple linear form:

$$\gamma = a + b \cdot u, \tag{2.39}$$

where a and b are functions of the absorption coefficients k's. The SST formula for their method, called the WVSST, is then:

$$WVSST = a_1 + a_2 T_4 + a_3(T_4 - T_5) + a_4 \frac{W}{\cos\phi}(T_4 - T_5), \tag{2.40}$$

where W is the total column atmospheric water vapour from the sea to the satellite, and ϕ is the satellite scan angle. For the value of W, *Emery et al.* used nearly coincident measurements of the SSM/I microwave sounder.

To compute the algorithm coefficients a_i $(i = 1, \ldots, 4)$ *Emery et al.* used the transmission model of *Barton* [1985] with the NOAA-11 filter functions, and 300 oceanic radiosonde profiles. With noise included, the WVSST produced SST errors with biases in the range -0.34–0 K, and rms's in the range 0.5–0.78 K (they gave error statistics for a range of satellite scan angles). Without noise, the error biases were -0.37–0 K and rms's 0.27–0.57 K. The zero Kelvin errors were reported only for the nadir view cases.

2.10.2 Quadratic $T_4 - T_5$ Term

Emery et al. [1994] also concluded that the value of W in (2.40) can be replaced by the channel temperature difference, $T_4 - T_5$. The notion that this difference is a credible estimate of the effect of atmospheric moisture is as old as the first

MCSST methods [*Anding and Kauth*, 1970, *Prabhakara et al.*, 1974]. So *Emery et al.* proposed another form of an SST retrieval equation, called Quadratic SST (QSST):

$$QSST = a_1 + a_2 T_4 + a_3(T_4 - T_5) + a_4(T_4 - T_5)^2. \quad (2.41)$$

The advantage of this formula is that there is no need for additional data to estimate the water vapour term.

By using the same method to derive coefficients as in Section 2.10.1, *Emery et al.* reported the SST statistics for the noise-free set at -0.68–0 K bias and 0.3–0.87 K rms. The set with the noise included had a bias of -0.8–0 K and rms of 0.54–1.09 K. The zero Kelvin errors were reported only for the nadir view cases.

Emery et al. reported that while the QSST made a considerable improvement over the MCSST and CPSST methods, the WVSST showed overall smaller errors when compared to both skin and bulk *in situ* observations. This is probably due to how the influence of water vapour is modelled in the algorithms. The WVSST uses the SSM/I measured value, whereas the QSST uses the channel temperature difference. The QSST also was found to underestimate the SST in the lower latitudes and overestimate the SST in the higher latitudes. Correlations between the AVHRR thermal channel differences and SSM/I water vapour demonstrated the inability of the channel difference to represent water vapour in the mid- and high-latitudes during summer. When compared against the drifting buoy data the WVSST and the QSST both exhibit the same general behaviour with relatively small differences to the buoy temperatures.

2.10.3 Method of *Steyn-Ross et al.* [1993]

This method represents the basis of the work in this thesis, so we are mentioning it here for the completeness only. An extensive description of the method is given in Chapter 3.

Chapter 3

Dynamic Water Vapour Method

In Chapter 2 we discussed the main methodologies and techniques developed in the past for the retrieval of sea surface temperatures. The common approach in the development of all these methods was the linearization of the radiative transfer equation (2.1). The values of the coefficients which appear in the linearized radiative transfer equation were normally obtained through best-fit regressions of coincidental buoy SST and satellite radiation observations. Although easy to implement, these methods can yield large SST errors if the local atmospheric conditions differ significantly from the conditions which prevailed during the regression averaging.

In this chapter, we describe the Dynamic Water Vapour method (DWV). This method was developed at the Physics Department of the University of Waikato by Moira and Alistair Steyn-Ross, and their MSc student Peter Smith in 1993 [*Smith*, 1993, *Steyn-Ross et al.*, 1993]. In contrast to the methods of Chapter 2, the DWV algorithm does *not* assume the atmosphere to be constant over any given spatial or temporal extent. In fact, DWV is perfectly suited for per-pixel analysis as it does not assume any similarity of the atmospheric conditions in adjacent AVHRR pixels. An added advantage of the DWV algorithm is its formulation in the radiance unit space, as opposed to more traditionally utilized temperature unit space. Radiance-space calculations allow for a more

consistent treatment of the nonlinearity corrections used in the calibration of AVHRR infrared channels 4 and 5 [*Steyn-Ross et al.*, 1992]; and have been shown to yield more accurate SST estimates than the temperature-unit based methods in coastal areas [*Shepherd*, 1993].

3.1 DWV Rationale

The DWV approach to the problem of SST determination from satellite radiance is conceptually equivalent to that used to retrieve atmospheric profiles of temperature and molecular composition: Given a set of observed at-satellite radiances, what is the optimal atmospheric profile that minimizes the differences between the predicted radiances (as found by ingesting the profile into a suitable atmospheric model) and the actual radiances?

This problem has been tackled by many workers. The physical methods of *Chahine* [1970] and *Smith* [1970] apply the equation of radiative transfer to retrieve atmospheric temperatures located at the peaks of weighting functions, iterating from a first-guess profile until convergence is reached.

Inverse-matrix methods [*Rodgers*, 1976, *Eyre*, 1987, 1989] linearize the equations of transfer about a first-guess atmospheric profile and cast them into matrix form. If the transmission is assumed to be independent of temperature, then the matrix equation is linear in temperature deviation about the first-guess values. The temperature profile can then be retrieved by inverting the matrix equation using a minimum variance technique. However, when the interaction and inter-dependence of atmospheric components need to be considered, the inverse problem becomes nonlinear, and, as described by *Rodgers* [1976], becomes one of estimation: What are the appropriate criteria which determine the optimum solution for a given set of observations?

The DWV approach attempts to solve the nonlinear estimation problem using a physical approach similar to that of *Chahine* [1970] and *Smith* [1970]. At each iteration, DWV adjusts the atmospheric profiles by a set amount, then

recalculates the transmissivities for each channel. Central to the estimation problem is the choice of the "forward" model: Given the atmospheric profiles, how does one compute the at-satellite radiances? The LOWTRAN-7 [*Kneizys et al.*, 1988] atmospheric model was used in the DWV investigation.

LOWTRAN-7[1] is a well-known propagation model and software for predicting atmospheric transmittance and upwelling/downwelling radiance for a specified atmospheric path at low spectral resolution ($20\,\mathrm{cm}^{-1}$). The software, written in FORTRAN, uses a single-parameter band model for molecular absorption, and includes the effects of continuum absorption, molecular scattering and aerosol extinction.

3.2 DWV Algorithm Formulation

The DWV retrieval method starts from the radiative transfer equation for a clear atmosphere assuming a mean-value approximation (for more information about this equation see Section 2.4):

$$I_\nu = B_\nu(T_s)\tau_\nu + B_\nu(\overline{T}_a)(1-\tau_\nu) \tag{3.1}$$

where I_ν is the upwelling radiance sensed by the satellite at a wavenumber ν; $B_\nu(T_s)$ is the Planck spectral black body radiance function (the formula is given in (2.7)) at the surface temperature T_s; τ_ν is the transmittance of the entire atmosphere; $\overline{T}_a$ is the average atmospheric temperature, defined via the following equation:

$$B_\nu(\overline{T}_a) = \frac{\int_{\tau_s}^{1} B_\nu(T(p))\mathrm{d}\tau_\nu(p)}{\int_{\tau_s}^{1} \mathrm{d}\tau_\nu(p)} \tag{3.2}$$

where $\tau_\nu(p)$ is the transmittance at pressure level p.

Central to the DWV algorithm is the assumption that the water vapour

[1]The model and software are developed and actively maintained by the Optical Physics Division of the U.S. Air Force Geophysics Laboratory at the Hanscom AFB, Massachusetts.

content of the atmosphere is the most important and most rapidly varying component. All other gas constituents are assumed constant. Hence, any mismatch between the assumed model atmosphere of the DWV algorithm and the actual atmosphere is primarily due to differences in the assumed water vapour profile.

Inversion of (3.1) for both AVHRR thermal infrared channels (channels 4 and 5) gives us an estimate of the true sea surface temperature.

$$T_{s,i} = B^{-1}\left(\nu_i, \frac{I_i - B_i(\overline{T}_a)(1-\tau_i)}{\tau_i}\right) \tag{3.3}$$

where i stands for AVHRR channels 4 and 5; ν_i is the central wavenumber for the i-th AVHRR channel; B^{-1} is the inverse Planck function defined as:

$$T \equiv B^{-1}(\nu, B) = \frac{hc\nu}{k \cdot \ln\left(1 + \frac{2hc^2\nu^2}{B}\right)}. \tag{3.4}$$

The difference $\Delta\text{SST} = T_{s,4} - T_{s,5}$, where $T_{s,4}$ and $T_{s,5}$ are SST estimates from (3.3), indicates by how much the assumed and actual water vapour profiles differ. If there were no error in the assumed atmosphere then $\Delta\text{SST} = 0$ (within the measurement and computational errors, of course). The value of ΔSST was used as an objective function (also referred to in the literature as *cost function*) in the generation of the algorithm's correction look-up table.

In the unlikely event the transmittance τ_ν and atmospheric radiance $B(\overline{T}_a)$ in both channels are the same, (3.3) will yield a single unambiguous solution for SST. In the more likely case, only approximate first guesses for channel transmittances and atmospheric radiances can be expected, leading towards a pair of SST estimates, $T_{s,4}$ and $T_{s,5}$. The DWV algorithm computes first-guess channel transmittances and atmospheric radiances by running LOWTRAN-7 initialized with a radiosonde profile recorded in the region of interest, i.e. spatially and temporally as close as practicable to the processed AVHRR pixel. The SST value is initialized using the monthly average, which could be ob-

tained, for example, from climatological archives.

The steps involved in creating a look-up table are:

1. Calculate the first-guess values for the atmospheric transmittance and radiance for AVHRR channels 4 and 5 using LOWTRAN-7 initialized with a radiosonde profile acquired from a nearby site.

2. Maintain the same temperature profile as used in Step 1, but adjust the water vapour profile by assuming there has been a systematic fractional shift, denoted by Δ, of the entire profile. At each atmospheric pressure level p, as defined by the initial radiosonde profile, the new water vapour content becomes:

$$H_2O'(p) = (1 + \Delta)H_2O(p) \tag{3.5}$$

   where $-1 \leq \Delta < \infty$ is a coefficient, the same for every p level.

   For easier description of the change in the amount of water vapour, we will introduce the coefficient $k = 1 + \Delta$. Thus, $k = 0$ means a completely dry atmosphere; $k = 1$ no change, i.e. initial water vapour profile; $k = 2$ means the amount of water vapour in the atmosphere is doubled.

3. Calculate new atmospheric transmittance and radiance using LOWTRAN-7 and the new water vapour profile; all other atmospheric constituents and temperature profile are held constant. Substitute the new atmospheric transmittance and radiance in (3.1) to obtain the channel radiance pair I'_4 and I'_5. These represent the predicted at-satellite AVHRR channel 4 and 5 radiances for the water vapour profile changed by k.

4. Using the new at-satellite radiances, I'_4 and I'_5, channel atmospheric transmittances and radiances, calculate channel SST estimates $T_{s,4}$ and $T_{s,5}$ from (3.3). Their difference ΔSST is more likely to be non-zero, thus establishing the correspondence with the water vapour change coefficient k.

5. Keep repeating Steps 2–4 for a range of k values (typically $0 < k \leq 2.5$). Record five variables (ΔSST, $B_4(\overline{T}_a)$, $B_5(\overline{T}_a)$, τ_4 and τ_5) for each k into a look-up table.

6. Convert the measured (raw) AVHRR channel 4 and 5 counts to satellite radiance with the claibration method of *Steyn-Ross et al.* [1992]. Ensure the AVHRR pixel in question is cloud-free.

7. Use ΔSST as an index to the water vapour correction table to estimate a first-guess value for k and corrected atmospheric transmittances (τ) and radiances ($B(\overline{T}_a)$). Substitute these along with the measured at-satellite radiance in (3.3) and obtain an improved estimate of ΔSST.

8. Select several table entries on either side of the initial k guess and repeat the previous step. The iteration that minimizes $\mid T_{s,4} - T_{s,5} \mid$ is taken as the best SST estimate. Due to measurement and computational errors (round-off and LOWTRAN-7 model imperfections) $T_{s,4}$ and $T_{s,5}$ for any k will never be the same. So, the final SST estimate is calculated as the average of the two channel SST estimates.

Shown in Figure 3.1 are DWV correction curves, i.e. ΔSST vs. k, for three notably different water vapour profiles from our data set (Section 3.3). The circles in this figure indicate the optimal k adjustment that gives rise to a zero ΔSST. Having obtained the optimal water vapour adjustment enables straightforward computation of other atmospheric profile properties, such as: total water vapour content between the satellite and the ocean surface for the pixel (found by integrating the modified water vapour profile along the ray path—performed in LOWTRAN-7), average atmospheric temperature (deduced by using (3.2)), etc.

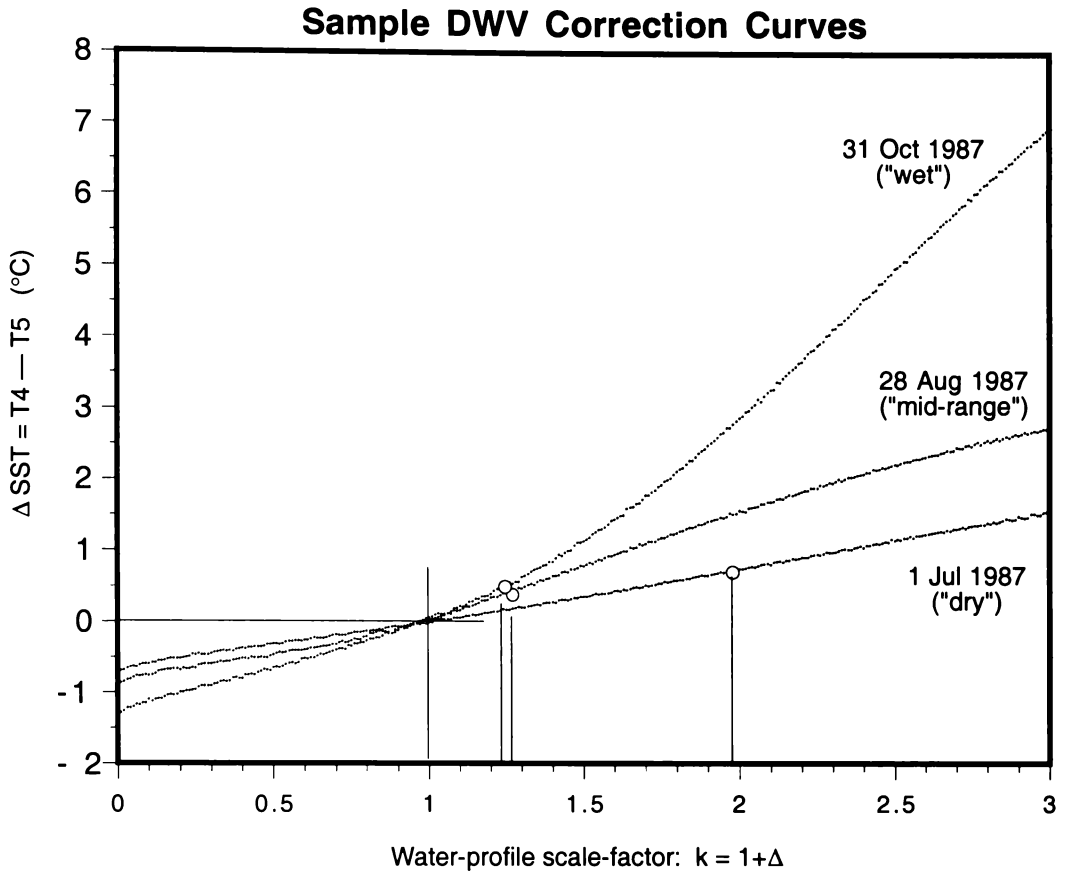

Figure 3.1: Calculated sea surface temperature mismatch as a function of water content adjustment for three water vapour profiles. The circles show the optimal value of the water vapour content adjustment that nullifies ΔSST. (From *Smith* [1993].)

3.3 The Test Data Set

The test data set consisted of buoy-measured sea surface temperatures (ground truth), radiosonde-measured atmospheric profiles from three locations closest to the buoy, and coincident cloud-free AVHRR infrared images.

3.3.1 Sea Surface Temperature Data Set

The ground truth data to test the DWV algorithm was collected by a Waverider buoy, moored and operated by the CSIRO[2] Marine Laboratories in Hobart, Tasmania. The location of the buoy was 145°9.4′ E, 42°8.7′ S, as shown in

[2]Commonwealth Scientific and Industrial Research Organization.

Figure 3.2. The location of the buoy had been checked three times during the

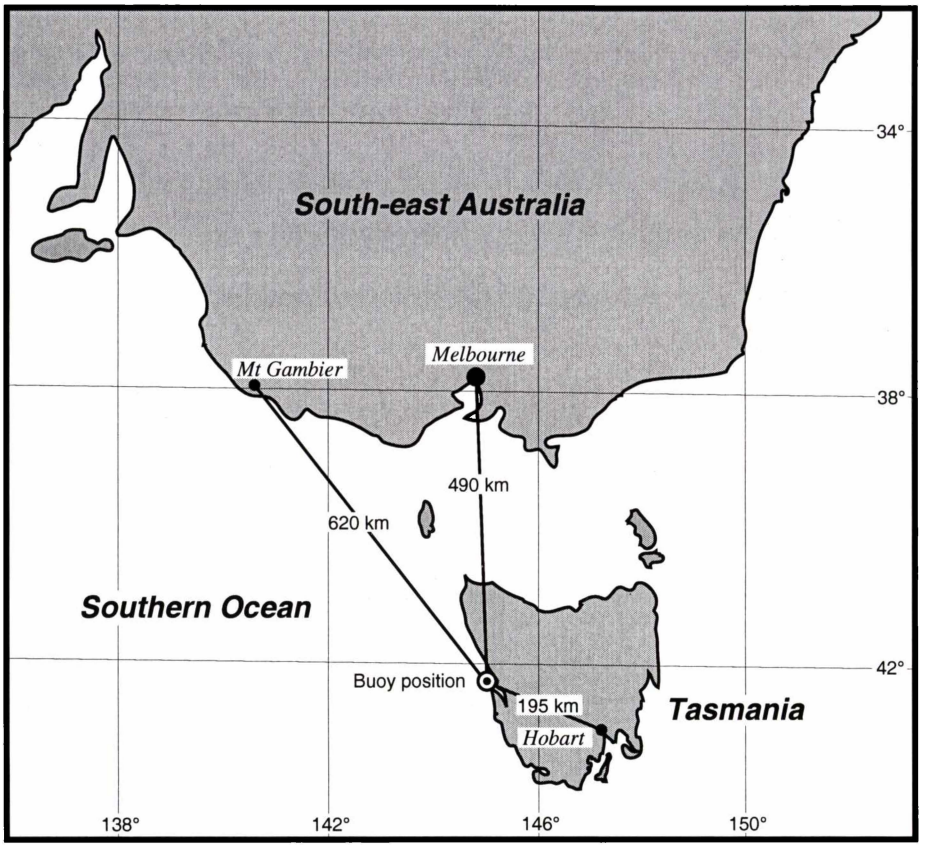

Figure 3.2: Location of the buoy and the three radiosonde sites. (Graph created by James Shepherd.)

duration of the measurement. The buoy operated from 27 April to 21 December 1987. The temperature was measured every 12 minutes, at an effective depth of 32 cm and to an absolute accuracy of ± 0.1°C. Technical details of the buoy are given in Table 3.1.

The buoy data is given in Table 3.2, together with the matching satellite pass. The passes are represented by their IFUT codes. IFUT is a base-36 code developed by CSIRO Hobart to unambiguously identify each satellite orbit. The result is a unique 4 character code for each received AVHRR image. The local time of the buoy SST measurements and satellite passes is also given for comparison. It can be seen from the table that the SST measurements were almost coincident with the AVHRR measurements. Since that amount of water

Table 3.1: Technical details for the Waverider buoy.

Manufacturer	Datawell BV, Haarlem, the Netherlands
Temperature range	0.7–39.5 °C
Accuracy	0.2 °C
Long Term Stability	1 year< 0.1 °C
Resolution	0.02 °C
Rate	Once every 6.037 minutes
Delay	6.415 minutes
Effective sensor operating depth	32 cm

has considerable thermal inertia, the set of SST and AVHRR measurements can be considered coincident.

3.3.2 Atmospheric Profile Data Set

The radiosonde data were purchased from the Bureau of Meteorology in Melbourne, Australia. The data obtained was from three nearest sites to the buoy (as shown in Figure 3.2): Hobart (Tasmania), Laverton (near Melbourne, Victoria) and Mount Gambier (South Australia).

The instrument used was the Astor 402 MHz Mark III radiosonde. Each radiosonde used a helium inflated balloon for uplift. As it travelled upwards, three properties of the atmosphere were measured. These were: pressure, temperature and relative humidity. The sensors used were:

- For pressure: Single aneroid capsule-type sensor, accurate to ± 1 mb;
- For temperature: A rod-type ceramic resistor, coated white and mounted on the outrigger; accurate to $\pm 1\,^{\circ}$C;
- For humidity: A carbon element, radiation shielded, with accuracy of 5%.

The data were delivered to us in the post-processed form, only with measurements at the preset number of levels defined by the atmospheric pressure. The levels were set to be: surface, 1000, 900, 850, 800, 700, 600, 500, 400,

Table 3.2: The buoy data together with corresponding satellite passes. The times in the table are local time (UTC+10); sea temperature is in °C.

IFUT code	Date	Sat. Time	Buoy Time	Sea Temp.
m9jr	9/5/87	3:25	3:28	13.83
m9k5	10/5/87	3:16	3:08	13.89
m9kc	10/5/87	15:35	15:28	14.11
m9n9	18/5/87	1:49	1:48	13.76
m9na	18/5/87	3:29	3:28	13.74
m9vi	8/6/87	3:07	3:08	12.73
ma4c	30/6/87	16:30	16:28	12.08
ma4i	1/7/87	2:17	2:08	11.45
mabk	19/7/87	2:23	2:28	10.77
mabz	20/7/87	3:54	3:48	11.21
mac6	20/7/87	16:15	16:08	12.40
macc	21/7/87	2:02	2:08	11.12
macd	21/7/87	3:43	3:48	11.35
macq	22/7/87	1:52	1:48	11.91
macr	22/7/87	3:32	3:28	11.64
mad5	23/7/87	3:21	3:28	11.32
maeb	26/7/87	2:48	2:46	13.08
maep	27/7/87	2:37	2:36	12.88
maf3	28/7/87	2:27	2:34	13.08
mafh	29/7/87	2:16	2:08	12.46
mafw	30/7/87	3:46	3:48	11.84
mald	13/8/87	2:55	2:46	11.19
malk	13/8/87	15:17	15:08	11.74
mar9	28/8/87	3:35	3:28	11.50
mazo	18/9/87	15:31	15:28	12.19
mb11	22/9/87	2:26	2:26	12.08
mb1f	23/9/87	2:16	2:08	12.33
mb1n	23/9/87	16:18	16:09	12.50
mb21	24/9/87	16:07	16:08	12.65
mb2m	26/9/87	3:23	3:28	12.39
mb9o	14/10/87	3:30	3:28	10.01
mbdz	25/10/87	3:12	3:08	12.42
mbg5	30/10/87	16:20	16:28	15.11
mbgc	31/10/87	3:48	3:48	14.59

300, 200, 150, 100, 80, 70, 60, 50, 40, 30, 20, 15, 10 and 5 hPa. The consequence of this was that the altitudes at which atmospheric profile properties were measured varied with each sounding. An example atmospheric pressure profile versus altitude is shown in Figure 3.3.

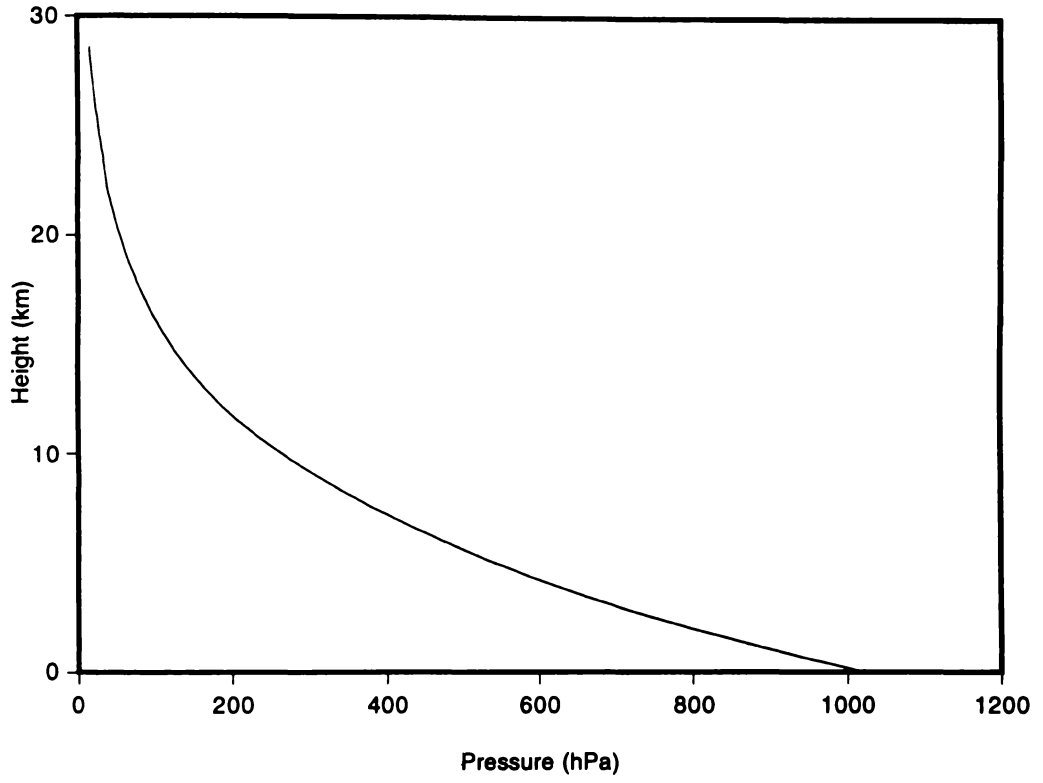

Figure 3.3: A sample atmospheric pressure profile, measured over Hobart on 29 July 1987. (From *Smith* [1993].)

3.3.3 AVHRR Data Set

The complete set of NOAA-9 AVHRR "quick look" images covering the buoy measurement campaign was inspected. The images were received at the CSIRO Marine Laboratories in Hobart. Seventy-one images, which appeared cloud-free, were selected for closer examination. The main criteria for the selection of these images, apart from being cloud-free, were temporal closeness to the buoy temperature readings and radiosonde data availability.

Accurate location of the AVHRR buoy pixel was performed by mapping

the Tasmanian coastline from latitude/longitude to raw image (row and pixel) coordinates and overlaying it on the selected images. The spacecraft attitude parameters (roll, pitch and yaw) were fine tuned to maximize the alignment between the coastline and the image. A 400-by-400 pixel subimage, centered on the buoy pixel, was then selected for closer examination. After completing this process, thirty-one images were left. The rest were either lost to cloud contamination, other problems related to incorrect radiance readings of the AVHRR instrument (for the discussion of these see *Smith* [1993]) or gaps in the atmosphere sounding data.

The final AVHRR data set delivered by CSIRO in Hobart contained thirty-one 400-by-400 pixel AVHRR multichannel images. Conversion of raw pixel readings to radiance was done following the algorithm proposed in *Steyn-Ross et al.* [1992]. The "buoy" radiance was actually calculated as an average of the 3-by-3 pixel window centered around the buoy. This was done to reduce the effects of digitization error and to produce a comparable radiance data set to the CSIRO-estimated SST (they had also used the 3-by-3 window averaging approach). The image data, containing IFUT code, local image acquisition time, AVHRR channel 4 and 5 radiance and scan angle is given in Table 3.3.

3.4 DWV Results

In this section we will analyze the results of the DWV algorithm. The main focus will be the error of the retrieved SST's, and we thus evaluate the premises of the method.

The main assumptions of the DWV method can be summarized as follows:

- The relationship between ΔSST and Δ (or k) is linear and monotonic (see Figure 3.1).
- Water vapour is the dominant atmospheric constituent; variation of aerosols and other gases is neglected (LOWTRAN-7 default profiles are

Table 3.3: IFUT code, local AVHRR image acquisition date and time (UTC+10), AVHRR channel 4 and 5 radiance (in units of $mW/(m^2\,sr\,cm^{-1})$), and AVHRR scanning angle (in units of degrees).

IFUT code	Date	Time	I_4	I_5	Scan angle
m9jr	9/5/87	3:25	88.1215	100.6107	37.492
m9k5	10/5/87	3:16	88.9273	100.6217	28.025
m9kc	10/5/87	15:35	89.2839	102.4234	26.185
m9n9	18/5/87	1:49	84.3386	96.0814	51.396
m9na	18/5/87	3:29	86.8782	99.0183	39.656
m9vi	8/6/87	3:07	87.2908	100.2876	12.876
ma4c	30/6/87	16:30	84.5357	97.3874	31.866
ma4i	1/7/87	2:17	83.6206	95.8213	40.414
mabk	19/7/87	2:23	83.797	96.2049	36.519
mabz	20/7/87	3:54	81.253	92.8878	49.665
mac6	20/7/87	16:15	86.2609	99.1915	15.094
macc	21/7/87	2:02	82.3337	93.9881	48.313
macd	21/7/87	3:43	82.049	94.0711	44.526
macq	22/7/87	1:52	80.5455	92.0604	51.938
macr	22/7/87	3:32	84.7569	97.2755	37.438
mad5	23/7/87	3:21	84.8809	97.8216	27.971
maeb	26/7/87	2:48	85.8024	98.2393	12.227
maep	27/7/87	2:37	83.0533	94.4876	24.562
maf3	28/7/87	2:27	85.1694	97.4545	34.354
mafh	29/7/87	2:16	84.684	97.0235	41.712
mafw	30/7/87	3:46	83.6209	95.6186	45.77
mald	13/8/87	2:55	85.6693	98.7929	5.41
malk	13/8/87	15:17	83.7452	95.7221	46.257
mar9	28/8/87	3:35	84.7034	97.0062	37.114
mazo	18/9/87	15:31	85.9333	98.667	40.63
mb11	22/9/87	2:26	85.1493	97.4991	39.061
mb1f	23/9/87	2:16	85.3195	97.6008	45.283
mb1n	23/9/87	16:18	87.1175	100.1087	10.874
mb21	24/9/87	16:07	84.2116	96.9406	3.679
mb2m	26/9/87	3:23	86.7458	99.4788	24.67
mb9o	14/10/87	3:30	82.6755	95.4738	29.864
mbdz	25/10/87	3:12	83.7825	96.4848	7.141
mbg5	30/10/87	16:20	90.1014	103.5429	9.197
mbgc	31/10/87	3:48	88.8211	101.3294	42.253

used to estimate them).

- DWV is not sensitive to the initial choice of SST (the so-called SST seed), which is chosen as the monthly historical average.
- Equation (3.5) represents a suitable model for the variation of the water vapour profile.

3.4.1 DWV-Derived SST's vs. Ground Truth

The retrieved DWV sea surface temperatures for all 34 cases are given in Table 3.4. For easier assessment, the actual SST's are replaced by errors calculated as Buoy $-$ SST_{DWV}. The data in the table shows the superior performance of the DWV method. The only pass where the method failed drastically is the mb21 pass. Excluding it from the set, the biggest error is close to 2 °C for the mbdz pass; the smallest error is 0.01 °C for the mb11 pass. In order to better evaluate the overall performance of the DWV method, two summary statistics for the SST errors were introduced: mean error (bias) and standard deviation of the errors (rms). The bias for the set without the mb21 pass was 0.22 °C, and the rms was 0.59 °C.

3.4.2 ΔSST vs. k Relationship

Figure 3.1 shows the ΔSST vs. k relationship as predicted by the DWV method for three different atmospheric profiles. They were classified as "wet", "mid-range" and "dry", predominantly on the basis of the shape of the water vapour profiles. Several significant conclusions can be drawn from the figure:

- ΔSST is generally a monotonically increasing function of Δ, or k (see Figure 3.1).
- The wetter the original profile, the greater the steepness of the ΔSST vs. k curve. This is obviously a consequence of the bigger initial amount of the total water vapour in the profile and the use of (3.5).

Table 3.4: Errors of DWV-derived sea surface temperatures as compared with the ground truth (buoy).

IFUT code	Buoy/[°C]	SST Error/[°C]
m9jr	13.83	-0.57
m9k5	13.89	-0.86
m9kc	14.11	-0.15
m9n9	13.76	0.36
m9na	13.74	-0.4
m9vi	12.73	-0.05
ma4c	12.08	1.0
ma4i	11.45	0.07
mabk	10.77	-0.36
mabz	11.21	0.42
mac6	12.40	0.22
macc	11.12	-0.55
macd	11.35	0.73
macq	11.91	1.16
macr	11.64	-0.18
mad5	11.32	0.2
maeb	13.08	0.66
maep	12.88	0.97
maf3	13.08	0.6
mafh	12.46	0.47
mafw	11.84	-0.03
mald	11.19	-0.12
malk	11.74	-0.11
mar9	11.50	-0.54
mazo	12.19	-0.19
mb11	12.08	0.01
mb1f	12.33	0.13
mb1n	12.50	0.11
mb21	12.65	9.4
mb2m	12.39	0.28
mb9o	10.01	0.43
mbdz	12.42	1.99
mbg5	15.11	0.86
mbgc	14.59	0.76

The dry profile curve appears to be very close to linear; this behaviour changes with an increase of water vapour in the initial profile. The mid-range profile curve is slightly nonlinear, and the wet profile curve is even more nonlinear. However, it is important to note this departure from linearity occurs at large values of k, typically $k > 2$, which are highly unlikely to occur in reality.

- The ΔSST vs. k curves generally pass very close to the (1, 0) point in Figure 3.1. This indicates the initial radiosonde soundings are close to the actual atmospheric profile above the buoy at the time of the satellite passes.

3.4.3 Effect of Aerosols

Aerosols can have large effect on SST calculations [*Liou*, 1980]. The inclusion of a measured aerosol profile over the buoy, in the true spirit of the DWV method, was not possible as this information was not available from the radiosonde measurements. Instead, default aerosol distributions available in LOWTRAN-7 were used. When tested however, LOWTRAN-7 produced physically unrealistic results when run using the Navy Maritime aerosol profile with a strong continental influence [*Smith*, 1993]. Such an aerosol setting was thought to give the best representation of the situation above the buoy.

Further LOWTRAN testing revealed that this problem occurred for all default aerosol models. Hence, the DWV analysis reported in the above sections were carried out with the aerosol influence in LOWTRAN-7 switched off. This decision was supported by a sensitivity analysis [*Smith*, 1993], which showed the differences in retrieved SST's to be only about 0.08 K with (Navy Maritime model) and without aerosols included in the LOWTRAN simulations.

3.4.4 Effect of Topping Up the DWV Atmosphere

Since radiosonde measurements only measure the first 30 km of the atmosphere, the rest of the atmosphere (100 km) was "topped up" from one of the default atmospheric profiles available in LOWTRAN-7. The topped-up data consisted of temperature and pressure profiles only; the atmosphere above the original, radiosonde measured, was considered completely dry.

The sensitivity tests reported in *Smith* [1993] showed that any default LOWTRAN atmosphere model used for top-up yielded the same retrieved SST's. Thus, the Middle Latitude Winter model was chosen for the top-up atmosphere data mainly because it corresponded to the geographical location of the buoy and the time of the year of the SST measurements.

3.4.5 Effect of Secondary Gases

As with the topping up, LOWTRAN simulations request the user to specify the vertical distribution of a set of atmospheric gases. Since no data on their distribution around the buoy were available, the default LOWTRAN models were used. Again, the analysis reported in *Smith* [1993] showed no important influence of the default models, so the Middle Latitude Winter model for atmospheric gases was chosen for all DWV runs.

3.4.6 Effect of SST First Guess

The effect of the first guess SST on the final result was investigated for the m9jr pass. The result is shown on Figure 3.4. Two DWV runs were initiated: one with a very inaccurate SST seed of 300 K, and the other with the "correct", i.e. derived from climatological data, seed of 278 K.

The two curves in Figure 3.4 show that the SST seed has a large effect on the slope of ΔSST vs. k curve. The slope appears to be steeper for larger initial SST's, i.e. warmer surfaces. This is due to the difference in relative radiation absorption in the atmosphere. A 300 K surface will produce more

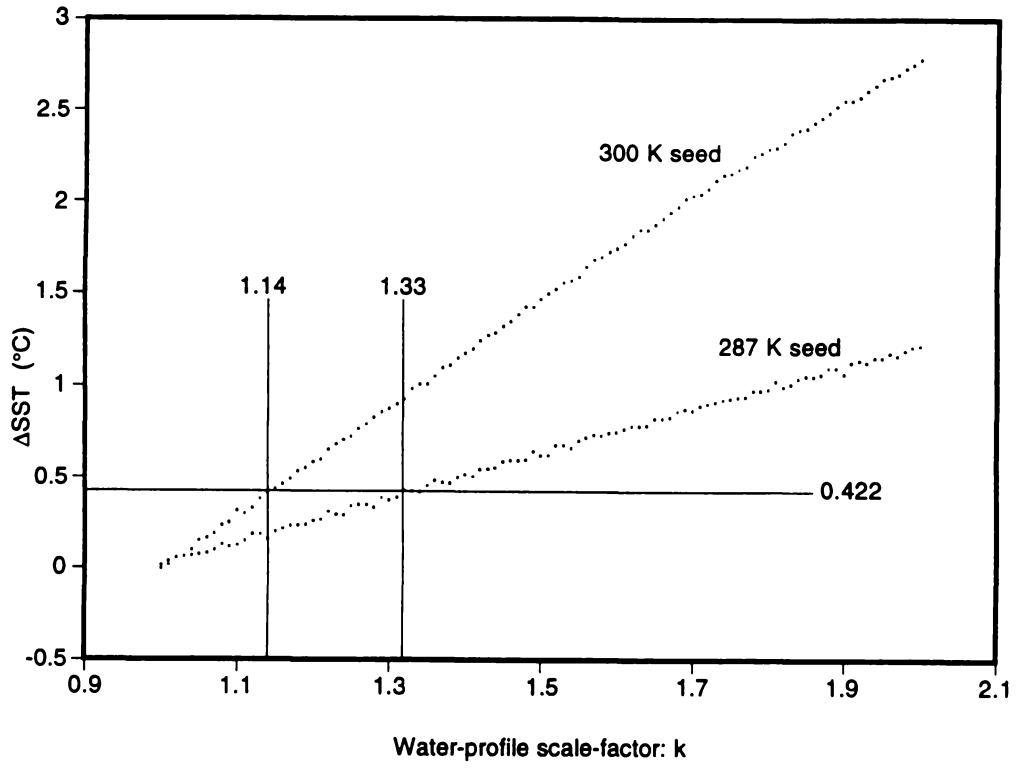

Figure 3.4: Effect of SST seed on ΔSST vs. k curve. (From *Smith* [1993].)

radiation, and hence more radiation will be absorbed for the same amount of increase in the water vapour (k) than from a 278 K surface.

Although the values of k indicated by the initial ΔSST's are different—$k = 1.14$ for the 300 K seed, and $k = 1.33$ for the 278 K seed—the final k and SST returned by the DWV algorithm were the same: 1.32 and 14.40 °C, respectively. The conclusion, therefore, was that the SST seed value does not affect the final retrieved SST.

3.5 Sensitivity Study of DWV

So far in the chapter, we have presented the original work on the development of the DWV method as reported in *Smith* [1993]. The initial results on the Tasmanian buoy data set (Section 3.3) indicated DWV had the potential to accurately estimate SST. *Osborne* [1995] carried out a sensitivity study in

order to better evaluate the algorithm and its response to the variation of the input data. His aim was also to seek an explanation for the occasional failures[3] of the DWV method. This section will present the methodology and major findings of *Osborne*'s analysis. His study focused on how the DWV algorithm responded to variation of atmospheric profiles and how temporally unmatched radiosonde soundings affect the final SST estimate.

3.5.1 Alternative Radiosonde Selection

Smith [1993] had already proven that DWV was not sensitive to inaccuracies of the initial, i.e. first guess, water vapour profile. *Osborne* [1995] discovered that the original search method of *Smith* [1993] for the temporally closest radiosonde sounding almost consistently failed to achieve its task. In the original DWV algorithm, radiosonde profiles had been selected solely based on the date of the nominated satellite pass. This meant that the morning radiosonde flight had always been chosen as the closest to a satellite pass. Another error stemmed from the confusion as to the convention for the radiosonde flight times. *Osborne* [1995] managed to confirm in a correspondence with the Australian Bureau of Meteorology that the format was in UTC time. Because Smith had assumed the format to be in Australian Eastern Standard Time, the sondes selected with his search method could have been in error by as much as 12 hours. Although this error did not seriously affect the DWV performance reported by Smith [*Smith*, 1993], the discovery allowed *Osborne* [1995] to redesign the radiosonde search method and introduce some new search options.

Osborne [1995] implemented four different radiosonde search options:

Mode 1: Original DWV Sonde Selection. The original search mode as implemented by *Smith* [1993].

Mode 2: Manual Sonde Selection (nearby sondes). This mode allows user selection of any radiosonde sounding within 20 sondes bracketing the

[3] "Failure" in the sense of a big SST error. DWV never failed to produce an estimate.

chosen satellite pass. It was designed for detailed analysis of the DWV sensitivity to the radiosonde data aging.

Mode 3: Automatic (Optimized) Sonde Selection. In this case the sonde closest to the chosen satellite pass is selected by default. The user in this mode also has the option of choosing a fixed sonde offset value—a positive or negative integer. A positive value for the offset, say 2, means that the sonde two flights after the closest flight will be selected; a negative value, e.g. -3, means the sonde three flights earlier than the closest one will be selected.

Manual Sonde Selection (full database). This mode caters for the selection of any radiosonde flight from the entire database for each of the three sites. It is the most general sonde selection mode available in the *Osborne* DWV software suite.

By using his improved sonde flight searching method, *Osborne* [1995] determined the time errors in sonde selection Smith's DWV algorithm had been making. Examination of the radiosonde database from Hobart revealed that the original DWV sonde selection correctly identified the closest sonde 8 out of 34 cases; 14 selections were one sonde flight late, and 12 were two flights late. By using *Osborne*'s optimized search method (Mode 3), the temporal matching between satellite passes and sonde flights was improved by about $9\frac{1}{2}$ hours on average.

Osborne [1995] ran the corrected version of the DWV software and obtained SST estimates for all 34 satellite passes. Comparison with the results of the original DWV revealed a very small improvement: the bias improved from 0.14 K to 0.12 K; the rms remained the same at 0.51 K. When eight of the passes that had the same sonde selected as in the original DWV were excluded from the comparison, the result was very similar: the bias changed from 0.1 K to 0.08 K (again, an improvement of 0.02 K); the rms was the same at 0.52 K (went up by only 0.01 K). *Osborne*'s conclusion was that for all practical purposes

an inconsistent sonde selection method of the original DWV [*Smith*, 1993] had not introduced any significant error in the estimated SST values.

3.5.2 DWV Sensitivity to Radiosonde Aging

Osborne [1995] carried out a detailed investigation into the sensitivity of the DWV performance caused by radiosonde aging on the radiosonde database from the Hobart site (site 74). The DWV was run for each satellite pass with 17 different sonde profiles: the closest sonde, plus the eight sondes (equivalent roughly to four days) on either side. The lack of later sondes for the last two satellite passes, mbg5 and mbgc, reduced the total number of cases to 569. The SST error, defined as buoy minus DWV SST, from this test is shown in Figure 3.5.

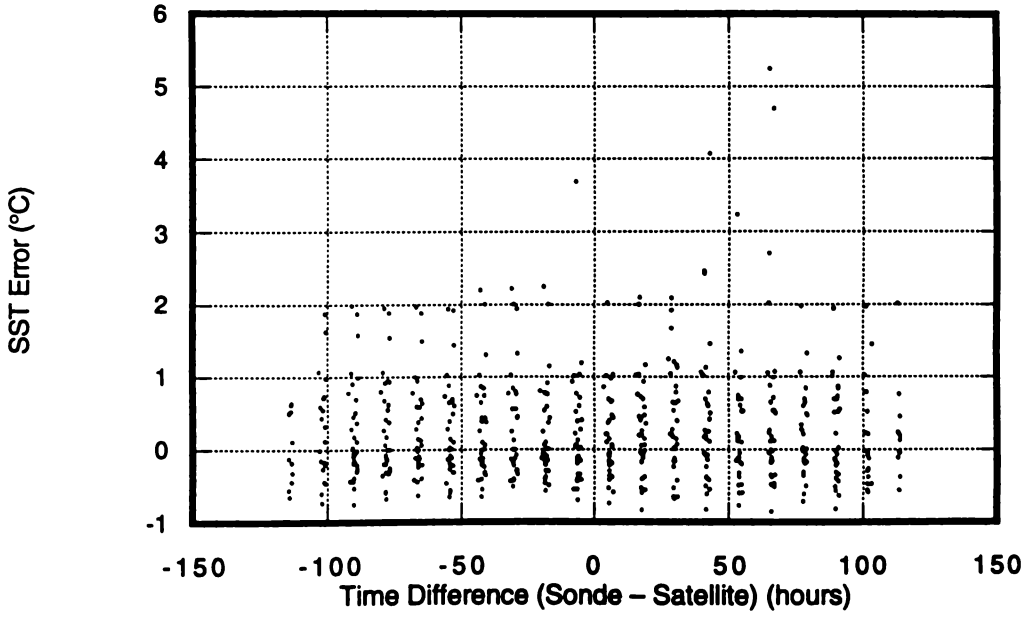

Figure 3.5: SST error as a function of time difference between radiosonde sounding and satellite pass. (From *Osborne* [1995].)

We note two important features of the graph in Figure 3.5:

- Clumping of the data is caused by a finite number of time-difference values. Since the sonde flights occurred usually at 9 a.m. and 9 p.m.,

and the satellite passes were also in two several-hour-wide intervals, there was only a limited amount of different time differences for the graph. *Osborne* [1995] determined that time difference values had strong bimodal distribution, with peaks at around -5 hours 20 min and 5 hours 15 min.

- The distribution of SST errors indicated negligible influence of sonde aging on the DWV. With the exception of few obvious outliers, the SST errors were never much more than 2 °C.

The conclusion was that the accuracy of the DWV had not shown any appreciable deterioration due to using up to four days old atmospheric profiles. The histogram of the SST errors is shown in Figure 3.6.

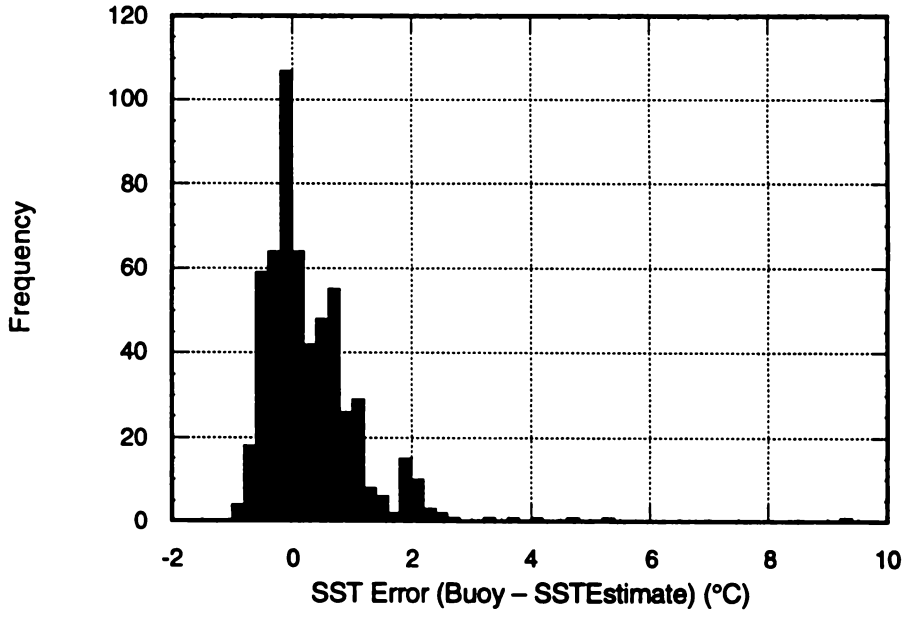

Figure 3.6: Histogram representation of SST errors shown in Figure 3.5. The bin width is 0.5 K. (From *Osborne* [1995].)

3.6 Examination of DWV Failures

The original testing by *Smith* [1993] revealed that the pass mb21 was the only drastic failure of the DWV. The SST estimate for this case was 3.3 °C when

the original Hobart radiosonde data was used; the ground truth was 12.65 °C. *Osborne*'s investigation into radiosonde aging influence on the DWV exposed several other problematic passes that bracket the mb21 pass. *Steyn-Ross et al.* [1993] ran the DWV for the passes mb1f, mb1n, mb21 and mb2m, for each of the three radiosonde sites. All of the retrieved SST estimates were lower than the buoy temperature; the errors of four out of the 12 cases were within 1 °C, four within 10 °C and four had errors greater than this.

The DWV requires three inputs: an atmospheric profile, a pair of satellite-measured AVHRR channel-4 and -5 radiances, and a satellite scan angle. Thus, the reason for failures of the DWV is associated with one of these inputs.

3.6.1 Influence of Satellite Radiance and Scan Angle

In order to examine if the satellite measured radiance of the 34 passes had any influence on the DWV failures, *Osborne* [1995] plotted them against time (see Figure 3.7). There's an expected drop in overall radiances in winter months, but no obvious outliers or any other problems with the data was observed. The radiance for the worst-performing pass, mb21, is boxed in the graph, but it does not reveal anything extraordinary when compared to the rest of the set.

Osborne [1995] had also examined the relationship between the DWV SST errors and satellite scan angles for the passes. The graph, in Figure 3.8, does not show any discernible trend either. In fact, one would expect that the smaller the scan angle, the smaller the DWV error due to the shorter radiation path through the atmosphere. The fact that the pass with the smallest scan angle (mb21; 3.68°) had the biggest DWV error clearly indicates that the scan angles are not responsible for DWV failures.

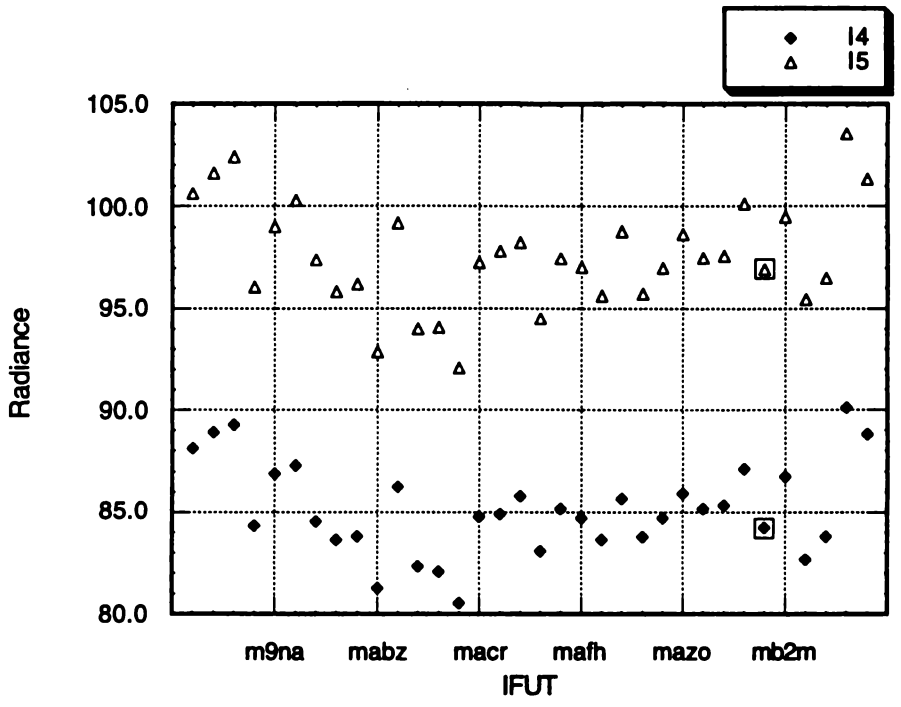

Figure 3.7: The spread of satellite-measured AVHRR channel 4 and 5 radiance for the 34 satellite passes. The boxed points belong to the mb21 pass. (From *Osborne* [1995].)

3.6.2 Influence of Radiosonde Data

As previously mentioned, *Osborne* [1995] discovered that a few other satellite passes (mb1f, mb1n and mb2m), neighbouring the troubling mb21 pass, also performed badly when initiated with the nearby alternative sondes. He decided to focus on those passes and sondes in his investigation on the influence of radiosonde data on DWV. His work was very detailed and extensive, so we will present here only the major findings of his analysis.

To establish a "normal" behaviour of the DWV, *Osborne* [1995] ran it on all 34 passes in the optimal sonde selection mode and recorded all internal DWV variables for every iteration. He selected the four most important for the functioning of the DWV—AVHRR channel sea surface temperatures and transmissivities—and plotted them against Δ, the factor indicating the amount of change in water vapour profile. Two general types of curves emerged, which

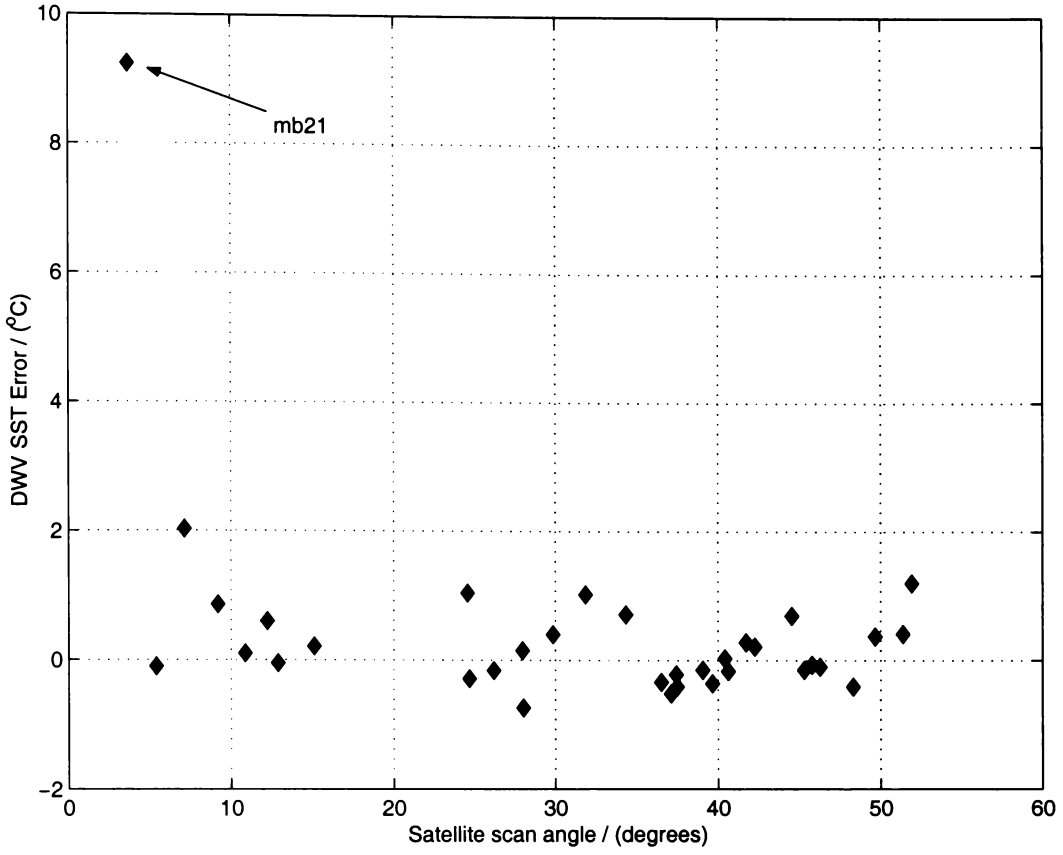

Figure 3.8: DWV SST errors vs. satellite scan angle for all the 34 passes. No trend is observed in the graph, except a big outlier for the mb21 pass.

are shown in Figures 3.9 and 3.10.

The graph in Figure 3.10 represents a typical "good" pass, whereas the graph in Figure 3.9 is the only "bad" pass. The following features are different in the two types of graphs:

- The surface temperature curves of the "good" passes gently concave upwards for all the values of Δ. In the case of the mb21 pass, the same curves first dip downwards as the point of crossover is approached. After the crossover point, the sea surface temperature in channel 5 sharply increases.

- The transmissivity curves for both channels of the "bad" pass are lower for all values of Δ. The average transmissivity in this case is 0.25, whereas the "good" passes exhibit average transmission of 0.4 or greater.

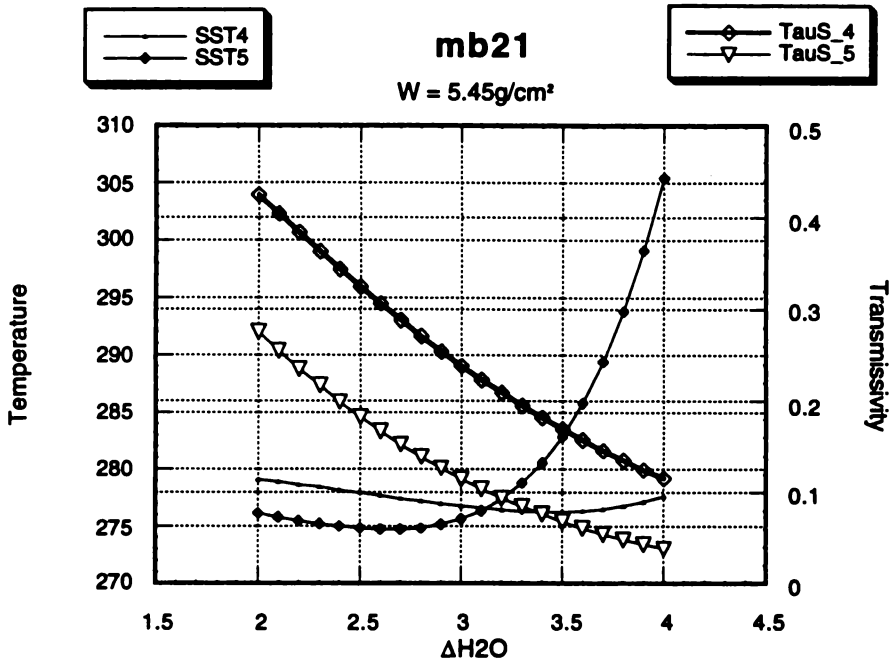

Figure 3.9: Surface temperature and transmissivity curves for the mb21 satellite pass (optimum sonde selection mode). The total water vapour column as calculated by the DWV is given also (variable W). (From *Osborne* [1995].)

- The value of Δ for which the two surface temperature curves intersect is much greater for the bad, mb21, pass than for the "good" passes. This is a direct consequence of the dip in the surface temperature curves for this case as the curves seem to "run away" from each other. The average slant-path value for water vapour column of the "good" passes was $2\,g/cm^2$, but the mb21 pass had $5.45\,g/cm^2$.

To prove that the optimal sonde for the mb21 pass was to blame for the failure of the DWV in this case, *Osborne* [1995] ran the DWV on the mb9o pass with this sonde. The resulting graph bore almost a perfect resemblance to the mb21 graph (Figure 3.9). It was clear that this particular radiosonde was responsible for the DWV failure in the case of the mb21 pass.

Identifying that atmospheric profile could produce a DWV failure, the analysis then focused on what property of the profiles caused DWV to fail. Since the profile input in DWV has two variables, atmospheric temperature and

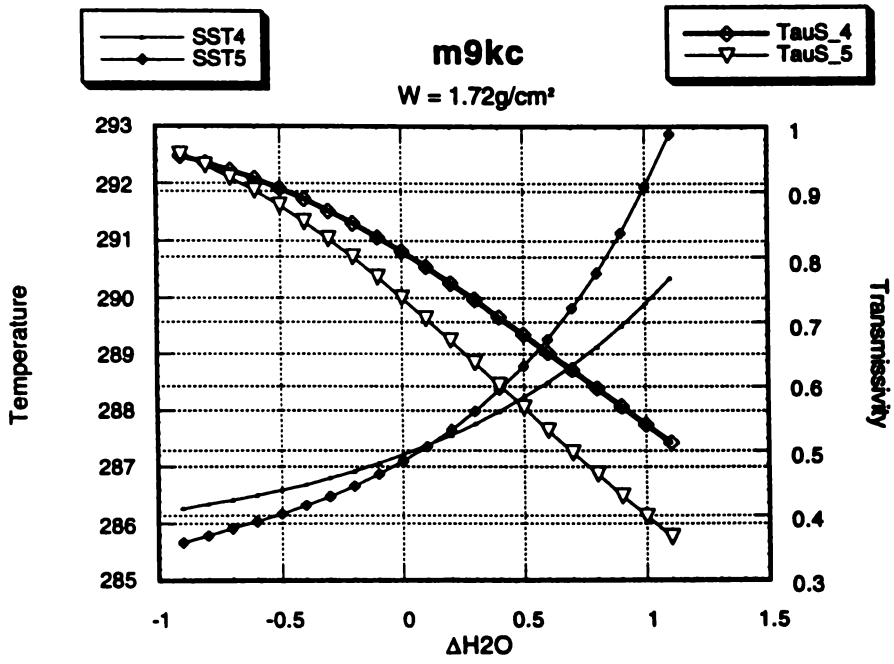

Figure 3.10: Surface temperature and transmissivity curves for the m9kc satellite pass (optimum sonde selection mode). The total water vapour column as calculated by the DWV is given also (variable W). (From *Osborne* [1995].)

water vapour, *Osborne* created 16 hybrid sondes out of the four troublesome sondes initially selected for further investigation. The water vapour and temperature profiles of these sondes are given in Figures 3.11 and 3.12. The hybrid sondes were created by making combinations of the temperature and water vapour profiles of the original four sondes.

He used these sondes for DWV runs on another "good" satellite pass. The surface temperature curves generated by DWV in these cases were grouped into five categories depending on the shape of the curves. The categories are shown in Figures 3.13–3.17.

Investigating what temperature and water vapour profiles caused the biggest DWV failures, it had been discovered that the temperature profile of Sonde -1 consistently forced DWV to produce Category 5 surface temperature curves. No matter what water vapour profile combined with the Sonde -1 temperature profile, DWV could not recover from absolute zero SST estimates.

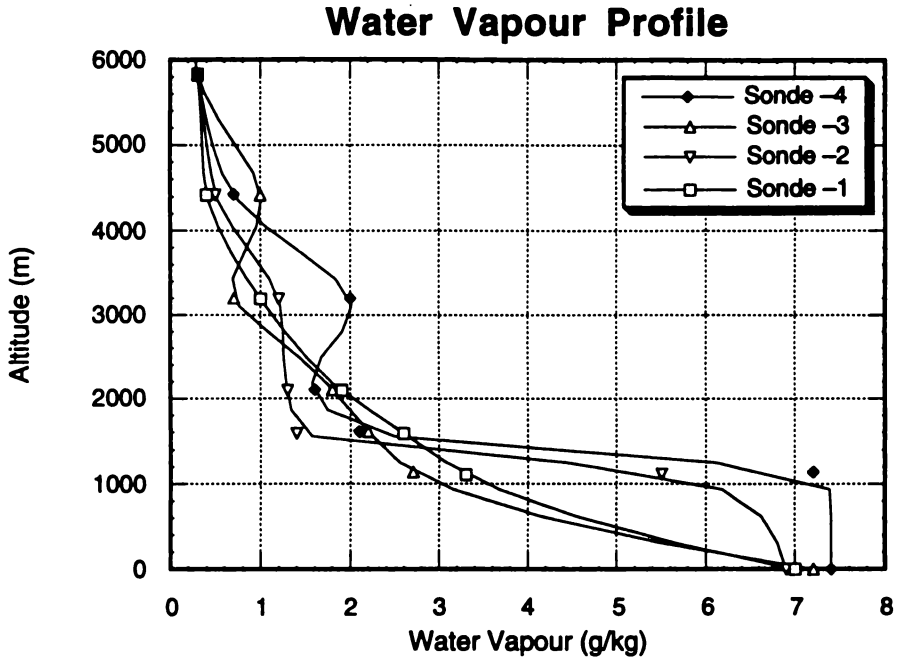

Figure 3.11: Water vapour profiles for the four sondes used to generate hybrid profiles. (From *Osborne* [1995].)

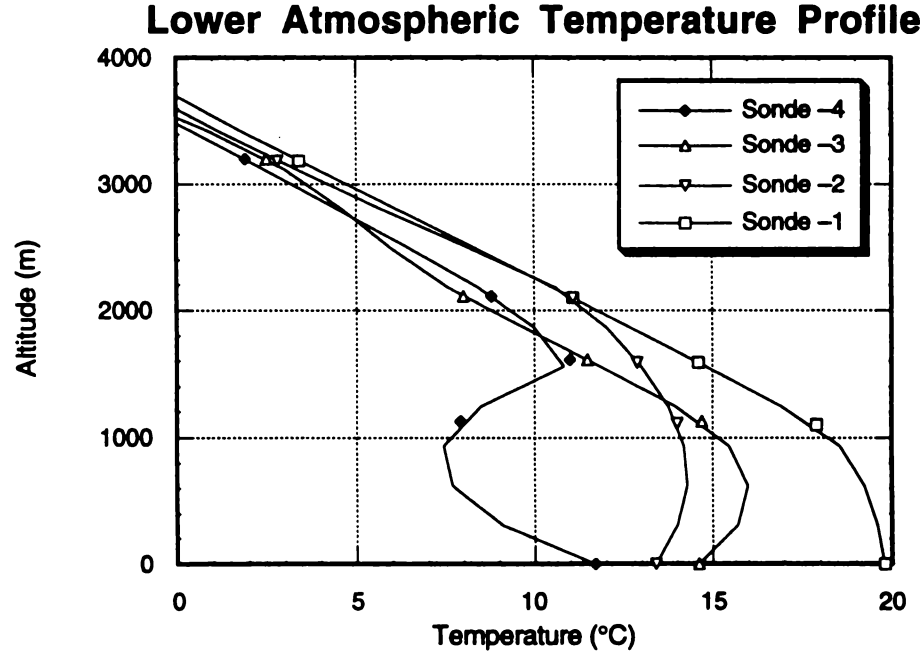

Figure 3.12: Atmospheric temperature profiles of the four sondes used to generate hybrid profiles. Only the lower altitudes are displayed for clarity. (From *Osborne* [1995].)

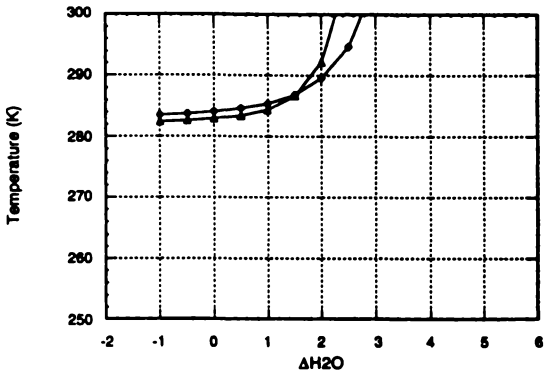

Figure 3.13: Category 1. Strictly increasing surface temperature curves, as witnessed in the "good" passes. The channel-5 curve starts off below the channel-4 curve. (From *Osborne* [1995].)

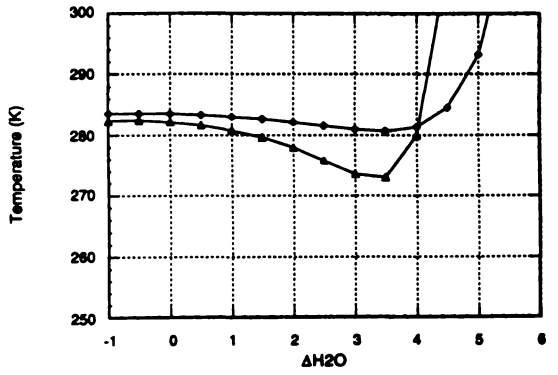

Figure 3.14: Category 2. Gradually decreasing curves, with channel-5 surface temperature curve dipping noticeably before sharply increasing. (From *Osborne* [1995].)

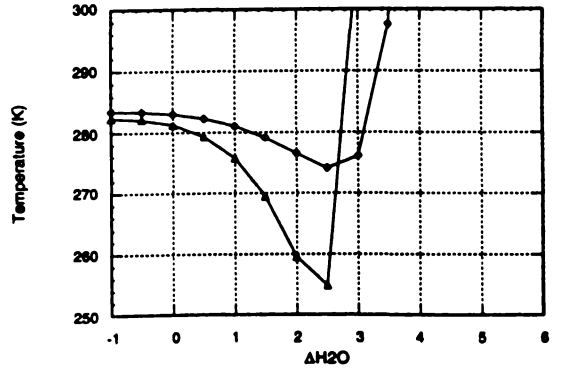

Figure 3.15: Category 3. Steeper decrease than in Category 2 of channel-5 surface temperature curve; channel-4 curve starts to dip too. (From *Osborne* [1995].)

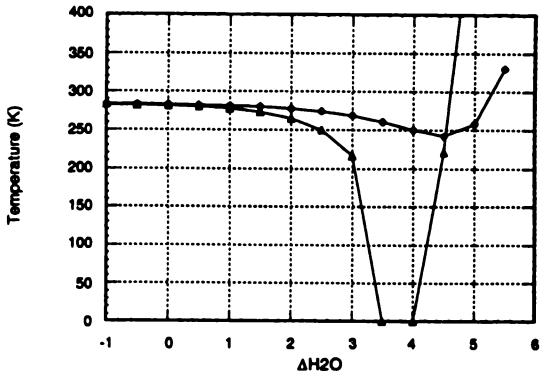

Figure 3.16: Category 4. Channel-5 surface temperature curve falls to absolute zero before sharply increasing; channel-4 curve still only slighlty dropping. (From *Osborne* [1995].)

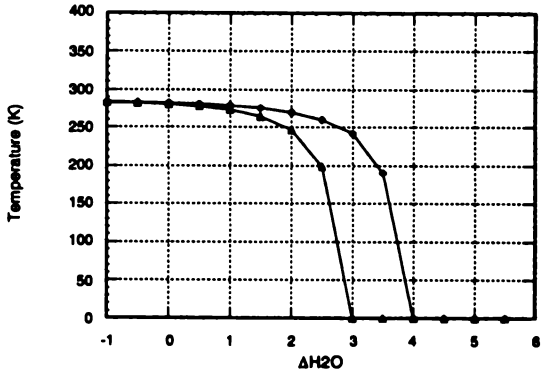

Figure 3.17: Category 5. Both surface temperature curves (channel-5 first) collapse to absolute zero without rising back. (From *Osborne* [1995].)

This temperature profile (Figure 3.12) is the warmest of those selected for analysis. It thus followed that the DWV could not deal with cases where atmospheric temperature profiles were too warm.

This was the major finding of *Osborne*'s investigation into the influence of radiosonde data on the DWV. It is much less sensitive to the amount of initial water vapour in the atmosphere and, in almost all the cases considered, it coped well if the temperature profile was not too warm.

He also showed that the lower part of the temperature profile was responsible for DWV failures, not the upper atmosphere part. This is easy to explain by noting that the biggest source of atmosphere-contributed radiation is the water vapour located in the lower part of the atmosphere (typically lower than 5000 m). The greater the water vapour amount, or the warmer the lower atmosphere, the stronger the screening of the surface.

It is now possible to replay the sequence of events that lead to a DWV failure. Being initiated with a warmer than usual[4] atmosphere, the atmosphere emitted radiation will be also high. The only way for DWV to reduce this is to increase the amount of water vapour in its atmosphere and, hence, decrease its transmissivity. In doing so, however, the atmospheric radiation contribution still increases since the rate at which transmission decreases is not enough to decrease the radiation contribution of the ever-increasing amount of water vapour in the profile. More water vapour produces more atmospheric radiation, resulting in a completely negligible contribution of the surface-emitted radiation to the satellite-sensed radiation. Also, small surface radiation leads to a very cold surface temperature as obtained from Planck's black body function. *Osborne* had even found cases with negative values for surface-emitted radiation, as calculated by the DWV from (3.1). This clearly is a non-physical case, showing the extent of the DWV failure.

Following from this explanation is another interesting finding: The passes more prone to DWV failure would be those with smaller satellite-sensed ra-

[4]Very difficult to define what "usual" is for the DWV though.

diances. In such cases, the DWV would very quickly screen out the surface radiation contribution, driving the SST estimate towards absolute zero for smaller values of Δ.

Osborne's suggestion to solve this problem was to vary atmospheric temperature instead of water vapour; he coined this new method the Dynamic Atmospheric Temperature (DAT) method. He tested it on the mb21 pass. The result was quite encouraging: the SST estimate in optimal sonde selection mode on the data from all three sonde sites gave almost identical results—10.7 °C for the Hobart site and 10.8 °C for the Mt. Gambier and Melbourne sites. This was a great improvement on the original DWV SST estimates of 3.3, -9.9 and -273.2 °C, respectively.

When applied to the whole set, the DAT returned the following statistics: bias of 0.12 °C and rms of 0.54 °C, for 30 passes (outliers mb21, mb9o, mbdz and mbgc were removed).

3.6.3 Non-physical Atmospheres in DWV

In the course of his analysis, *Osborne* [1995] realized that the original DWV method had not taken care of supersaturated atmospheric levels in the profile. These were the levels at which relative humidity exceeded 100%. LOWTRAN-7 was correctly indicating these profiles but continued to do the calculations. *Smith* [1993] had probably not been aware of it having to worry about other important issues of the DWV algorithm. As a solution, *Osborne* introduced a water vapour limiting procedure in the DWV software using the data published in *Byers* [1959]. The procedure was not perfect due to the lack of data for pressures of 1000 mb and more.

When tested, the new version of the DWV code returned similar overall SST estimates. The novelty was a DWV failure of the maep pass, which in the original DWV implementation yielded an error of 1 °C. The overall statistics for 29 passes (excluded were mb21, mb9o, mbdz, maep and mbgc) was: bias

of 0.17 °C and rms of 0.56 °C. *Osborne* concluded that using supersaturated atmospheres did not have any adverse effect on the overall DWV accuracy and stability.

3.7 Conclusions of *Osborne*'s Analysis of the DWV

The very detailed study of DWV failures done by *Osborne* [1995] yielded many interesting results. It is very important to list those, since his work laid the foundation for our modifications and improvements to the DWV.

- The exact form of radiosonde profile is not essential.
- Using out-of-date sondes does not have detrimental effects in all but a few cases.
- DWV failure is very likely if the first-guess atmospheric temperature profile is one of the warmest in the data set. DWV failures are not influenced by either satellite-sensed radiation or satellite scan angle alone.
- Changing the initial water vapour profile does not have a significant effect on the resultant SST; however changing the atmospheric temperature profile has dramatic consequences.
- A combination of warmer than usual atmosphere and lower than usual at-satellite radiance can yield a potential DWV failure.
- The failure is best diagnosed by observing the shape of channel 4 and 5 surface temperature curves during a DWV execution. For best SST estimates, these curves must be concave and monotonically rising with the increase of water vapour in the profile.
- Instead of changing water vapour, atmospheric temperature should be changed, *Osborne* [1995] called it the Dynamic Atmospheric Temperature

(DAT) method. It gives much better results in the cases where the DWV has failed.

- The DAT should be used whenever the surface temperature curves of the DWV resemble anything other than Category 1 curves.

In the next chapter we present an improved DWV method, developed following many of the findings listed above.

Chapter 4

Dynamic Water Vapour or Atmospheric Temperature Method

The extensive sensitivity study of the original DWV [*Smith*, 1993] done by *Osborne* [1995] provided some very important insights into the functioning of the DWV algorithm. The main outcomes of *Osborne*'s work are summarized in Section 3.7. His analysis confirmed that the original DWV algorithm was in general capable of retrieving quite accurate SST estimates, and was not too sensitive to the age of the first-guess radiosonde-measured atmospheric profile. The latter finding is especially important for any operational application of the DWV.

The investigation of a few failures[1] of the DWV revealed the algorithm's weaknesses when dealing with a first-guess temperature profile (from a non-local radiosonde) that is warmer than the actual profile above the pixel. Starting from the foundations of the original DWV, we created a new method which incorporated the findings from *Osborne* [1995]. The tasks of this new method were defined as:

[1]Large SST errors.

- Devise a criterion which will successfully detect a possible failure of the original DWV algorithm.
- Be able to handle a warmer-than-actual atmospheric temperature profile by merging both the DWV and DAT algorithms for modifying the first-guess sonde profile.
- Yield the smallest possible SST errors when applied to our Tasmanian data set (Section 3.3).

We named this new method the Dynamic Water Vapour or Atmospheric Temperature (DWVT), to indicate that either the water vapour or the temperature profile can be modified. The algorithm and results of the DWVT when applied to the full Tasmanian data set are presented in this chapter. We also compare it with a selection of TRSST methods (Section 4.7) and a suite of operational NESDIS equations derived for a range of NOAA satellites, from NOAA-9 to NOAA-14.

4.1 The DWVT Algorithm

DWVT proceeds as follows (the numbers 4 and 5 appearing in the text below refer to data of the respective AVHRR channels):

1. *Establish the atmospheric profile.* If this is the first iteration, take the profile obtained from a nearby radiosonde as the first-guess atmosphere. Otherwise use the adjusted atmosphere produced by the tuning in Step 5 (or 6) below.
2. *Compute atmospheric variables.* Initialize the LOWTRAN-7 transmittance code with this atmosphere, and hence compute τ_4, τ_5, and $\overline{T}_a$.
3. *Solve for SST_4 and SST_5.* Using the known at-satellite radiances I_4 and I_5, and the computed atmospheric variables, apply (3.4) to calculate two independent estimates for the surface temperature, SST_4 and SST_5.

4. *Test for convergence.* If $SST_4 = SST_5$, we have retrieved the surface temperature $T_s = SST_4 = SST_5$. If $SST_4 \neq SST_5$, then the assumed atmospheric state is in error, and should be tuned, either in water vapour (step 5), or, if necessary, in temperature profile (step 6).

5. *DWV* : Tune the water vapour profile.

   5a) Adjust m_i. Adjust (increase or decrease) the mixing ratio at each level i by a fractional amount Δm:

   $$m_i' = (1 + \Delta m) \cdot m_i \tag{4.1}$$

   (Adjusted mixing ratio is never allowed to exceed the saturation amount, see Section 4.4 for more information on this procedure.)

   5b) Iterate DWV. Repeat steps 1 to 5a, ensuring that the $(SST_4 - SST_5)$ difference steadily diminishes with each iteration.

   5c) Test for DWV failure. If the sequence of differences stops converging (i.e., starts to increase, or shows a constant difference), then DWV is about to fail, so halt water vapour adjustment, and switch to atmospheric temperature adjustment (step 6).

6. *DAT* : Tune the atmospheric temperature profile.

   6a) Adjust $T_{a,i}$. Restore the water vapour profile to its first-guess setting. Replace step 5a with the corresponding temperature profile shift for each level i:

   $$T_{a,i}' = (1 + \Delta_T) \cdot T_{a,i} \tag{4.2}$$

   where Δ_T is a constant fraction of the absolute temperature.

   6b) Iterate $T_{a,i}$ adjustments. Repeat steps 1–4, 6a until $SST_4 = SST_5$.

7. *Test for convergence failure.* If no convergence is detected, settle on

that profile adjustment (either DWV or DAT) which minimizes the $|SST_4 - SST_5|$ difference, taking the average as the retrieved surface temperature, $T_s = (SST_4 + SST_5)/2$.

8. *The DWVT has converged*:

   8a) If the SST curves cross each other, use linear interpolation of the points on both sides of the crossover to find T_s and final profile adjustment factor.

   8b) If the SST curves do not cross over but the $|SST_4 - SST_5|$ difference has a minimum, use a second order polynomial fit of the points surrounding the minimum to find the final T_s and adjustment factor.

The DWVT algorithm formulated above is based on the following premisses:

- The SST curves intersect only once for the entire interval of the profile adjustment factor (either DWV or DAT).
- If the SST curves do not intersect, the $|SST_4 - SST_5|$ difference has only one minimum for the entire interval of the profile adjustment factor (either DWV or DAT).
- The DWVT fails to converge when the $|SST_4 - SST_5|$ difference is either a monotonically increasing or decreasing function in the entire interval of the profile adjustment factor.
- The DWV failure and convergence tests are performed on-the-fly. This speeds up the overall execution time, especially when a switch-over to the DAT algorithm occurs.

4.2 DWV Failure Test

The major improvement of the DWVT over the DWV algorithm was the ability of the DWVT method to detect a possible failure of the DWV algorithm

and switch automatically to the DAT algorithm. *Osborne* [1995] showed that increasing or decreasing water vapour in the profile cannot compensate a too-warm first-guess atmosphere, and that the only viable option is to alter the temperature profile instead. His suggestion for a suitable DWV failure test was to use channel 4 and 5 surface temperature curves and examine their shape as a function of water vapour adjustment factor.

After doing test runs of the DWV software and monitoring all the internal variables, we concurred the shape of channel-4 and -5 surface temperature vs. water vapour adjustment factor curves is the most accurate and early predictor of a potential DWV algorithm failure. The shape of a pair of "normal" channel 4 and 5 curves is shown in Figure 3.13.

The main feature of the SST_4 and SST_5 curves in Figure 3.13 is their continuous rise with an increase of the water vapour. This signals a cool-enough atmosphere, so that an increase in water vapour efficiently dampens the atmospheric radiation to preserve a correct surface radiation contribution. Thus, our algorithm for a DWV failure test is formulated as:

> During a DWV execution, the slope of SST_4 and SST_5 curves is monitored for each new value of water vapour adjustment factor. The switch over to the DAT method will occur if the slope of any of the two monitored curves becomes zero or negative.

This is the second version of the DWV failure test. Guided by the graphs from our test runs and those reported by *Osborne* [1995], we expected the increase rate to be geometrical. After implementing this DWV failure test in the DWVT algorithm, we discovered that more cases triggered the test criterion than originally anticipated. A careful examination revealed a very small rippling pattern in the SST curves. This explained the unexpected increase in DWV algorithm failures. The condition of ever-increasing slope for increase in water vapour was violated in the troughs of the ripple pattern, regardless of the true condition of the DWV algorithm. *Smith* [1993] first discovered the rip-

pling pattern problem in the DWV and associated it with the single-precision calculation inaccuracies of LOWTRAN-7. Since the triggering for the majority of the test satellite passes occurred at the onsets of ripple troughs, we decided to relax the condition for the curve slope to being positive in sign only.

4.3 Influence of Radiance Units Selection on DWVT Accuracy

After implementing the DWVT algorithm (Section 4.1), we tested the influence of the two different radiance units available for doing calculations in LOWTRAN-7 [*Kneizys et al.*, 1988] on DWVT accuracy:

- $\frac{\mathrm{W}}{\mathrm{cm}^2\,\mathrm{sr}\,\mu\mathrm{m}}$ called LOWTRAN style (a) unit; and
- $\frac{\mathrm{W}}{\mathrm{cm}^2\,\mathrm{sr}\,\mathrm{cm}^{-}1}$ called LOWTRAN style (b) unit.

We took the initial DWVT source code and modified it to carry out calculations in both (a) and (b) LOWTRAN radiance units depending on the user input. We then ran the modified code with the optimal sonde searching method on the full Tasmanian SST set. The results of the both runs are given in Table 4.1. The statistics for the SST results in the table are: bias of -0.24 and -0.3 K, and rms of 0.65 K for LOWTRAN style (a) and (b) units, respectively. For 17 out of 34 cases, the LOWTRAN style (a) units produced a more accurate SST estimate; in 16 out 34 cases, using the LOWTRAN style (b) units proved to be better.

Since neither LOWTRAN units showed an obvious advantage over the other, we decided to operate DWVT in the LOWTRAN style (a) radiance unit only. It gave a slightly better bias, and the vast majority of the data handled by our software was already in this form.

Table 4.1: SST retrievals of the DWV software from *Osborne* [1995] when two different LOWTRAN radiance units (style (a) and (b)) were used for calculations. The SST result closest to the ground truth is highlighted with bold font.

IFUT	Buoy SST	LOWTRAN (a)	LOWTRAN (b)
m9jr	13.83	14.24	**14.19**
m9k5	13.89	14.64	**14.58**
m9kc	14.11	14.26	**14.20**
m9n9	13.76	**13.32**	13.22
m9na	13.74	14.12	**14.05**
m9vi	12.73	12.77	**12.73**
ma4c	12.08	**11.07**	11.03
ma4i	11.45	**11.43**	11.38
mabk	10.77	11.10	**11.06**
mabz	11.21	**10.83**	10.75
mac6	12.40	**12.18**	12.14
macc	11.12	11.54	**11.47**
macd	11.35	**10.66**	10.60
macq	11.91	**10.72**	10.63
macr	11.64	11.87	**11.82**
mad5	11.32	**11.16**	11.12
maeb	13.08	**12.48**	12.44
maep	12.88	**11.84**	11.79
maf3	13.08	**12.36**	12.31
mafh	12.46	**12.16**	12.10
mafw	11.84	11.92	**11.84**
mald	11.19	11.29	**11.25**
malk	11.74	11.84	**11.76**
mar9	11.50	12.03	**11.96**
mazo	12.19	12.37	**12.29**
mb11	12.08	12.23	**12.17**
mb1f	12.33	12.49	**12.39**
mb1n	12.50	**12.39**	12.37
mb21	12.65	**10.71**	10.66
mb2m	12.39	12.69	**12.61**
mb9o	10.01	**9.61**	9.55
mbdz	12.42	**10.36**	10.31
mbg5	15.11	**14.25**	14.20
mbgc	14.59	14.29	14.29

4.4 Dealing with Non-Physical Atmospheres

During the LOWTRAN radiance units test of the DWVT software, we accidentally noticed LOWTRAN-7 was still reporting supersaturated atmospheric levels during execution. This problem was first reported by *Osborne* [1995] and we expected that his water vapour limiting procedure (Section 3.6.3) would have prevented this problem from reoccurring.

Since it was still present, we had to devise our own water vapour (WV) limiting procedure. *Osborne* [1995] used experimental data from *Byers* [1959] which lacked the measurements for pressures of 1000 mb and greater. Instead of investigating why *Osborne*'s WV limiting procedure and LOWTRAN-7 disagreed in the calculation of relative humidity (RH), we ventured to find formulae that would ensure LOWTRAN-7 never exceeds 100% RH.

4.4.1 DWVT Water-Vapour Limiting Algorithm

Instead of using measured data and fitting our own curve as in *Osborne* [1995], we used already published formulae and tested the LOWTRAN output. The DWVT water vapour limiting algorithm starts from an atmospheric profile (either the first-guess or a modified one) defined with the atmospheric temperature (in Kelvins), pressure (in millibars) and water vapour amount expressed as mixing ratio[2] (in g/kg) for each radiosonde-measured layer.

The algorithm checks every layer for supersaturation by comparing the current mixing ratio amount with its saturation (maximal) mixing ratio given by a formula from *Wallace and Hobbs* [1977, page 73]:

$$m_{sat} = \frac{\epsilon}{p/e_{sat} - 1}, \tag{4.3}$$

where $\epsilon = M_w/M_a$; $M_w = 18.02\,\mathrm{g/mol}$ is the molecular weight of water;

[2]Mixing ratio is defined as the mass of water vapour in a fixed mass of remaining dry air. NB: Changing the temperature of the air parcel does not affect the parcel's mixing ratio.

$M_a = 28.97\,\mathrm{g/mol}$ is the apparent molecular weight of dry air; p is atmospheric pressure. e_{sat} is the water vapour saturation pressure calculated using a formula from *Richards* [1971]:

$$T_r = 1.0 - \frac{373.15}{T}, \tag{4.4}$$

$$e_{sat} = 1013.25\,\exp\left(13.3185\,T_r - 1.9760\,T_r^2 - 0.6445\,T_r^3 - 0.1299\,T_r^4\right), \tag{4.5}$$

where T represents the atmospheric temperature. *Brutsaert* [1982] states that the above formula for e_{sat} is accurate to 0.01% of the Goff-Gratch standard [*List*, 1968].

If the saturation mixing ratio for given p and T is exceeded in an iteration, the mixing ratio at that layer is capped at its m_{sat} value. The consequence of this is that in the unlikely case of ever-increasing water vapour amount in the profile, the DWVT WV limiting algorithm will eventually freeze the water vapour profile by preventing an increase at all layers.

Being very cautious about the DWVT not exceeding 100% RH in the future, we created a special parser[3] designed to catch any error message signalling supersaturated atmospheric layer in the LOWTRAN output files. It is very encouraging that since incorporating equations (4.3) and (4.5) into the DWVT algorithm, LOWTRAN-7 still hasn't reported finding supersaturated atmospheric layer.

4.5 DWVT Examples

Before presenting the results of the DWVT on our full Tasmanian SST set, we will show two characteristic examples of DWVT runs. For this presentation, we have slightly modified the operational version of the DWVT program by switching off the on-the-fly DWV failure and SST convergence tests. This

[3] *Parser* is a special procedure or program for processing lines of text in search for a pattern. In our case, the pattern was `***ERROR RELHUM` in LOWTRAN output files.

allowed us to obtain DWVT internal variables pertinent to the full range of the atmospheric profile adjustment factor (both DWV and DAT). In both examples featured here we used radiosonde data from Hobart (Section 3.3).

The first example is the satellite pass mafw, from 30 July 1987. The DWV method was sufficient to yield SST convergence in this case. Figure 4.1 shows graphs of AVHRR channel-4 and -5 surface temperature curves as the functions of the DWV profile adjustment factor, and the initial and final atmospheric water vapour and temperature profiles. Only the layers which contain any change are displayed for clarity. Note that in the graphs that follow a value of 1 for the adjustment factor denotes the original, first-guess atmospheric profile.

The intersection of the channel surface temperature curves in Figure 4.1 occurred when the initial water vapour amount in the profile was increased by about 60% (the water vapour adjustment factor was ≈ 1.6), giving a DWVT SST estimate error of just -0.04 °C (the buoy reading was 11.84 °C). We can see from the same graph that our decision to relax the DWV failure test (Section 4.2) was correct. The surface temperature curves monotonically increase throughout the interval of water vapour adjustments, but at a rate that is neither constant nor steadily increasing. In fact, the rate of increase for this satellite pass shows a noticeable two-stage feature. The channel SST estimates for the water vapour adjustment factor smaller than 1 lie on an almost perfectly straight line. The same is true when the water vapour adjustment factor is greater than 1, with a kink located close to the first-guess water vapour profile.

The initial and final atmospheric profiles are also shown in Figure 4.1. The temperature profile is unchanged from the first-guess since the DWV algorithm was used. Comparing the initial and final water vapour profiles we see that our water vapour limiting algorithm (Section 4.4.1) was invoked at the second layer from the ground (at about 1 km altitude). The water vapour mixing ratios on all the other layers deviated markedly from the sonde-measured values, indicating that the mixing ratio of that layer quickly reached its saturation

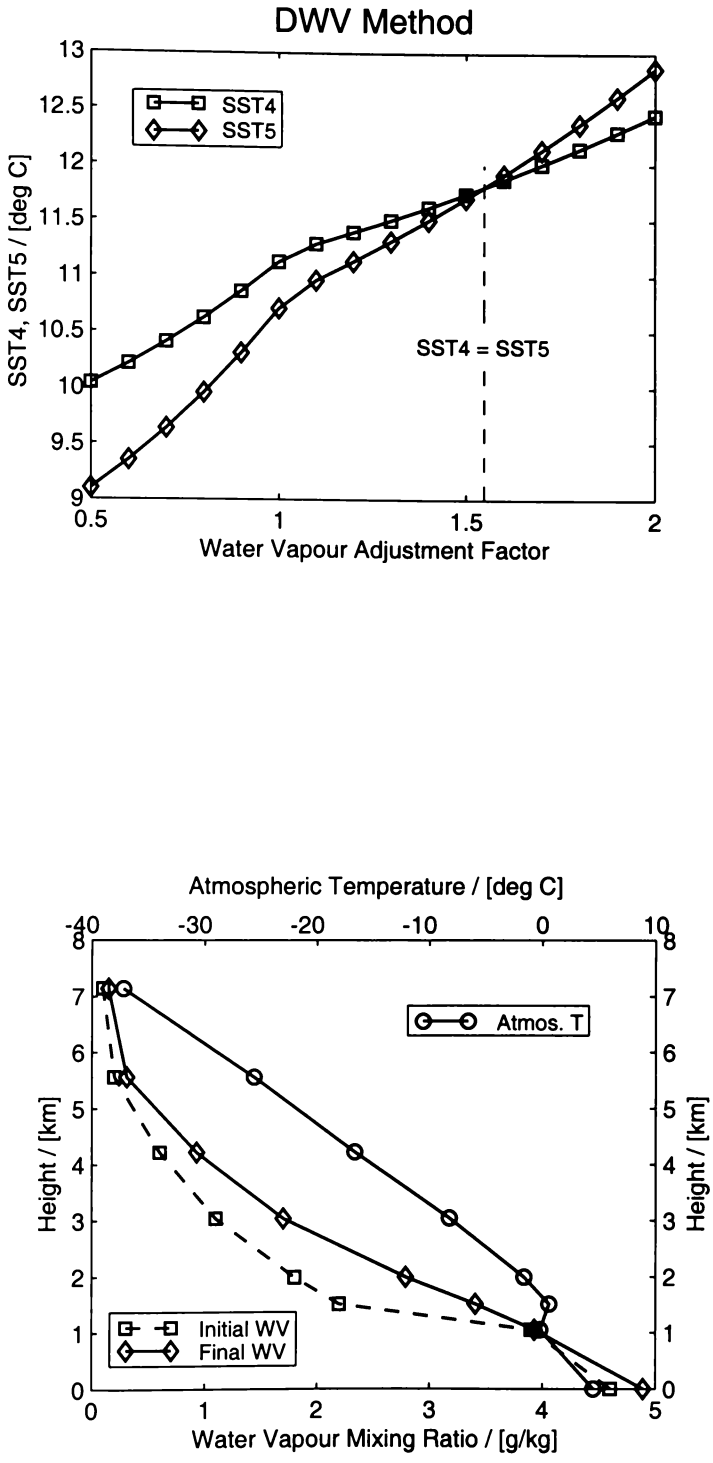

Figure 4.1: DWV method: SST retrieval via water vapour tuning. (Top graph) The pair of SST predictions from AVHRR channels 4 and 5 match when the radiosonde-derived water vapour profile at each level has been increased by a factor of 1.6. (Bottom graph) First-guess and final atmospheric profiles. The upper solid curve (circles) shows variation of atmospheric temperature (upper axis) with altitude. Dashed curve (squares) shows initial water vapour profile (lower axis), while the middle solid curve (diamonds) shows final tuned water vapour profile obtained after the water vapour at each level has been increased by factor 1.6. These curves apply to satellite pass mafw (July 30, 1987).

(maximal) level and was kept there throughout the DWV iteration process by our water vapour limiting procedure.

The second example is for the satellite pass m9n9 of 18 May 1987, when the DAT was invoked. The graphs of the channel surface temperature curves for the failed DWV attempt and the successful DAT, along with the initial and final atmospheric profiles is shown in Figure 4.2.

The shape of the surface temperature curves of the DWV method in Figure 4.2 indicate that the DWVT would immediately switch from the DWV to the DAT method. The SST_5 curve assumes a negative trend immediately, even when the water vapour amount is half of the first-guess. The shape of the SST_4 curve shows an almost perfectly flat response for water vapour adjustment factors smaller than 1. We associate this with an initial atmospheric profile so warm that even halving the first-guess water vapour profile was not sufficient to reduce the contribution of the atmospheric radiation to the at-satellite radiance in the AVHRR channel-4.

The DAT curves of SST_4/SST_5 in Figure 4.2 are completely different in shape from their DWV counterparts indicating how different the DAT and DWV SST-retrieval methods are. The temperatures of SST_4/SST_5 curves of the two methods also differ significantly. The DWV SST_4/SST_5 curves are limited to relatively narrow intervals of 10–10.5 °C and 7.5–8.5 °C, respectively, for a comparatively wide interval of water vapour change—from a 50% reduction to a 50% increase of the initial value. On the other hand, the DAT SST_4/SST_5 curves go from almost 14 °C down to 6 °C for only a 6% change interval (-5% to 1%) of the atmospheric temperature profile. This strong influence of the DAT on SST_4/SST_5 curves is the reason why we decided to use it as our last resort in a search for a SST_4/SST_5 curve convergence. By setting a default DWV adjustment factor interval to 0.5–3, we hoped to give the DWV enough "room" to find a SST_4/SST_5 curve intersection. The intersection of the DAT SST_4/SST_5 curves in Figure 4.2 occurred when the initial atmospheric temperature profile was decreased by about 3.5% (the DAT adjustment factor was

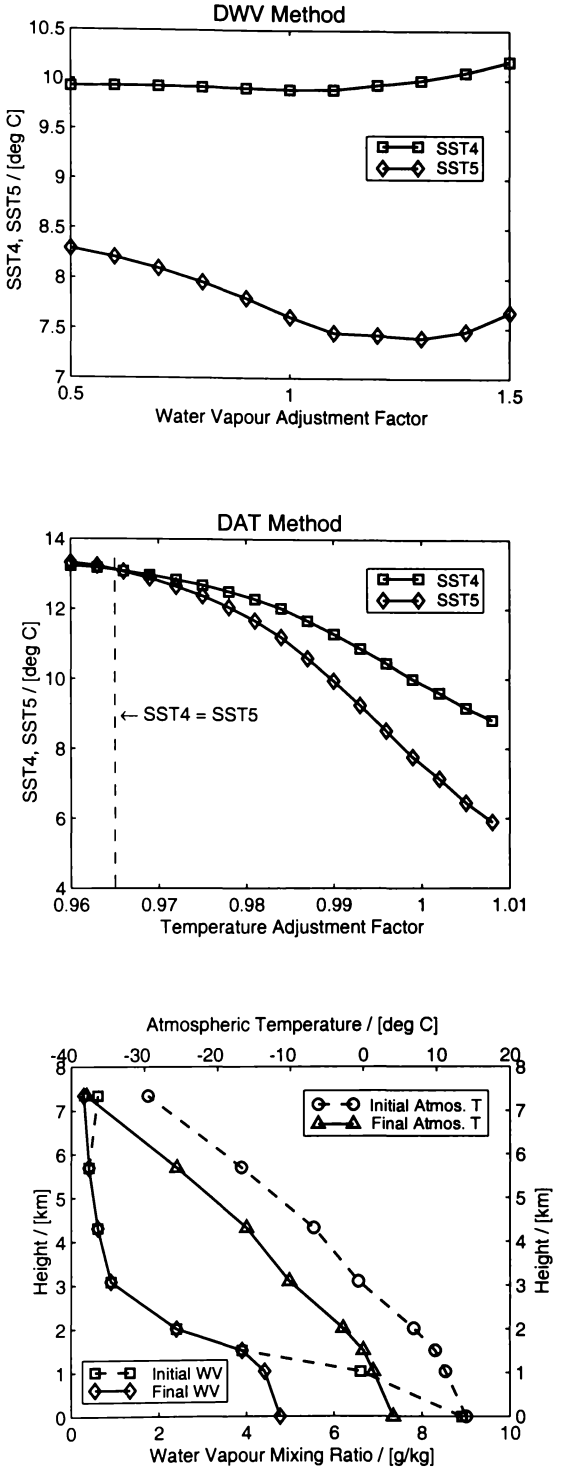

Figure 4.2: DAT method: SST retrieval via atmospheric temperature tuning. (Top graph) DWV failure. Tuning of the water vapour profile has produced SST_4/SST_5 curves which are not monotonically increasing functions of the water vapour adjustment factor, indicating that the DWV will not produce an accurate SST estimate. (Middle graph) DAT convergence. Water vapour profile is returned to the first-guess values, and the atmospheric temperature is tuned instead. SST_4/SST_5 curves intersect when atmospheric temperature (in Kelvin) at each level has been scaled by multiplicative factor 0.965 (i.e., reduced by 3.5%). (Bottom graph) Initial and final atmospheric profiles. The reduction in atmospheric temperature has forced a lowering in water vapour amount at altitudes below 1.5 km and above 7 km. These curves apply to satellite pass m9n9 (May 18, 1987).

≈ 0.965), giving a DWVT SST estimate error of -0.65 °C.

The initial and final atmospheric profiles are also shown in Figure 4.2. The temperature profile is just a scaled down first-guess profile. The final water vapour profile had reduced amounts at three layers (below 1.5 km and above 7 km). Since the atmospheric temperature was allowed to change, the water vapour amounts at those layers are the saturation mixing ratios for the given atmospheric pressure and temperature.

4.6 DWVT SST Retrieval Results

The results of SST retrievals using the DWVT method are presented in this section. The DWVT algorithm utilizes the water vapour limiting procedure explained in Section 4.4.1. All internal radiance-based calculations are performed using the LOWTRAN style (a) units (Section 4.3).

The presence of a water vapour limiting procedure in the DWVT allowed us to choose units of water vapour for use in our software. We decided to use the mixing ratio for two reasons: (i) the radiosonde data we use reports the water vapour in this unit, and (ii) we did not want to create any discrepancy between our formula for converting the mixing ratio to relative humidity and LOWTRAN-7. Hence we left it to LOWTRAN-7 to convert mixing ratios to its default unit—relative humidity. This decision was corroborated with the results of test runs during which our LOWTRAN output file error parser reported finding a few layers with relative humidity exceeding 100%.

The radiosonde data for the DWVT results came from the Mt. Gambier and Hobart sites (Section 3.3). The data from the third site, Laverton, are not as complete as from the other two sites—they lack soundings for the last four satellite passes. This would prevent us from doing a full analysis (various sonde selections) of the DWVT for this site, so we decided not to use it. Our decision not to use the Laverton site did not hamper probably the most interesting point to investigate about the DWVT: the influence of sonde selection, both

temporally and spatially, on SST retrieval accuracy. Of the three sites, the Mt. Gambier site was the farthest from the buoy (see Figure 3.2); the Hobart site was the closest. We can thus expect the Hobart site data to yield the best DWVT SST results.

We now introduce some terminology and variables we will use for comparing SST results of various methods. We have used four different sonde selections:

Closest The time of ascent of the selected sonde is closest to the satellite overpass.

5d-before The selected sonde was about five days earlier than the satellite overpass (the closest sonde to five days before the pass).

5d-after The selected sonde was was about five days later than the satellite overpass (the closest sonde to five days after the pass).

Night/day Night-time satellite passes are matched with the closest "night" sonde, and daytime passes are matched with the closest "day" sonde.

We decided to implement the last sonde selection method (night/day) because we felt there might be an important difference between the daytime and night-time temperature profiles.

The comparative performance of the various algorithms is assessed in terms of bias, rms and Q. The bias is the average value for the $(T_{\text{Alg}} - T_{\text{buoy}})$ difference,

$$\text{bias} = \frac{1}{N}\sum_{i=1}^{N}\left(T_{\text{Alg},i} - T_{\text{buoy},i}\right), \qquad N = 34 \tag{4.6}$$

and the rms is the standard deviation of these differences,

$$\text{rms} = \sqrt{\frac{1}{N-1}\sum_{i=1}^{N}\left(T_{\text{Alg},i} - T_{\text{buoy},i}\right)^2} \tag{4.7}$$

where T_{Alg} is the surface temperature retrieved by the given algorithm. We

introduce Q as an overall quality factor which combines the bias and rms error contributions in quadrature:

$$Q = \sqrt{\text{bias}^2 + \text{rms}^2}. \tag{4.8}$$

The smaller the Q, the better the performance of the method.

4.6.1 DWVT Results Using Hobart Radiosondes

The DWVT SST retrieval results on the whole Tasmanian buoy data set (Section 3.3) using the Hobart radiosondes and the "closest" sonde selection is given in Table 4.2. Along with the DWVT results, the table contains also the SST retrievals of the original DWV [*Smith*, 1993], and the DWV and DAT results of *Osborne* [1995].

The overall statistics in Table 4.2 reveals that the DAT method of *Osborne* [1995] produced the most accurate SST retrievals in the DWV family of methods. This is not surprising, recalling the strong influence of atmospheric temperature changes on channel surface temperatures as depicted in Figure 4.2. Water vapour is just one—albeit the most influential for SST applications—absorber in the atmosphere, whereas the temperature profile has much more profound influence on the transfer of radiation. For example, gas absorption coefficients depend on temperature as well as pressure [*Liou*, 1980]. In support of this we note that LOWTRAN-7, like many other radiation transfer models, assumes each atmospheric layer to be in a state of local thermodynamic equilibrium, so its radiance can be modelled using Planck's black body function. Hence changing the temperature of the layer has a much stronger impact on the atmospheric contribution to radiation than increasing the water vapour. Although the exclusive utilization of the DAT method yielded the smallest overall SST retrieval error, we decided to stay loyal to the original DWV algorithm approach of changing the water vapour profile first for the reasons just explained.

Table 4.2: SST retrieval results of the DWVT, original DWV [*Smith*, 1993], and DWV and DAT of *Osborne* [1995]. The results are expressed as differences between the algorithm and the buoy readings. An asterisk next to an entry in the DWVT column marks the use of the DAT algorithm.

IFUT	DWVT	DWV [*Smith*, 1993]	DWV [*Osborne*, 1995]	DAT [*Osborne*, 1995]
m9jr	0.36	0.57	0.41	0.49
m9k5	0.71	0.86	0.74	0.76
m9kc	0.14	0.15	0.16	0.13
m9n9	-0.61	-0.36	-0.41	-0.53
m9na	0.26	0.40	0.36	0.28
m9vi	0.04	0.05	0.05	0.05
ma4c	-1.02	-1.00	-1.02	-0.99
ma4i	-0.12	-0.07	-0.03	-0.01
mabk	0.32	0.36	0.34	0.37
mabz	-0.68	-0.42	-0.37	-0.51
mac6	-0.23	-0.22	-0.21	-0.21
macc	0.24	0.55	0.41	0.31
macd	-0.88	-0.73	-0.69	-0.75
macq	-1.58	-1.16	-1.20	-1.42
macr	0.16	0.18	0.22	0.25
mad5	-0.16	-0.20	-0.15	-0.17
maeb	-0.69	-0.66	-0.60	-0.62
maep	-2.46*	-0.97	-1.04	-1.12
maf3	-0.74	-0.60	-0.71	-0.72
mafh	-0.41	-0.47	-0.28	-0.32
mafw	0.05	0.03	0.07	0.01
mald	0.07	0.12	0.10	0.22
malk	0.13	0.11	0.10	0.14
mar9	0.47	0.54	0.52	0.51
mazo	0.13	0.19	0.17	0.24
mb11	0.13	-0.01	0.15	0.12
mb1f	0.15	-0.13	0.15	0.33
mb1n	-0.11	-0.11	-0.10	0.02
mb21	-1.91*	-9.40	-9.24	-1.97
mb2m	0.27	-0.28	0.29	0.44
mb9o	-0.45	-0.43	-0.40	-0.38
mbdz	-2.02	-1.99	-2.03	-2.05
mbg5	-0.87	-0.86	-0.86	-0.81
mbgc	-0.32	-0.76	-0.21	0.20
bias	-0.342	-0.492	-0.45	-0.227
rms	0.751	1.68	1.66	0.686

Examination of the results in Table 4.2 unveils that the two biggest discrepancies between the methods are for satellite passes maep and mb21. The latter is the well-known problematic pass for which the DWV method does not work. The DWVT employing DAT algorithm gave a slightly better result over the DAT of *Osborne* [1995]. We believe this is because we have implemented a more sophisticated method of calculating the intersection of SST_4/SST_5 curves (Section 4.1). The case of the maep pass is, however, more intriguing. Here, the DWVT returned by far the least accurate SST estimate despite having used the DAT algorithm. In fact, the DWVT SST error is almost two and a half times that of the original DWV [*Smith*, 1993]. We recall that *Osborne* [1995] reported getting a larger SST error for the maep pass after the introduction of his water vapour limiting procedure. Our own experience with supersaturated layers in LOWTRAN simulations is that they yield smaller SST errors. Thus it is very likely that the true SST error of the DWV method for this pass was "masked" by the problem of supersaturated layers, especially since this was one of the passes for which LOWTRAN-7 reported supersaturation of atmospheric layers in the DWV software of *Osborne* [1995]. The graph showing errors of the four DWV methods for each satellite pass is given in Figure 4.3.

The SST retrieval results of the DWVT for the Hobart site sondes and all four different sonde selection modes are presented in Tables 4.3 and 4.4.

To better assess the effect of different sonde selections on the DWVT results we decided to use the Q factor from (4.8). The bias (column Average) and rms (column Std. Dev.) in this case are calculated for each pass from the DWVT results of different sonde ages. The passes are then ranked in two ways, according to their rms and Q value. The rms ranking accentuates the passes for which DWVT produced more consistent but not necessarily more accurate SST estimates. The Q ranking, on the other hand, emphasizes the passes which were least sensitive to the sonde age overall.

The column average of Table 4.4 has some very interesting results. The average DWVT error for the passes mb1n and mafw is practically zero, with

Table 4.3: DWVT SST retrieval errors for the Hobart sonde site and four different sonde selection modes. An asterisk next to an entry marks the use of the DAT algorithm.

IFUT	5d-before	Closest	Night/Day	5d-after
m9jr	0.47	0.36	0.53	0.41
m9k5	0.68	0.71	0.66	0.68
m9kc	0.14	0.14	0.11	0.12
m9n9	-0.65*	-0.61	-0.61	-0.67
m9na	0.12	0.26	0.30	0.13
m9vi	0.06	0.04	-0.04	0.09
ma4c	-1.08	-1.02	-1.02	-1.13
ma4i	-0.12	-0.12	-0.12	-0.14
mabk	0.36	0.32	0.32	0.29
mabz	-0.66	-0.68	-0.69	-0.68
mac6	-0.31	-0.23	-0.23	-0.29
macc	-0.35*	0.24	0.20	0.23
macd	-0.94	-0.88	-0.88	-0.94
macq	-1.65	-1.58	-1.57	-1.54
macr	0.08	0.16	0.16	0.10
mad5	-0.23	-0.16	-0.15	-0.14
maeb	-0.68	-0.69	-0.66	-0.67
maep	-3.41*	-2.46*	-2.46*	-3.03*
maf3	-0.73	-0.74	-0.74	-0.81
mafh	-0.46	-0.41	-0.41	-0.36
mafw	-0.04	0.05	0.05	-0.08
mald	0.18	0.07	0.08	0.20
malk	0.18	0.13	0.13	0.21
mar9	0.40	0.47	0.50	0.44
mazo	0.16	0.13	0.14	0.19*
mb11	0.24	0.13	0.15	0.09*
mb1f	0.31	0.15	0.15	0.30
mb1n	0.13	-0.11	-0.11	0.09
mb21	-1.99*	-1.91*	-1.88*	-1.95
mb2m	0.37	0.27	0.37	0.33
mb9o	-0.47	-0.45	-0.44	-0.40
mbdz	-1.93	-2.02	-2.04	-1.96*
mbg5	-0.77	-0.87	-0.94	-1.08
mbgc	0.34	-0.32	0.33	-0.21
bias	-0.36	-0.34	-0.32	-0.36
rms	0.86	0.75	0.77	0.82
Q	0.93	0.82	0.83	0.89

Table 4.4: DWVT SST error statistics for every satellite pass for the Hobart sonde site and four different sonde selection modes. The data for this table is in Table 4.3. Bias, rms and Q were calculated for the average column for comparison with the DWVT results of different sonde selections. The satellite passes are ranked according to the IFUT std. dev. and Q factors.

IFUT	Average	IFUT-rms	IFUT-Q	Rank (IFUT-rms)	Rank (IFUT-Q)
m9jr	0.442	0.074	0.449	27	21
m9k5	0.683	0.021	0.683	5	26
m9kc	0.128	0.015	0.128	4	5
m9n9	-0.635	0.030	0.636	9	23
m9na	0.202	0.091	0.222	29	12
m9vi	0.037	0.056	0.067	23	2
ma4c	-1.063	0.053	1.064	22	30
ma4i	-0.125	0.010	0.125	1	3
mabk	0.323	0.029	0.324	7	16
mabz	-0.678	0.013	0.678	2	25
mac6	-0.265	0.041	0.268	15	14
macc	0.080	0.287	0.298	32	15
macd	-0.910	0.035	0.911	10	28
macq	-1.585	0.047	1.586	18	31
macr	0.125	0.041	0.132	16	6
mad5	-0.170	0.041	0.175	13	11
maeb	-0.675	0.013	0.675	3	24
maep	-2.840	0.465	2.878	34	34
maf3	-0.755	0.037	0.756	11	27
mafh	-0.410	0.041	0.412	14	19
mafw	-0.005	0.066	0.066	25	1
mald	0.133	0.067	0.148	26	7
malk	0.163	0.039	0.167	12	10
mar9	0.453	0.043	0.455	17	22
mazo	0.155	0.026	0.157	6	8
mb11	0.153	0.063	0.165	24	9
mb1f	0.227	0.090	0.245	28	13
mb1n	0.000	0.128	0.128	30	4
mb21	-1.932	0.048	1.933	20	32
mb2m	0.335	0.047	0.338	19	17
mb9o	-0.440	0.029	0.441	8	20
mbdz	-1.988	0.051	1.988	21	33
mbg5	-0.915	0.130	0.924	31	29
mbgc	0.035	0.349	0.351	33	18
bias	-0.34				
rms	0.79				
Q	0.86				

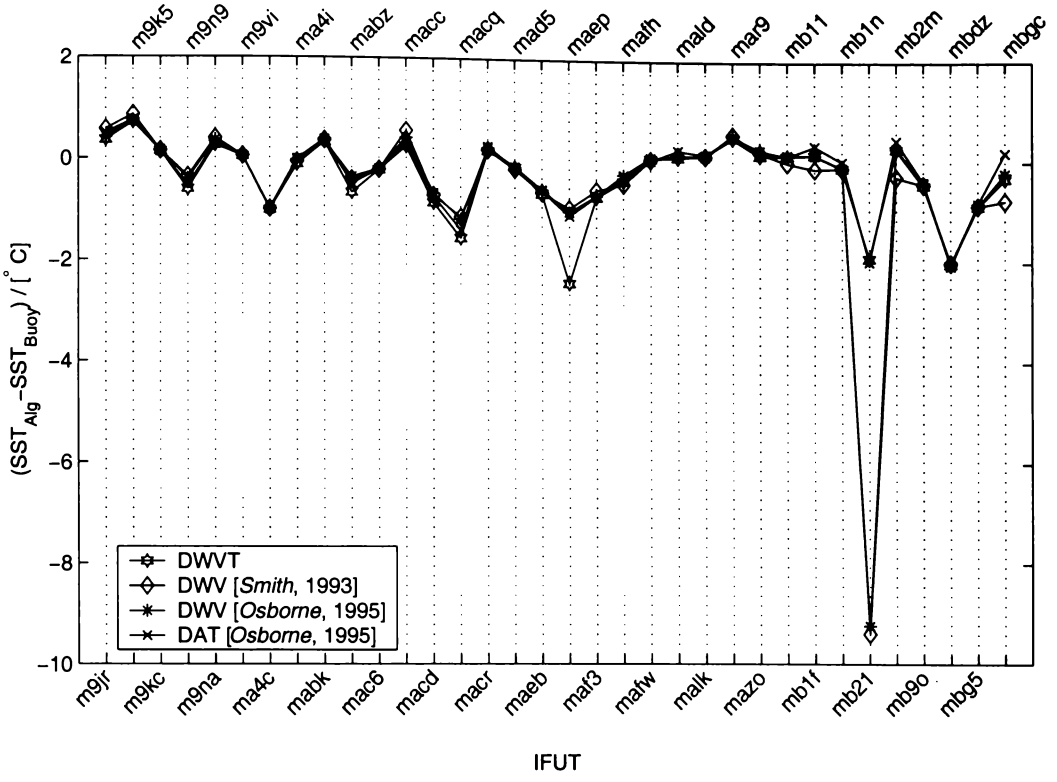

Figure 4.3: SST retrieval errors of the DWVT, DWV [*Smith*, 1993], DWV [*Osborne*, 1995] and DAT [*Osborne*, 1995], for every satellite pass of our Tasmanian data set. Radiosonde data came from the Hobart site; the sondes used were the closest to the satellite passes. Note large variations of the methods for the maep and mb21 passes, and comparatively smaller variations for the mb1f, mb2m and mbgc passes.

the passes m9vi, macc and mbgc also small. The results in the whole column however indicate that the performance of the DWVT method cannot be improved by initializing it with several different sondes for the same pair of at-satellite radiances and then finding the average.

The IFUT-rms ranking revealed the passes mb1n and mafw achieved the smallest average SST error by having their SST errors conveniently arranged around zero, since their rms ranking is 30th and 25th, respectively, out of 34. The pass with the worst rms was maep; the pass with the smallest rms was ma4i.

The best overall DWVT performance based on the Q ranking was for the mafw pass. In this case the DWVT showed the smallest sonde-sensitivity of the

SST estimate. The worst three passes were mb21, mbdz and maep, due to their large SST errors. Of the three passes, the mbdz was least affected by sonde age (rms=0.051 K). Comparing both rankings we found several passes whose rms and Q rankings did not change markedly. They could be labelled *consistent*, since they exhibited a balanced behaviour under both criteria. These passes are: m9kc, ma4i, mac6, mad5, maep, malk, mazo and mb2m.

The DAT algorithm was not used extensively overall (see Table 4.3). It was invoked four times with the "5d-after" and "5d-before" sondes, and twice with the "closest" and "night/day" sondes. We note as a curiosity that the maep pass required the DAT algorithm in all four cases, whereas the mb21 pass—the worst performing pass in *Smith* [1993] and *Osborne* [1995]—avoided DAT for the "5d-after" sonde. The fact the maep pass emerged as the worst performing in our DWVT can only be explained by the effect of the DWVT water vapour limiting algorithm.

The fact that the mb21 pass did not need the DAT for the "5d-after" sonde is yet another indication of how first-guess profiles can influence the DWV algorithm. The SST error for this case was just slightly larger than for the three previous ones when the DAT was used.

The overall DWVT performance for four different sonde selection methods (the rows bias, rms and Q in Table 4.3) shows a slight influence of sonde aging on the accuracy of SST retrieval. Although the bias for the "night/day" sondes was smaller than for the "closest" sondes, its rms was slightly larger, assuring the superiority of the "closest" sondes. The Q factor for the "5d-before" was somewhat larger than that for the "5d-after" sondes. Since we have calculated the average SST error for each pass (the column average in Table 4.4), we reported the bias, rms and Q for such "algorithm" as well. It does not compare favourably with the others, despite having two passes with almost zero SST error. Hence, we conclude that initializing the DWVT with more than one sonde for the same satellite pass does not necessarily ensure better SST accuracy.

A graph of SST errors for the four sonde selections is shown in Figure 4.4. A useful way of finding if any trends exist in SST errors is plotting them against several key variables. We chose those variables to be average atmospheric temperatures for channels 4 and 5, and total water vapour column of the final DWVT atmospheric profile, as well as the buoy-measured SST values. The first three quantities macroscopically describe the atmosphere's ability to generate and absorb radiation, whereas the last one defines the radiation-generating capability of the ocean surface. The graphs are given in Appendix A.1.1.

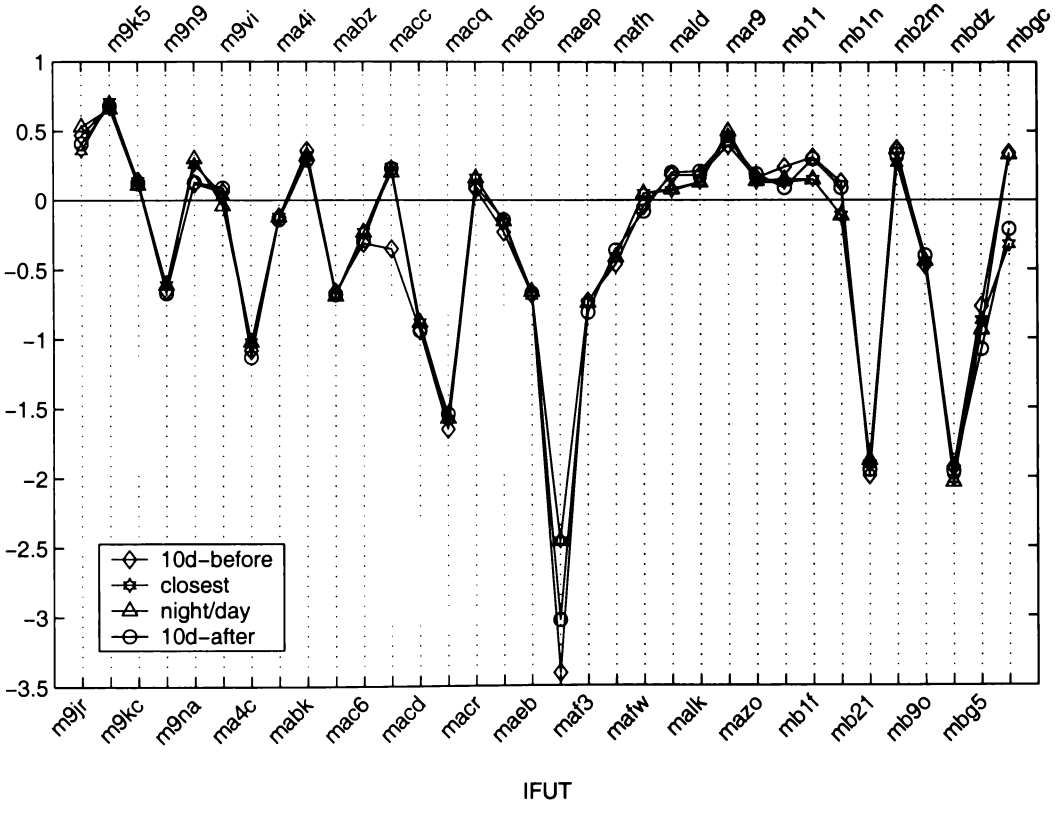

Figure 4.4: The results of the DWVT method for four different sonde selections: "5d-before", "closest", "night/day" and "5d-after". The radiosonde data are from the Hobart site.

4.6.2 DWVT Results with the Mt. Gambier Radiosondes

We now present the DWVT results using sondes from the Mt. Gambier site. The data set from this site did not contain evening soundings, so we were unable to perform the "night/day" sonde selection analysis. The results are given in Tables 4.5 and 4.6.

The SST errors in Table 4.5 exhibit an interesting feature for quite a few IFUTs. We noted dramatic changes in the DWVT SST retrievals depending on the sonde selection, something not observed for the Hobart site (Table 4.3). Certainly the most notable is the maeb pass, where the SST error reduced from 0.66 K for the "5d-before" sonde to just 0.01 K for the "closest" sonde, only to return again to 0.66 K for the "5d-after" sonde. The complete opposite is exhibited by the mafw pass. There, the "5d-before" and "5d-after" sondes yielded the same, small SST error of -0.02 K, whereas the "closest" sonde created a -0.27 K error. Similar cases are mazo, mb11, mb1f, mb1n and mbgc. For mbgc, the SST error dropped from 0.5 K for the "5d-before" sonde to only 0.03 K for the "closest" and "5d-after" sondes.

For the maeb and mb1n passes, the reason for such dramatic SST error variations is the use of the DAT algorithm. For the others of the mentioned passes we were not able to find any reason for this behaviour. We were lacking any records of prevailing meteorological conditions at the time of the soundings, so we could not tell whether or not the observed changes are due to a weather front. We were also unable to determine if the sonde data was erroneous in any way.

Due to the dramatic changes in DWVT SST errors for different sonde ages, we could not find as many *consistent* passes as in the case of the Hobart sondes (Table 4.3). The only two passes that qualify are mald and malk. The top three passes are m9vi, m9kc and macr; the worst three passes are again—albeit in different order—mbdz, maep and mb21.

Table 4.5: DWVT SST retrieval errors for the Mt. Gambier sonde site and three different sonde selection modes. An asterisk next to an entry marks the use of the DAT algorithm.

IFUT	5d-before	Closest	5d-after
m9jr	0.59	0.54	0.59
m9k5	0.67	0.59	0.71
m9kc	0.08	-0.01	0.13
m9n9	-0.73	-0.65	-0.63
m9na	0.28	0.27	0.28
m9vi	0.08	0.10	0.05
ma4c	-1.18	-1.08	-1.11
ma4i	-0.22	-0.11	-0.14
mabk	0.25	0.32	0.35
mabz	-0.71	-0.55	-0.83
mac6	-0.32	-0.26	-0.44
macc	0.19	0.34	0.21
macd	-0.99	-0.85	-0.94
macq	-1.59	-1.54	-1.56
macr	0.11	0.16	0.05
mad5	-0.19	-0.19	-0.18
maeb	-0.66	0.01*	-0.66
maep	-3.12*	-2.70*	-3.11*
maf3	0.19*	-0.71	-0.77
mafh	-0.46	-0.41	-0.38
mafw	-0.02	-0.27	-0.02
mald	0.18	0.15	0.17
malk	0.21	0.17	0.15
mar9	0.52	0.51	0.50
mazo	0.23	-1.53	-1.90*
mb11	0.27	0.17	-1.86*
mb1f	0.45	0.11	-1.81*
mb1n	0.17	-0.98*	-1.34*
mb21	-3.36*	-3.80*	-1.87
mb2m	0.42	-0.67*	0.33
mb9o	-0.69	-0.51	-0.55
mbdz	-2.02	-2.05	-3.53*
mbg5	-0.72	-0.98	-0.98
mbgc	0.50	0.03	0.03
bias	-0.34	-0.48	-0.62
rms	0.97	0.96	1.02
Q	1.03	1.07	1.20

Table 4.6: DWVT SST error statistics for every satellite pass for the Mt. Gambier sonde site and the three different sonde selection modes. The data for this table is in Table 4.5. Bias, rms and Q were calculated for the average column for comparison with the DWVT results of different sonde selections. The satellite passes are ranked according to the IFUT-rms and IFUT-Q factors.

IFUT	Average	IFUT-rms	IFUT-Q	Rank (IFUT-rms)	Rank (IFUT-Q)
m9jr	0.573	0.029	0.574	7	16
m9k5	0.657	0.061	0.660	15	20
m9kc	0.067	0.071	0.097	16	2
m9n9	-0.670	0.053	0.672	12	21
m9na	0.277	0.006	0.277	1	10
m9vi	0.077	0.025	0.081	5	1
ma4c	-1.123	0.051	1.125	10	27
ma4i	-0.157	0.057	0.167	14	4
mabk	0.307	0.051	0.311	11	11
mabz	-0.697	0.140	0.711	21	23
mac6	-0.340	0.092	0.352	19	13
macc	0.247	0.081	0.260	18	9
macd	-0.927	0.071	0.929	17	25
macq	-1.563	0.025	1.564	6	31
macr	0.107	0.055	0.120	13	3
mad5	-0.187	0.006	0.187	2	8
maeb	-0.437	0.387	0.583	26	17
maep	-2.977	0.240	2.986	24	33
maf3	-0.430	0.538	0.689	27	22
mafh	-0.417	0.040	0.419	9	14
mafw	-0.103	0.144	0.178	22	6
mald	0.167	0.015	0.167	4	5
malk	0.177	0.031	0.179	8	7
mar9	0.510	0.010	0.510	3	15
mazo	-1.067	1.138	1.560	32	30
mb11	-0.473	1.202	1.292	33	29
mb1f	-0.417	1.219	1.288	34	28
mb1n	-0.717	0.789	1.066	29	26
mb21	-3.010	1.011	3.175	31	34
mb2m	0.027	0.605	0.606	28	19
mb9o	-0.583	0.095	0.591	20	18
mbdz	-2.533	0.863	2.676	30	32
mbg5	-0.893	0.150	0.906	23	24
mbgc	0.187	0.271	0.329	25	12
bias	-0.48				
rms	0.91				
Q	1.03				

Table 4.7: DWVT statistics for six different sonde selection modes. The last four satellite passes are not included in the results in column 10d-after due to the lack of suitable sondes. The radiosonde data was from Mt. Gambier.

Statistics	15d-before	10d-before	5d-before	Closest	5d-after	10d-after
bias	-0.36	-0.34	-0.34	-0.48	-0.62	-0.26
rms	1.01	0.87	0.97	0.96	1.02	0.81
Q	1.07	0.94	1.03	1.07	1.20	0.85

The DAT algorithm was used slightly more often in the case of Mt. Gambier sondes. Except for the maeb and maep passes, utilization of the DAT algorithm yielded starkly worse SST estimates. This is particularly obvious for the mb21 pass. Its SST error almost halved when the DWV algorithm was used for the "5d-after" sonde.

The overall results for the three different sonde selections (the rows bias, rms and Q in Table 4.6) show a decrease in SST accuracy when compared to the results of the Hobart sondes. The dip in the Q factor for the "closest" sonde selection is not present; instead, it increases steadily from 1.03 K ("5d-before" sondes) to 1.2 K ("5d-after" sondes). The rms of the three different sonde selections is about 20-30% higher than that for the Hobart sondes, but is likewise quite steady in value (0.96–1.02 K). The smallest rms (0.96 K) is for the "closest" sondes. The reason for the increasing value of the Q factor comes from the biases. They decrease monotonically from -0.34 K ("5d-before") to -0.62 ("5d-after").

In an attempt to clarify whether or not the missing decrease in the Q factor for the "closest" sondes was due to a weather front we ran the DWVT software with "15d-before", "10d-before" and "10d-after" sonde selections. The last selection mode, "10d-after", could not find suitable sondes in the Mt. Gambier radiosonde database for the final four satellite passes (mb9o, mbdz, mbg5, and mbgc) so they were not taken into account. The DWVT statistics are given in Table 4.7. The best DWVT result was for the "10d-after sondes", but we must take this with caution since the last four passes were missing in that

DWVT run. The drop in the Q factor for the "10d-before" and "5d-before" sondes might be caused by passing weather fronts. The Mt. Gambier site was located to the west from the buoy, whereas the Hobart site was to the east. The predominant weather movement pattern in that region of the world is eastwards. Hence, weather fronts that were above the Hobart site at the time of the satellite overpasses, as captured in that site's "closest" sondes, might have been over the Mt. Gambier site a couple of days before. Whether or not this is the real explanation we cannot tell, due to the lack of any other information about the weather at the radiosonde launch sites.

A graph of SST errors for the three different sonde selections is shown in Figure 4.5. The graphs of the SST errors vs. channel-4 and -5 average atmospheric temperatures, and total water vapour column of the final DWVT profile, as well as the ground truth temperatures are given in Appendix A.1.2.

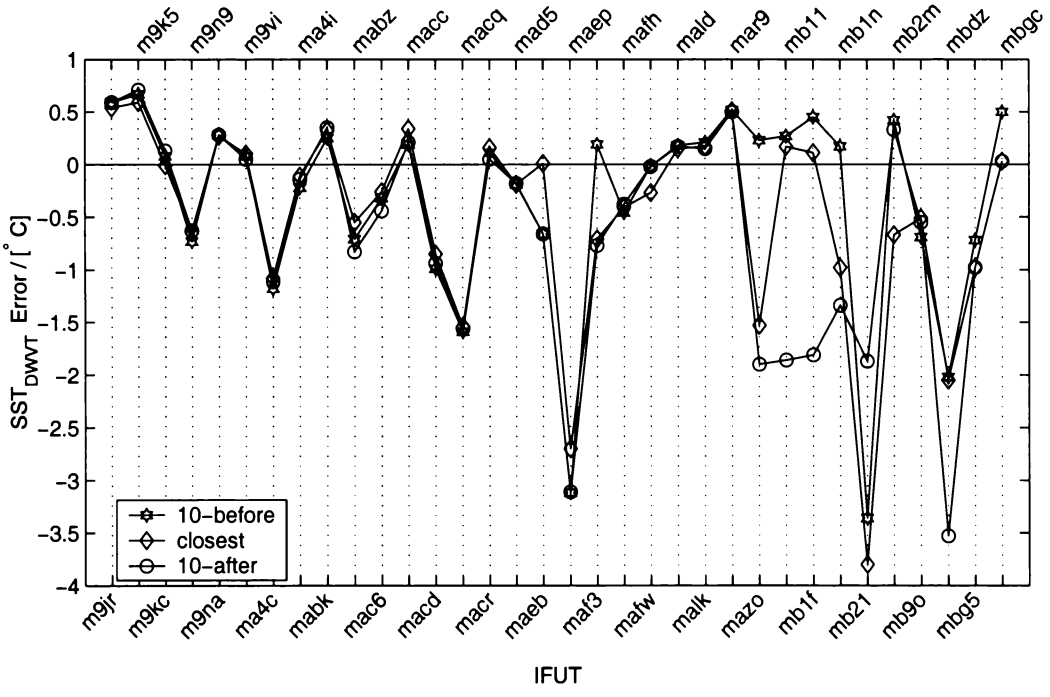

Figure 4.5: The results of the DWVT method for three different sonde selections: "5d-before", "closest" and "5d-after". The radiosonde data are from the Mt. Gambier site.

Because of the lack of evening radiosonde launches in the Mt. Gambier radiosonde set and worse overall DWVT performance when using sondes from this site, we decided to use only the sondes from Hobart when comparing the DWVT to the TRSST methods (Section 2.9) and a suite of operational NESDIS SST equations.

4.7 Comparison between the DWVT and the TRSST Methods

The performance of our DWVT was compared with that of the Transmission Ratio SST methods introduced in Section 2.9: *Harris and Mason* [1992], *Sobrino et al.* [1993] and *Sobrino et al.* [1994]. We could not implement the method of *Yu and Barton* [1994] because they did not provide any equations in the paper.

We note the following properties of the three TRSST methods used:

- *Harris and Mason* [1992] method was developed for nadir view only.
- *Sobrino et al.* [1994] was developed predominantly for land surface temperature retrieval.
- All three methods were developed for the AVHRR instrument aboard the NOAA-11 satellite.

Since our satellite data was acquired by the AVHRR on NOAA-9, the use of methods developed for another AVHRR instrument certainly will introduce biases in the results. *Czajkowski et al.* [1998] investigated the impact of different AVHRR instruments on land surface temperature estimation from MCSST-type equations. They used simulated data with filter functions for the AVHRR instruments onboard NOAA-7, -11, -12 and -14 satellites. Their finding was that the results for the AVHRR on NOAA-11 were closest to that

of the AVHRR on NOAA-9 (not exceeding 0.2 K). Encouraged by this finding, we decided to compare the TRSST methods with the DWVT.

One of the inputs in the TRSST methods is the transmittance ratio R_{54} defined in (2.32). Its use requires a knowledge of the atmospheric state, however it is often the case that local radiosondes are not available. *Kleespies and McMillin* [1990] and *Jedlovec* [1990] introduced the concept of using ratios of the spatial variance of the brightness temperatures to determine atmospheric and surface parameters. This idea was expanded by *Harris and Mason* [1992] for SST's and by *Sobrino et al.* [1994] for LSTs. *Barton* [1995] investigated these variance methods and found that while they work on simulated satellite data, they are quite unstable when applied to real satellite data. In addition, because our surface truth was provided by a buoy which was moored only a few km from the Tasmanian coast, it was not feasible to compute a spatial variance measure for the region centred on the buoy which would be guaranteed to be uncontaminated by nearby land pixels. For these reasons we elected not to employ the variance method to estimate R_{54}, since it is likely that the performance of the TRSST methods would have been compromized. Instead, we used the R_{54} values derived from the LOWTRAN-calculated channel-4 and -5 transmittances for first-guess and final DWVT atmospheric profiles.

Tables with the detailed results of the TRSST and DWVT methods are given in Appendix A.2. We present here only their overall statistics for different sonde selections.

The bias, rms and Q values for H&M [*Harris and Mason*, 1992], Sob93 [*Sobrino et al.*, 1993] and Sob94 [*Sobrino et al.*, 1994] methods for the first-guess value of R_{54} are given in Table 4.8. The data from this table are also shown in Figure 4.6.

The same statistics but with the R_{54} value calculated from the final DWVT profile is displayed in Table 4.9. Also shown are the DWVT statistics because the same atmospheric profile is used for all the methods in the table. The data from this table are also shown in Figure 4.7.

Table 4.8: SST error statistics for the methods of H&M [*Harris and Mason*, 1992], Sob93 [*Sobrino et al.*, 1993] and Sob94 [*Sobrino et al.*, 1994]. The value of R_{54} was calculated using LOWTRAN-7 from the first-guess atmospheric profiles from Hobart.

Statistic	H&M	Sob93	Sob94
5d-before sondes			
bias	-0.97	-0.96	-1.16
rms	0.73	0.70	0.73
Q	1.21	1.19	1.37
Closest			
bias	-0.98	-0.93	-1.12
rms	0.71	0.71	0.75
Q	1.21	1.18	1.35
Night/Day			
bias	-0.98	-0.93	-1.12
rms	0.72	0.70	0.73
Q	1.22	1.16	1.34
5d-after			
bias	-0.96	-0.97	-1.16
rms	0.73	0.69	0.72
Q	1.21	1.19	1.37

All four methods had similar rms statistics, though the tendency was for more 'complex' algorithms to show larger rms errors ($\sim$ 0.71 K for H&M and Sob93; $\sim$ 0.75 K for Sob94 and $\sim$ 0.8 K for DWVT)—that of the DWVT being always the biggest. Because the bias error for DWVT was much smaller than for the others, the summary Q-statistic reported DWVT as having the best performance.

Of the four methods, DWVT was the most sensitive to sonde aging. H&M displayed almost no sensitivity, though this was somewhat more apparent when R_{54} from the final DWVT profiles was used. Sob93 and Sob94 showed more sensitivity than H&M, but of a differing trend. When the first-guess profile R_{54} was used, the Q factor for Sob93 and Sob94 exhibited a decrease for recent soundings. However, the Q values of Sob93 and Sob94 increased for the values

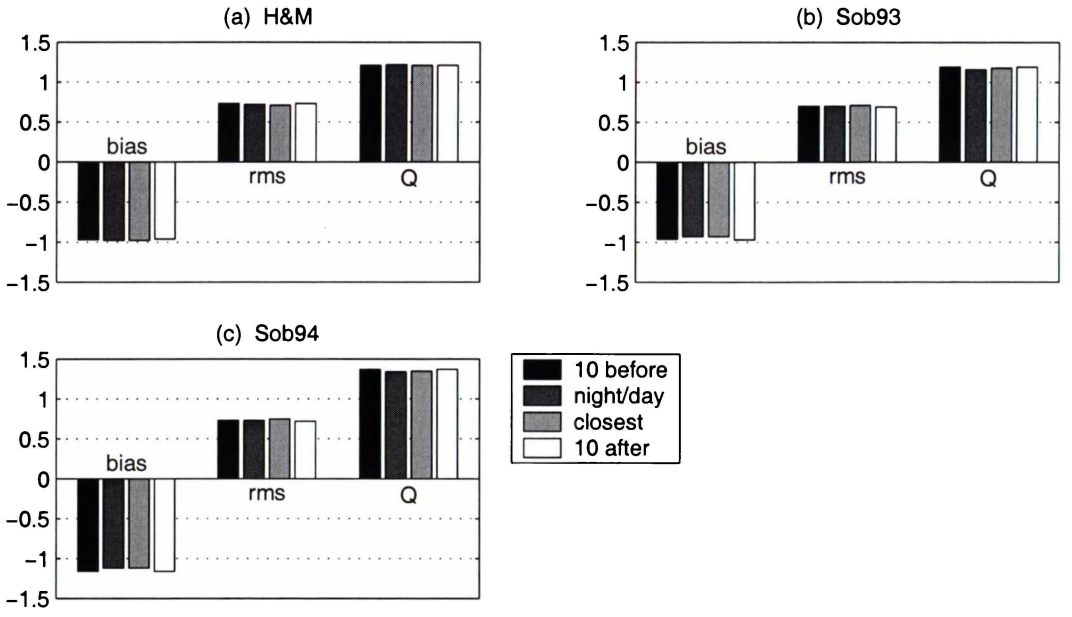

Figure 4.6: Comparison of the H&M [*Harris and Mason*, 1992], Sob93 [*Sobrino et al.*, 1993] and Sob94 [*Sobrino et al.*, 1994] methods when first-guess atmospheric profiles from the Hobart site are used to calculate the R_{54} ratio. (a) H&M shows no sensitivity to sonde age, whereas (b) Sob93, and (c) Sob94 are slightly more sensitive.

of R_{54} from the final DWVT profiles. Examining the statistics in Tables 4.8 and 4.9 we find that only the H&M method improved with the use of DWVT final profiles, while the performance of Sob93 and Sob94 degraded slightly.

4.8 Comparison of DWVT with NESDIS Operational SST Equations

To round out the method comparisons, we used our NOAA-9 and buoy data set to compare the relative performance of the DWVT with eight operational SST retrieval formulas which have been developed by NESDIS for NOAA-9, -11, -12, and -14. We ask the question: How large are the retrieval errors when NOAA-9 brightness temperatures from our Tasmanian data set are applied to the various operational algorithms developed for the later NOAA satellites?

Ideally the AVHRR instruments carried on different NOAA satellites would

Table 4.9: SST error statistics for the DWVT, H&M [*Harris and Mason*, 1992], Sob93 [*Sobrino et al.*, 1993] and Sob94 [*Sobrino et al.*, 1994] methods. The value of R_{54} was calculated using LOWTRAN-7 from the final DWVT atmospheric profiles. The first-guess profiles came from Hobart.

Statistic	DWVT	H&M	Sob93	Sob94
5d-before sondes				
bias	-0.36	-0.96	-0.95	-1.14
rms	0.86	0.72	0.71	0.74
Q	0.93	1.20	1.19	1.37
Closest				
bias	-0.34	-0.91	-1.03	-1.24
rms	0.75	0.74	0.68	0.71
Q	0.82	1.17	1.24	1.43
Night/Day				
bias	-0.32	-0.92	-1.00	-1.21
rms	0.77	0.73	0.68	0.71
Q	0.83	1.18	1.21	1.40
5d-after				
bias	-0.36	-0.94	-0.97	-1.17
rms	0.82	0.71	0.70	0.74
Q	0.89	1.17	1.20	1.38

be identical so that particular coefficients of an SST algorithm, developed for say NOAA-9, might be expected to work equally well on a later satellite. However, there are subtle instrument-to-instrument differences [*Czajkowski et al.*, 1998] in the channel-4 and -5 bandpass characteristics (and therefore in the published central wavenumber values). In addition, SST algorithm coefficients depend on the average atmospheric state which prevailed during the time of the buoy-vs-satellite temperature regressions. For these two reasons, the operational split-window algorithms vary both with satellite and with time. Nevertheless, it is of interest to know just how consistent the various operational algorithms are.

The methods we selected for testing are drawn from Appendix E of the NOAA Polar Orbiter Data User's Guide, published on the World Wide Web at:

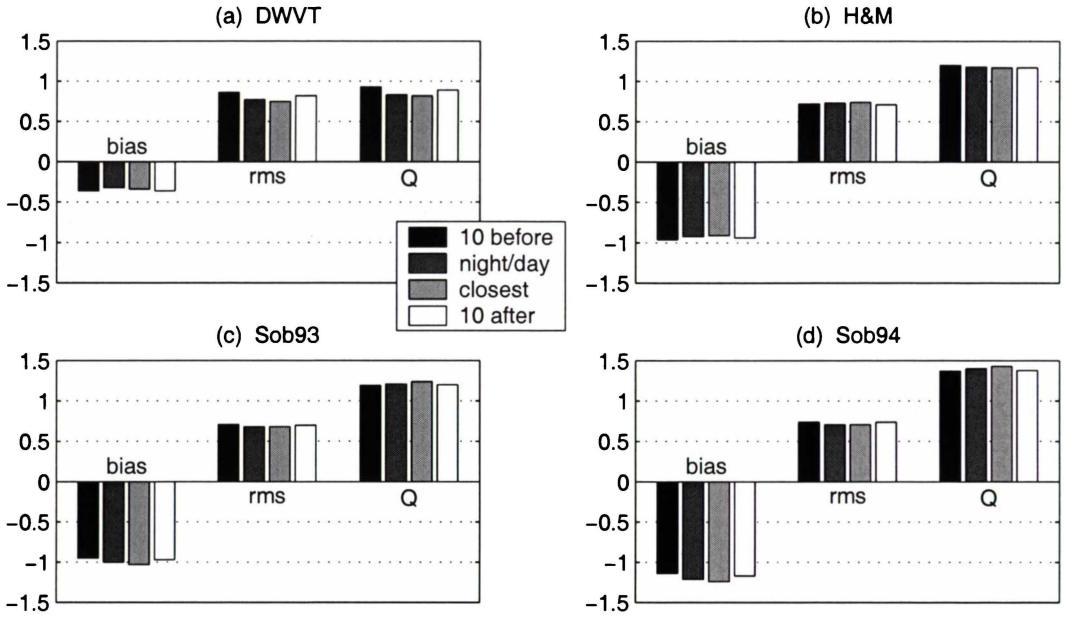

Figure 4.7: Comparison of the DWVT, H&M [*Harris and Mason*, 1992], Sob93 [*Sobrino et al.*, 1993] and Sob94 [*Sobrino et al.*, 1994] methods when final DWVT atmospheric profiles are used to calculate the R_{54} ratio.

`http://perigee.ncdc.noaa.gov/docs/podug/html/e/app-e.htm`. For each satellite we selected representative algorithms (multichannel, cross-product, nonlinear) which were both operational and closest in time to our 1987 data set. By "operational", we mean that the equation was either used operationally by NESDIS to derive SST values, or was a close relative which formed part of the bundle of equations published by NESDIS at that time. (Our investigation is restricted to NESDIS equations which utilize brightness temperatures for channels 4 and 5 only, and not channel 3.)

Listed below are the tested algorithms, together with the date when each became operational. The nonlinear SST equations (NLSST) need a first guess of the sea surface temperature, T_{guess}. The NOAA recommendation is to use the 100-km analyzed field temperature from the previous day. Since we could not obtain this information, we followed the NOAA alternative suggestion of generating the first guess by using the multichannel SST (MCSST) equations introduced at the same time as the nonlinear SST equations. T_4 and T_5 are the brightness temperatures (in K) for AVHRR channels 4 and 5; SST is the resulting temperature estimate in °C. The angle θ is the satellite zenith angle.

4.8.1 MCSST: Multichannel SST

- **NOAA-9 MCSST** (16 July 1987)

$$\begin{aligned}\mathrm{MCSST}_{9,\mathrm{night}} &= 3.6037\,T_4 - 2.6316\,T_5 \\ &\quad - 0.27(T_4 - T_5)(\sec\theta - 1) + 0.738(\sec\theta - 1) - 265.0117 \qquad (4.9)\end{aligned}$$

$$\mathrm{MCSST}_{9,\mathrm{day}} = 3.4317\,T_4 - 2.5062\,T_5 - 251.2163 \qquad (4.10)$$

- **NOAA-11 MCSST** (17 November 1988)

$$\begin{aligned}\mathrm{MCSST}_{11,\mathrm{night}} &= 0.9843\,T_4 + 2.0942(T_4 - T_5) \\ &\quad + 2.0994(T_4 - T_5)(\sec\theta - 1) - 1.1838(\sec\theta - 1) - 268.74 \qquad (4.11)\end{aligned}$$

$$\begin{aligned}\mathrm{MCSST}_{11,\mathrm{day}} &= 0.9712\,T_4 + 2.0663(T_4 - T_5) \\ &\quad + 1.8983(T_4 - T_5)(\sec\theta - 1) - 1.9790(\sec\theta - 1) - 264.79 \qquad (4.12)\end{aligned}$$

- **NOAA-12 MCSST** (15 September 1994)

$$\begin{aligned}\mathrm{MCSST}_{12,\mathrm{night}} &= 0.967077\,T_4 + 2.384376(T_4 - T_5) \\ &\quad + 0.480788(T_4 - T_5)(\sec\theta - 1) - 263.94 \qquad (4.13)\end{aligned}$$

$$\begin{aligned}\mathrm{MCSST}_{12,\mathrm{day}} &= 0.963563\,T_4 + 2.579211(T_4 - T_5) \\ &\quad + 0.242598(T_4 - T_5)(\sec\theta - 1) - 263.006 \qquad (4.14)\end{aligned}$$

- **NOAA-14 MCSST** (20 March 1995)

$$\begin{aligned}\mathrm{MCSST}_{14,\mathrm{night}} &= 2.275385(T_4 - T_5) + 1.029088\,T_4 \\ &\quad + 0.752567(T_4 - T_5)(\sec\theta - 1) - 282.24 \quad (4.15)\end{aligned}$$

$$\begin{aligned}\mathrm{MCSST}_{14,\mathrm{day}} &= 2.139588(T_4 - T_5) + 1.017342\,T_4 \\ &\quad + 0.779706(T_4 - T_5)(\sec\theta - 1) - 278.43 \quad (4.16)\end{aligned}$$

4.8.2 CPSST: Cross-Product SST

- **NOAA-11 CPSST** (2 March 1990)

$$\begin{aligned}\mathrm{CPSST}_{11,\mathrm{night}} &= \frac{0.19817\,T_5 - 49.15}{0.20524\,T_5 - 0.17334\,T_4 - 6.10}(T_4 - T_5 + 1.47) \\ &\quad + 0.96554\,T_5 + 0.96(T_4 - T_5)(\sec\theta - 1) - 267.13 \quad (4.17)\end{aligned}$$

$$\begin{aligned}\mathrm{CPSST}_{11,\mathrm{day}} &= \frac{0.19410\,T_5 - 48.15}{0.20524\,T_5 - 0.17334\,T_4 - 6.25}(T_4 - T_5 + 1.32) \\ &\quad + 0.94575\,T_5 + 0.60(T_4 - T_5)(\sec\theta - 1) - 260.99 \quad (4.18)\end{aligned}$$

4.8.3 NLSST: Nonlinear SST

- **NOAA-11 NLSST** (10 April 1991)

$$\begin{aligned}\mathrm{NLSST}_{11,\mathrm{night}} &= 0.96042\,T_4 + 0.087516\,T_{\mathrm{guess}}(T_4 - T_5) \\ &\quad + 0.852(T_4 - T_5)(\sec\theta - 1) - 261.46 \quad (4.19)\end{aligned}$$

$$\mathrm{NLSST}_{11,\mathrm{day}} = 0.94649\,T_4 + 0.08412\,T_{\mathrm{guess}}(T_4 - T_5) + 0.751(T_4 - T_5)(\sec\theta - 1) - 257.20 \quad (4.20)$$

where

$$T_{\mathrm{guess}} = 1.02455\,T_4 + 2.45(T_4 - T_5) + 0.64(T_4 - T_5)(\sec\theta - 1) - 280.67 \quad (4.21)$$

- **NOAA-12 NLSST** (15 September 1994)

$$\mathrm{NLSST}_{12,\mathrm{night}} = 0.888706\,T_4 + 0.081646\,T_{\mathrm{guess}}(T_4 - T_5) + 0.576136(T_4 - T_5)(\sec\theta - 1) - 240.229 \quad (4.22)$$

$$\mathrm{NLSST}_{12,\mathrm{day}} = 0.876992\,T_4 + 0.083132\,T_{\mathrm{guess}}(T_4 - T_5) + 0.349877(T_4 - T_5)(\sec\theta - 1) - 236.667 \quad (4.23)$$

where NOAA-12 MCSST equations (4.13) and (4.14) provided respective night and day values for T_{guess}.

- **NOAA-14 NLSST** (20 March 1995)

$$\mathrm{NLSST}_{14,\mathrm{night}} = 0.078095\,T_{\mathrm{guess}}(T_4 - T_5) + 0.933109\,T_4 + 0.738128(T_4 - T_5)(\sec\theta - 1) - 253.428 \quad (4.24)$$

$$\mathrm{NLSST}_{14,\mathrm{day}} = 0.076066\,T_{\mathrm{guess}}(T_4 - T_5) + 0.939813\,T_4 + 0.801458(T_4 - T_5)(\sec\theta - 1) - 255.165 \quad (4.25)$$

where NOAA-14 MCSST equations (4.15) and (4.16) provided respective night and day values for T_{guess}.

4.8.4 Results of NESDIS Equations

The previously mentioned NESDIS operational SST equations were used to retrieve SST's for our Tasmanian buoy and satellite data set. The at-satellite radiance was converted to brightness temperature using the NOAA-9 channel-4 and -5 central wavenumber values. The retrieved SST's for each satellite pass are given in Appendix A.3. We here present only the SST error statistics (Table 4.10) using the variables (bias, rms and Q) as we have previously in this chapter.

Table 4.10: SST error statistics for the selected test set of NESDIS operational algorithms. The method acronym and subscript identifies the equations used, thus MCSST_9 indicates multichannel SST using NOAA-9 equations (4.9) (night passes) and (4.10) (day passes). The NLSST equations were tested twice; once using the T_{guess} equations listed in Section 4.8.3 (e.g., NLSST_{11}), then a second time using NOAA-9 MCSST to provide the first guess (e.g., $\text{NLSST}_{11,9}$). Rank orders the methods based on the Q-statistic.

Method	Bias	rms	Q	Rank
MCSST_9	-0.26	0.64	0.69	1
MCSST_{11}	-0.91	0.63	1.11	5
MCSST_{12}	-0.90	0.64	1.11	4
MCSST_{14}	-1.56	0.67	1.70	11
CPSST_{11}	-1.43	0.70	1.59	10
NLSST_{11}	-1.21	0.72	1.41	9
$\text{NLSST}_{11,9}$	-1.15	0.71	1.35	8
NLSST_{12}	-0.40	0.69	0.79	3
$\text{NLSST}_{12,9}$	-0.36	0.68	0.77	2
NLSST_{14}	-1.07	0.72	1.29	7
$\text{NLSST}_{14,9}$	-0.99	0.71	1.22	6

Table 4.10 shows that MCSST for NOAA-9 gives excellent retrievals with a bias of -0.26 K and an rms error of 0.64 K. With one exception (NLSST for NOAA-12), we find that applying the NOAA-9 brightness temperature data to the SST equations for the later satellites produces notably degraded bias values. This degradation is not unexpected, since the regression equations en-

capsulate the average atmospheric state prevailing at the time of the regression experiments, and this average atmospheric state changes with time. Also, the channel-4 and -5 filter functions for the NOAA satellites are similar, but not identical; however, the filter function effect on algorithm accuracy is probably minor. We note that all three NLSST statistics are improved when $MCSST_9$ values are used for the first guess; this is not surprising since it is simply underscoring the importance of an accurate first guess seed for the nonlinear method. It is interesting to observe that the rms statistics for the NESDIS formulas confirm the trend observed in the previously described methods: rms error increases with algorithm complexity. Complex algorithms require more data, which inherently contain error and, thus, leads to increased uncertainty in the retrieved SST values.

A plot of DWVT and $MCSST_9$ errors for our Tasmanian data set is shown in Figure 4.8. It was encouraging to see the two methods following each other closely for the majority of 34 cases. The biggest discrepancy was for the maep pass where $MCSST_9$ produced about three times smaller SST error. This pass is evidently the predominant reason why the $MCSST_9$ equations outperformed our DWVT with a clear margin. Less prominent differences between the two methods occurred for the mb1n, mb21 and mbgc passes.

4.9 Discussion

In this chapter, we have formulated a new method for SST retrieval, the Dynamic Water Vapour or Atmospheric Temperature (DWVT), starting from the original Dynamic Water Vapour method [*Smith*, 1993, *Steyn-Ross et al.*, 1993]. The DWVT algorithm was implemented (Section 4.1) using the findings reported in *Osborne* [1995] on DWV's sensitivity and stability. This study focused on the reason why the DWV sometimes produced grossly inaccurate SST estimates (the absolute zero in some cases), mainly for the mb21 pass.

The DWVT represents a functional merger of the DWV and DAT algo-

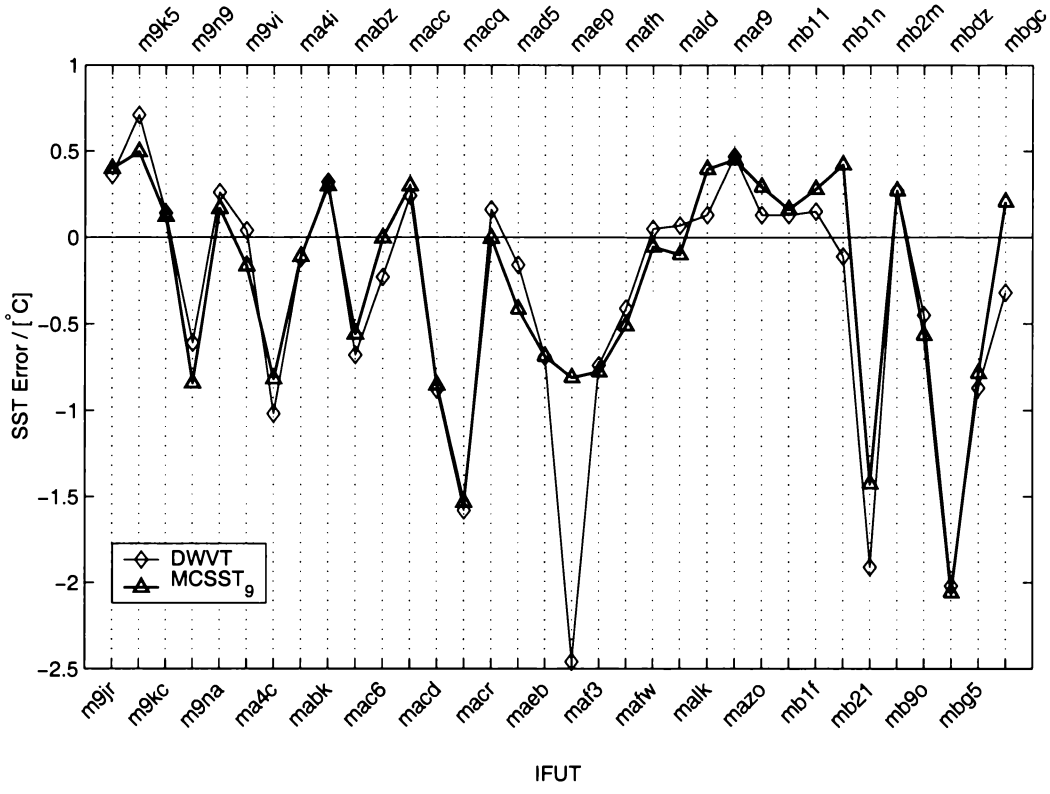

Figure 4.8: Plot of SST retrieval errors of the DWVT and the operational NESDIS MCSST equation for NOAA-9 (4.9). DWVT used the "closest" sondes from Hobart.

rithms. In order to achieve this functionality, a DWV failure test (Section 4.2) was built into the DWVT. In the case of a DWV failure, the DWVT switches over to the DAT algorithm in a search for an SST convergence. The DWV failure test was devised using the channel-4 and -5 surface temperature curves, which are monitored for each new atmospheric profile in the DWV. If either of the two stops increasing while the amount of water vapour is increased in the profile, the DWVT switches over to the DAT algorithm. Because of this test's ability to be implemented during execution of the DWV, we were able to do on-the-fly failure testing and significantly cut down the overall execution time of the DWVT.

While developing a working version of the DWVT software, we discovered that LOWTRAN-7 was still reporting supersaturated water-vapour layers in some of the tuned atmospheric profiles. This problem was first reported by

Osborne [1995] and he had addressed it by implementing a water-vapour limiting procedure. It was obvious that there was a difference between his and LOWTRAN's equations for water vapour limits. Instead of using experimental data and fitting our equations as *Osborne* did, we collected already published equations and created our own water vapour limiting algorithm (Section 4.4.1). Although we don't know by how much our method and LOWTRAN's differ, we have no longer observed supersaturated layers in LOWTRAN's output.

To test the DWVT for sonde aging, we defined four different sonde selections (Section 4.6) based on the time difference between the sonde launch and the satellite pass. The first-guess sondes were chosen from the interval of five days around the satellite pass. Another option was the "night/day" selection, where we matched the closest night sonde launches of night satellite passes and vice versa for the daytime satellite passes. This presented an interesting opportunity to study how daytime and night-time atmospheric profiles influence DWVT performance. Along with temporally mismatched first-guess sondes, we also presented results using radiosondes from two different launch sites: Hobart (located approx. 200 km eastward from the buoy) and Mt. Gambier (approx. 600 km north-west from the buoy).

The DWVT method was first compared (Section 4.6) with its "next of kin": the DWV of *Smith* [1993], and the DWV and DAT of *Osborne* [1995]. Somewhat surprisingly, the older methods of *Smith* [1993] and *Osborne* [1995] outperformed our DWVT in quite a few cases. However, the differences in question were not large, and we have attributed them to the newly employed water vapour limiting procedure (Section 4.4.1). Our experience was that having supersaturated layers during LOWTRAN-7 calculations produced better SST estimates. Although we have obviously degraded the performance of the DWVT, we judged that maintaining physically realistic atmospheric profiles was in the spirit of the original DWV.

The DWVT was second best, behind the DAT of *Osborne* [1995], mainly due to the success of the DAT algorithm in the case of the mb21 pass. Al-

though the performance of *Osborne*'s DAT method suggests one should tune atmospheric temperature exclusively, we decided to use it only in the rare occasions when the DWV approach is likely to fail. Firstly, we were not sure in how many cases *Osborne* had supersaturated layers which would have yielded smaller SST errors, and secondly, we deemed that changing the atmospheric temperature causes much more fundamental changes to the profile than tuning the water vapour. We believe that the DWVT results with Hobart and Mt. Gambier sondes validates the use of the DAT algorithm for extreme cases only.

The most notable DWVT error was for the maep pass. We were surprised with this finding, since both *Smith* [1993] and *Osborne* [1995] never indicated this pass as problematic. It turned out, however, that this pass was the worst overall performer of the DWVT method.

Digesting the DWVT results for the radiosondes from Hobart and Mt. Gambier (Sections 4.6.1 and 4.6.2) revealed that the DAT algorithm was relatively seldom used. Its utilization rate ranged from two to six passes per sonde selection, with a tendency of higher rates for the Mt. Gambier sondes of the same sonde age. Of all these cases, only two produced SST errors smaller than 0.5 °C (macc pass, "5d-before" sonde from Hobart, SST error of -0.35 °C; maeb pass, "closest" sonde from Mt. Gambier, SST error of 0.01 °C), and only in one case the DAT SST error was smaller than its DWV counterparts (maeb pass, "closest" sonde from Mt. Gambier, SST error of 0.01 °C).

DWVT in general underestimated sea surface temperatures. SST errors of the DWVT never exceeded 1 °C, whereas they went almost as low as -4 °C (mb21 pass, "closest" sonde from Mt. Gambier, SST error of -3.8 °C).

Three passes—maep, mb21 and mbdz—consistently produced SST errors of -2 °C or larger. The macq pass had SST errors of around -1.5 °C, while all the other passes were located in the interval ±1 °C around the buoy SST. The only exception to this pattern was a set of adjacent passes, mazo, mb11, mb1f and mb1n, with SST errors around -2 °C for "5d-after" sondes from Mt. Gambier. Table 4.5 indicate that DAT algorithm was employed for the four

passes.

The graphs of SST errors against intrinsic variables of the final DWVT atmospheric profiles (Appendix A.1.1 and A.1.2) further confirm the pitfalls of using the DAT algorithm. The maep pass is a good example since it required the DAT algorithm to converge more often than any other pass. Average channel-4 and -5 atmospheric temperatures for this pass were always smaller than -5 °C, clearly making that pass stand out. Thus a cold atmosphere drives down the amount of water vapour in it, making all the final DWVT profiles for this pass optically thin. Such an atmosphere produces very little radiation, so the major contribution to the satellite-sensed radiance comes from the surface. Nevertheless, the SST errors were around -2.5 °C or more. Although surely ensuring DWVT convergence, the DAT algorithm produces atmospheres that do not provide a good approximation of the true atmospheric conditions. We believe that the evidence presented so far on the DWVT accuracy when DAT algorithm is used supports our decision to use it only when DWV algorithm cannot achieve SST convergence.

Further analysis of the graphs in Appendix A.1.1 and A.1.2 revealed that the passes with large SST errors have something in common—the final DWVT atmospheric profiles of these passes had a total water vapour column of around 1 g/cm^2. Their respective average channel-4 and -5 atmospheric temperatures are more variable though. For the maep pass, $\overline{T}_{a4}$ and $\overline{T}_{a5}$ were always smaller than -5,°C, whereas the mb21 and mbdz passes were usually around 0 °C. However, we cannot single out optically thin atmospheres as the reason for large SST errors because there were other passes with even quite accurate SST retrievals for similar values of total water vapour column.

The DWVT results for each satellite pass exhibited smaller variation in the case of Hobart sondes (Table 4.4), though it may not be only due to the age of radiosondes. In choosing the Mt. Gambier site we have also introduced the weather propagation component in our analysis.

The weather over Southern-east Australia and Southern Ocean usually

propagates eastwards. On its way towards the buoy, a weather front first reaches the Mt. Gambier site. Earlier sonde launches relative to a particular satellite pass from Mt. Gambier site can potentially capture a similar atmospheric profile as the sondes launched closer to the same pass from Hobart. Unfortunately, we did not have any additional meteorological data to substantiate this conjecture.

Further examples that weather propagation might have influenced the DWVT results came from analyzing the Q-statistic in Tables 4.3, 4.5 and 4.7. The Q values of the sondes from Mt. Gambier centered around the times of satellite passes did not show an expected dip in their values as the sonde launch time approaches that of the satellite pass. The opposite was observed in the case of Hobart sondes. To study this further for the Mt. Gambier site, we ran the DWVT for sondes up to 15 days (Table 4.7) from satellite passes. The Mt. Gambier radiosonde database limited the time interval we could use before and after the satellite passes. The bias statistic for "15d-before", "10d-before" and "5d-before" sondes of Mt. Gambier was the same as for the Hobart sondes, an improvement when compared to its "closest" and "5d-after" counterparts.

Overall, our conclusion is that spatially and temporally closer first-guess atmospheric profiles produce better DWVT SST estimates. Use of first-guess atmospheric profile data temporally and spatially farther from the AVHRR pixel increases the likelihood of DAT algorithm and larger SST errors.

The DWVT method was compared with a set of regression based SST retrieval methods. This set included methods that attempt to account for the water vapour state of the atmosphere by using a channel-4 to -5 ratio of transmissivities R_{54} (Transmission Ratio SST (TRSST); Section 4.7) and a more traditional suite of operational NESDIS SST retrieval equations (Section 4.8) developed for NOAA-9, -11, -12 and -14 satellites.

The transmission ratio methods (TRSST) were tested with two different values of R_{54}, one derived from first-guess profiles and the other derived from final DWVT profiles. Surprisingly, the first-guess R_{54} values for all sonde

selections yielded smaller values of the Q-statistic for the Sobrino methods [*Sobrino et al.*, 1993, 1994]; the method of *Harris and Mason* [1992] was the only one to benefit from the final DWVT profiles. We found this to be very interesting; the profiles which supposedly should have matched more closely the true atmospheric conditions did not improve the performance of the TRSST methods we tested. The use of R_{54} values from the final DWVT profiles also worsened the sensitivity of the Sobrino methods to sonde aging, with both methods reporting larger Q-statistic for temporally matched sondes ("closest" and "night/day"). The opposite was for the *Harris and Mason* [1992] method.

Of all the NESDIS methods we tested, the suite of NOAA-9 MCSST equations, operational exactly during the Tasmanian data gathering campaign, outperformed our DWVT by a clear margin. The other NESDIS method scoring a slightly smaller Q-statistic was the NOAA-12 NLSST method. While the NOAA-9 MCSST achieved a noticeably smaller bias than our DWVT, the NOAA-12 NLSST outperformed the DWVT due to a smaller rms statistic only. We note that a smaller rms than DWVT's was the case for all the TRSST and NESDIS methods. Obviously, regression-based methods are more robust and less prone to reporting hugely variable SST estimates.

When a regression-based algorithm is developed, the aim is to produce a single-line equation whose accuracy is independent of atmospheric state. Any single-line algorithm will work best when the prevailing atmospheric conditions are similar to some average atmospheric state defined by the suite of sondes/buoys/satellite data used to craft the algorithm. The resulting regression coefficients represent the best-fit curve which maps at-satellite brightness temperature to surface temperature through this notional average atmosphere.

The excellent results of the NOAA-9 MCSST indicate that the standard regression methods work very well in mid-latitude locations where atmospheric water vapour loading is usually not excessive. We have not been able to test the relative performances of the algorithms in tropical situations where the water vapour column could be significant, though we would expect a DWVT

approach to work well.

We believe that DWVT has potential for improved accuracy. In the next chapter we develop a method which allows the profiles for water vapour and atmospheric temperature to be tuned simultaneously, rather than sequentially as in the DWVT.

Chapter 5

Simultaneous Water Vapour and Atmospheric Temperature Method

The retrieval of sea surface temperature from satellite radiation observations is fundamentally a nonlinear optimization problem due to the complex interaction and interdependence of atmospheric constituents with radiation. The Dynamic Water Vapour (DWV) [*Smith*, 1993, *Steyn-Ross et al.*, 1993] and the Dynamic Water Vapour or Atmospheric Temperature (DWVT) (Chapter 4) methods try to address this optimization problem by altering either the water vapour content or the temperature of a first-guess atmospheric profile. This is essentially a one-dimensional approach to the nonlinear optimization problem of at least two variables (water vapour and atmospheric temperature; the other atmospheric constituents are assumed constant) and has a few pitfalls.

The DWV performed badly when dealing with a too warm first-guess atmospheric profiles by changing the water vapour profile content only. To circumvent this, we formulated the DWVT, presented in Chapter 4. This method switches over to tune the atmospheric temperature (the Dynamic Atmospheric Temperature (DAT) algorithm) as soon as the DWV failure test (Section 4.2)

is triggered. Although the introduction of the DAT algorithm in the DWVT seems to have alleviated some of the problems of the DWV, we have identified two weaknesses in DWVT's formulation:

- How robust is the current form of the DWV failure test? How sure are we that this test is triggered optimally, i.e. only when it is really required?

- The DAT algorithm prevented the DWVT from producing SST retrieval errors as large as the DWV, but the DAT-generated SST errors were still the largest in our Tasman data set.

By restricting DWVT to alter only one of the atmospheric variables in our model at a time, we may be missing an atmospheric profile yielding a better SST estimate that could be achieved by changing both the water vapour and atmospheric temperature profiles at the same time. To avoid this, we were inspired to formulate a new method which we describe in this chapter—the Simultaneous Water Vapour and Atmospheric Temperature (SimWVT) method.

Starting from the equation of radiative transfer, we use variational calculus to derive an expression relating ΔI, the difference between the radiance calculated using a first-guess atmospheric profile and the observed satellite radiance, to the corresponding changes in atmospheric temperature (ΔT) and water vapour (Δu). By requiring the same SST to be predicted in channels 4 and 5, while keeping $\Delta I = 0$, we estimate the SST.

In the following sections, we derive the SimWVT equation, then show how it is incorporated into the SimWVT algorithm. We compare SimWVT with its direct predecessor the DWVT, and discuss the differences in their performances.

5.1 Derivation of the SimWVT Equation

As in all SST algorithms, the derivation starts with the radiative transfer equation (2.1):

$$I_\nu = B_\nu(T_s)\tau_\nu(0) + \int_0^\infty B_\nu(T(z))\,\mathrm{d}\tau(z), \tag{5.1}$$

where: ν is the wave number, T_s is the surface temperature, $\tau_\nu(0)$ is the total atmospheric transmittance, $B_\nu(T)$ is the blackbody monochromatic radiance at temperature T, $T(z)$ is the atmospheric temperature profile, and z is the height above the ground.

The core philosophy of SimWVT is to find temperature and water vapour corrections such that I_ν remains unchanged for the new atmospheric profile. We firstly obtain an expression for the change in I_ν by writing (5.1) in its total differential form:

$$\mathrm{d}I_\nu = \mathrm{d}B_\nu(T_s)\tau_\nu(0) + B_\nu(T_s)\,\mathrm{d}\tau_\nu(0) + \mathrm{d}\left(\int_0^\infty B_\nu(T(z))\,\frac{\partial\tau_\nu}{\partial z}\,\mathrm{d}z\right). \tag{5.2}$$

In order to evaluate total differential of the integral in (5.2), we first recall the definition of atmospheric transmission [*Liou*, 1980]:

$$\tau_\nu(z) = \exp(-\kappa_\nu\, u(z)), \tag{5.3}$$

where κ is the mass absorption coefficient of water vapour, and $u(z)$ is the water vapour path length at the height z evaluated along the radiation slant path. The partial derivative of τ in the integral of (5.2) is:

$$\frac{\partial\tau_\nu}{\partial z} = -\kappa_\nu \exp(-\kappa_\nu\, u(z))\,\frac{\partial u(z)}{\partial z} = -\kappa_\nu\,\tau_\nu\,\frac{\partial u(z)}{\partial z}. \tag{5.4}$$

With the use of (5.4), the integral in (5.2) can be expressed in a new form:

$$\int_0^{\infty} B_\nu(T(z)) \frac{\partial \tau_\nu}{\partial z} \, \mathrm{d}z = -\kappa_\nu \int_{u_0}^{0} B_\nu(T) \, \tau \frac{\partial u(z)}{\partial z} \, \mathrm{d}z = \kappa_\nu \int_0^{u_0} B_\nu(T) \, \tau \, \mathrm{d}u, \quad (5.5)$$

where $u_0 \equiv u(z = 0)$ is the total water vapour path length.

The first-guess atmospheric profiles consist of a discrete set of measurements performed at preset values of atmospheric pressure. LOWTRAN-7 assumes the atmosphere to be constructed out of layers as defined by the input atmospheric profile. Hence, we could approximate the integrals in (5.2) and (5.5) to reflect this. The approximations also allow easier evaluation of the total differential. A graph showing the positions of various profile-derived variables which we use in the derivation on LOWTRAN's "atmospheric" grid is displayed in Figure 5.1.

To avoid confusion and simplify notation we will assume wavenumber dependency in all future equations. Thus, the integral from (5.2) is approximated as:

$$\int_0^{\infty} B(T) \, \mathrm{d}\tau \;\approx\; \sum_{i=0}^{N} B(T)_i \, \Delta\tau_i \;\equiv\; F_1, \quad (5.6)$$

where i is the atmospheric layer index, N the total number of layers, $B(T)_i$ the amount of upwelling radiance from ith layer as calculated by LOWTRAN-7, and $\Delta\tau_i$ is ith's layer atmospheric transmission as calculated by LOWTRAN-7. Likewise, the integral from (5.5) is approximated as:

$$\kappa \int_0^{u_0} B(T) \, \tau \, \mathrm{d}u \;\approx\; \kappa \sum_{i=0}^{N} B(T)_i \, \tau_i \, (u_i - u_{i+1}) \;\equiv\; F_2, \quad (5.7)$$

where τ_i and u_i are the cumulative atmospheric transmission and water vapour path length, respectively, from the ith layer to the top of atmosphere.

The total differential of the integral in (5.2) will now be evaluated using

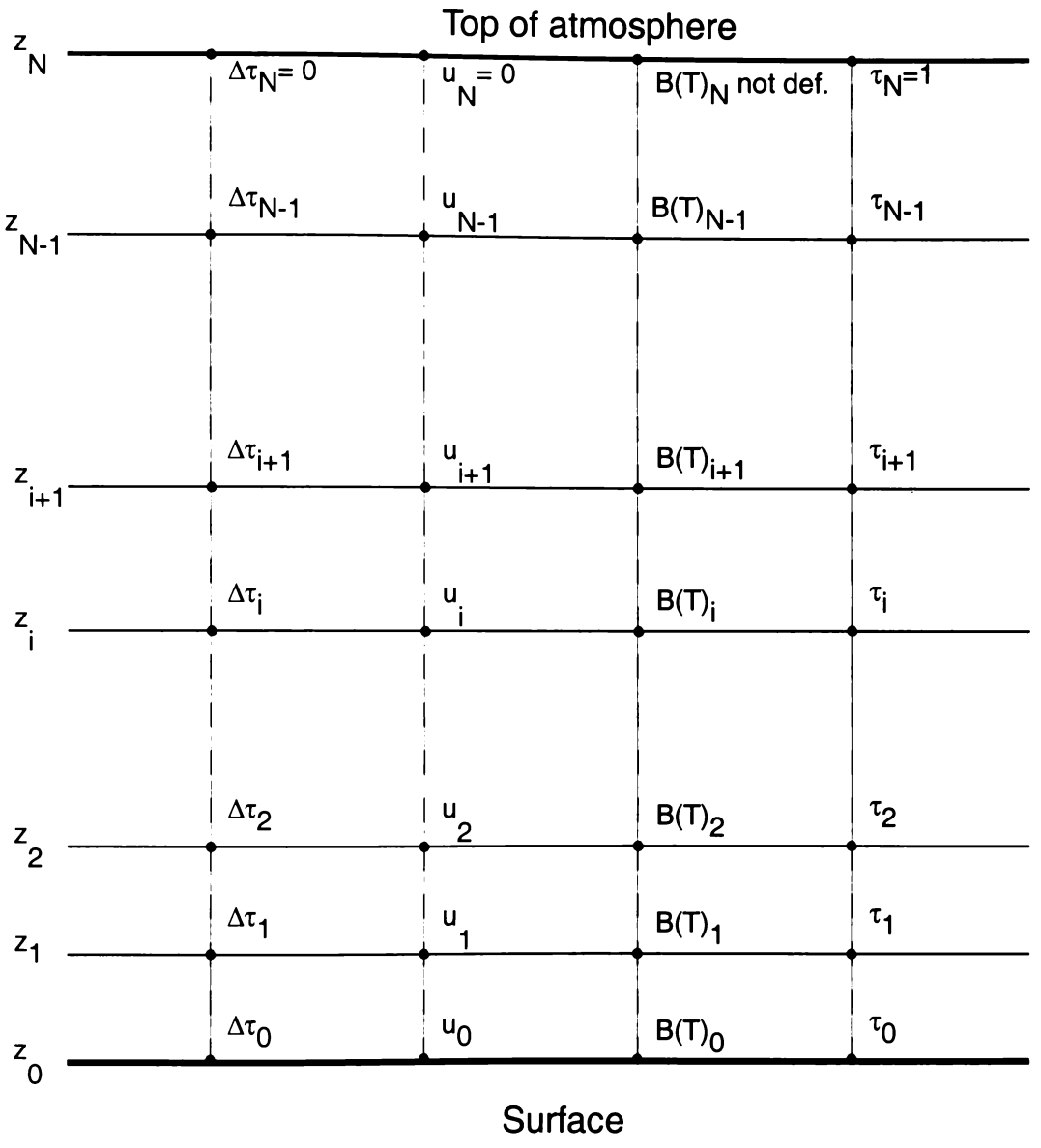

Figure 5.1: The grid showing locations of the atmospheric quantities used in SimWVT as reported by LOWTRAN-7. They all relate to the layers defined by the input radiosonde profile despite their localized position on the grid. The layers are not of equal thickness.

(5.6) and (5.7).

$$\mathrm{d}\left(\int_0^\infty B(T)\,\mathrm{d}\tau\right) \approx \sum_{j=0}^{N} \frac{\partial F_1}{\partial T_j}\,\mathrm{d}T_j + \sum_{j=0}^{N} \frac{\partial F_2}{\partial u_j}\,\mathrm{d}u_j. \tag{5.8}$$

The first term on the right-hand side of (5.8) is the contribution of the atmospheric temperature profile to the total differential, and the second term is the contribution of the water vapour profile.

Evaluation of the partial derivatives in (5.8) is greatly simplified by recalling that they all vanish for $j \neq i$. The expression for the partial derivative at layer j for the atmospheric temperature contribution is:

$$\frac{\partial F_1}{\partial T_j} = \frac{\partial}{\partial T_j} \sum_{i=0}^{N} B(T)_i\,\Delta\tau_i = \left.\frac{\partial B}{\partial T}\right|_{T=T_i} \Delta\tau_i, \tag{5.9}$$

where $T_i = B^{-1}(B(T)_i, \nu)$, and B^{-1} is the inverse Planck black-body spectral radiance function. In evaluating (5.9) we assumed that $\Delta\tau_i$ is not a function of atmospheric temperature. Summing them all up, we get the total contribution of the atmospheric profile:

$$\sum_{j=0}^{N} \frac{\partial F_1}{\partial T_j}\,\mathrm{d}T_j = \sum_{i=0}^{N} \left.\frac{\partial B}{\partial T}\right|_{T=T_i} \Delta\tau_i\,\mathrm{d}T_i. \tag{5.10}$$

We identify two different cases for the water vapour contribution in (5.8):

- $j > 0$:

$$\begin{aligned}
\frac{\partial F_2}{\partial u_j} &= \frac{\partial}{\partial u_j}\left(\kappa \sum_{i=0}^{N} B(T)_i\,\tau_i\,(u_i - u_{i+1})\right) \\
&= \frac{\partial}{\partial u_j}\left[\kappa \sum_{i=j-1}^{j} B(T)_i\,\tau_i\,(u_i - u_{i+1})\right] \\
&= \kappa \frac{\partial}{\partial u_i}\Big[B(T)_{i-1}\,\tau_{i-1}\,(u_{i-1} - u_i) + B(T)_i\,\tau_i\,(u_i - u_{i+1})\Big] \\
&= \kappa\Big(-B(T)_{i-1}\,\tau_{i-1} - \kappa\,B(T)_i\,\tau_i\,(u_i - u_{i+1}) + B(T)_i\,\tau_i\Big)
\end{aligned} \tag{5.11}$$

- $j = 0$:

$$\begin{aligned}\frac{\partial F_2}{\partial u_0} &= \frac{\partial}{\partial u_0}\left(\kappa \sum_{i=0}^{N} B(T)_i\, \tau_i\, (u_i - u_{i+1})\right) \\ &= \kappa \frac{\partial}{\partial u_0}\left[B(T)_0\, \tau_0\, (u_0 - u_1)\right] \\ &= \kappa\left[-\kappa B(T)_0\, \tau_0\, (u_0 - u_1) + B(T)_0\, \tau_0\right] \\ &= \kappa\, B(T)_0\, \tau_0\, \left[1 - \kappa(u_0 - u_1)\right]\end{aligned} \tag{5.12}$$

Combining (5.11) and (5.12) the contribution of the water vapour profile to the total differential in (5.8) is:

$$\begin{aligned}&\sum_{j=0}^{N} \frac{\partial F_2}{\partial u_j}\, \mathrm{d}u_j = \\ &\quad = \kappa\, B(T)_0\, \tau_0\, \left[1 - \kappa(u_0 - u_1)\right] \\ &\qquad + \kappa \sum_{i=1}^{N} \kappa\big(-B(T)_{i-1}\, \tau_{i-1} - \kappa\, B(T)_i\, \tau_i\, (u_i - u_{i+1}) + B(T)_i\, \tau_i\big) \\ &\quad = \kappa \left(\sum_{i=0}^{N} B(T)_i\, \tau_i \big(1 - \kappa(u_i - u_{i-1})\big)\mathrm{d}u_i - \sum_{i=1}^{N} B(T)_{i-1}\, \tau_{i-1}\, \mathrm{d}u_i\right).\end{aligned} \tag{5.13}$$

The first two right-hand side terms in (5.2) are easily calculated using (5.3) (note the change in notation from (5.2), $\tau(0) \equiv \tau_0$):

$$\mathrm{d}B(T_s)\tau(0) + B(T_s)\, \mathrm{d}\tau(0) = \tau_0 \left.\frac{\partial B}{\partial T}\right|_{T=T_s} \mathrm{d}T_s - \kappa\, B(T_s)\, \tau_0\, \mathrm{d}u_0. \tag{5.14}$$

Finally, using (5.10), (5.13) and (5.14), the total differential in (5.2) is approximated as:

$$\begin{aligned}\mathrm{d}I \approx &\tau_0 \left.\frac{\partial B}{\partial T}\right|_{T=T_s} \mathrm{d}T_s - \kappa\, B(T_s)\, \tau_0\, \mathrm{d}u_0 \\ &+ \sum_{i=0}^{N} \left.\frac{\partial B}{\partial T}\right|_{T=T_i} \Delta\tau_i\, \mathrm{d}T_i \\ &+ \kappa \left(\sum_{i=0}^{N} B(T)_i\, \tau_i \big(1 - \kappa(u_i - u_{i-1})\big)\mathrm{d}u_i - \sum_{i=1}^{N} B(T)_{i-1}\, \tau_{i-1}\, \mathrm{d}u_i\right).\end{aligned} \tag{5.15}$$

Equation (5.15) states that the change in at-satellite radiance I is a function of changes in the surface temperature $\mathrm{d}T_s$, and the water vapour and atmospheric temperature profiles $\mathrm{d}u_i$, $\mathrm{d}T_i$ $(i = 0, \ldots, N)$. In order to effectively use this equation we have to find a way of reducing the number of variables from $2N+1$ to a more manageable size. Applying the same idea from DWV/DWVT to modify atmospheric temperature or water vapour profiles by a fixed amount at each layer enabled us to express the change in u_i and T_i with two coefficients common to all layers.

Let us introduce two coefficients δ_{WV} and δ_{T} $(-1 \leq \delta_{\mathrm{WV}}, \delta_{\mathrm{T}} < \infty)$, which provide a measure of the amount of change to the water vapour or atmospheric temperature profile, respectively. The changes in the profiles can now be expressed as:

$$\left.\begin{aligned} T_i^{\mathrm{New}} &= (1+\delta_{\mathrm{T}})\, T_i^{\mathrm{Old}} \\ u_i^{\mathrm{New}} &= (1+\delta_{\mathrm{WV}})\, u_i^{\mathrm{Old}} \end{aligned}\right\} \Longrightarrow \left\{\begin{aligned} \mathrm{d}T_i &= \delta_{\mathrm{T}}\, T_i \\ \mathrm{d}u_i &= \delta_{\mathrm{WV}}\, u_i \end{aligned}\right. \tag{5.16}$$

Including the result from (5.16) in (5.15), we find:

$$\mathrm{d}I \;\approx\; A\,\mathrm{d}T_s + B\,\delta_{\mathrm{T}} + C\,\delta_{\mathrm{WV}}, \tag{5.17}$$

with

$$\begin{aligned} A &= \tau_0 \left.\frac{\partial B}{\partial T}\right|_{T=T_s}, \\ B &= \sum_{i=0}^{N} \left.\frac{\partial B}{\partial T}\right|_{T=T_i} \Delta\tau_i\, T_i, \\ C &= \kappa \left(\sum_{i=0}^{N-1} B(T)_i\, \tau_i (1-\kappa\, u_i)(u_i - u_{i+1}) - B(T_s)\, \tau_0\, u_0 \right). \end{aligned} \tag{5.18}$$

Since the AVHRR thermal infrared channels cannot be regarded as monochromatic, (5.17) has to be integrated with the appropriate channel filter

functions. This process yields the following set of equations:

$$\begin{aligned} \Delta I_4 &= A_4(\mathrm{SST} - T_{s,4}) + B_4\,\delta_\mathrm{T} + C_4\,\delta_\mathrm{WV}, \\ \Delta I_5 &= A_5(\mathrm{SST} - T_{s,5}) + B_5\,\delta_\mathrm{T} + C_5\,\delta_\mathrm{WV}, \end{aligned} \tag{5.19}$$

where SST is the exact value of the surface temperature, and $T_{s,4}$ and $T_{s,5}$ are sea surface temperatures derived from AVHRR channels 4 and 5. Our objective of finding atmospheric corrections which do not alter the at-satellite observed radiances can now be expressed in mathematical form: ΔI_4 and ΔI_5 must be equal to zero. Setting $\Delta I_4 = \Delta I_5 = 0$ and eliminating SST from the set of equations (5.19), we obtain the SimWVT equation:

$$T_{s,5} - T_{s,4} = \left(\frac{B_4}{A_4} - \frac{B_5}{A_5}\right)\delta_\mathrm{T} + \left(\frac{C_4}{A_4} - \frac{C_5}{A_5}\right)\delta_\mathrm{WV}. \tag{5.20}$$

Given the first guess for SST from both channels, $T_{s,4}$ and $T_{s,5}$, water vapour and temperature correction factors can be related with a single equation. This, however, leaves one of the correction factors unknown. In the next section we discuss how (5.20) is utilized.

5.2 SimWVT Algorithm

We have chosen that the temperature correction, δ_T, should have a user-defined range of permissible values, thus making the water vapour correction δ_WV the dependent variable in (5.20). This was done partly to simplify the SimWVT algorithm and partly because of our experience with DWVT on how strongly changing the atmospheric temperature influences the final SST estimate. Specifying a range for δ_T also streamlined the computation of other profile-related quantities since the pressure and temperature profiles were already defined.

The SimWVT algorithm proceeds as follows:

1. A range for δ_T is supplied, normally by the user. An optional argument is the step-change; if not available the default ten-point evaluation within

the range is assumed.

2. A first-guess atmospheric temperature and water vapour profile is chosen.

3. Run LOWTRAN-7 for this atmospheric profile and calculate $T_{s,4}$, $T_{s,5}$, and the A, B and C channel-4 and -5 coefficients from the LOWTRAN output. $T_{s,4}$ and $T_{s,5}$ are obtained from (3.3) using the at-satellite radiance.

4. Using (5.20), $T_{s,4}$ and $T_{s,5}$, calculate δ_{WV} for every value of δ_{T} in the range.

5. For every pair of $(\delta_{\mathrm{WV}}, \delta_{\mathrm{T}})$ modify the first-guess atmospheric profile; first the temperature profile, then the water vapour profile. Check the newly-created water vapour profile for supersaturation. (The same water vapour limiting procedure as in the DWVT algorithm. See Section 4.4.1.)

6. Run LOWTRAN-7 on the new atmospheric profiles obtaining channel-4 and -5 surface temperature estimates, SST_4 and SST_5, using the satellite-measured radiance.

7. Search for the $|\mathrm{SST}_4 - \mathrm{SST}_5|$ minimum:

   7a) Find the pair of the closest (SST_4,SST_5) values.

   7b) Use their respective δ_{WV} and δ_{T} as seed values in a two-dimensional minimization of the $|\mathrm{SST}_4 - \mathrm{SST}_5|$ difference. The minimization routine is Brent's method, taken from *Press et al.* [1992]. The main advantage of this method is that it does not require a gradient evaluation of the function being minimized.

   7c) Test all atmospheric profiles created during the minimization for supersaturation.

   7d) The minimization process stops either if a minimum is found, or the preset limit of iterations is achieved (default is 100). In the latter case, the last smallest $|\mathrm{SST}_4 - \mathrm{SST}_5|$ is taken as the solution.

8. The final SimWVT SST estimate is the average of the channel surface temperature estimates returned by the minimization routine: SST = (SST_4+SST_5)/2. The corresponding δ_{WV} and δ_T define the final SimWVT atmospheric profile.

Instead of a minimization routine, we first implemented an extensive search technique around the pair (δ_{WV}, δ_T) which yielded the minimal $|SST_4 - SST_5|$. The results were very similar to those obtained from the current minimization routine, but were achieved with larger number of iterations. As our aim at this stage was not to make SimWVT an efficient and fast method at the expense of accuracy, the change to a minimization routine was warranted.

The differences of the SimWVT algorithm from its DWVT counterpart (Section 4.1) are:

- No DWV failure test.
- Atmospheric temperature and water vapour profiles are both altered for next iteration. In order to make a meaningful supersaturation test, the temperature profile is changed first, then the water vapour profile.
- The utilization of a multidimensional minimization procedure.
- We expect the SimWVT convergence to be a direct reflection of the minimum of the $|SST_4 - SST_5|$ difference.
- The algorithm is cohesively formulated, unlike the DWVT where two completely different algorithms were used (the DWV and the DAT).

5.3 SimWVT Results

The SimWVT algorithm has been tested with our Tasman radiosonde, buoy and AVHRR data set (Section 3.3). We used radiosondes from two sites: Hobart and Mt. Gambier. The temporal selection of the sondes from these two sites was done in the same manner as for the DWVT method:

Closest: The time of ascend of the selected sonde is closest to the satellite overpass.

5d-before: The selected sonde was about five days earlier than the satellite overpass (the closest sonde to five days before the pass).

5d-after: The selected sonde was was about five days later than the satellite overpass (the closest sonde to five days after the pass).

Night/day: Night-time satellite passes are matched with the closest "night" sonde, and daytime passes are matched with the closest "day" sonde.

The accuracy of the SST estimates produced by SimWVT are assessed against the buoy measurements using the same statistics introduced for the DWVT: bias (4.6), rms (4.7) and Q (4.8). In the next two sections we present SimWVT results for the two radiosonde sites.

5.3.1 SimWVT Results for the Hobart Site

The SimWVT SST results using the Hobart sondes are displayed in Tables 5.1 and 5.2. SimWVT SST retrieval errors for the four different sonde selections are shown in the first table. The second table contains IFUT-specific statistics of the data from the first table, and the rankings of the passes based on the IFUT-rms and IFUT-Q.

The majority of passes in Table 5.1 have consistent SST retrieval errors across all four different sonde selections. This is reflected in the IFUT rms values (Table 5.2), with 19 of 34 being smaller than 0.1 °C. Passes that exhibited noticeable variation for different sonde selections were: m9jr, m9n9, macc, maep, mb21 and mbg5. Four passes (m9vi, macc, mafw and mb1n) had average IFUT SST errors very close to zero (in the range -0.01–0.03 °C). The three best-overall results were for the mafw, m9vi and mb1n passes (IFUT-$Q \leq 0.11$ °C). The three worst-overall predicted passes were mb21, mbdz and maep (IFUT-$Q \sim 2$ °C or greater).

Table 5.1: SimWVT SST retrieval errors for the Hobart sonde site and four different sonde selection modes.

IFUT	5d-before	Closest	Night/Day	5d-after
m9jr	0.47	0.29	0.66	0.39
m9k5	0.69	0.79	0.70	0.73
m9kc	0.07	0.09	0.07	0.23
m9n9	-0.46	-0.71	-0.70	-0.64
m9na	0.22	0.20	0.23	0.17
m9vi	0.11	0.04	-0.06	0.03
ma4c	-0.98	-1.05	-0.97	-0.95
ma4i	-0.13	-0.17	-0.18	-0.17
mabk	0.35	0.36	0.36	0.12
mabz	-0.75	-1.27	-0.89	-0.75
mac6	-0.30	-0.22	-0.23	-0.24
macc	0.01	0.22	-0.43	0.22
macd	-1.05	-1.21	-0.96	-0.88
macq	-1.72	-1.91	-1.91	-1.60
macr	0.08	0.19	0.16	0.13
mad5	-0.20	-0.16	-0.16	-0.11
maeb	-0.86	-0.70	-0.71	-0.57
maep	-3.15	-2.47	-2.47	-2.81
maf3	-1.11	-0.70	-0.70	-0.83
mafh	-0.54	-0.43	-0.43	-0.32
mafw	-0.07	0.05	-0.07	0.05
mald	0.23	0.24	0.24	0.17
malk	0.14	0.18	0.15	0.20
mar9	0.47	0.39	0.43	0.46
mazo	0.14	0.16	0.14	0.14
mb11	0.28	0.18	0.16	0.04
mb1f	0.27	0.34	0.38	0.35
mb1n	0.17	-0.09	-0.03	0.04
mb21	-1.90	-1.84	-1.48	-1.96
mb2m	0.40	0.56	0.44	0.48
mb9o	-0.42	-0.41	-0.36	-0.23
mbdz	-1.95	-1.90	-1.95	-2.02
mbg5	-0.92	-0.78	-0.82	-1.22
mbgc	0.40	0.31	0.31	-0.27
bias	-0.35	-0.34	-0.33	-0.34
rms	0.85	0.81	0.77	0.81
Q	0.92	0.87	0.83	0.87

Table 5.2: SimWVT SST error statistics for every satellite pass for the Hobart sonde site and the four different sonde selection modes. The data for this table is in Table 5.1. Bias, rms and Q were calculated for the Average column for comparison with the SimWVT results of different sonde selections. The satellite passes are ranked according to the IFUT rms and Q factors.

IFUT	Average	IFUT-rms	IFUT-Q	Rank (IFUT-rms)	Rank (IFUT-Q)
m9jr	0.45	0.16	0.48	27	22
m9k5	0.73	0.05	0.73	10	25
m9kc	0.12	0.08	0.14	17	4
m9n9	-0.63	0.12	0.64	22	23
m9na	0.21	0.03	0.21	3	11
m9vi	0.03	0.07	0.08	16	2
ma4c	-0.99	0.04	0.99	9	29
ma4i	-0.16	0.02	0.16	2	8
mabk	0.30	0.12	0.32	23	15
mabz	-0.92	0.25	0.95	31	27
mac6	-0.25	0.04	0.25	7	13
macc	0.01	0.31	0.31	32	14
macd	-1.02	0.14	1.03	25	30
macq	-1.79	0.15	1.79	26	31
macr	0.14	0.05	0.15	12	6
mad5	-0.16	0.04	0.16	8	7
maeb	-0.71	0.12	0.72	24	24
maep	-2.73	0.33	2.74	34	34
maf3	-0.83	0.19	0.86	28	26
mafh	-0.43	0.09	0.44	19	20
mafw	-0.01	0.07	0.07	15	1
mald	0.22	0.03	0.22	5	12
malk	0.17	0.03	0.17	4	9
mar9	0.44	0.04	0.44	6	19
mazo	0.15	0.01	0.15	1	5
mb11	0.17	0.10	0.19	20	10
mb1f	0.34	0.05	0.34	11	16
mb1n	0.02	0.11	0.11	21	3
mb21	-1.80	0.22	1.81	30	32
mb2m	0.47	0.07	0.47	14	21
mb9o	-0.35	0.09	0.37	18	18
mbdz	-1.96	0.05	1.96	13	33
mbg5	-0.94	0.20	0.96	29	28
mbgc	0.19	0.31	0.36	33	17
bias	-0.34				
rms	0.80				
Q	0.87				

Table 5.3: SimWVT statistics for seven different sonde selection modes. The radiosonde data was from Hobart.

Statistic	15d-before	10d-before	5d-before	Closest	5d-after	10d-after	15d-after
bias	-0.30	-0.31	-0.35	-0.34	-0.34	-0.38	-0.35
rms	0.80	0.83	0.85	0.81	0.81	0.85	0.82
Q	0.85	0.88	0.92	0.87	0.87	0.93	0.89

Comparing the IFUT-rms and IFUT-Q rankings in Table 5.2, we found several "consistent" passes: mad5, maeb, maf3, mafh, mb9o and mbg5. A pass is called "consistent" if its IFUT-rms and IFUT-Q rankings do not differ significantly.

The overall SimWVT performance for the four different sonde selections (Table 5.1) demonstrates a very weak dependence on sonde age. The bias changes by only 0.02 °C across all sonde selections. The main source of variability in the Q statistic is due to the rms, which is in the 0.77-0.85 °C range. The Q statistic shows an expected drop as the sonde selections approach the satellite overpass. The best SimWVT result was obtained for the "night/day" sondes (Q=0.83 °C), followed by the "closest" and "5d-after" sondes with the identical result (Q=0.87 °C). A graph of SST errors for the four sonde selections is shown in Figure 5.2.

To study further the trend of the Q statistic with sonde aging, we performed additional SimWVT runs with the sondes 10 and 15 days before and after the satellite passes. The results are presented in Table 5.3.

The overall statistics of SimWVT SST errors for sondes up to 15 days old (Table 5.3) do not exhibit a steady increase in SST accuracy exclusively for temporally closer sondes. Instead, the Q statistic displays an oscillatory behaviour, with one minimum for the "closest" and the other for the "15d-before" sondes. The latter selection of sondes yielded the best SimWVT results of all that were generated using the Hobart sondes. The variation of the bias, rms and Q over the whole 30-day period around the satellite passes is only 0.08 °C, 0.05 °C and 0.08 °C, respectively.

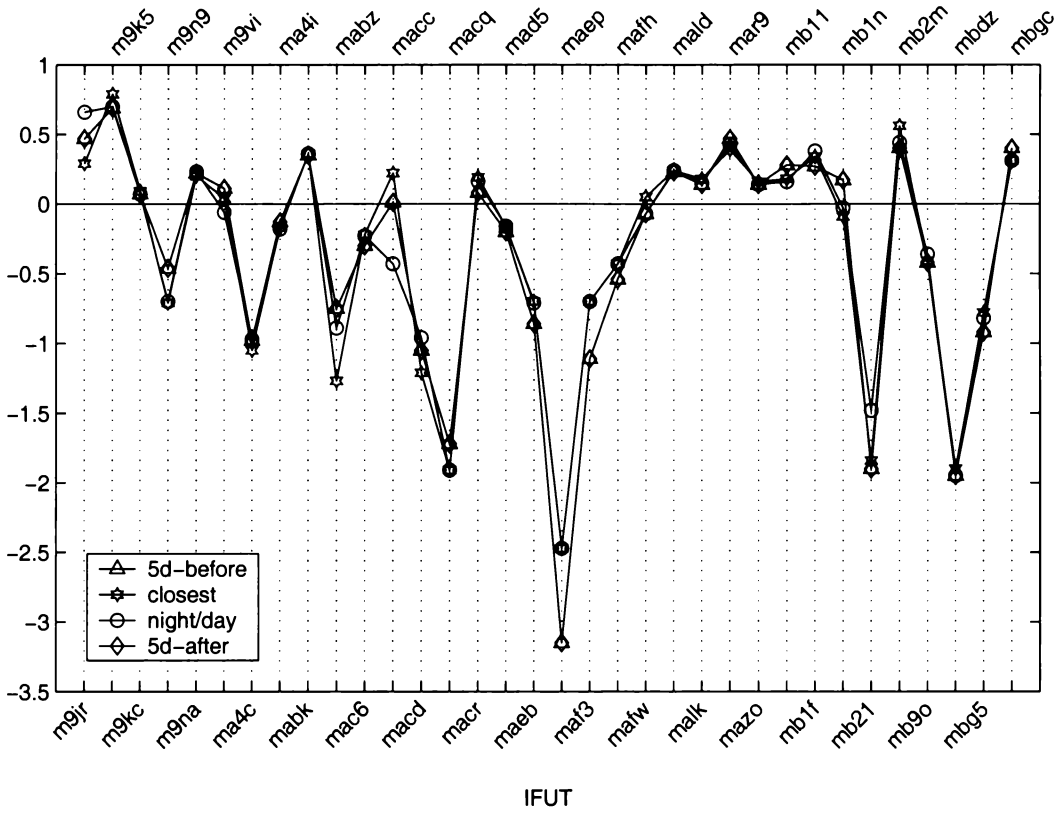

Figure 5.2: The results of the SimWVT method for four different sonde selections: "5d-before", "closest", "night/day" and "5d-after". The radiosonde data came from the Hobart site.

Comparison of the DWVT and SimWVT results using the same sonde selections revealed that both methods yielded almost identical results. The biggest difference in the Q statistic occurred for the "closest" sondes—a negligible 0.05 °C. The detailed results are given in Appendix B.1.1; the collated overall statistics of the methods is shown in Table 5.4.

Analyzing the SimWVT and DWVT results in Appendix B.1.1 for each sonde selection, we found that both methods were almost equally successful. The number of passes more accurately retrieved by the SimWVT ranged from 11 ("night/day" sondes) to 19 ("5d-after"). The number of passes with the same SimWVT and DWVT errors was always small, never exceeding three; there were no such passes for the "5d-after" sondes.

There was relatively a small number of passes with stark differences in

Table 5.4: The bias, rms and Q statistics for comparison of SimWVT and DWVT methods. Radiosondes were from Hobart.

Statistic	SimWVT	DWVT
5d-before sondes		
bias	-0.35	-0.36
rms	0.85	0.86
Q	0.92	0.93
Closest		
bias	-0.34	-0.34
rms	0.81	0.75
Q	0.87	0.82
Night/day		
bias	-0.33	-0.32
rms	0.77	0.77
Q	0.83	0.83
5d-after		
bias	-0.34	-0.36
rms	0.81	0.82
Q	0.87	0.89

SST errors from the two methods. And of those, SimWVT reported a much better result only for two passes—macc ("5d-before" sonde; DWVT: -0.35 °C; SimWVT: 0.01 °C) and mb21 ("night/day" sonde; DWVT: -1.88 °C; SimWVT: -1.48 °C). For the opposite cases, those worth noting are the mabz (DWVT: -0.68 °C; SimWVT: -1.27 °C), macd ("5d-before" sonde; DWVT: -0.88 °C; SimWVT: -1.21 °C) and macq (DWVT: -1.58 °C; SimWVT: -1.91 °C) passes, all for the "closest" sondes. These three passes are mainly responsible for generating the largest difference of the rms of the two methods (DWVT rms: 0.75 °C; SimWVT rms: 0.81 °C).

5.3.2 SimWVT Results for the Mt. Gambier Site

The SimWVT SST results for the Mt. Gambier sondes are given in Tables 5.5 and 5.6. The first table presents SimWVT SST errors for the three different

sonde selections: "5d-before", "closest" and "5d-after". As pointed out in Section 4.6.2, the sonde launches from Mt. Gambier were performed only in the morning (9 a.m. local time), so we could not perform the "night/day" sonde analysis. The second table contains IFUT-specific statistics, together with the rankings according to the IFUT rms and Q values.

The results in Table 5.5 reveal that the well-known trio of passes—maep, mb21 and mbdz—has again produced the largest SST errors (in the 2–2.5 °C range). The three best-overall predicted passes are mafw, ma4i and m9kc (SST errors in the ±0.15 °C range).

The SimWVT results with the Mt. Gambier sondes do not show the sharp change of errors for different sonde selections as some of their DWVT counterparts did. The only two passes in the SimWVT Mt. Gambier set with this kind of behaviour were macc and mb2m. We attribute this general lack of such cases in the SimWVT results to the unified formulation of the SimWVT algorithm as opposed to the DWVT method (with two quite different algorithms—the DWV and the DAT). This finding is further reinforced with the IFUT-rms values where 24 out of 34 passes had rms smaller than 0.1 °C. Comparing the IFUT-rms and IFUT-Q rankings in Table 5.6, we found only three "consistent" passes: macr, mafw and mald—less than the DWVT case (Table 4.6). A graph of SST errors for the four sonde selections is shown in Figure 5.3.

The overall statistics for the three sonde selections in Table 5.5 shows a gradual increase starting from the "5d-before" sondes. We have already speculated in Section 4.9 that this might have been caused by the prevailing weather conditions in that part of the world. Weather fronts usually first arrive over the Mt. Gambier site, and then over the buoy and the Hobart site. In order to confirm this, we ran SimWVT on additional sonde selections: "15d-before", "10d-before" and "10d-after". We could not obtain passes 10 days in advance because our Mt. Gambier radiosonde database lacked the required data. The results of the overall statistics are presented in Table 5.7.

The Q statistic in Table 5.7 shows a drop with a decrease in the sonde

Table 5.5: SimWVT SST retrieval errors for the Mt. Gambier sonde site and three different sonde selection modes.

IFUT	5d-before	Closest	5d-after
m9jr	0.63	0.65	0.59
m9k5	0.77	0.68	0.71
m9kc	0.15	0.06	0.10
m9n9	-0.56	-0.90	-0.87
m9na	0.32	0.24	0.23
m9vi	0.09	0.18	0.15
ma4c	-1.10	-1.14	-1.18
ma4i	-0.14	-0.03	0.04
mabk	0.42	0.38	0.33
mabz	-0.87	-0.63	-0.62
mac6	-0.22	-0.22	-0.33
macc	0.05	0.34	0.23
macd	-0.89	-0.82	-0.90
macq	-1.46	-1.68	-1.66
macr	0.15	0.13	0.16
mad5	-0.39	-0.18	-0.10
maeb	-0.63	-0.71	-0.74
maep	-2.35	-2.67	-2.51
maf3	-0.78	-0.73	-0.79
mafh	-0.43	-0.54	-0.47
mafw	-0.06	-0.09	-0.06
mald	0.25	0.18	0.25
malk	0.23	0.15	0.15
mar9	0.53	0.56	0.55
mazo	0.33	0.29	0.20
mb11	0.32	0.19	0.17
mb1f	0.17	0.18	0.30
mb1n	0.21	0.24	-0.22
mb21	-1.92	-1.92	-2.25
mb2m	0.57	-0.01	0.47
mb9o	-0.31	-0.36	-0.74
mbdz	-1.92	-2.00	-2.04
mbg5	-0.73	-0.84	-0.84
mbgc	0.30	0.34	0.34
bias	-0.27	-0.31	-0.33
rms	0.78	0.81	0.83
Q	0.83	0.87	0.89

Table 5.6: SimWVT SST error statistics for every satellite pass for the Mt. Gambier sonde site and the three different sonde selection modes. The data for this table is in Table 5.5. Bias, rms and Q were calculated for the Average column for comparison with the SimWVT results of different sonde selections. The satellite passes are ranked according to the IFUT rms and Q factors.

IFUT	Average	IFUT rms	IFUT-Q	Rank (IFUT rms)	Rank (IFUT-Q)
m9jr	0.62	0.03	0.62	5	22
m9k5	0.72	0.05	0.72	12	25
m9kc	0.10	0.05	0.11	11	3
m9n9	-0.78	0.19	0.80	30	27
m9na	0.26	0.05	0.27	15	12
m9vi	0.14	0.05	0.15	13	4
ma4c	-1.14	0.04	1.14	7	30
ma4i	-0.04	0.09	0.10	24	2
mabk	0.38	0.05	0.38	10	17
mabz	-0.71	0.14	0.72	26	24
mac6	-0.26	0.06	0.26	20	11
macc	0.21	0.15	0.25	27	10
macd	-0.87	0.04	0.87	9	29
macq	-1.60	0.12	1.60	25	31
macr	0.15	0.02	0.15	1	5
mad5	-0.22	0.15	0.27	28	14
maeb	-0.69	0.06	0.70	17	23
maep	-2.51	0.16	2.52	29	34
maf3	-0.77	0.03	0.77	6	26
mafh	-0.48	0.06	0.48	16	19
mafw	-0.07	0.02	0.07	3	1
mald	0.23	0.04	0.23	8	8
malk	0.18	0.05	0.18	14	6
mar9	0.55	0.02	0.55	2	21
mazo	0.27	0.07	0.28	21	15
mb11	0.23	0.08	0.24	23	9
mb1f	0.22	0.07	0.23	22	7
mb1n	0.08	0.26	0.27	33	13
mb21	-2.03	0.19	2.04	31	33
mb2m	0.34	0.31	0.46	34	18
mb9o	-0.47	0.24	0.53	32	20
mbdz	-1.99	0.06	1.99	18	32
mbg5	-0.80	0.06	0.81	19	28
mbgc	0.33	0.02	0.33	4	16
bias	-0.31				
rms	0.80				
Q	0.86				

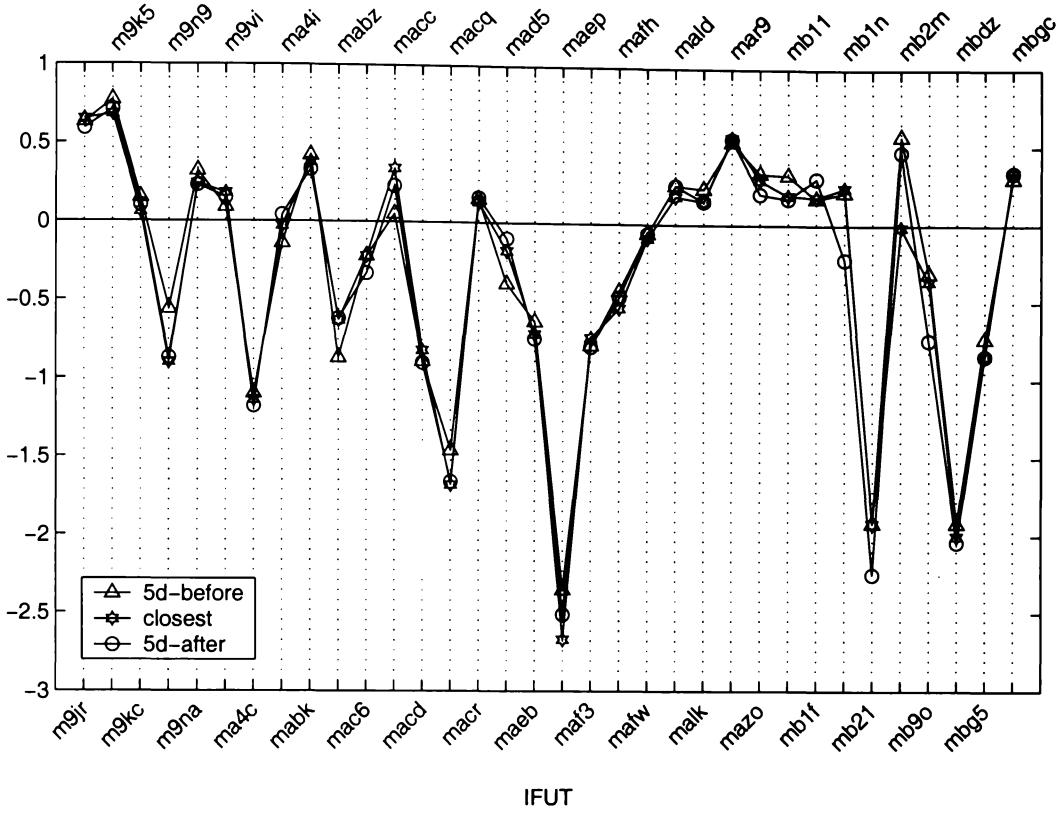

Figure 5.3: The results of the SimWVT method for four different sonde selections: "5d-before", "closest", and "5d-after". The radiosonde data came from the Mt. Gambier site.

Table 5.7: SimWVT statistics for six different sonde selection modes. The last four satellite passes are not included in the results in column 10d-after due to the lack of suitable sondes. The radiosonde data was from Mt. Gambier.

Statistic	15d-before	10d-before	5d-before	Closest	5d-after	10d-after
bias	-0.30	-0.28	-0.27	-0.31	-0.33	-0.33
rms	0.79	0.80	0.78	0.81	0.83	0.76
Q	0.85	0.85	0.83	0.87	0.89	0.83

temporal mismatch. The fact that the lowest Q was reported for the "5d-before" sondes seems to bolster our hypothesis of favourable weather conditions propagating from Mt. Gambier towards the buoy and Hobart. As in the case of Hobart sondes, the bias, rms and Q exhibited a negligible variation of only 0.06 °C, 0.07 °C and 0.04 °C, respectively, for sondes spanning 25 days around the satellite passes.

Analysis of the DWVT and SimWVT results for same sonde selections revealed the superiority of the SimWVT method. The detailed results are given in Appendix B.1.2; we show in Table 5.8 only the overall statistics of the methods.

Table 5.8: The bias, rms and Q statistic for comparison of SimWVT and DWVT methods. Radiosondes were from Mt. Gambier.

Statistic	SimWVT	DWVT
5d-before sondes		
bias	-0.27	-0.45
rms	0.78	0.98
Q	0.83	1.08
Closest		
bias	-0.31	-0.48
rms	0.81	0.96
Q	0.87	1.07
5d-after		
bias	-0.33	-0.34
rms	0.83	0.84
Q	0.89	0.90

SimWVT clearly outperformed the DWVT for the cases of "5d-before" and "closest" sondes, whereas their results for the "5d-after" sondes are very similar. Examination of the tables in Appendix B.1.2 with the data for each pass offers some insight into why the SimWVT surpassed the DWVT. Along with the SST errors, these tables have a column with the relative change from the DWVT result, expressed as a percentage.

The biggest difference between the methods was for the "5d-before" sondes.

The reason for this is because SimWVT improved SST accuracy in 17 out of 34 cases, with three passes producing the same SST error as for the DWVT. The most notable improvements leading to much better overall performance for the SimWVT were: m9na (DWVT: -2.64 °C; SimWVT: 0.32 °C), macc (DWVT: 0.21 °C; SimWVT: 0.05 °C), m9n9 (DWVT: -1.86 °C; SimWVT: -0.56 °C) and maep (DWVT: -3.13 °C; SimWVT: -2.35 °C). On the other hand, the cases for which SimWVT reported larger SST error than DWVT were of smaller absolute values, thus not being able to "counterweigh" SimWVT's advantage.

For the "closest" sondes, SimWVT improved the accuracy of 16 passes, with now only one pass producing the same SST error. This time, however, there were not many passes with significant improvements using the SimWVT, explaining slightly worse overall performance when compared with the "5d-before" case. The SST retrieval was noticeably improved for the passes mb2m (DWVT: -0.67 °C; SimWVT: -0.01 °C), mazo (DWVT: -1.53 °C; SimWVT: 0.29 °C) and mafw (DWVT: -0.27 °C; SimWVT: -0.09 °C). These results were somewhat offset with the passess where SimWVT returned a larger SST error than the DWVT, of which we mention the two most prominent: maeb (DWVT: 0.01 °C; SimWVT: -0.71 °C) and mbgc (DWVT: 0.03 °C; SimWVT: 0.34 °C).

The smallest number of passes with improved SST accuracy using the SimWVT was for the "5d-after" sondes—thirteen, with two passes unchanged. The best SimWVT improvements were for ma4i (DWVT: -0.18 °C; SimWVT: 0.04 °C) and maep (DWVT: -2.89 °C; SimWVT: 2.51 °C). SimWVT's largest decreases in SST accuracy were for mbgc (DWVT: 0.07 °C; SimWVT: 0.34 °C) and mb1n (DWVT: 0 °C; SimWVT: -0.22 °C).

5.4 Discussion

A novel method for SST retrieval was presented in this chapter—the Simultaneous Water Vapour and Atmospheric Temperature (SimWVT) method. It

is based on the same idea of atmospheric profile tuning as the DWV [*Smith*, 1993, *Steyn-Ross et al.*, 1993] and the DWVT (Chapter 4) methods. However, unlike these methods which allow only one property (either temperature or water vapour) of the profile to be changed, SimWVT alters both at the same time.

The essence of the SimWVT method is an equation which relates the change in the at-satellite radiance with the changes in the atmospheric temperature and water vapour profiles at every layer (5.15). It was derived by applying variational calculus to the monochromatic radiative transfer equation (5.1).

The resulting equation had a large number of variables (double the number of layers in the profile) which rendered it impossible to implement in an efficient manner. To reduce the number, we used the same approach as in the DWVT and DWV methods. The changes of the atmospheric temperature and water vapour at every layer were expressed via two coefficients, δ_{T} and δ_{WV}, common to all the layers. This formulation greatly simplified (5.15), allowing the reduction in the number of variables to only three (5.17): δ_{T}, δ_{WV} and the change in surface temperature.

Since (5.17) was derived for the case of monochromatic radiation, its integration over the AVHRR channel-4 and -5 filter functions yielded a system of equations (5.19), which when solved (5.20) provided the final equation which enabled the utilization of the new method. The required corrections of the atmospheric temperature and water vapour profile (δ_{T} and δ_{WV}) were linked with the difference in the channel-4 and -5 surface brightness temperatures for the first-guess profile.

There were two important assumptions used in the derivation of (5.20):

- Atmospheric transmittance of the layers was not a function of atmospheric temperature. We considered this valid if the changes in atmospheric temperature were not significant (more than a few percent of its first-guess value).

- The integrals in (5.6) and (5.7) are approximated with simple sums. This was a deliberate decision, based on the following reasons:
  - Any quadrature formula requires equidistant data. This was not the case here, because the layers in the input atmospheric profile have different thicknesses.
  - The atmospheric profile variables in the integrals (5.6) and (5.7) are assigned to entire layers. Any attempt to use a quadrature formula would first require interpolation of these variables onto an equidistant grid. In our view, this process would introduce non-physical results simply because the values of these variables for new, equally-thick layered atmosphere were not properly calculated (by LOWTRAN-7).

The operational implementation of the SimWVT equation (5.20) took into account that one of the profile coefficients, δ_T or δ_{WV}, could not be determined from the equation. Given the strong influence of atmospheric temperature changes on the DWVT SST results, we decided to predefine the range of δ_T within $\pm 5\%$ of the first-guess values on every layer. This allowed us to prevent any larger value of δ_T that might compromise our approximations mentioned above.

The results of the SimWVT method (Section 5.3) displayed more consistency regarding different sonde age than the DWVT results. There were just a few passes where different first-guess sondes caused hugely variable SST errors. Very reassuring were the results for a wide range of sonde ages (Tables 5.3 and 5.7)—25 days for the Mt. Gambier and 30 days for the Hobart sondes—around the satellite passes. Unlike the DWVT, the SimWVT showed very little change for the sondes of both sites: the bias values had a variation of 0.11,°C, the rms variation was similar with 0.09 °C, and the Q values fluctuated within only 0.1 °C.

The best SimWVT result was for the "5d-before" sondes of Mt. Gambier.

(The same Q value was obtained also for the "10d-after" sondes from Mt. Gambier but the set lacks the last four passes and, hence, is not complete.) In fact, the top two SimWVT results are all for the Mt. Gambier sondes; the best SimWVT result for the Hobart sondes ("15d-before") ranks third, together with two SimWVT results for the Mt. Gambier sondes ("15d-before" and "10d-before"). From these results, we conclude that SimWVT coped better with the sondes which were both spatially and temporally farther away from the satellite passes.

When compared with the DWVT results for same sonde selections, the SimWVT clearly outperformed the DWVT in the case of Mt. Gambier sondes. For the Hobart sondes, SimWVT either compared similar or slightly worse than the DWVT. The consistency of the SimWVT performance for a wide range of spatially and temporally mismatched sondes makes this method more applicable than the DWVT.

As some sort of a test of the strength of the SimWVT formulation, we plotted the SimWVT SST errors against a set of SimWVT variables that were obtained as by-products of the search for the optimal SST retrieval. The common feature of these variables is that they describe the state of the final SimWVT atmosphere, as well as the transition from the first-guess profile. The selected variables are: channel-4 and -5 average atmospheric temperatures, their difference from the first-guess profile values, the total water vapour column for the final SimWVT profile, its difference from the first-guess profile value, and buoy-measured SST. The graphs are given in Appendices B.2.1 and B.2.2.

Our conjecture was that any trend in the graphs might signal a potential deficiency of our SimWVT method. Examination of the graphs in Appendices B.2.1 and B.2.2 revealed only one where some kind of grouping was detected. It was the graph (f) of the "night/day" sondes from Hobart, where the SST errors displayed a mild negative correlation with the difference in the total water vapour column between the final SimWVT and the first-guess profiles. Since this was the only case we don't think it has any real significance,

nor suggests any inadequacy of the SimWVT algorithm.

An interesting feature was observed in the (b), (d) and sometimes (f) graphs. These graphs depict the relationship between the SimWVT SST errors and the changes in either average atmospheric temperature or water vapour column of the initial and final atmospheric profiles. For some sonde selections (for example, "5d-before" from Mt. Gambier and "5d-before" from Hobart) quite a few passes were lined up around the zero value of the abscissa. These would be the traditional "search regions" of the DWV and DAT algorithms of the DWVT method. Hence, we could describe those passes as "pure DWV " or "pure DAT ", depending on which zero-value abscissa they occupy.

As a very encouraging sign of the soundness of the SimWVT algorithm, we noticed that only very few passes had an increase in the average atmospheric temperature. Cases with the final water vapour columns in the range 0.5–1 g/cm^2 occurred more frequently than for the DWVT method, but their SST errors did not seem to have suffered from such low water vapour amounts in the profile.

Of the features in stark contrast to the same DWVT cases, we single out the maep pass. While it always had the coldest average atmospheric temperature of the passes in the DWVT results, this was not true for the SimWVT results. For quite a few sonde selections, the final average atmospheric temperature reported by the SimWVT was with the bulk of the other passes of much smaller SST errors.

Taking into account all the presented SimWVT results in this chapter, we think that the following factors make the SimWVT the preferred method to the DWVT:

- Less sensitivity of the SimWVT to sonde aging.
- Lack of any "failure" criterion in SimWVT.
- Streamlined formulation of the SimWVT via (5.20).

- Unified approach to the nonlinear problem of optimization in the search for the optimal SST estimate.

Chapter 6

Part I: Conclusion

We conclude our presentation on novel methods for the retrieval of sea surface temperatures using AVHRR data with this chapter. We first give an overview of the material in the previous chapters. A discussion of our two new methods for SST retrieval and their results on a test data set follows next. We finish this chapter with some remarks on future work, especially in the context of the proposed SST retrieval methods.

6.1 Overview of Previous Chapters

Chapter 2 presented a short history of weather satellites (Section 2.1) and the predecessors of the AVHRR instrument. The main spectral characteristics of the AVHRR, as well as the new features of its latest version, were described in Section 2.2.

We continued with a discussion of an effect that mars every direct measurement of the sea surface temperature, the so-called skin effect (Section 2.3). It has a very practical consequence for every SST retrieval method, since the ground truth results contain a bias that is very difficult to remove. Some attempts at quantifying the magnitude of the skin effect [*Hepplewhite*, 1989, *Schlüessel et al.*, 1990], as well as a numerical model of its daytime and night-

time behaviour [*Schlüessel et al.*, 1990] were also presented. The conclusions were that the skin effect is more prominent during the day and in regions of low humidity. The estimated magnitude of the effect, as obtained from field studies [*Hepplewhite*, 1989, *Schlüessel et al.*, 1990, *Burns et al.*, 2000], was within the range of 0.1–0.5 °C, with observed variations of as much as 1 °C.

An overview of the previously developed SST retrieval methods began by introducing their common starting point—the radiative transfer equation for a clear, horizontally-stratified, plane-parallel atmosphere (Section 2.4). Rather than discussing the many published SST retrieval methods, we grouped them into categories depending on the approach used to approximate the radiative transfer equation, and showed how they are derived from it.

The pioneering theoretical work of *Anding and Kauth* [1970, 1972], *McMillin* [1971], *Prabhakara et al.* [1974] and *McMillin* [1975] that lead to the development of the oldest and most widely used family of methods—the Multi-Channel Sea Surface Temperature (MCSST)—was discussed in Section 2.6. The idea to use satellite observations at two adjacent wavelengths came from *Anding and Kauth* [1970]. *McMillin* [1971, 1975] and *Prabhakara et al.* [1974] provided a rigorous physical justification of *Anding and Kauth*'s suggestion using the radiative transfer equation. The principal MCSST equation is derived in two forms, the temperature-space and radiance-space (Section 2.6.1), following the work of *McMillin* [1971, 1975], *Prabhakara et al.* [1974]. Although the two forms are generally considered equally applicable [*McMillin and Crosby*, 1984], *Shepherd* [1993] found the radiance-based MCSST equation more accurate (by as much as 0.5 °C) on a set of near-shore AVHRR observations.

The Cross-Product SST (CPSST) method (Section 2.7) of *Walton* [1988] was an attempt to address the weakness of the MCSST in cases with high water vapour loading of the atmosphere. We derived the CPSST equation starting from the MCSST equation; instead of assuming the channel-4 and -5 equivalent absorption coefficients and average atmosphere temperatures to be unconditionally constant, we allowed them to differ on a large scale. Collating

AVHHR measurements in "bins" of similar values, we could establish a set of MCSST-like equations for each "bin". Solving this set of equations yielded the well-known CPSST equation of *Walton* [1988]. This made the CPSST equation coefficients weakly dependent on the channel brightness temperatures, making the method, unlike the MCSST, basically non-linear. The CPSST equation, however, is not self-sufficient, as its MCSST "parent". It requires a surface temperature seed, for which *Walton* [1988] proposed a simple single-channel linear equation.

The next step in improving the MCSST equation was the Nonlinear SST (NLSST) method, proposed by *Walton et al.* [1990] shortly after the CPSST. The previously constant coefficient in the MCSST, and the mildly-dependent function of channel brightness temperatures in the CPSST, became a function of surface temperature in the NLSST. This feature of the NLSST makes it more a "correction procedure" rather than an SST retrieval method in its own right, given its need for an *a priori* estimate of the surface temperatures and the simple form (2.31). Nevertheless, recent studies of *May* [1993] and *Walton et al.* [1998], and our own results when using the NOAA NLSST equations (Section 4.8.4), indicate that this method does provide an improvement over the MCSST and CPSST methods.

The common property of the MCSST, CPSST and NLSST methods is the notion that the influence of water vapour in the atmosphere can be accounted for via a difference of channel-4 and -5 brightness temperatures. An advancement in the treatment of this issue came from the Transmission Ratio SST methods (Section 2.9). The idea to use the variance in brightness temperature AVHHR images over a certain spatial extent for estimation of surface temperature and precipitable water amounts was proposed by *Kleespies and McMillin* [1990] and *Jedlovec* [1990]. *Harris and Mason* [1992] expanded this technique and showed that if the atmosphere is assumed horizontally homogeneous over a specified area, and thus any variation in the brightness temperatures is solely due to the SST field, the ratio of the variation is represented by

the ratio of channel-5 and -4 transmittances. The algorithms developed using this technique reported marked improvements in SST accuracy when applied to simulated data [*Harris and Mason*, 1992, *Sobrino et al.*, 1993, 1994, *Yu and Barton*, 1994]. However, their performance using real data did not produce the same success [*Yu and Barton*, 1994, *Barton*, 1995].

Essentially returning to the basic principles of the MCSST, *Emery et al.* [1994] developed two methods which extended the traditional MCSST equation. First they tried including directly the total water vapour column; in the second method, the channel-4 and -5 brightness temperature difference was included up to second order. The originality of their method was the use of another spaceborne instrument's data in the model—total water vapour column was estimated using the SSM/I microwave sounder data.

The method of *Smith* [1993], *Steyn-Ross et al.* [1993] which formed the starting point for the work in this thesis was summarized in detail in Chapter 3. This method, called the Dynamic Water Vapour (DWV), marked a radical departure from all the SST retrieval methods up to that time. Instead of approximating the radiative transfer equation, it employed a detailed atmospheric transmittance model and software—the LOWTRAN-7 [*Kneizys et al.*, 1988]. To increase the relevance of computed atmospheric properties, the DWV advocated utilization of geographically-relevant atmospheric profiles instead of the standard atmospheres available from the LOWTRAN-7 model. Like the CPSST and NLSST methods, the DWV needed a "seed" surface temperature.

The crux of the DWV method was physically simple: Given a pair of satellite-measured chanel-4 and -5 surface brightness temperatures, what is the correction for the first-guess atmospheric profile that would generate the same difference of the LOWTRAN-computed channel-4 and -5 surface brightness temperatures? The underlying assumption was that the difference between the first-guess and true intervening atmospheres was due only to the difference in the water vapour, expressed as the percentage of the water vapour amount equal for every layer in the profile.

The DWV method was tested with a data set of coincident AVHRR and buoy measurements of the Southern Ocean, off the west coast of Tasmania, Australia (Section 3.3). Radiosonde-measured atmospheric pressure, temperature and water vapour mixing ratio from the three nearest sites around the buoy were used as first-guess profiles in the DWV. The DWV SST estimates were the best amongst a set of MCSST and CPSST equations of that time [*Smith*, 1993].

It was the wish to further improve the DWV method that inspired the work in this thesis. Two new methods are proposed, which are discussed in the next section with more detail.

6.2 The Newly Proposed Methods for SST Retrieval

Two novel methods for SST retrieval were proposed in this thesis: the Dynamic Water Vapour or Atmospheric Temperature (DWVT; Chapter 4) and the Simultaneous Water Vapour and Atmospheric Temperature (SimWVT; Chapter 5).

The DWVT was directly instigated by the work of *Smith* [1993] and *Osborne* [1995] on the original DWV method. The goal was to start from the original DWV algorithm and incorporate the findings of *Osborne* [1995] (Section 3.7) in order to achieve a more robust method. This was accomplished by adding another algorithm—the Dynamic Atmospheric Temperature (DAT)—to the DWVT. The DAT is a complete equivalent to the DWV algorithm, except that the atmospheric temperature is altered.

The key question in the DWVT algorithm was when to switch from the DWV to the DAT algorithm. To be sure that the switching criterion is soundly formulated, we monitored the behaviour of the DWV internal variables. We concluded that the only feature that unambiguously correlated with the large

DWV SST errors was the shape of the LOWTRAN-computed channel-4 and -5 surface brightness temperature curves for DWV-modified atmospheric profiles.

The work on the SimWVT method was prompted by our wish to circumvent the DWV failure criterion. It was formulated using the information from only 34 cases, which originated from the same geographical location. How sure could we be that it was applicable to a wide range of localities and sources of input data (primarily first-guess atmospheric profiles)? The only answer to this question, in the absence of a larger data set, was to devise a method that would not necessitate the use of such a condition. And the only way to do so was to alter atmospheric temperature and water vapour simultaneously.

Changing these two properties in the search for an optimal atmosphere would have been a computationally very cumbersome task requiring utilization of a multidimensional optimization technique. Although such an approach could be described as "ultimate", it would probably also be described as "operationally unattainable".

The SimWVT method offers an elegant solution for achieving the benefits of a multidimensional optimization in SST retrieval for less than the full number-crunching price such a technique requires. The SimWVT equation (5.20) can be thought of as a shortcut in the search for an optimal atmosphere.

The DWVT and SimWVT methods were tested with the same test data set (Section 3.3) as the original DWV [*Smith*, 1993, *Steyn-Ross et al.*, 1993]. Although since the introduction of the DWV method a newer version of LOWTRAN-7 became available (MODTRAN-3.7/4), we decided to use it in order to preserve the baseline comparison across all the methods. To study the effect of first-guess profile aging in detail we initiated the DWVT and SimWVT with the sondes of up to 5 days around the satellite passes. The results for sondes up to 15 days old (before and after) were used to examine the trend in SST errors only.

In the case of radiosonde data from Hobart, both DWVT (Section 4.6.1) and SimWVT (Section 5.3.1) produced very similar results. The bias, rms and

Q values of the two methods combined varied for 0.04 °C, 0.11 °C and 0.11 °C, respectively. This can be regarded as negligible for all practical purposes.

The DWVT (Section 4.6.2) and SimWVT (Section 5.3.2) results using the Mt. Gambier sondes, however, displayed a much larger variation. The bias, rms and Q values fluctuated within 0.35 °C, 0.24 °C and 0.37 °C, respectively. The SimWVT in this case yielded noticeably more accurate SST estimates than the DWVT. In fact, the SimWVT results with the sondes from this site were even slightly more accurate than with the Hobart sondes.

Using the average SST estimates from different sonde selections (Tables 4.4, 4.6, 5.2 and 5.6) did not improve the overall accuracy of the methods. For a small number of passes, however, the SST estimates managed to cancel each out giving an almost perfect result.

The trend in the DWVT and SimWVT results when initiated with sondes of up to 15 days before and after the satellite passes revealed that DWVT is prone to much larger fluctuations than the SimWVT. We think this is caused by the DAT algorithm, because a per-pass analysis showed that the utilization of this technique usually coincided with large SST errors. Somewhat unexpectedly, the SimWVT reported better results when initiated with temporally and spatially more mismatched sondes than the DWVT.

For all sonde ages and sites, both methods reported largest errors for three passes: maep, mb21 and mbdz. Occasionally, the macq pass would have an SST error very close to these three. We could not determine the cause for the large SST errors. We are confident in ruling out any errors in first-guess radiosonde profiles because we used 14 different (7 sonde ages, two sonde sites) combinations and the largest SST errors were always reported for these four passes. Since we did not have any additional information or data that would help us in explaining these large SST errors, we conjecture that if some errors in our test data set were to exist, it would have to be in either the AVHRR radiances or buoy SST measurements. One plausible explanation might be AVHRR cloud contamination. This seems likely recalling that AVHRR pixels

are at best of $\sim 1 \times 1$ km resolution. Hence a cloud formation must be at least 2 km in size in order to be visible in AVHRR-acquired scenes. We could not verify this since the AVHRR data set was prepared almost ten years ago and delivered to us as channel-4 and -5 radiances over the buoy only.

To compare DWVT and SimWVT with other types of SST retrieval techniques, we employed a suite of TRSST (Section 4.7) and operational NESDIS (Section 4.8) methods on our test data set. Strictly speaking, only one of these methods was developed for the same AVHRR instrument that measured the radiance over the buoy (the NESDIS NOAA-9 MCSST; (4.9) and (4.10)). However, a recent paper by *Czajkowski et al.* [1998] reported that the NOAA-11 AVHRR was very similar to the NOAA-9 AVHRR, thus making the TRSST and NESDIS NOAA-11 methods applicable to our data set as well. For the NESDIS methods developed for other AVHRR instruments, it was interesting to see how well they would compare.

In general, all the TRSST methods reported larger biases and comparatively smaller rms values (Tables 4.8,4.9). They responded better with R_{54} values derived from the first-guess profiles. Of the NESDIS methods, the NOAA-9 MCSST (MCSST_9) and NOAA-12 NLSST ($\text{NLSST}_{12,9}$ and NLSST_{12}) methods outperformed our DWVT and SimWVT (Table 4.10). The reason why $\text{NLSST}_{12,9}$ and NLSST_{12} were better was because of their smaller rms. The bias value almost identical to that of MCSST_9 was reported by SimWVT for the "5d-before" sondes from Mt. Gambier. Unfortunately, none of the DWVT and SimWVT results had an rms smaller than 0.7 °C, therefore underperforming in the Q statistic. The other NESDIS methods reported much larger SST errors (biases of ~ 1 °C and greater), confirming how much regression-based methods depend on the data set used to craft the coefficients.

An indication that something could really be wrong with the worst performing passes—macq, maep, mb21 and mbdz—comes from comparison of DWVT and MCSST_9 results (Figure 4.8). Except the maeb pass, the MCSST_9 SST errors for the other three passes are very close to those of the DWVT. Excluding

the four passes from the analysis, and using the DWVT and SimWVT results for the "closest" sondes from Hobart, yields the following results: $MCSST_9$ (bias=-0.1 °C; rms=0.46 °C; Q=0.47 °C), DWVT (bias=-0.12 °C; rms=0.45 °C; Q=0.46 °C) and SimWVT (bias=-0.11 °C; rms=0.53 °C; Q=0.54 °C). Clearly, all three methods now report very similar results.

Although SimWVT and DWVT did not offer any improvement over the $MCSST_9$ on our test data set, it should be noted that the results presented here represent only one geographical location. To be able to better judge the relative performance of DWVT and SimWVT with respect to the conventional SST retrieval methods, one would have to incorporate data with much larger variation in SST, time of the year and geographical origin. Especially important should be data from regions known to be problematic using the conventional methods, such as the tropics with very high water vapour loading in the atmosphere. Between the DWVT and SimWVT, the results suggest that the latter has a more balanced performance with outdated sondes. SimWVT's unified formulation and ability to modify both the atmospheric temperature and water vapour profile make it a more advanced method over the DWVT. We believe that the performance of DWVT or SimWVT can still be improved and offer some suggestions in the next section.

6.3 Future Work

Clearly, the DWVT and SimWVT are not computationally efficient methods. Some improvements could be achieved by using a less comprehensive atmospheric transmittance model than LOWTRAN-7 (or newer MODTRAN-3.7/4); but that would violate the underlying philosophy of the methods to reflect as closely as possible the real physical situation.

The ever-increasing price-to-performance ratio of modern computers surely make the utilization of these two methods more realizable. However, we don't think that methods similar to DWVT/SimWVT will be used operationally in

the short to medium term. Such methods can now be used for SST retrievals over smaller areas, where increased accuracy is important or when atmospheric conditions prevent the use of the traditional methods (a typical example would be a volcanic eruption).

Another vulnerabilty of DWVT/SimWVT is in their reliance on an initial atmospheric profile, as atmospheric soundings are not so well distributed geographically. This problem is certainly more pronounced over the oceans, which is where these methods would be employed. One option could be to use climatologically derived data. Much better, and more in tune with the DWVT/SimWVT doctrine, would be to utilize temporally and spatially more recent atmospheric soundings. We mention here two possibilities:

- Judging from the literature over the past few years [for example *Ohtani and Naito*, 2000, *Flores et al.*, 2001], the idea to utilize GPS signals for atmospheric water vapour retrieval is steadily gaining momentum. The time delay of these signals is directly related to the amount of water vapour in the signal's path. Since GPS technology is finding widespread use, it is not so farfetched to expect the establishment of permanent atmospheric-sounding stations.
- Of the more readily available atmospheric sounding data sources, we recommend two spaceborne instruments well established for this purpose: the TIROS Operational Vertical Sounder (TOVS) and the Special Sensor Microwave Imager (SSM/I). The former has the advantage for sharing the same spacecraft as the AVHRR.

Of the two mentioned options, the latter seems more attractive to us as it offers direct measurement of the atmosphere. TOVS soundings are also truly concident with AVHRR measurements.

We envisage the following SST retrieval procedure involving methods such as DWVT/SimWVT:

1. For a cloud-free AVHRR pixel, find the appropriate TOVS sounding.

2. Since retrieval of atmospheric temperature and water vapour profiles from TOVS measurements requires known surface temperature, use the operational NESDIS equation to estimate SST.

3. Retrieve the atmospheric temperature and water vapour profile from the selected TOVS sounding.

4. Use this profile to initiate DWVT/SimWVT.

5. When DWVT/SimWVT converges, compare the new SST estimate with the previous one (the NESDIS SST, if it is the first iteration).

6. Stop if the change in estimated SST is within the tolerance. If it is not, repeat the previous three steps by initiating the atmospheric profile retrieval with the last SST estimate.

Although such an algorithm may suffer from "noise" in the retrieved atmospheric profile from TOVS measurements, we believe that this would not pose a serious problem to DWVT/SimWVT-like algorithms, given their relative robustness to sondes of different age.

The history of SST retrieval methods using AVHRR data is more than twenty years long. There have not been many new methods proposed in the past decade. It seems that the effort of the SST research community is focusing primarily on the development of regionally-optimized traditional SST methods, operational world-wide monitoring for meteorological/commercial purposes, and generation of AVHRR products and methods for long-term climatological studies (such as the AVHRR Pathfinder programme). Nevertheless, there will always be a need for more accurate SST retrievals. We believe that the methods proposed in this thesis, DWVT and SimWVT, make a worthwhile contribution towards that goal.

Part II

Pasture Biomass Estimation Using an Airborne Multispectral Imaging System

Chapter 7

Part II: Introduction

In late 1998, an opportunity arose to organize flights using Charles Sturt University's airborne multispectral imaging system over the North Island of New Zealand. An *ad hoc* consortium of several research and commercial companies and the University of Waikato was formed to fund the flights. The intention was to study the applicability of airborne multispectral remote sensing to agriculture and forestry in New Zealand with a series of small-scale pilot projects.

One of the pilot projects was high-resolution imaging of specially prepared patches of pastures near the University of Waikato's campus in Hamilton. This project was carried out in collaboration with AgResearch Ltd. and the Dairy Research Corporation (now operating under the name Dexcel Ltd.) whose scientists cultivated the test patches. In this part of the thesis we present the results of the feasibility study on pasture status prediction using the acquired multispectral pasture images.

7.1 Project Rationale

Meat and dairy production are amongst the major industries in New Zealand. What makes New Zealand meat and dairy products competitive overseas is

largely related to the main source of food for the livestock. Due to the year-round temperate climate, the livestock in New Zealand is predominantly grass-fed, which significantly reduces on-farm production costs.

In order to sustain productivity, the farmer must balance the feed demand of his livestock with the growth requirements of his paddocks. The feed supply and feed demand must satisfy the needs of the livestock, but not at the expense of future pasture growth. While feed demand is relatively straightforward to predict, pasture growth supply depends on many factors, which affect the growth rate in a very complex manner. The only viable solution for predicting pasture growth is direct measurement in combination with a steady monitoring practice.

Remote sensing is one possible candidate for such a direct measurement technique. Due to the characteristic spectral signature of vegetation (for more details see Section 7.3.2) it is possible to monitor its status from afar. The main advantage of remote sensing over other techniques (see Section 7.2) for pasture monitoring is its ability to provide a "big picture" by acquiring data over large areas simultaneously. Also, the scale of this "big picture" can be altered to address specific requirements of different applications. This feature has the potential of reducing the cost of "standard sample" remote sensing analysis to the level acceptable to the ultimate user—the farmer.

The work of *Hanna et al.* [1999] and *Lin* [1999] is particularly pertinent to this study. *Hanna et al.* used the measurements from a field trial in the Waikato region employing a portable three-channel radiometer (Section 8.3) to estimate pasture biomass. They found that a three-channel linear regression equation provided reasonably accurate biomass estimates (correlation coefficient squared, $R^2 = 0.927$). An attempt to predict biomass based on a widely-used Normalized Difference Vegetation Index (NDVI) (Section 7.3.4) revealed a saturation in its values for even modest amounts (for New Zealand circumstances) of biomass.

Hanna et al. [1999] developed a simple theoretical model of canopy re-

flectance to explain the reported experimental findings. The canopy model was a variant of the two-stream approximation to radiative transfer used by *Meador and Weaver* [1980] to describe atmospheric scattering of radiation, extended later by *Dickinson* [1983] and *Sellers* [1985] to the canopy environment to describe multiple scattering of light by leaves. The canopy model of *Hanna et al.* [1999] was formulated in terms of leaf area index[1] (LAI). For Waikato pastures, LAI values rarely fall below 2, and can go as high as 12. The output of the model—top-of-canopy albedos for the same three channels as the radiometer—was then compared with the experimental measurements. The model predicted well the observed saturation of the NDVI vegetation index for LAI values in excess of about 1.5 and confirmed the generally held view that NDVI has not proved to be very useful in the New Zealand farming context.

Lin [1999] analyzed a set of aerial colour infrared photographs taken in 1985 of a farm in the lower central North Island (Manawatu plains). The photographs provided an equivalent of a three channel imaging system, in the near infra-red (NIR), red and green bands. Along with the pasture targets, a set of calibration targets of known reflectances was photographed to allow direct conversion between photographic intensity and top-of-canopy reflectance. The obtained pasture reflectance was then used in a variety of regression and vegetation index-type algorithms to predict the true biomass. The prediction accuracy for vegetation index type-equations was in the range R =0.55–0.68 without correction for ground slope and bidirectional reflectance effects (Section 7.3.3), to R =0.7–0.8 with these corrections. The three channel regression equation before the corrections yielded $R = 0.71$, and after the corrections $R = 0.83$. *Lin* [1999] concluded that it was possible to predict pasture biomass with a reasonable accuracy using aerial false-colour infrared photographic technology, and that prediction improves with corrections for

[1]Leaf area index is the average number of leaves encountered in a vertical traverse through the canopy.

ground slope and bidirectional reflectance effects of vegetation.

The main task of our feasibility study was to estimate the precision and prediction uncertainty of an airborne multispectral remote sensing technique for pasture status monitoring. In many ways our study was similar to that of *Lin* [1999]. The major differences were in the technology for image acquisition and the number of channels. Our airborne imaging system utilized charged-coupled device (CCD) technology (Section 8.4) to directly convert observed light into the digital domain in four channels in the visible and near-infrared part of the electromagnetic spectrum. The results from the study could be used in a cost-benefit analysis or a farm management software to evaluate the end-benefits of the technique for the farmer.

7.2 Current Pasture Status Monitoring Techniques

The term "pasture status" usually refers to the measurable quantity of pasture biomass, which can be directly linked to the nutritional value of the grass. It is expressed in kilograms of dry matter per hectare (kgDM/ha). Very rarely, the term "pasture status" refers to other content in grass, usually related to some chemical element or mineral (e.g. nitrogen, phosphate, etc.).

All the techniques used to assess various pasture attributes fall into several broad categories, which are listed below with a brief comment on their advantages and disadvantages.

- *Visual pasture assessment*

  Probably the oldest method, and still widely used. An experienced person assesses the status of the paddock based on the colour of grass and other visible features. This method, however convenient for the farmer, is prone to very large errors due to the subjective nature of the assessor, effectively hindering any chance of long-term monitoring. The only advantage is that it usually does not permanently damage the grass.

- *Harvesting method*

  The grass from a small sample region, typically of area 0.1–0.25 m^2, is carefully harvested to soil level. The harvested material is slowly dried (e.g. at 80 °C for one or two days) to eliminate the moisture, and then weighed. Knowing the sample area, the pasture biomass can be readily converted from grams of dry matter per square meter (obtained from the sample) to that of the paddock (in kgDM/ha).

  This method is very often used as the standard for calibration of other objective measurement methods of pasture biomass. It is very labour intensive and destroys the sample.

- *Chemical analysis*

  Such methods are used for determination of chemically-related pasture status factors (trace elements, minerals, etc.). They all involve some kind of sample collection, usually harvesting. These methods are the standard for all other measurement techniques of chemical composition of grass. They are labour intensive and destroy the sample.

- *Spectroscopic methods*

  A very large family of methods, predominantly used in the past as a faster alternative to the chemical analysis methods (which are used to calibrate them). They depend on very expensive laboratory equipment—spectrophotometers. They require sample collection, usually by harvesting. Their results are often difficult to compare as each spectrophotometer has a different calibration; however, the measurements within one laboratory can be very precise and fast.

  Portable spectrophotometers have become available in recent years, allowing direct measurements without harvesting. Such methods are still largely in the developmental stage though.

- *Remote sensing*

  The remote sensing methods can be thought of as variants of the on-site (portable) spectroscopic methods. However, the major difference is that the remote sensing methods obtain measurements from much larger distances (either from air or low Earth orbit). The number of wavelengths (in the remote sensing parlance called *channels*) at which measurements are recorded is usually significantly smaller than that of the spectroscopic methods.

  These methods do not destroy the sample, but require calibration using one of the previously mentioned methods. The remote sensing methods from space are very much dependent on the weather since cloud cover over the area of interest renders them unusable. Remote sensing methods are still in the research stage, with emphasis on reducing the costs and enhancing the accuracy.

One issue relevant to all assessment methods is how to infer the changes on a large scale from smaller, localized measurements. The remote sensing methods are inherently suitable for this task because they allow simultaneous measurements over a wide area. Proper association of the results requires only the so-called geometrical correction of the acquired images. This correction correlates the location of a set of ground features with their position in the image. Once this is determined, the entire image can then be associated with the imaged area.

For the other methods, this task is more complex and involves the use of spatial statistic principles. A sampling pattern over the area under examination is determined depending on the application and desired accuracy. The problem with this approach is that the spatial variation of the measured property is not known when the sampling pattern is designed, thus ultimately producing erroneous conclusions.

7.3 The Principles of Remote Sensing of Vegetation

In this section, we discuss the issues related to the remote sensing of vegetation. We start with a discussion on how leaf structure and chlorophyll affect absorption and reflection of light. The reflective properties of canopies are described next. We finish with a short overview of the most popular remote sensing technique for vegetation monitoring—vegetation indices.

7.3.1 Structure of the Leaf

Remote sensing techniques developed for vegetation monitoring depend on the knowledge of spectral properties of individual leaves and plants. These properties are best understood by studying the leaf structure in fine detail.

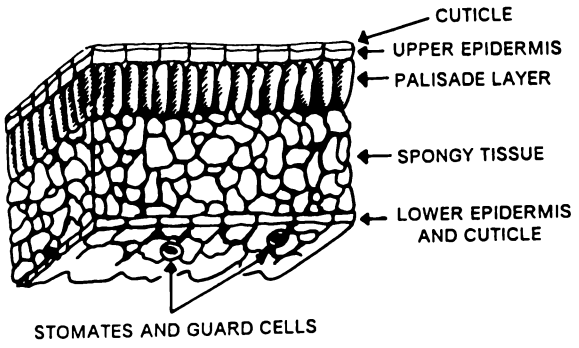

Figure 7.1: Diagram cross section of a typical leaf. (From *Campbell* [1996].)

The cross section of a typical leaf is depicted in Figure 7.1. The upper surface of the leaf is covered with a translucent, waxlike layer known as the *cuticle*, which serves to prevent uncontrolled moisture loss from the leaf interior. Below the cuticle lies the *upper epidermis*. The leaf underside has a similar structure, consisting of a layer of cuticle and the *lower epidermis*. However, it also includes very tiny openings called *stomates*. Each stomate is guarded by a pair of cells that open and close to control the movement of air

through stomates into the leaf interior. The stomates also play a critical role in maintaining the moisture balance of the leaf.

Below the upper epidermis is the *palisade* tissue. The vertically elongated cells of the palisade include *chloroplasts*, cells composed of chlorophyll and other pigments active in the process of photosynthesis. Below the palisade tissue is the spongy, *mesophyll* tissue. It consists of irregularly-shaped cells separated by interconnected openings. The mesophyll tissue utilizing its large surface area serves as the exchange medium for the oxygen and carbon dioxide required for photosynthesis and respiration.

7.3.2 Chlorophyll and Spectral Properties of the Leaf

Chlorophyll is one of the most important biological compounds for life on Earth as a whole. It acts as a photoreceptor and catalyst for the conversion of sunlight into chemical energy, in the form of carbohydrates stored by plants. The chemical reaction of the photosynthesis process is:

$$6\,CO_2 + 6\,H_2O \longrightarrow C_6H_{12}O_6 + 6\,O_2$$

The role of the chlorophyll in the process of photosynthesis is to capture light (energy) which is needed for the above chemical reaction. Chlorophyll belongs to the class of pyrrole dyes, and exists in two chemical variants: Chlorophyll *a* ($C_{55}H_{72}MgN_4O_5$) and Chlorophyll *b* ($C_{55}H_{70}MgN_4O_6$). Spectral characteristics of the forms of chlorophyll differ slightly. Two major absorption bands exist (Figure 7.2), one at about 430/450 nm and the other at 660/640 nm. The natural abundance of the blue-greenish Chlorophyll *a* to the yellow-greenish Chlorophyll *b* is around 3:1.

The determination of the spectral behaviour of chlorophyll in plants is complicated by its adaptability [*Schanda*, 1986]. In weak light conditions, protochlorophyll is created as a preliminary stage, whereas chlorophyll becomes bleached and inactive under intense light. Diurnal changes in the amount of

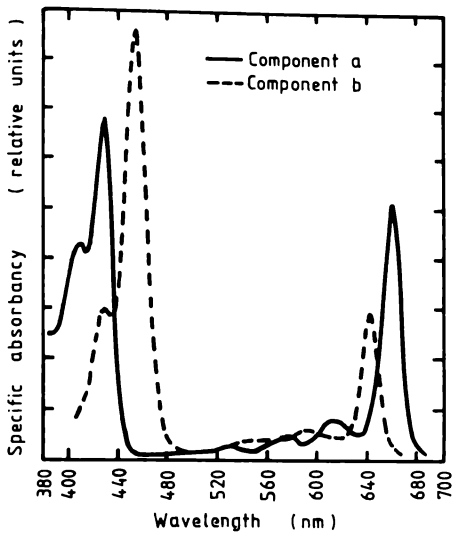

Figure 7.2: Absorption spectra of *in vitro* chlorophyll *a* and *b*. (From *Schanda* [1986].)

chlorophyll in plants have also been observed [Mac Hanna, priv. comm.].

Reflectance and transmittance spectra of a plant leaf are shown in Figure 7.3. Chlorophyll controls much of the spectral response of the living leaf in the visible part of the spectrum (0.4–0.75 μm) by absorbing strongly in the blue and the red parts (Figure 7.2) by as much as 70–90%. Hence the green appearance of live vegetation. It is found predominantly in the chloroplast cells of the palisade tissue.

In the near-infrared (NIR) spectrum from 0.75 μm to about 1.35 μm, spectral characteristics of the leaf are chiefly controlled by the inner structure of the leaf and not its pigments. The cuticle and epidermis are practically transparent to NIR radiation. The majority of NIR radiation passing through the upper epidermis layer is scattered by the mesophyll tissue. Very little of the scattered NIR radiation is absorbed internally, and up to about 60% [*Campbell*, 1996] is scattered outside the leaf. Some studies indicate that a strong scatterer of NIR radiation could also be the palisade tissue [*Campbell*, 1996]. In the 1.35–2.5 μm range of the NIR spectrum, the spectral characteristics are dominated by the water absorption bands at 1.45 and 1.95 μm.

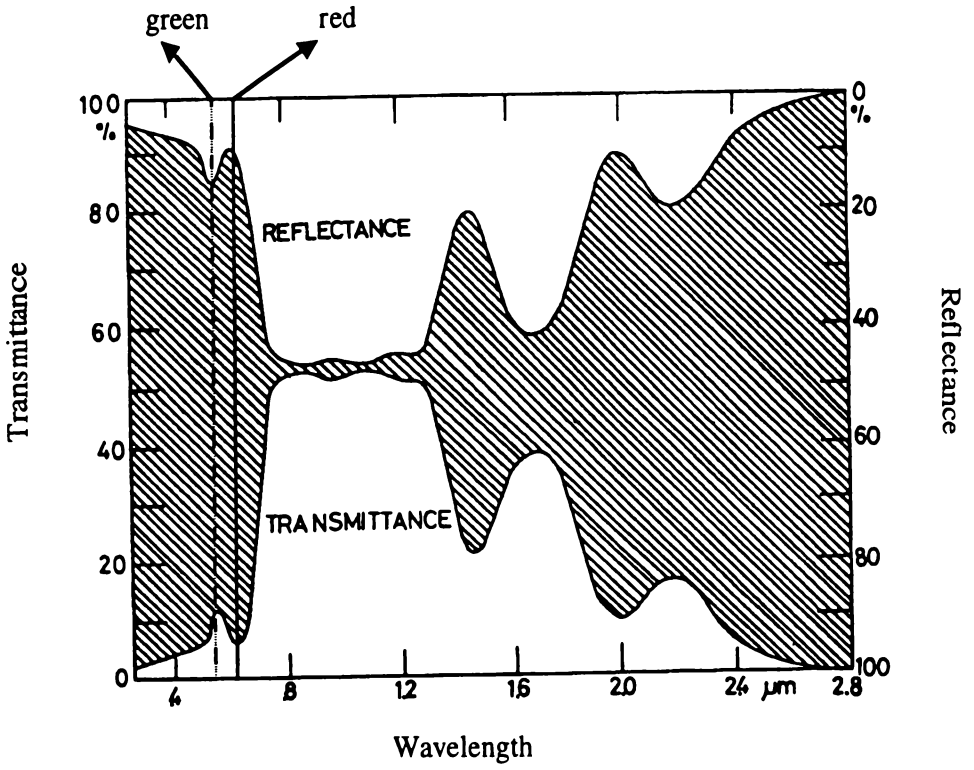

Figure 7.3: Reflectance and transmittance spectra of a plant leaf. (From *Lin* [1999].)

At the edge of the visible spectrum, roughly between 680 and 750 nm, lies a noticeably sharp increase in reflectance caused by the decline of chlorophyll pigment absorption. This steep part of the leaf reflectance curve is known as the *red edge*. It is a dynamic feature of the leaf spectrum, as its location in the spectrum tends to shift as the plant matures. The causes of its shift are still not very well understood [*Campbell*, 1996]. *Collins* [1978] suggested that the predominant reason is the increase in Chlorophyll *a* abundance during the plant's lifetime. Increased concentrations of this chlorophyll variant "build up" the absorption band in the red edge region of the visible spectrum thus effectively causing a red edge shift towards longer wavelengths.

Any plant during its lifetime is subject to some kind of stress by disease, insect attack, lack of moisture, etc. Stresses in general have an impact on the leaf spectrum, apparently altering both its visible and NIR parts. The

changes in the NIR spectrum are somewhat better documented due to the high reflectivity, i.e. easier and more reliable detection, than in the visible spectrum [*Asrar*, 1989]. Since leaf reflectance in the NIR depends strongly on the structure of the complex cavities of the mesophyll tissue and internal leaf reflection, any effect causing destruction of this tissue or the internal structure of the leaf is likely to be noticed as a decrease in NIR reflectivity. There is still much uncertainty about how different stresses to the plant affect the change in NIR reflectivity [*Campbell*, 1996]. Some scientists maintain that moisture stress and natural maturing causes these cavities to collapse; others are of the opinion NIR reflectance decreases mostly due to the changes in the cell walls of the mesophyll and palisade tissues rather than physical changes in the cavities themselves. Whatever the correct explanation, any decrease of NIR reflectivity in subsequent measurements of the same plant are taken as a clear indication of some kind of stress.

7.3.3 Reflection Properties of Canopies

Canopies exhibit different spectral characteristics to that of a separate leaf. They are composed of leaves of different age, size, orientation and shape; many layers of leaves form a canopy, and their vertical distribution provides different amounts of shade masking the lower leaves and the ground. Leaf orientation changes diurnally, as the plant tries to maximize the exposure of its canopy to the Sun [Mac Hanna, priv. comm.].

Shadowing tends to decrease canopy reflectance below the values usually measured from individual leaves [*Campbell*, 1996]. Hence the reflectance of a canopy is lower than what is observed for separate leaves. However, the brighter canopy reflectance in the NIR is associated with the fact that many plant leaves contribute to its value since individual leaves transmit large amounts of NIR radiation. NIR radiation passes through the upper leaf layers of the canopy largely unobstructed; the amount reflected from the lower layers

of leaves is transmitted back through the upper layers, resulting in bright NIR reflectance [*Gobron et al.*, 1997].

Due to the very complex effects of many factors (some of which we have mentioned here) on canopy reflectance, this property is usually measured *in situ* [for a review of methods see *Asrar*, 1989, chap. 2] and reported as the *bidirectional reflectance distribution function* (BRDF).

BRDF is not an exclusive property of canopies; it is a fundamental and intrinsic property of any reflective surface. It is defined as the ratio of the reflected radiance from an infinitesimal surface area in the direction (θ_r, ϕ_r) to the incident radiance upon the same surface from the direction (θ_i, ϕ_i). (θ and ϕ are azimuth and elevation coordinates of a spherical coordinate system centered on the infinitesimal surface of reflection.)

BRDF, as geometrically and mathematically defined, can never be directly measured because truly infinitesimal solid angles around the directions of incoming or reflecting radiation do not include measurable amounts of radiant flux [*Asrar*, 1989]. Therefore, BRDF values reported in practice are actually related to another reflectance property called *bidirectional reflectance factor*. This is defined as the ratio of the radiant flux actually reflected by a sample surface to that which would be reflected into the same reflected-beam geometry by an ideal, perfectly diffuse (that is Lambertian) standard surface irradiated in exactly the same way as the sample. However, it is generally accepted that bidirectional reflectance factor measurements of sufficient angular density provide useful estimates of the true BRDF [*Verstraete et al.*, 1990].

There are many published models of BRDF. They vary from completely theoretical [for example *Qiu*, 2001, *Roujean*, 2000, *Chen and Cihlar*, 1997, *Verstraete et al.*, 1990, *Wanner et al.*, 1995, *Kuusk*, 1996], semiempirical [*Gobron et al.*, 1997, *Otterman et al.*, 1995, *Roujean et al.*, 1992, *Dymond et al.*, 2000, *Shepherd and Dymond*, 1999], to those derived from experiments [*Asrar*, 1989]. The experimentally derived BRDF models are very important in remote sensing, due to the inherent complexity of factors contributing to the canopy

reflectance which cannot be modelled easily [*Lillesand and Kiefer*, 1994]. One promising, relatively new stream in BRDF research is ray tracing using Monte Carlo techniques [*Campbell*, 1996].

The BRDF model we will consider using in this study is the WAK model [*Dymond et al.*, 2000, *Shepherd and Dymond*, 1999]. It was formulated for BRDF correction of AVHRR images over New Zealand by taking into account physical principles of light scattering from a closed canopy. We found it acceptable for our study because it was devised for New Zealand vegetation in particular. Another advantage of the WAK model was that it allowed derivation of a BRDF correction that was optimized for the application in hand. Since we knew that our test pasture patches would have many different vegetation species, ability to "tune" the BRDF correction with the WAK model to our needs seemed very appealing.

The WAK model [*Dymond et al.*, 2000] depends on two factors, one each for the visible and the NIR band, that allow correction of top-of-canopy reflectance to a standard illumination and viewing geometry. Their formulas are:

$$\lambda_{\text{Vis}} = \frac{\cos\theta_i + \cos\theta_e}{\cos\theta_{\hat{i}} + \cos\theta_{\hat{e}}} \left[\frac{a + (\pi - a)e^{-k\hat{\alpha}^2}}{a + (\pi - a)e^{-k\alpha^2}} \right] \tag{7.1}$$

$$\lambda_{\text{NIR}} = \frac{\cos\theta_i + \cos\theta_e}{\cos\theta_{\hat{i}} + \cos\theta_{\hat{e}}} \left[\frac{\frac{8}{3\pi}(a + (\pi - a)e^{-k\hat{\alpha}^2}) + H(\theta_{\hat{i}}, w)\, H(\theta_{\hat{e}}, w) - 1}{\frac{8}{3\pi}(a + (\pi - a)e^{-k\alpha^2}) + H(\theta_i, w)\, H(\theta_e, w) - 1} \right] \tag{7.2}$$

where $\theta_{\hat{i}}$, $\theta_{\hat{e}}$, $\hat{\alpha}$ are the standard illumination, viewing and phase (the difference between the illumination and the viewing) angles, respectively, specified by the user; θ_i, θ_e, α are the illumination (solar zenith), viewing (satellite scan angle) and phase angles derived from the image, respectively; the H function accounts for multiple scattering within the canopy, and was first proposed by *Hapke* [1981]:

$$H(\theta, w) = \frac{1 + 2\cos\theta}{1 + 2\cos\theta\sqrt{1 - w}}. \tag{7.3}$$

The w parameter is proportional to leaf reflectance, whilst the a and k parameters are influenced by canopy roughness and describe its backscatter and hotspot properties, respectively. Thus the WAK model is a function of three variables (θ_i, θ_e, α) and three parameters (w, a, k)—hence its name. The three variables θ_i, θ_e, and α are derived from remotely sensed data, allowing determination of the three parameters using a nonlinear model fitting procedure [*Shepherd and Dymond*, 1999].

When the WAK parameters are determined, top-of-canopy reflectance (ρ) is corrected to reflectance at a standard orientation ($\hat{\rho}$) using the formula:

$$\hat{\rho} = \lambda \rho. \tag{7.4}$$

7.3.4 Vegetation Indices

Vegetation indices are quantitative measures that attempt to relate remotely sensed data to different biophysical properties of vegetation. These indices are calculated from either raw (as measured) or post-processed (reflectance, BRDF and/or atmospheric corrected) data. Vegetation indices commonly include observations of several spectral values, that are manipulated to yield a single value that predicts vegetation status within a pixel. Usually vegetation indices attempt to predict biomass or leaf area index, but they have also been used for leaf water content, chlorophyll, percentage cover and other biophysical characteristics of vegetation [*Purevdorj et al.*, 1998].

The applications of vegetation indices can be loosely grouped in two categories: quantitative and qualitative. Quantitative applications attempt to use vegetation indices to predict biophysical properties of vegetation as accurately as possible. Such studies typically examine test plots during an entire growing season and compare the derived vegetation indices measured throughout the season with samples of vegetation taken at the same time. Qualitative applications use vegetation indices as "mapping" tools, to assist in image classifica-

tion, separation of vegetated from non-vegetated areas, distinguishing between different types and densities of vegetation, monitoring seasonal variations in vegetation abundance, etc.

However, it should be noted that vegetation indices seem to rely more on numerology than science. Although results of many studies [*Campbell*, 1996, *Asrar*, 1989, *Lillesand and Kiefer*, 1994] have in general confirmed the utility of vegetation indices, their success vary significantly with the type of vegetation considered, atmospheric conditions and the instrument type used for data acquisition. This underscores their inherent reliance on empirical evidence rather than basic biology or physics.

Over the years, many types of vegetation indices have been developed. A major part of their derivation is dedicated to the treatment of the so-called *soil line*. The soil line is a hypothetical line in spectral space that describes the variation in the spectrum of bare soil in the image; this line is considered to be the line of zero vegetation. The spectral space which is commonly used to observe this line is the plot of NIR vs. red channel reflectance because these channels have the strongest contrast in spectral signature of vegetation [*Campbell*, 1996]. The assumption inherent in all vegetation indices is that bare soil pixels in an image lie on or very near the soil line in the NIR-red reflectance graph. At this point, the vegetation indices diverge depending on the orientation of lines of equal vegetation (isovegetation lines) [*Asrar*, 1989]:

1. All isovegetation lines converge at a single point. The indices that use this assumption are the ratio based indices, which measure the slope of the line between the point of convergence and the NIR-red point of the pixel.

2. All isovegetation lines remain parallel to the soil line. This family of indices are known as perpendicular indices since they measure the perpendicular distance from the soil line to the NIR-red point of the pixel.

We finish the discussion about vegetation indices by listing those most frequently encountered in the literature (in the following equations R and NIR refer to the red and near-infrared channel reflectance, respectively):

- Ratio Vegetation Index (RVI) [*Jordan*, 1969]

$$\mathrm{RVI} = \frac{\mathrm{NIR}}{\mathrm{R}} \tag{7.5}$$

- Normalized Difference Vegetation Index (NDVI) [*Kriegler et al.*, 1969, *Rouse et al.*, 1973]

$$\mathrm{NDVI} = \frac{\mathrm{RVI} - 1}{\mathrm{RVI} + 1} = \frac{\mathrm{NIR} - \mathrm{R}}{\mathrm{NIR} + \mathrm{R}} \tag{7.6}$$

- Infrared Percentage Vegetation Index (IPVI) [*Crippen*, 1990]

$$\mathrm{IPVI} = \frac{\mathrm{NDVI} + 1}{2} = \frac{\mathrm{NIR}}{\mathrm{NIR} + \mathrm{R}} \tag{7.7}$$

- Perpendicular Vegetation Index (PVI) [*Richardson and Wiegand*, 1977]

$$\mathrm{PVI} = \sin(\alpha)\mathrm{NIR} - \cos(\alpha)\mathrm{R} \tag{7.8}$$

where α is the angle between the soil line and the NIR axis.

- Weighted Difference Vegetation Index (WDVI) [*Clevers*, 1988]

$$\mathrm{WDVI} = \mathrm{NIR} - a\,\mathrm{R} \tag{7.9}$$

where a is the slope of the soil line in the NIR-R plot.

- Soil Adjusted Vegetation Index (SAVI) [*Huete*, 1988]

$$\mathrm{SAVI} = \frac{\mathrm{NIR} - \mathrm{R}}{\mathrm{NIR} + \mathrm{R} + L}(1 + L) \tag{7.10}$$

where L is an adjustment factor, ranging from 0 (very high vegetation

density) to 1 (very low dense vegetation). The standard value typically used in applications is 0.5 [*Lillesand and Kiefer*, 1994].

- Transformed Soil Adjusted Vegetation Index (TSAVI) [*Baret et al.*, 1989, *Baret and Guyot*, 1991]

$$\mathrm{TSAVI} = \frac{a(\mathrm{NIR} - a\mathrm{R} - b)}{a\mathrm{NIR} + \mathrm{R} - a\,b + X(1 + a^2)} \tag{7.11}$$

where a and b are the soil line slope and intercept, respectively, and X is an adjustment factor which is set to minimize soil noise (0.08 in the original papers).

- Modified Soil Adjusted Vegetation Index (MSAVI) [*Qi et al.*, 1994]

$$\begin{aligned} \mathrm{MSAVI} &= \frac{\mathrm{NIR} - \mathrm{R}}{\mathrm{NIR} + \mathrm{R} + L}(1 + L) \\ L &= 1 - a\,\mathrm{NDVI}\,\mathrm{WDVI} \end{aligned} \tag{7.12}$$

where a is the slope of the soil line.

- Second Modified Soil Adjusted Vegetation Index (MSAVI2) [*Qi et al.*, 1994]

$$\mathrm{MSAVI2} = \frac{1}{2}\left(2\mathrm{NIR} + 1 - \sqrt{(2\mathrm{NIR} + 1)^2 - 8(\mathrm{NIR} - \mathrm{R})}\right) \tag{7.13}$$

- Global Environmental Monitoring Index (GEMI) [*Pinty and Verstraete*, 1991]

$$\begin{aligned} \mathrm{GEMI} &= \eta\left(1 - \frac{\eta}{4}\right) - \frac{\mathrm{R} - 0.125}{1 - \mathrm{R}} \\ \eta &= \frac{2(\mathrm{NIR}^2 - \mathrm{R}^2) + 1.5\mathrm{NIR} + 0.5\mathrm{R}}{\mathrm{NIR} + \mathrm{R} + 0.5} \end{aligned} \tag{7.14}$$

Chapter 8

Pasture Targets, Measurement Methods and Instruments

In this chapter we describe the test pasture targets, and the measurement methods and instruments used to collect the data for this project.

8.1 Characteristics of the Test Pasture Targets

As this pilot-project was done in collaboration with AgResearch Ltd. and Dexcel Ltd., their scientists prepared a set of test pasture plots[1] with various types of pasture species, grown under different regimes. The plots were 3×3 meters in size, delineated from the rest of the pasture with 75 cm wide hay wrap plastic on all four sides. Forty five plots were prepared by AgResearch Ltd., and twenty plots were prepared by Dexcel Ltd, for a total of 65 test plots.

The regimes of growing and/or the types of plant species in the plots as supplied by the AgResearch and Dexcel scientists are listed in Table C.1. As can be seen from the table, the AgResearch plots featured different irrigation, nutritional and grazing regimes, whereas the Dexcel plots featured different irrigation and pasture species.

[1] We refer to the plots as *targets* also.

The plots were physically located in three groups. The AgResearch plots P01–P29 were located on the edge of its Ruakura campus, adjacent to Tramway Rd; the plots P30–P37, and P40–47 were located on the Dexcel experimental paddocks A5 and E1, respectively. All of the Dexcel plots were located on its No. 5 dairy station. The three groups of plots were all within a 2 km radius from each other, near the University of Waikato's campus in Hamilton.

8.2 Data Collection Protocol

The protocol for the pasture plot measurements for our project was as follows:

1. The plots were first imaged by Charles Sturt University's airborne multispectral imaging system (ABVS; Section 8.4).
   (a) A pair of calibration ground targets (two $6 \times 6\,\mathrm{m}^2$ canvases of known spectral characteristic) were placed near the P40–47 group of test plots. Since the plots were reasonably close together (within a 2 km radius), the canvases were not moved during the imaging campaign.
   (b) The airborne imaging started at 11 a.m. and finished by 1 p.m. on February 11, 1999.
   (c) The test plots were imaged from two nominal altitudes—1000 and 3000 ft (1 ft = 0.3048 m), although no attempt was made to keep the plane exclusively at those altitudes.
2. Other pasture plots measurements started immediately after the airborne imaging was completed.
3. Sample collection from the Dexcel plots was performed by harvesting the central 0.5–1 m^2 of each plot to the ground. One hundred grams of the ryegrass/white clover plot samples, or 300 g for the turnips/chicory samples, was prepared for a NIR spectroscopy analysis for trace elements and minerals. One hundred fifty grams of each sample was prepared for

dry matter (biomass) measurements. Whenever possible, a full botanical dissection was performed on the rest of the sample.

4. The protocol for the AgResearch plots was different:

   (a) Five $0.25 \times 0.5\,\mathrm{cm}^2$ sampling patches were randomly selected within each "P" plot and were labelled "A" to "E".

   (b) Two different types of the Hanna radiometer (Section 8.3) were used to collect measurements from the five sampling patches. This required two radiometer measurements per patch to cover the whole area. The radiometers were always calibrated in-between patches.

   (c) Immediately after radiometer measurements were completed, the patch was harvested to ground level and samples were collected.

   (d) The contents of every patch sample was classified into: green leaf, green stem, non-green, legume leaf, legume stem and inedible. Dry matter (biomass) for each of the categories, excluding inedible, was measured, and the total dry matter was calculated from the measurements.

It is important to note that the sample collection procedures differed for the Dexcel and AgResearch plots. The Dexcel data contained only the total dry matter, while the AgResearch data lacked information on trace elements. Thus, our study will deal with the prediction of total dry matter only from both data sets. The biomass for the AgResearch and Dexcel plots, as supplied by these two organizations, is listed in Appendix C.2.

8.3 Hanna Radiometer

Because of the proof-of-concept nature of our study, the decision was made to concurrently use several forms of pasture biomass measurements. Apart from the airborne imaging, the biomass of test patches was assessed by the

harvesting method and two different versions of the Hanna radiometer. The design and functioning of these radiometers is now described.

In the late 1970's, the agricultural community became aware of the advantages of employing objective measurement methods for assessing pasture status in New Zealand. Mac Hanna, a Waikato dairy farmer, decided to make a portable radiometer capable of reporting green biomass; this was inspired by the SPOT and Landsat satellites whose imagery had been used for the same purpose.

Both versions of his radiometer for our study used artificial illumination, two well-regulated 12 V incandescent bulbs, to eliminate errors associated with the daily and seasonal variations in the sunlight and skylight. An inverted 45 litre black plastic bucket provided the required shielding from the natural light and the frame to carry all the components. The older version of the radiometer detected reflected light in three wavelength intervals similar to the Landsat Thematic Mapper bands 2, 3 and 4: centered at 800, 670 and 550 nm, with a 20 nm bandwidth.

The newer version of the radiometer utilized a light-collecting fibre optic cable. The fiber had a microlens attached to its entrance, limiting the light gathering capabilities to an approximately 10 cm diameter circle on the ground. The fibre cable fed the collected light into a Zeiss Monolithic Miniature Spectrometer (MMS 1). The spectrometer was designed to measure radiation at 256 different wavelengths in the range 305–1150 nm. Due to the internal noise, reliable spectra could be obtained for the 360–900 nm range only. The integration time of the spectrometer was 100 milliseconds.

The detector system and the incandescent bulbs were mounted inside at the top of the inverted bucket (i.e. the bottom of the bucket). Thus the pasture was illuminated directly overhead, and the detector system was oriented to observe the directly backscattered radiance in both versions of the radiometers.

The measured signal from the three channel detectors of the older radiometer was collected by a Psion 1 hand-held programmable calculator. The read-

out from the spectrometer of the newer radiometer was directed to a laptop, running data acquisition software.

Both radiometers were calibrated in between measurements to compensate for instrument drift. The older radiometer used a Kodak gray card, whose nominal reflectance was 18%. The newer version of the Hanna radiometer measured the spectrum of a 17.5° tilted white ceramic tile. The tile was tilted to eliminate specular reflection.

The three-channel Hanna radiometer was powered by batteries, allowing completely independent operation. The hyperspectral radiometer was powered with a petrol-fueled 240 V single-phase portable electric generator.

8.4 The Airborne Multispectral Imaging System

Charles Sturt University's Airborne Video System (ABVS) used in this project consisted of four CCD[2] monochrome cameras, tightly mounted in a group of 2×2 on a steel frame. The characteristics of the ABVS system are given in Table 8.1. A narrow-band optical filter was affixed onto the lens of each camera, effectively creating a four-channel (blue, green, red and NIR) imaging system. The iris settings of the cameras were controlled by a mechanical device, ensuring all the cameras had the same iris during operation. An on-board PC computer, fitted with a four-input frame-grabber card, captured and digitized signal streams from the cameras into four 576×740 pixel[3] images. Image acquisition was synchronized by the frame-grabber card to ensure capture of the same scenes by all the cameras.

Two things are important to note about the ABVS imaging system:

[2]Charge Coupled Device.
[3]Pixel stands for picture element [*Holst*, 1998].

Table 8.1: Details of the ABVS airborne imaging system.

Component	Description
Camera type	COHU 4910, monochrome
CCD type	Interline transfer
CCD readout rate	50 Hz per field
CCD size	6.4 × 4.8 mm (1/2" format)
CCD active pixels	752 (H) × 582 (V)
Lens type	C mount
Lens focal length	12 mm
"Blue" optical filter	460 nm (centre); 25 nm (bandwidth)
"Green" optical filter	550 nm (centre); 25 nm (bandwidth)
"Red" optical filter	650 nm (centre); 25 nm (bandwidth)
"NIR" optical filter	770 nm (centre); 25 nm (bandwidth)
Frame-grabber	Up to four inputs simultaneous, 8 bits per input

- Since its cameras used interline CCD sensors, odd and even rows of the acquired images held physically displaced features of the scene in the same image columns. This effect is caused by the interline technique for reading out a CCD sensor when the scene is not static. First, the "odd" frame (odd rows of the CCD array) is read, then the "even" frame (even rows of the CCD array). Since the scene is moving, the two image frames contain different parts of the scene, and the resultant image (made out of the odd and even frame) displays artificial ragged features. This effect in the electronic imaging technology is known as the *comb* effect.

  The ABVS cameras were positioned sideways with respect to the flight direction, so that the comb effect would be most pronounced along-track. Having a strong across-track comb effect would lead to potential overlap of the acquired scene in the odd and even rows of an image.

- Because the ABVS cameras and the frame grabber were analog, the number of pixels captured by the frame grabber was slightly different from the number of active (i.e. useable) pixels in the CCD sensors (Ta-

ble 8.1). To better understand the reason for this, we will explain the process of transferring information from a CCD sensor in the camera to the computer's memory.

Odd or even frame readout from a CCD sensor is a sequence of electrical pulses, whose magnitude is proportional to the amount of light impinging on the sensor. This signal stream is converted to an analog signal in the camera, embedded into a standard video signal (CCIR[4] in our case), and then sent out. A frame grabber, at the other end of the cable, receives this analog signal and, recognizing the same standard video signal, picks out only those parts which contain the information related to the CCD pixels. This information is in forms of "lines", each line being the analog representation of the information captured by a row of pixels in the CCD. This analog line signal is then digitized by the frame grabber and stored in memory. Depending on the frame (odd or even), and the time location within the analog stream from the camera, the row and column position of each, digitally recreated pixel in the image is determined. It is the mismatch in the sampling rates between the camera and the frame grabber that causes the difference in the number of original and recreated pixels.

In some literature [for example *Holst*, 1998], different terminology is used to emphasize the difference between a CCD pixel and a basic element of image information stored in computer memory. *Holst* [1998] uses the term *datel* for the latter, to emphasize it does not have anything to do with the CCD pixel. We will retain the more traditional term, pixel, in our presentation, noting that we are aware of the fundamental differences between the CCD and the image pixel.

[4]Comité Consultatif International des Radiocommunications.

8.4.1 ABVS Image File Format

The images captured by the four ABVS cameras were stored on the hard disk of the on-board PC. The image file format allowed storage of the complete multispectral scene in a single file, together with other information regarding airplane position, speed and settings of the ABVS cameras.

The first 128 bytes of the file belong to its header; the rest contains the image data itself in the *band interleaved by pixel* (BIP) format [*Campbell*, 1996] with one byte per ABVS band per pixel. Pixel data of the BIP format are stored sequentially: row 1, column 1, band 1; row 1, column 1, band 2; row 1, column 1, band 3; row 1, column 1, band 4; row 1, column 2, band 1, etc. The total file size is always the same: $128 + 4 \cdot (576 \times 740) = 1705088$ bytes.

The ABVS image header consists of 22 lines of text, delimited with the carriage return character. Each line belongs to one image header tag; not all of the tags were in use. Table 8.2 describes only the tags that we used in this study.

Table 8.2: Description of ABVS image header tags used in this study.

Tag	Description
aperture	Iris settings of the ABVS cameras
rows	Number of rows of each multispectral image
cols	Number of columns of each multispectral image
gps_altitude	Airplane's altitude in metres from the on-board GPS; standard accuracy
velocity	Airplane's velocity in knots from the on-board GPS
lens	Focal length (in mm) of the lenses mounted on the ABVS cameras
latitude	Airplane's latitude from the on-board GPS; standard accuracy
longitude	Airplane's longitude from the on-board GPS; standard accuracy
time	Time of image acquisition as Australian Eastern Time, sourced from the on-board GPS

8.4.2 ABVS Effective Ground Pixel Size

Although the physical size of a CCD pixel stays the same, depending on the distance between the sensor and the scene, the effective scene image pixel size may differ. It is a function of the optics (e.g. lens focal length) and imaging geometry (CCD sensor type, distance between the sensor and the scene, etc.). When imaging a moving scene, the effective image pixel size is influenced by the CCD sensor integration time (analogous to exposure time in traditional photography) as well. In such a case, the effective pixel size as defined by the optics and geometry represents only its instantaneous value.

To derive the formula for instantaneous effective ground pixel size of the ABVS system, we started from the equation relating the lens focal length (f) to the distance from the scene (in our case aeroplane's altitude, ALT) and the magnification ratio (m).

$$f = \frac{ALT}{1 + 1/m}. \tag{8.1}$$

Magnification ratio (m) is a measure of the relative size of visual image of the object in the physical world (l_o) to the size of the image (l_i) formed on the sensor located at the CCD sensor plane in the camera: $m = l_i/l_o$. Thus, the size of the object in the physical world whose image size is l_i is calculated from (8.1) to be:

$$l_o = l_i \left(\frac{ALT}{f} - 1 \right). \tag{8.2}$$

If, instead of an object, the width (w) and the height (h) of a CCD sensor for l_i in (8.2) is used, the instantaneous effective size of the CCD sensor projected

onto the scene is:

$$\begin{aligned} W &= w\left(\frac{ALT}{f} - 1\right) \text{ instantaneous sensor scene width} \\ H &= h\left(\frac{ALT}{f} - 1\right) \text{ instantaneous sensor scene height} \end{aligned} \tag{8.3}$$

By dividing W and H with the number of rows and columns of an image (not CCD active pixels; see Section 8.4 for discussion), we obtain the instantaneous effective scene image pixel size along and across track:

$$\begin{aligned} l &= \frac{w}{740}\left(\frac{ALT}{f} - 1\right) \text{ along-track} \\ c &= \frac{h}{576}\left(\frac{ALT}{f} - 1\right) \text{ across-track} \end{aligned} \tag{8.4}$$

As can be seen from (8.4), for a given airborne imaging system, the ground resolution (effective pixel size) is affected by altitude only. Table 8.3 shows the calculated effective along- and across-track pixel sizes using the formula from (8.4) for the ABVS system for a range of typical aeroplane altitudes.

Table 8.3: ABVS along and across track instantaneous effective scene image pixel sizes from (8.4). Focal length f=12 mm; CCD sensor width w=6.4 mm; CCD sensor height h=4.8 mm. Altitude and pixel sizes are in metres.

Altitude	250	500	1000	1250	1500	2000
along-track	0.18	0.36	0.72	0.90	1.08	1.44
across-track	0.17	0.35	0.69	0.87	1.04	1.39

8.5 Reflectance Measurements of Calibration Targets

The ABVS readout was not calibrated, i.e. there was no known relationship between pixel digital numbers (DNs) and radiance or at-camera reflectance. Therefore, to allow easier conversion of pixel digital numbers (DNs) to ground

reflectance values we used two $6 \times 6\,\mathrm{m}^2$ canvases supplied to us by the ABVS imaging team. The canvases were located near a group of test plots (for more details see Section 8.2), so were not available for imaging all the time. However, we assumed this would not seriously affect the accuracy of the images, provided that the canvases were imaged regularly during the campaign.

In the absence of a proper field spectrometer which would allow characterization of the canvases during the imaging campaign, an *ad hoc* canvas reflectance measurement experiment was set up using the available equipment. A $105 \times 85\,\mathrm{mm}^2$ wide and 50 mm high aluminium box with an open bottom was housing our reflectance measurement probe. The probe was a multi-fibre optic cable, of which the middle fibre was used for feeding light into the aluminium box. The light was generated by a halogen bulb, specifically designed for fibre optic output. The outer fibres of the cable were used to collect reflected light and channel it to a Zeiss MMS-1 spectrometer (Section 8.3). Thus this system featured a direct illumination and viewing geometry (in some literature it is referred to as a $0\,°/0\,°$ system). The canvas reflectance measurement system was calibrated with four diffuse reflectance standards of nominal 2, 50, 75 and 99% reflectance. The standards were manufactured from Spectralon by Labsphere Inc., North Sutton, NH (part number: RSS-04-010).

The measurement procedure was as follows:

1. The halogen light source was switched on and left to warm-up thirty minutes before any measurement.

2. Due to the large size of the canvases, their spectral reflectance was measured at ten locations, approximately equally spaced from each other on the canvases.

3. The spectrum measurement at each canvas location consisted of:

   (a) Dark current measurements (no light; system "noise" only) before and after every spectrum measurement.

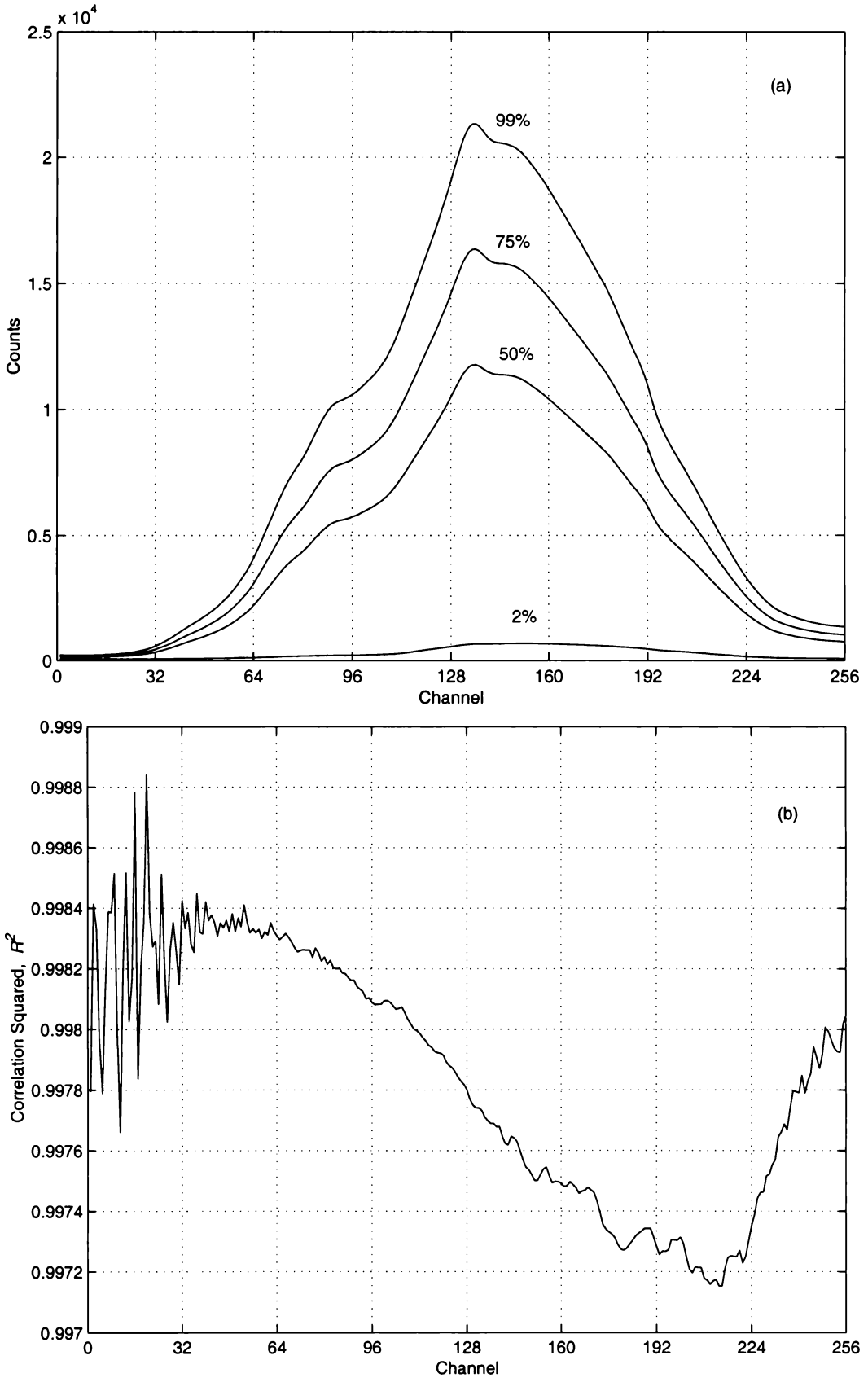

Figure 8.1: Calibration curves for the four reflectance standards (a). Correlation coefficients squared (b) display very small variation, showing that the relationship between spectrometer's digital counts and reflectance is almost perfectly linear.

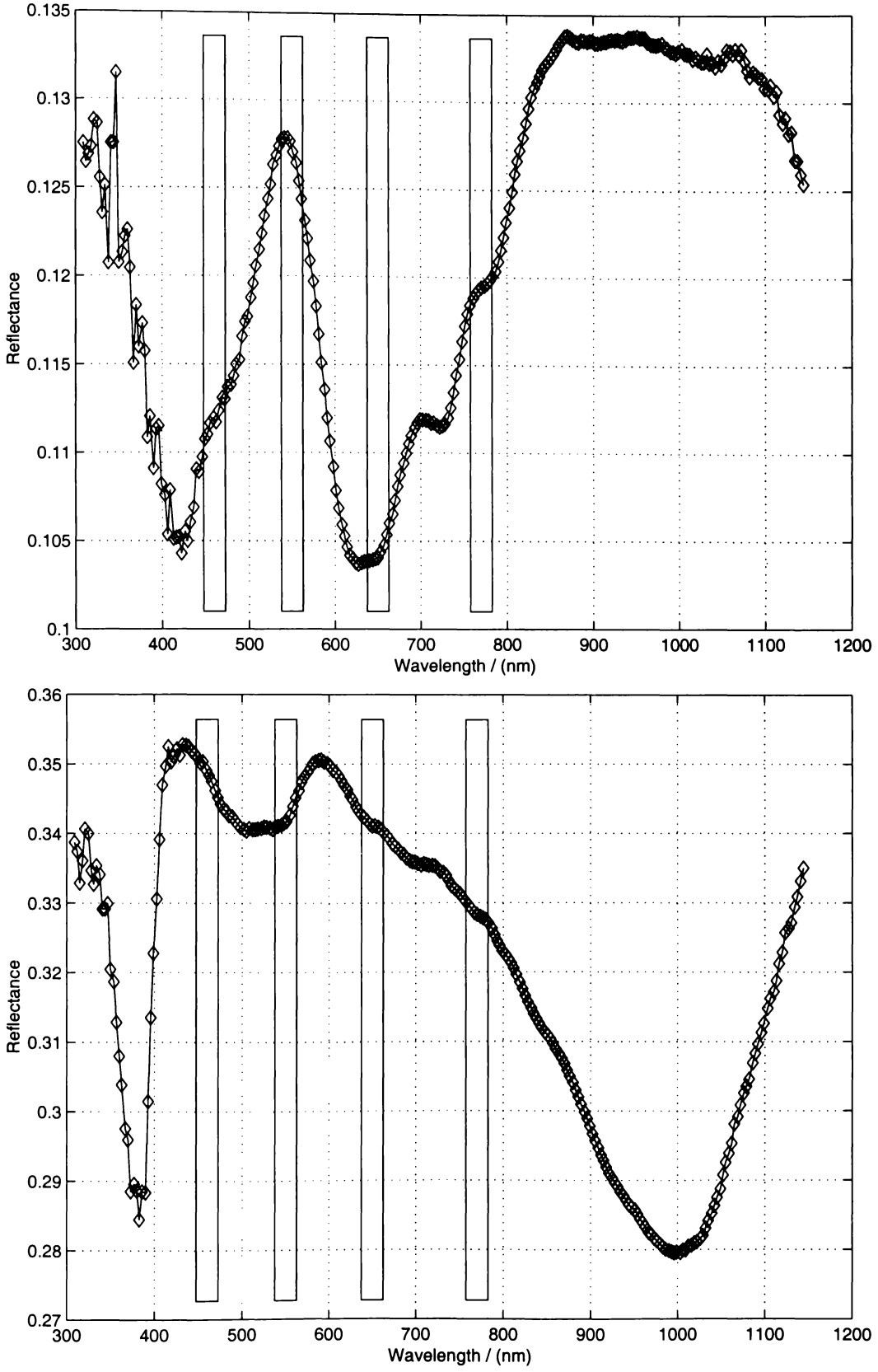

Figure 8.2: Reflectance curves of two ground calibration canvases, Federation Green (top) and Dove Gray (bottom), as measured by our *ad hoc* spectral measurement system. The displayed curves are averages of the results from ten different locations on each canvas. The boxed regions show the spectral positions and widths of the four channels of the ABVS imaging system.

(b) Calibration with the reflectance standards.

(c) Integration time of the Zeiss spectrometer was 100 ms. It was chosen to avoid saturation for the highest reflectance calibration standard, but also to exploit the full dynamic range of the spectrometer.

(d) Output spectrum from the spectrometer was an average of ten consecutive measurements (1 s measurement time in total).

Processing the spectra of the reflectance standards calibrated the output from the spectrometer (in digital counts). The calibration curves are shown in Figure 8.1, together with the plot of squared correlation coefficients (R^2) for 256 channels (i.e. wavelengths) of the spectrometer's output. The values of R^2 were in the range 0.997–0.999, confirming that we could use a simple linear function to convert digital counts to reflectance. The coefficients of variation for the four reflectance standard spectra curves are given in Appendix C.3.

Once the relationship between the spectrometer's output and reflectance was determined (Figure 8.1), the reflectance curves of the two canvases were readily obtained using linear interpolation for each spectrometer's channel. The reflectance curves of the two canvases—'Federation Green' and 'Dove Gray'—are shown in Figure 8.2. The coefficients of variation of the reflectance curves for the two canvases are given in Appendix C.3.

Knowing the reflectance of the two canvases allowed us to calculate their channel-equivalent reflectance for the ABVS system. Due to the lack of information on the spectral properties of the ABVS optical filters, we could not perform the proper calculation—an integral convolution of the canvas reflectance and optical filter transmission curves. Thus the channel-equivalent reflectance was computed as an average of the canvas reflectance values within the bandwidth of the four ABVS channels. The results are given in Table 8.4.

Table 8.4: ABVS-equivalent reflectance (ρ) of the two canvases: Federation Green and Dove Gray. They were calculated by averaging the canvas reflectance values within the bandwidth of each ABVS channels. The standard deviation and the number of values used to derive each average are also given.

ABVS	'Federation Green'		'Dove Gray'		Num.
Channel	ρ	std. dev.	ρ	std. dev.	of values
Blue	0.112	8.5×10^{-4}	0.348	2.1×10^{-3}	8
Green	0.127	1.3×10^{-3}	0.342	1.5×10^{-3}	8
Red	0.104	5.5×10^{-4}	0.341	6.1×10^{-4}	7
NIR	0.119	3.4×10^{-4}	0.328	7.3×10^{-4}	7

Chapter 9

Post-Processing of the Test Plots Multispectral Images

Post-processing of the multispectral images of the AgResearch and Dexcel pasture test plots involves:

- Geometrical correction (removal of the comb effect (Section 8.4)) from the images.
- Radiometric correction of the images due to the camera CCD sensor and lens imperfections, if required.
- Extraction of pasture test plot data from the images.
- Conversion of test plot pixel DN values to reflectance using two ground calibration targets (Section 8.5).
- BRDF correction (Section 7.3.3) of image reflectances, if required.

The goal of these procedures is to minimize the influence of measurement imperfections on the final set of test pasture plot reflectances.

9.1 Removal of the Comb Effect

We discussed this effect and explained its cause in Section 8.4. The comb effect is especially significant at low altitudes, and hence high-resolution imaging, as the ground misalignment between the odd and even frame in an image can be as large as several pixels. Since there were only 31 images (of which 19 were of higher resolution), we decided to perform a manual comb-effect correction. To make this and several other post-processing tasks easier we created a graphical user interface (GUI) using MATLAB (The MathWorks Inc., Nattick, Massachusetts).

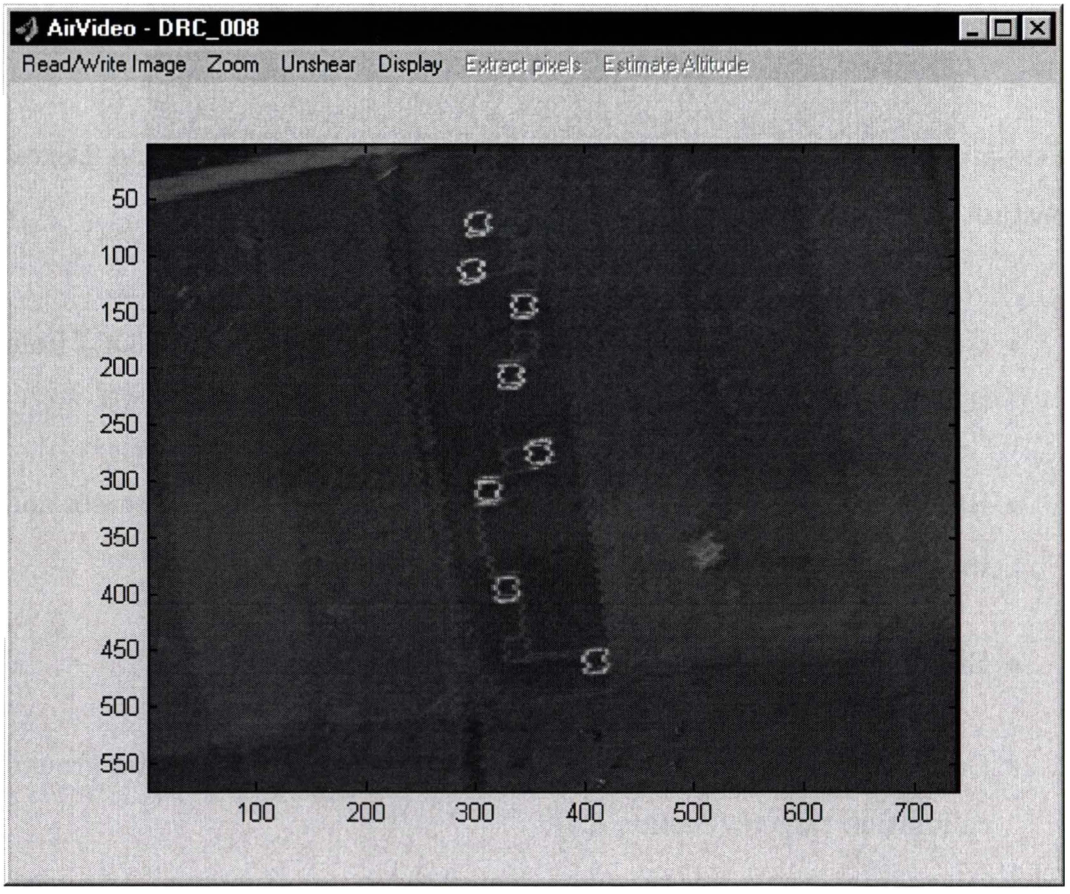

Figure 9.1: Graphical user interface for some of the post-processing tasks. The loaded image in the GUI is DRC_008, showing AgResearch test plots P30–P37 on the Dexcel's experimental paddock A5 near Hamilton. The comb effect is quite pronounced, causing jagged edges of the plots and the road in the middle of the image.

The GUI, with one of the images loaded, is shown in Figure 9.1. It allowed simple manipulation of the images, such as zooming, displaying false-colour images with different colour schemes, comb effect correction, etc.

Geometrical correction (comb effect removal) of the loaded image started with a selection of a region of interest (ROI). The purpose of a ROI was to provide more detail during this process. The GUI was designed in such a way as to prevent any other post-processing task if the geometrical correction was not performed first. The selected ROI is shown in Figure 9.2.

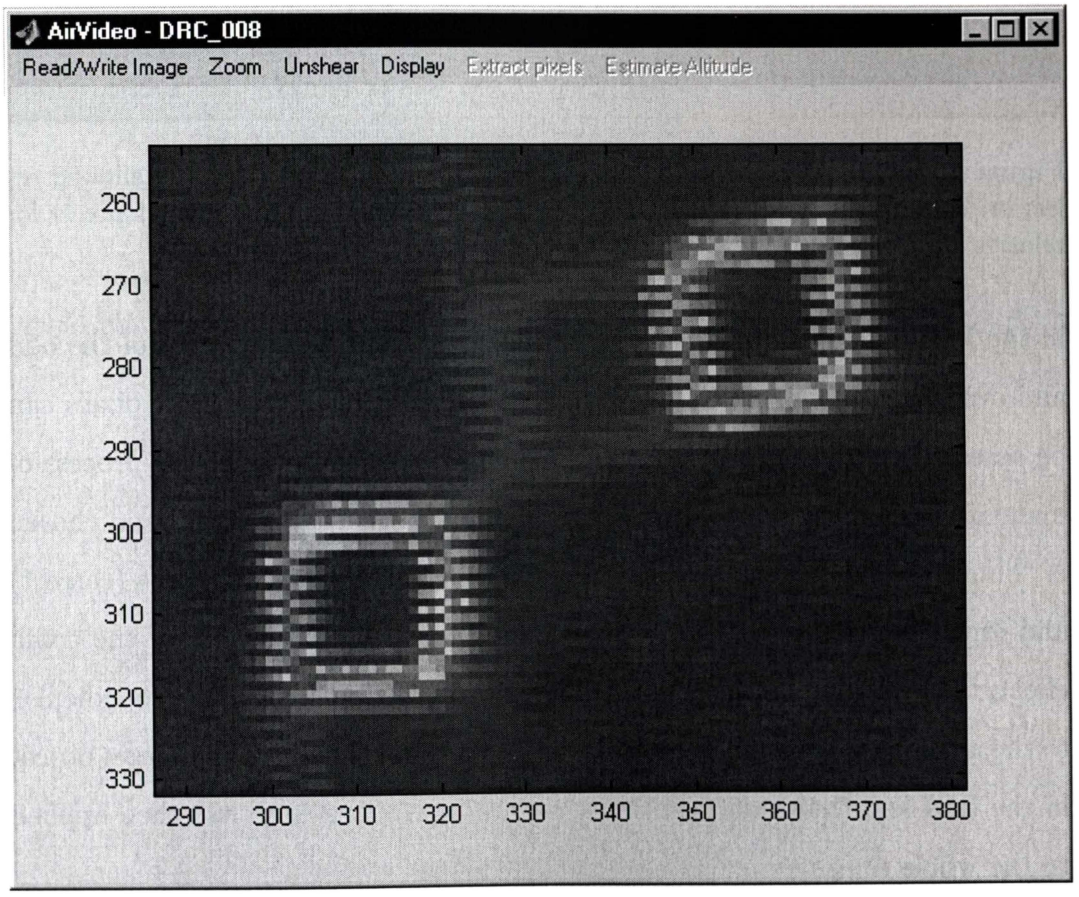

Figure 9.2: The selected ROI for geometrical correction of the DRC_008 image. Test plots P32 (left) and P33 (right) are within the ROI.

Geometrical correction was controlled with another GUI (Figure 9.3), which allowed user selection of different bands and pixel shifts of the ROI. By selecting different ABVS band images the user could find a band with the best contrast between the object selected as a target for comb removal and the surroundings

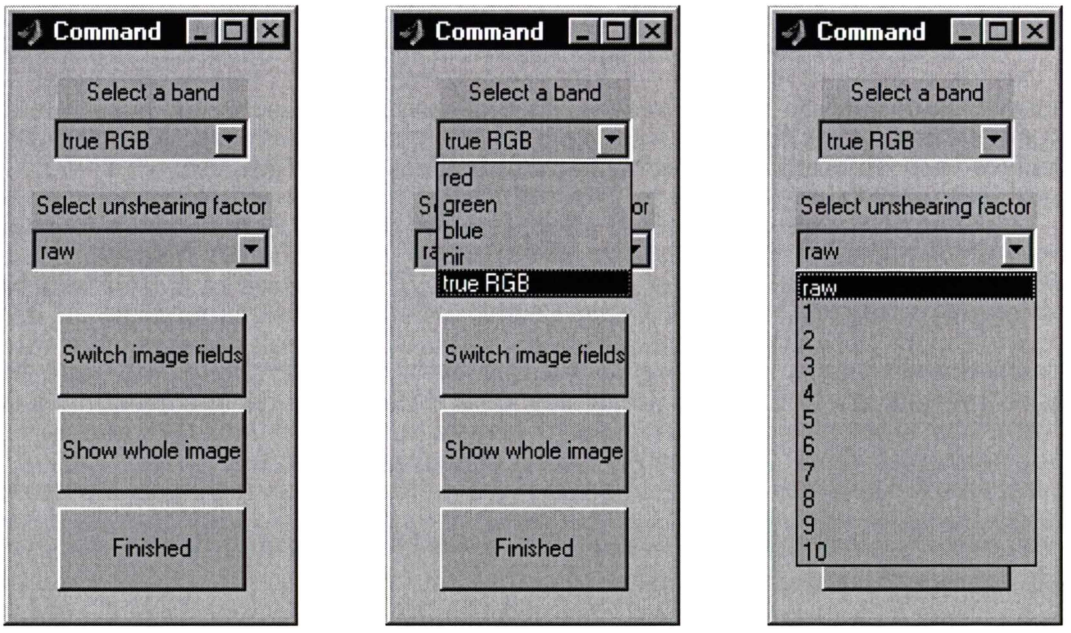

Figure 9.3: The GUI controlling the geometrical correction (left). It allowed selection of different bands for ROI display (middle), and the number of pixels for relative shift of the odd and even frames of the ROI (right).

in the ROI; our default object was hay wrap. Then, the alignment of the odd and even frames of the ROI for a different number of relative shift pixels can be assessed using the target object in the ROI. An example of the process of manual comb effect removal is shown in Figure 9.4. The ABVS band chosen is "blue"; the ROI for three different relative pixel shifts—two, three (correct) and four—is displayed in successive images. Due to the nature of the comb effect, the best target objects for geometrical correction are those perpendicular to the airplane's direction of motion. The pixel shift for which the target object in the ROI had the smoothest, most natural appearing edge was then applied to the whole image.

The DRC_008 image was selected also as an example of a problem discovered while performing geometrical correction. We observed by accident that the ROI alignment of some of the images could be greatly enhanced if the odd and even frames were switched. DRC_008 was one of the affected images, along with the DRC_006, DRC_007, DRC_009, DRC_011 and DRC_014. Switching the odd and even frames failed to remedy only the DRC_006 image; the shift of

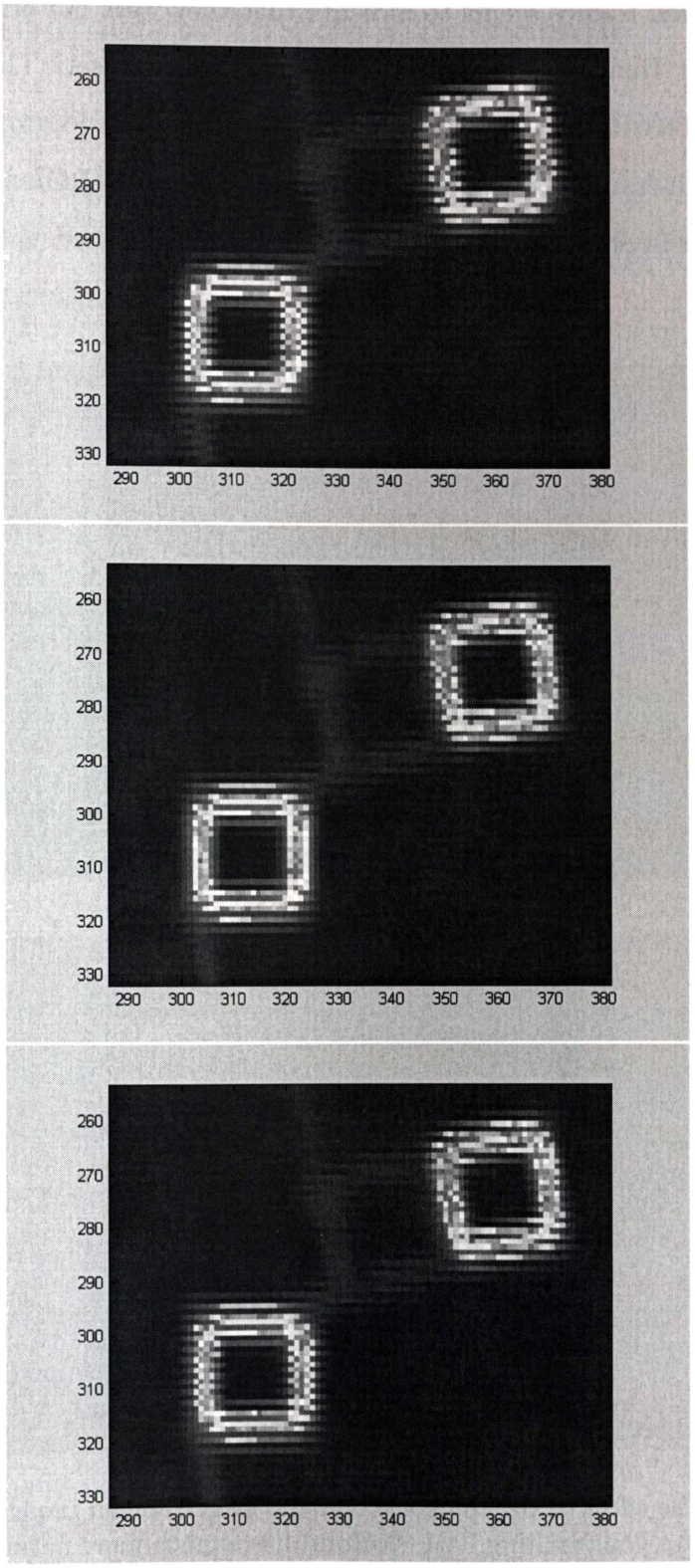

Figure 9.4: Three different relative shifts of the ROI odd and even frames: two (top), three (middle) and four pixels (bottom). A three-pixel shift gives the best odd-even-frame alignment of the ROI, and hence the whole image (DRC_008 in this case). The ROI is displayed in the "blue" ABVS band.

its odd and even frames seems to indicate that they were not acquired successively in time. Hence we discarded this image from the set. The three-pixels shifted DRC_008 ROI from Figure 9.4 is shown again in Figure 9.5, together with its switch-frame version. The improvement in the ROI appearance for the latter case is obvious.

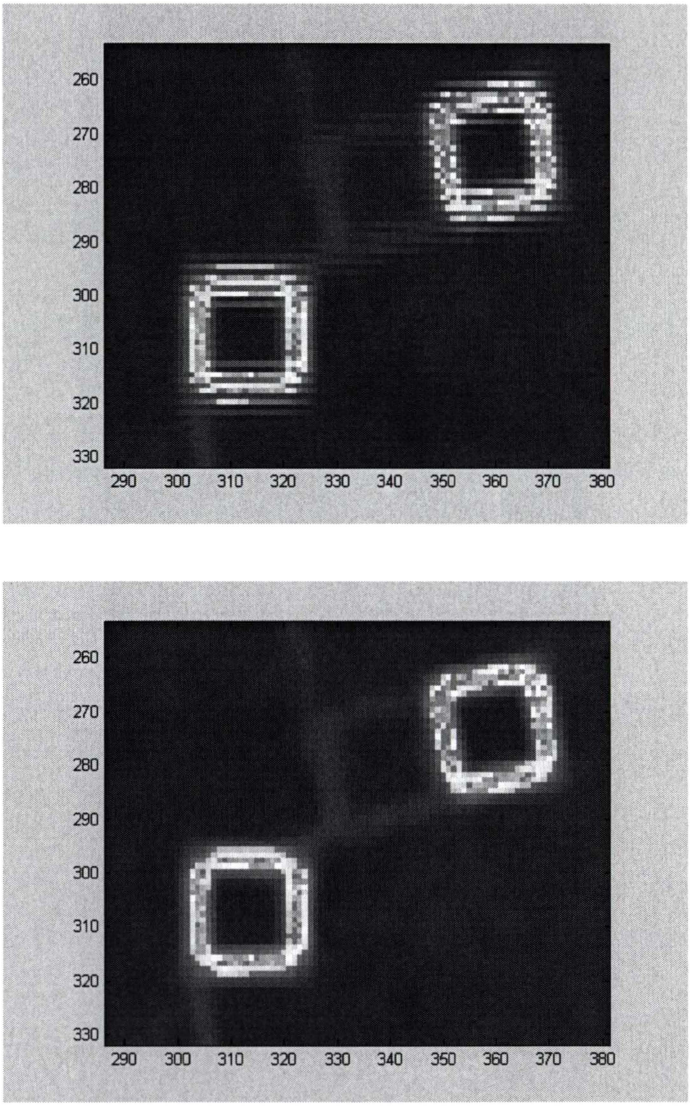

Figure 9.5: The effect of switching the odd and even frame in the DRC_008 ROI of Figure 9.4 (top). The resulting ROI (bottom) has a much more natural appearance. Both ROIs feature a three-pixel shift between the frames.

9.2 Radiometric Image Correction

This type of correction attempts to compensate for all the imperfections of a real optical imaging system with the goal of creating a uniform output across the whole image for uniform illumination of the imaging system. These imperfections generally fall into four categories:

1. Exposure fall-off
2. Lens system imperfections
3. Pixel response nonuniformity (PRNU)
4. Fixed pattern noise (FPN) of the CCD sensor

Exposure fall-off is purely associated with the laws of radiation transfer, thus affecting even an ideal optical imaging system. Any pixel off the centre of the CCD sensor observes less radiation than its central counterpart. The theoretical formula for exposure fall-off is [*Lillesand and Kiefer*, 1994]:

$$I_\theta = I_0 \cos^4 \theta, \tag{9.1}$$

where θ is the angle between the optical axis and the ray to the off-axis pixel, I_θ is the radiance at the off-axis pixel, and I_0 is the radiance along the optical axis, i.e. at the central pixel.

Since the other three categories cannot be easily modelled, and all four act in unison, the standard practice is to acquire a series of images of a uniformly illuminated surface. A correction for every pixel is obtained by requiring that all image pixels (as opposed to CCD sensor's pixels; see Section 8.4 for the difference) have the same output.

Unfortunately, we could not obtain this type of information for the ABVS imaging system. Discussions with the ABVS imaging team's leader, Dr. David Lamb, led to an alternative approach. A "typical" image for each of the ABVS channels was formed by averaging all the available images. The typical

images, shown in Appendix C.4.1, were then heavily smoothed and the result was taken as the radiometric correction for that particular ABVS channel. There were two choices for a smoothing technique: low-pass or median filtering. We decided to test both and choose the one that according to our subjective evaluation performed the task best.

The low-pass filter was designed as a two-dimensional, circularly-symmetric ideal filter with a cut-off normalized frequency of 0.025 (normalized frequency of 1 corresponds to half the sampling frequency). The desired frequency response is shown in Figure C.5 (Appendix C.4.2). The low-pass filter was implemented as a finite impulse response (FIR) filter. Such filters have several characteristics that make them very suitable for image processing applications:

- FIR filters are easy to represent as matrices of coefficients.
- FIR filter coefficients are real numbers, and are thus easy to implement.
- FIR filters can be designed to have linear phase, which helps prevent distortion.
- There are several well-known, reliable methods for FIR filter design [*Lim*, 1990].

The FIR filter was designed using the frequency sampling method [*Lim*, 1990, chap. 4] which adjusts the coefficients of the filter so that its frequency response follows the desired response as closely as possible in the least square sense. The frequency response of the two-dimensional FIR filter is shown in Figure C.5 also. It is impossible to discern any difference between the desired and resulting frequency responses due to the very small cut-off frequency. We chose this cut-off frequency as it was the largest for which we could not observe ground features, such as hay wrap, buildings or roads, in the "typical" ABVS band images (Appendix C.4.1).

The low-pass filtered "typical" ABVS band images are shown in Appendix C.4.2. Ground features are still slightly noticeable in the filtered blue band

image. All the four filtered images featured a steep drop in intensity around the edges, a well-known effect of finite image dimensions on filtering.

Median filtering was performed by finding a median value of a 41×49 pixel window which was "sliding" across every pixel of the "typical" ABVS band images. This window size was chosen as optimal for this operation after experimenting with different window sizes. The task was to find a window size that removed as much of the ground features as possible, and yet was not to big to result in coarse output. The resulting median-filtered "typical" images are shown in Appendix C.4.3. Ground features, especially house roofs, are quite pronounced, though strongly blurred, in all the filtered images except the NIR band image.

Comparing the low-pass and median filtered "typical" band images, we concluded that the low-pass filtering operation was much more successful in removing ground features than the median filtering. Hence, we decided to use the low-pass filtered images as the base for our radiometric correction. However, we note its following deficiencies:

- The "typical" surface was far from uniformly illuminated. Even after averaging, ground features were strongly visible in the "typical" band images.
- Our correction does not take into account pixel dark current output.
- Strong low-pass filtering has certainly removed the effect of the PRNU- and FPN-type effects from the correction images.

Radiometric correction coefficients for every pixel of the four ABVS cameras were calculated using the following formula:

$$p' = \frac{\bar{c}_{16\times16}}{p_f} \cdot p, \tag{9.2}$$

where p' is the corrected pixel value, $\bar{c}_{16\times16}$ the average value of 16×16 central pixels of the filtered image, p_f the pixel value of the low-pass filtered "typical" image, and p the actual pixel value.

9.3 Extraction of Test Plot Data from Images

Extraction of pixel values of the pasture test plots from the multispectral ABVS images was done using the same graphical user interface (GUI) as for the comb removal (Figure 9.1). The process was initiated by loading a geometrically (Section 9.1) and radiometrically corrected (Section 9.2) multispectral image, and selecting a test plot from which pixel values were to be extracted. A test plot was selected using the same region of interest (ROI) selection tool as for the comb removal.

Because the test plot boundaries were not ideally aligned with image rows and columns (causing some image pixels to only partially view test plot areas), the selection of image pixels from which data would be extracted was manual. The user selected pixels within the test plot with a mouse, by clicking at points which defined the corners of a polygon. This approach allowed maximal flexibility to avoid pixels "contaminated" with hay wrap. Every pixel within the polygon was considered selected. An example is shown in Figure 9.6.

A right-click on the mouse signalled the end of polygon selection, and invoked another GUI which presented the multispectral data extracted from the polygon pixels. The exact location of the harvesting subplots within each test plot could not be recorded, so we decided to use all the polygon pixels and average their values for each ABVS band. The pixel data corresponding to the plot DRC16 from the DRC_011 image (Figure 9.6) is shown in Figure 9.7. The data was reported using histograms for every ABVS band. Corresponding band average pixel values were indicated in the corresponding histograms. The user had an option of choosing or rejecting the reported data, in case it did not appear "normal". If accepted, the average pixel value and its standard error of the mean were recorded. This procedure was repeated for every test plot in every processed ABVS image. Once finished, all the test plot pixel data was collated according to which test plot it belonged.

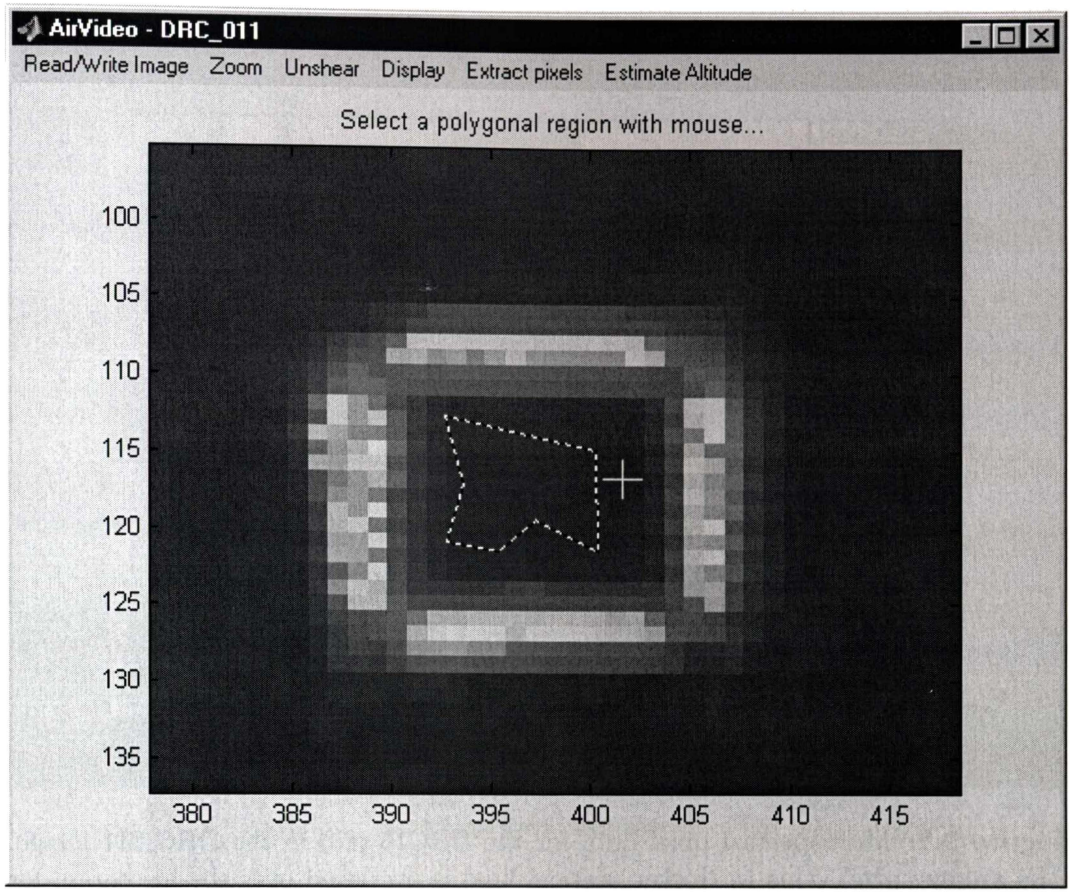

Figure 9.6: The GUI for selection of pixels within a test plot. The image is DRC_011; the test plot is DRC16. The broken line defines the pixel selection polygon. The fuzzy, bright square object in the GUI is the hay wrap.

Pixel data in the near-infrared ABVS band had a much larger variation when compared with the data of the other three bands in the vast majority of cases. For the example in Figure 9.7, standard errors of the mean for the blue, green and red ABVS bands were 1.3, 1.4 and 1, respectively; the corresponding value for the NIR band was 22.

Histograms of average band pixel values and standard errors of the means for the four ABVS bands is shown in Figure 9.8. The average band pixel values of the visible ABVS bands were all below 100, whereas the NIR pixel values were greater than 100. The red band average pixel values exhibited comparatively smaller variation than the blue and green average pixel values. The spread of the NIR average pixel values was much more prominent (from

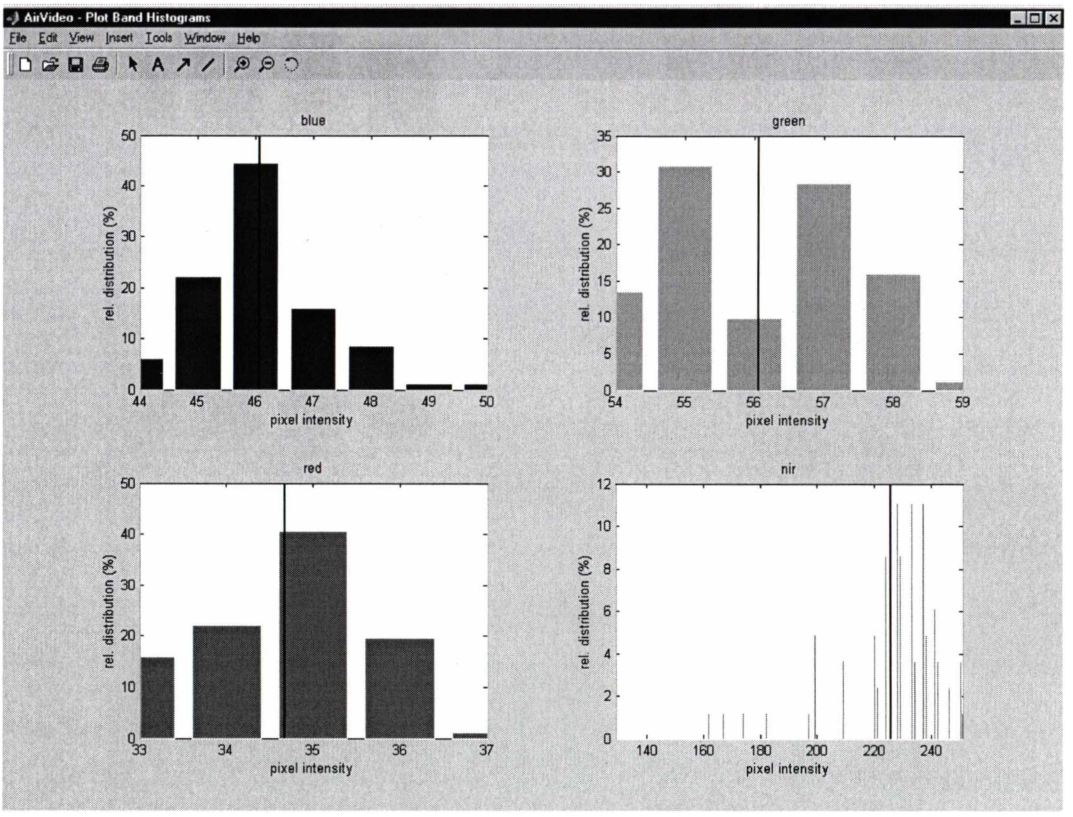

Figure 9.7: Multispectral pixel data for the DRC16 plot in the DRC_011 image. The average pixel value (a thicker vertical line) is overlayed over the histogram for each ABVS band.

about 100 and up), but they were mainly located above 150. The histogram of standard errors of the mean clearly shows the extent of the variation of the values in the NIR band. The smallest NIR standard error value was 3, and the largest was 44.7. Except for a "hump" in the NIR histogram between 30 and 40, standard errors of the mean appear almost equally distributed across the whole range.

9.4 Conversion of Pixel Values to Reflectance

The average band pixel values of the test plots were converted to reflectance using the two canvases (Section 8.5). Since their reflectance was measured, a relationship to the average band pixel values of the canvases could be easily established. As we used two canvases, the conversion involved a simple linear

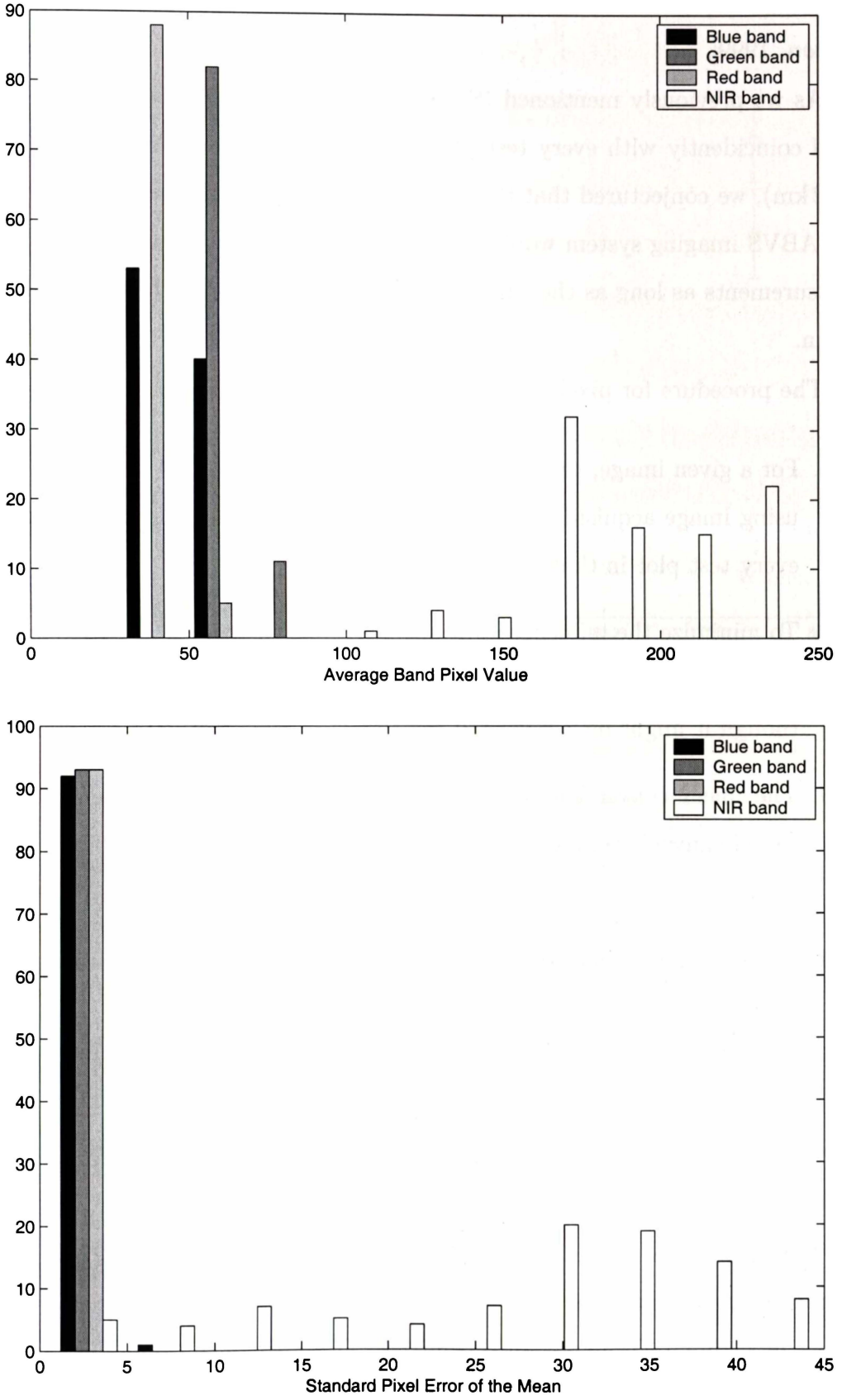

Figure 9.8: Average band pixel values (top) and their standard errors of the mean (bottom) for the four ABVS bands. The data presented in the histograms is from all the test plots and images.

equation. This method is known as the *empirical line method* [*Smith and Milton*, 1999].

As we previously mentioned (Section 8.2), the canvases could not be imaged coincidently with every test plot. Since the plots were reasonably close ($\sim 2\,\text{km}$), we conjectured that the changes in the intervening atmosphere and the ABVS imaging system would not significantly influence the quality of the measurements as long as the canvases were regularly imaged during the campaign.

The procedure for pixel conversion was as follows:

1. For a given image, the nearest observations for both canvases was found using image acquisition times. These canvas observations were used for every test plot in that image.

2. To minimize the influence of atmospheric and instrumental change, canvas data derived from the same image was used preferentially, even though it might have not been the closest in time to the test plot data.

3. The linear conversion equations for each ABVS band between the selected canvas' average band pixel values and their reflectance were constructed.

4. The conversion equations were then applied to the test plot average pixel values.

5. This process was repeated for every test plot in every image.

The largest time difference between test plot and canvas data used for conversion was 21 minutes.

To illustrate the results obtained, we present graphs of ABVS-equivalent reflectance for two test plots, DRC1 and P40, in Figure 9.9. Different reflectance values in Figure 9.9 were obtained using test plot pixel data from different images. The error bars are located at a 95% confidence interval, calculated using

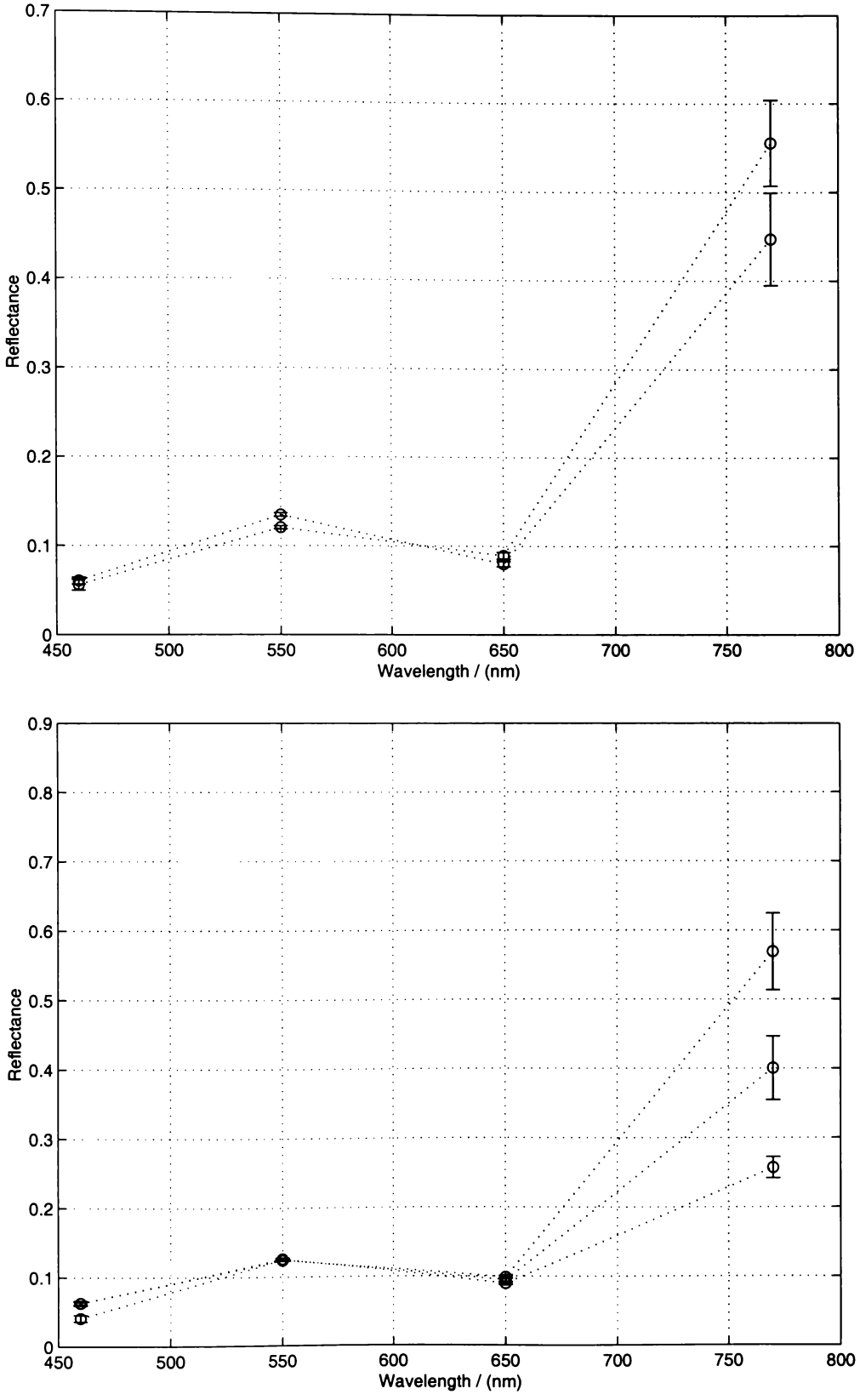

Figure 9.9: ABVS-equivalent reflectance of the DRC1 (top) and P40 (bottom) plots as calculated by our conversion procedure (Section 9.4). Different reflectance values are from different images. Uncertainty in calculating reflectance (error bar plots) represents 95% confidence interval, and was calculated using the standard error of the mean values. The biggest discrepancy is in the NIR band.

the accompanying standard error of the mean data. The NIR reflectance derived from different images exhibited large variation, unlike the visible band reflectance. The large variation of NIR reflectance was probably caused by a BRDF (Section 7.3.3) effect since the test plots images encompassed a variety of different viewing angles.

9.5 BRDF Correction of Test Plot Reflectance

Test plot reflectance data was corrected for a BRDF effect using the WAK model introduced in Section 7.3.3 and the technique described in *Shepherd and Dymond* [1999]. Their procedure for the derivation of WAK model parameters used AVHRR-measured channel-1 and -2 radiance of the same area from consecutive satellite passes. By combining different measurements of the same vegetation area, *Shepherd and Dymond* constructed a set of equations involving the WAK model and its three unknown parameters. The parameters were then determined using a nonlinear optimization procedure which minimized the difference between the AVHRR-measured and WAK-predicted vegetation reflectance.

As in the AVHRR set of *Shepherd and Dymond* [1999], our ABVS set of images also included observations of test plots viewed from different directions and with various relative positions to the sunlight. The imaging campaign lasted about two hours, so the changes in the vegetation were negligible. To increase the number of cases for the calculation of the WAK model parameters, the vegetation type of the test plots was assumed to be the same. Hence only one set of the WAK model parameters (w, a and k) needed to be derived. Since the method of *Shepherd and Dymond* [1999] required at least two observations of the same test plot, this reduced the number of cases to 46 (out of 93) from 18 (out of 65) test plots.

Derivation of the WAK model parameters requires reflectance from a visible and an NIR band [*Shepherd and Dymond*, 1999]. For our case, we selected the

ABVS green and NIR bands as the most similar to the AVHRR channels 1 and 2 (Section 2.2) used by *Shepherd and Dymond*. For every pair of observations of a test plot, there are two equations—one for the visible and one for the NIR band—which are minimized in the least square sense [*Shepherd and Dymond*, 1999]. The equation for the visible band is:

$$\frac{\cos\theta_{i_l} + \cos\theta_{e_l}}{\cos\theta_{i_m} + \cos\theta_{e_m}} \left[\frac{a + (\pi - a)e^{-k\alpha_m^2}}{a + (\pi - a)e^{-k\alpha_l^2}} \right] - \frac{\rho_m}{\rho_l} = \mathcal{R}, \tag{9.3}$$

where the subscripts l and m denote different observations of the same test plot; the subscripts i and e denote incident and exitant angles, and α is the phase angle (for a more detailed description see Section 7.3.3). $\mathcal{R}$ represents the fitting residual of (9.3). The equation for the NIR band is slightly more complex:

$$\frac{\cos\theta_{i_l} + \cos\theta_{e_l}}{\cos\theta_{i_m} + \cos\theta_{e_m}} \left[\frac{\frac{8}{3\pi}(a + (\pi - a)e^{-k\alpha_m^2}) + H(\theta_{i_m}, w)\, H(\theta_{e_m}, w) - 1}{\frac{8}{3\pi}(a + (\pi - a)e^{-k\alpha_l^2}) + H(\theta_{i_l}, w)\, H(\theta_{e_l}, w) - 1} \right] - \frac{\rho_m}{\rho_l} = \mathcal{R}. \tag{9.4}$$

The main difference between (9.3) and (9.4) is the presence of the w WAK model parameter in the latter.

Since every pair of observations of a test plot generated one (9.3) and (9.4), the number of visible and NIR band equations was 40. For the test plots for which more than two observations existed, we wrote a pair of (9.3) and (9.4) for all the possible combinations. For example, four observations (P44–P47 test plots) yielded six pairs of (9.3) and (9.4) equations.

The incidence angles (solar zenith angles) θ_i in (9.3) and (9.4) were calculated using the algorithm of *Michalsky* [1988]. The exitance angles θ_e were calculated from the ABVS images using the distance of the centre of the test plot to the centre pixel of the image for the nominal airplane altitude of 1000 ft (304.8 m) during the imaging campaign. The calculation of the incidence and

exitance angles did not take into account any topographic effects since the test plots were located on almost perfectly flat land.

The minimum for the visible band equations (9.3) was obtained with the values of a=1.47 and k=1.17. In the case of the NIR band equations (9.4), the minimum was attained for w=0.16, a=1.7 and k=2.53. Using the obtained WAK model parameters, the test plot reflectance was corrected to the standard geometry of nadir view and 45 ° solar zenith angle as per (7.4) (Section 7.3.3).

The WAK BRDF correction was applied to all the test plot observations, 93 in total. Since the WAK parameters were determined by a fitting procedure, the standardized reflectance of test plots with more than one observation was not the same for all the cases. Final values of BRDF-corrected reflectance in these cases were found by averaging. The range of reflectance differences for every ABVS band were: -0.02–0.03 for the blue band, -0.01–0.03 for the green band, -0.01–0.02 for the red band, and -0.08–0.07 for the NIR band. Again, the NIR reflectance showed the greatest variation of all the ABVS bands. This was also the case for the average band pixel values (Figure 9.8).

Chapter 10

Results and Discussion

After performing various corrections to the ABVS images of the test plots, we obtained three reflectance data sets: raw (before radiometric correction), radiometrically corrected (Section 9.2) and BRDF corrected (Section 9.5). The BRDF-corrected reflectance set was obtained from the radiometrically-corected test plot reflectance data.

The results of biomass prediction using the three reflectance data sets are presented in this chapter. The prediction was based on a selected set of vegetation indices (Section 7.3.4) and ABVS band reflectance data. The values of vegetation indices corresponding to the different ABVS image processing stages were calculated using the appropriate band reflectance data.

The vegetation index prediction model was a simple linear regression:

$$\text{Biomass} = slope \cdot x_{\text{Veg. Index}} + bias. \tag{10.1}$$

Equations involving ABVS band reflectance were derived using a multiple linear regression technique. The prediction results will be given for the complete, and AgResearch and Dexcel biomass data sets separately.

Along with the prediction equation coefficients, the P-statistic of the coefficients, root mean square error (RMSE) and adjusted squared correlation (R^2_{Adj}) will be reported for each prediction model. The P-statistic gives the

probability that the reported value of a coefficient was achieved purely by chance. The smaller the P-statistic, the higher the confidence in the reported value of a coefficient. Usually, the threshold for the P-statistic is set to be 0.05, i.e. 95% confidence. Since the standard squared correlation coefficient (R^2) is known to be influenced by the number of variables in the model (it increases when a variable is added to the model even if the variable is of no statistical importance), we decided to use its adjusted counterpart, R^2_{Adj}. This provides an unbiased estimate of the population of R^2 because it takes into account the number of variables in the regression equation.

Our choice of vegetation index formula did not include any which explicitly required use of the soil line data. None of our images contained a noticeable patch of bare soil from which we could try to deduce a soil line in the red-NIR reflectance graphs. Also, since practically complete soil cover is a feature of New Zealand pastures, we wanted to focus our study on only those vegetation indices which would best suit such conditions. Therefore, we selected the following vegetation indices: RVI (7.5), NDVI (7.6), IPVI (7.7), SAVI (7.10), MSAVI2 (7.13) and GEMI (7.14). In the case of the SAVI which depends on a vegetation-dependent parameter L, we will report only the results for the L that best predicts biomass.

10.1 Biomass Ground Truth Data

The test plot biomass data which was used as ground truth for our study is given in Table 10.1. Since the AgResearch plots (prefix "P") were harvested at five randomly-located sampling areas within each plot (labelled "A" through "E"; see Appendix C.2), the biomass of the whole plot was estimated by averaging the data of the five sampling areas. The 95% confidence interval for each AgResearch plot is also given in Table 10.1. The Dexcel plots were sampled only from one location, so the reported biomass was taken as absolutely accurate as no 95% confidence interval could have been calculated.

Table 10.1: The test plot biomass ground truth data. The biomass values for the AgResearch plots ("P" prefix) are averages of the five reported values in Appendix C.2 for each plot. Consequently, 95% confidence interval values for these plots are also reported. The biomass data is in the units of kgDM/ha.

Plot ID	Biomass	95% CI	Plot ID	Biomass	95% CI
P01	4106.8	357.29	P34	3415.6	1024.45
P02	3430.4	663.88	P35	2133.4	292.06
P03	2301.8	408.63	P36	1395.4	554.87
P04	2135	258.3	P37	1651.8	531.01
P05	1572.8	222.43	P40	2605.2	485.08
P06	1635.6	546.55	P41	3857.4	1650.64
P07	2666.4	376.23	P42	2367	602.42
P08	2638.6	348.67	P43	1658.6	514.26
P09	3318.8	455.79	P44	1435.6	408.41
P10	2759.4	678.51	P45	1820.6	288.12
P11	3120.4	301.27	P46	614.6	129.66
P12	2895.6	221.7	P47	567	147.69
P13	2251.8	554.04	DRC01	1628	
P14	1921.6	476.62	DRC02	1341	
P15	2552.8	326.43	DRC03	2397	
P16	2023	380.98	DRC04	1555	
P17	6209.4	624.5	DRC05	2788	
P18	5910.6	1089.74	DRC06	1395	
P19	3040.4	567.17	DRC07	2059	
P20	3869.8	503.98	DRC08	2491	
P21	3034.6	349.31	DRC09	2552	
P22	2393.6	328.49	DRC10	1646	
P23	2108.4	459.71	DRC11	3688	
P24	3574.4	656.31	DRC13	3999	
P25	5097.2	979.95	DRC14	4140	
P26	4830.2	1204.47	DRC15	3081	
P27	4654.6	672.83	DRC16	4082	
P28	1089	583.93	DRC17	4690	
P29	1296.4	395.86	DRC18	8447	
P30	5543.8	944.91	DRC19	3354	
P31	7639.4	1777.75	DRC20	1530	
P32	5280	1112.85	DRC21	2628	
P33	3635.2	1426.81			

There were 45 AgResearch and 20 Dexcel test plots, out of a total of 65 cases. The range of the combined biomass data set was 567–8447 kgDM/ha. The range of the AgResearch and Dexcel sets separately was 567–7639 kgDM/ha and 1341–8447 kgDM/ha, respectively. Their histograms are given in Figure C.10 of Appendix C.5. The Dexcel biomass set was slightly skewed towards lower values of biomass, featuring at the same time the largest biomass of the combined data set—8447 kgDM/ha from the DRC18 plot.

10.2 Biomass Prediction Using the Raw ABVS Reflectance

The plot matrix diagrams of the biomass and the raw ABVS band reflectance and vegetation indices for the three different sets considered are shown in Figures C.11 and C.12 (Appendix C.5).

10.2.1 Prediction of the Complete Biomass Data Set

The coefficients of the vegetation index prediction equation (10.1) and the accompanying statistics are given in Table 10.2. SAVI(0) refers to the SAVI

Table 10.2: Slope and bias values of the vegetation index prediction equations (10.1) for the complete biomass data set using the raw ABVS reflectance data. RMSE reported is in units of kgDM/ha. R^2_{Adj} is expressed as a percentage.

Vegetation	Bias		Slope			
Index	coeff.	P-value	coeff.	P-value	R^2_{Adj}	RMSE
RVI	1988.6	0.004	285.6	0.126	2.1	1550
NDVI	1197.4	0.171	3385	0.039	5.1	1526
IPVI	-2188	0.377	6770	0.039	5.1	1526
SAVI(0)	1197.4	0.171	3385	0.039	5.1	1526
MSAVI2	2024.7	0.002	2758	0.106	2.6	1547
GEMI	1058	0.377	2932	0.107	2.5	1547

index for $L = 0$ (7.10). The SAVI for that value of L gave the best prediction

of the biomass. We note that the SAVI for $L = 0$ is exactly the NDVI (7.6).

The best ABVS band reflectance prediction equation was:

$$\text{Biomass} = 5565 - 98318\,\text{B} + 30426\,\text{R} + 2008\,\text{NIR}, \tag{10.2}$$

The equation's RMSE was 1423 kgDM/ha, and R^2_{Adj}=17.5%. The P-statistic was the following: less than 0.001 for the constant term, 0.02 (B), 0.056 (R) and 0.353 (NIR). B, R and NIR represent the ABVS reflectance of the blue, red and near-infrared band, respectively.

10.2.2 Prediction of the AgResearch Biomass Data Set

The coefficients of the vegetation index prediction equation (10.1) and the accompanying statistics are given in Table 10.3.

Table 10.3: Slope and bias values of the vegetation index prediction equations (10.1) for the AgResearch biomass data set using the raw ABVS reflectance data. RMSE reported is in units of kgDM/ha. R^2_{Adj} is expressed as a percentage.

Vegetation	Bias		Slope			
Index	coeff.	P-value	coeff.	P-value	R^2_{Adj}	RMSE
RVI	483.7	0.508	765	0.001	21.3	1373
NDVI	49.1	0.957	5800	0.002	19	1393
IPVI	-5752	0.033	11602	0.002	19	1393
SAVI(0)	49.1	0.957	5800	0.002	19	1393
MSAVI2	1064	0.106	5825	0.003	16.8	1411
GEMI	-801	0.532	5906	0.004	15.5	1422

The best ABVS band reflectance prediction equation for this case was:

$$\text{Biomass} = 5542 - 97126\,\text{B} + 23529\,\text{R} + 4539\,\text{NIR}. \tag{10.3}$$

The equation's RMSE was 1307 kgDM/ha, and R^2_{Adj}=28.6%. The P-statistic of the equation coefficients was: <0.001 for the constant term, 0.017 (B), 0.236 (R) and 0.061 (NIR).

10.2.3 Prediction of the Dexcel Biomass Data Set

The coefficients of the vegetation index prediction equation (10.1) and the accompanying statistics are given in Table 10.4.

Table 10.4: Slope and bias values of the vegetation index prediction equations (10.1) for the Dexcel biomass data set using the raw ABVS reflectance data. RMSE reported is in units of kgDM/ha. R^2_{Adj} is expressed as a percentage.

Vegetation	Bias		Slope			
Index	coeff.	P-value	coeff.	P-value	R^2_{Adj}	RMSE
RVI	4909	0.002	-493.7	0.153	6	1600
NDVI	5132	0.032	-3766	0.334	0	1651
IPVI	8903	0.154	-7538	0.334	0	1651
SAVI(0)	5132	0.032	-3766	0.334	0	1651
MSAVI2	4791	0.002	-4739	0.183	4.6	1612
GEMI	6435	0.024	-5030	0.198	4	1618

The best ABVS band reflectance prediction equation for the Dexcel plots was:

$$\text{Biomass} = 4264 - 93516\,\text{B} + 45520\,\text{R} + 4539\,\text{NIR}. \tag{10.4}$$

The equation's RMSE was 1588 kgDM/ha, and R^2_{Adj}=7.5%. The P-statistic of the equation coefficients was: 0.083 for the constant term, 0.086 (B) and 0.138 (R).

10.3 Biomass Prediction Using the Radiometrically-Corrected ABVS Reflectance

The plot matrix diagrams of biomass, radiometrically-corrected ABVS band reflectance and vegetation indices for the three different sets considered are shown in Figures C.13 and C.14 in Appendix C.5.

10.3.1 Prediction of the Complete Biomass Data Set

The coefficients of the vegetation index prediction equation (10.1) and the accompanying regression fit statistics are given in Table 10.5.

Table 10.5: Slope and bias values of the vegetation index prediction equations (10.1) for the complete biomass data set using the radiometrically-corrected ABVS reflectance data. RMSE reported is in units of kgDM/ha. R^2_{Adj} is expressed as a percentage.

Vegetation	Bias		Slope			
Index	coeff.	P-value	coeff.	P-value	R^2_{Adj}	RMSE
RVI	2385	0.001	173.6	0.348	0	1568
NDVI	1773.5	0.033	2323	0.132	2	1551
IPVI	-550	0.813	4647	0.132	2	1551
SAVI(0)	1773.5	0.033	2323	0.132	2	1551
MSAVI2	2284	<0.001	2048	0.223	0.8	1561
GEMI	1525	0.192	2242	0.207	2.5	1559

The linear combination of the ABVS band reflectance which predicted the biomass set best was:

$$\text{Biomass} = 8902 - 77957\,\text{B} - 26783\,\text{G} + 24951\,\text{R}. \tag{10.5}$$

The equation's RMSE was 1403 kgDM/ha, and R^2_{Adj}=19.8%. The P-statistic was the following: less than 0.001 for the constant term, 0.02 (B), 0.143 (G) and 0.035 (R). B, G and R represent the ABVS reflectance of the blue, green and red band, respectively.

10.3.2 Prediction of the AgResearch Biomass Data Set

The coefficients of the vegetation index prediction equation (10.1) and the accompanying regression fit statistics are given in Table 10.6.

The linear combination of the ABVS band reflectance which predicted the

Table 10.6: Slope and bias values of the vegetation index prediction equations (10.1) for the AgResearch biomass data set using the radiometrically-corrected ABVS reflectance data. RMSE reported is in units of kgDM/ha. R^2_{Adj} is expressed as a percentage.

Vegetation	Bias		Slope			
Index	coeff.	P-value	coeff.	P-value	R^2_{Adj}	RMSE
RVI	1141.1	0.136	572.9	0.014	11.2	1458
NDVI	901.2	0.298	4186	0.016	10.8	1462
IPVI	-3286	0.196	8374	0.016	10.8	1462
SAVI(0)	901.2	0.298	4186	0.016	10.8	1462
MSAVI2	1493.3	0.024	4622	0.018	10.4	1465
GEMI	7	0.996	4698	0.021	9.8	1469

AgResearch plot biomass set best was:

$$\text{Biomass} = 11188 - 74812\,\text{G} + 4980\,\text{NIR}. \tag{10.6}$$

The equation's RMSE was 1293 kgDM/ha, and R^2_{Adj}=30.1%. The P-statistic was the following: less than 0.001 for the constant and G terms, and 0.037 for the NIR term.

10.3.3 Prediction of the Dexcel Biomass Data Set

The coefficients of the vegetation index prediction equation (10.1) and the accompanying regression fit statistics are given in Table 10.7.

The linear combination of the ABVS band reflectance which predicted the Dexcel biomass set best was:

$$\text{Biomass} = 5075 - 115632\,\text{B} + 50814\,\text{R}. \tag{10.7}$$

The equation's RMSE was 1444 kgDM/ha; R^2_{Adj}=23.5%, with the following coefficient's P-statistic: 0.027 for the constant term, 0.016 (B) and 0.039 (R).

Table 10.7: Slope and bias values of the vegetation index prediction equations (10.1) for the Dexcel biomass data set using the radiometrically-corrected ABVS reflectance data. RMSE reported is in units of kgDM/ha. R^2_{Adj} is expressed as a percentage.

Vegetation	Bias		Slope			
Index	coeff.	P-value	coeff.	P-value	R^2_{Adj}	RMSE
RVI	4801	0.002	-471.3	0.163	5.5	1604
NDVI	5307	0.023	-4106	0.282	1.2	1641
IPVI	9414	0.123	-8213	0.282	1.2	1641
SAVI(0)	5307	0.023	-4106	0.282	1.2	1641
MSAVI2	4702	0.003	-4576	0.197	4	1617
GEMI	6274	0.027	-4837	0.216	3.3	1623

10.4 Biomass Prediction Using the BRDF-Corrected ABVS Reflectance

The plot matrix graphs of biomass, BRDF-corrected ABVS band reflectance and vegetation indices for the three different sets considered are shown in Figures C.15 and C.16 in Appendix C.5.

10.4.1 Prediction of the Complete Biomass Data Set

The coefficients of the vegetation index prediction equation (10.1) and the statistics associated with the regression are given in Table 10.8. SAVI(1) represents the SAVI index for $L = 1$ (7.10). The SAVI derived from the BRDF-corrected ABVS reflectance gave the best prediction of the biomass for that value of L.

The linear combination of the ABVS band reflectance which most accurately predicted the complete biomass set best was:

$$\text{Biomass} = -344.1 - 20676\,\text{B} + 16234\,\text{G} + 2985\,\text{NIR}. \tag{10.8}$$

The equation's regression statistic was: RMSE=1166 kgDM/ha; R^2_{Adj}=44.6%.

Table 10.8: Slope and bias values of the vegetation index prediction equations (10.1) for the complete biomass data set using the BRDF-corrected ABVS reflectance data. RMSE reported is in units of kgDM/ha. R^2_{Adj} is expressed as a percentage.

Vegetation	Bias		Slope			
Index	coeff.	P-value	coeff.	P-value	R^2_{Adj}	RMSE
RVI	2648	<0.001	43	0.343	0	1568
NDVI	1086	0.292	2669	0.064	3.8	1536
IPVI	-1538	0.516	5339	0.064	3.8	1536
SAVI(1)	689.7	0.338	3650	0.002	13.5	1458
MSAVI2	973	0.222	3042	0.011	8.4	1500
GEMI	612	0.677	2561	0.108	2.5	1547

P-values of equation's coefficients: 0.647 (constant term), 0.086 (B), 0.001 (G) and 0.004 (NIR).

10.4.2 Prediction of the AgResearch Biomass Data Set

The coefficients of the vegetation index prediction equation (10.1) and the statistics associated with the regression are given in Table 10.9.

Table 10.9: Slope and bias values of the vegetation index prediction equations (10.1) for the AgResearch data set using the BRDF-corrected ABVS reflectance data. RMSE reported is in units of kgDM/ha. R^2_{Adj} is expressed as a percentage.

Vegetation	Bias		Slope			
Index	coeff.	P-value	coeff.	P-value	R^2_{Adj}	RMSE
RVI	2392.8	<0.001	75.3	0.156	2.4	1529
NDVI	211	0.856	3891	0.019	10.1	1467
IPVI	-3681	0.187	7784	0..019	10.1	1467
SAVI(1)	374.7	0.644	4119	0.002	18.8	1394
MSAVI2	526.4	0.56	3701	0.007	13.6	1438
GEMI	-1227	0.469	4536	0.015	10.9	1461

The linear combination of the ABVS band reflectance which best predicted the biomass set was:

$$\text{Biomass} = -1337.1 - 26470\,\text{G} - 12925\,\text{R} + 2308\,\text{NIR}. \qquad (10.9)$$

The equation's regression statistic was: RMSE=1206 kgDM/ha; R^2_{Adj}=39.2%. P-values of equation's coefficients: 0.26 (constant term), 0.002 (G), 0.059 (R) and 0.12 (NIR).

10.4.3 Prediction of the Dexcel Biomass Data Set

The coefficients of the vegetation index prediction equation (10.1) and the statistics associated with the regression are given in Table 10.10.

Table 10.10: Slope and bias values of the vegetation index prediction equations (10.1) for the Dexcel data set using the BRDF-corrected ABVS reflectance data. RMSE reported is in units of kgDM/ha. R^2_{Adj} is expressed as a percentage.

Vegetation	Bias		Slope			
Index	coeff.	P-value	coeff.	P-value	R^2_{Adj}	RMSE
RVI	3235.8	<0.001	-35.43	0.698	0	1689
NDVI	3256	0.137	-400	0.893	0	1695
IPVI	3653	0.475	-797	0.893	0	1695
SAVI(1)	1515	0.339	2375	0.343	0	1653
MSAVI2	2100	0.22	1345	0.594	0	1682
GEMI	4523	0.124	-1693	0.584	0	1682

The linear combination of the ABVS band reflectance which best predicted the Dexcel biomass set was:

$$\text{Biomass} = 1441.7 - 17781\,\text{G} - 14262\,\text{R}. \tag{10.10}$$

The equation's regression statistic was: RMSE=1026 kgDM/ha; R^2_{Adj}=61.3%. P-values of equation's coefficients: 0.01 (constant term), 0.001 (G), 0.106 (R).

10.5 Discussion

The predictions of the vegetation indices confirmed their inadequacy when dealing with highly dense vegetation. The highest reported R^2_{Adj} of the vegetation index prediction equation (10.1) was 21.3% for the RVI index, in the

case of the raw reflectance and AgResearch test plot data set. Even more telling was the P-statistic of the regression coefficients; at least one coefficient in all the vegetation index prediction equations had a large P-value, indicating that its value was speculative. The graphs of biomass against vegetation indices in Appendix C.5 clearly give a reason for such a poor performance: strong scatter of biomass values.

The performance of all the vegetation index algorithms was very similar. The reason for this was high correlation amongst the indices, as shown by the plot matrix graphs in Appendix C.5. The NDVI (7.6) and IPVI (7.7) had exactly the same results, due to their similar mathematical formulation. The SAVI index (7.10) for the raw and radiometrically-corrected reflectance data sets best predicted the biomass when its vegetation-dependent parameter L was set to zero. This, however, effectively turned the SAVI into the NDVI. For the BRDF-corrected reflectance, the best-fit SAVI L parameter was equal to one. This was an unexpected result, given that $L = 1$ indicates very low density vegetation areas [*Huete*, 1988].

The performance of the vegetation indices for the reflectance data at three different stages of post-processing (Section 9) did not show the expected steady improvement with increasing level of data transformation. Most oftenly the best predictions were achieved with the raw reflectance; the worst with the radiometrically-corrected reflectance. Five (NDVI, IPVI, SAVI, MSAVI2 and GEMI) out of six examined vegetation indices improved their performance from the worst case with the BRDF-corrected reflectance.

The situation was markedly different when ABVS band-equivalent reflectance data was used. The prediction equations in this case were derived using the multiple regression technique; thus, biomass was estimated as a linear combination of ABVS band reflectance. Not only were the predictions noticeably more accurate, but the results clearly showed steady improvement for higher stages of post-processing. The use of the BRDF-corrected reflectance yielded the best predictions. The graphs of correct vs. predicted biomass from the

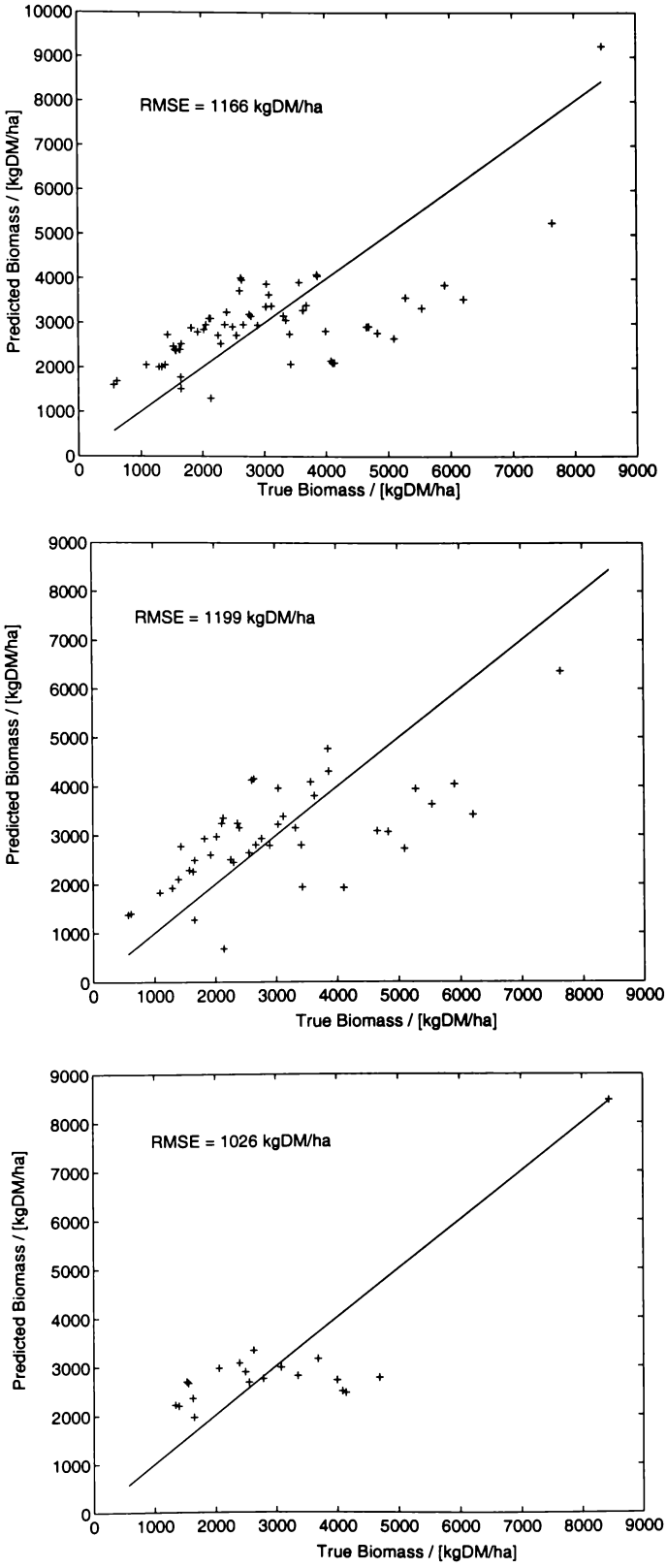

Figure 10.1: Graphs of true vs. predicted biomass with the ABVS band-equivalent BRDF-corrected reflectance for the three data sets: complete (AgResearch and Dexcel combined; top graph), AgResearch only (middle) and Dexcel only (bottom). The prediction equations (10.8), (10.9) and (10.10) were derived using the multiple regression technique.

best multiple regression equations (10.8), (10.9), (10.10), and the three different biomass data sets are shown in Figure 10.1.

Common to both groups of prediction equations (vegetation indices and ABVS band-equivalent reflectance) was a sharp difference in the results between the AgResearch and Dexcel biomass data sets. The predictions were much more accurate for the former set. The only exception to this rule was when the BRDF-corrected ABVS band-equivalent reflectance was used in a multiple regression equation to predict the Dexcel biomass (see Figure 10.1), which yielded the best overall prediction result for all our equations (R^2_{Adj}=61.3%). However, the reason for such an outstanding result (in comparison to our other equations) was the entry for the DRC18 plot—the largest biomass in the whole data set, 8447 kgDM/ha—which strongly influenced the regression equation. We believe that this was the main cause of the noticed differences in prediction between the AgResearch and Dexcel plots for the other cases also.

Chapter 11

Part II: Conclusion

In the second part of this thesis, we have presented the results of a feasibility study on the applicability of airborne multispectral remote sensing to pasture status monitoring. Our study has focused on the estimation of biomass as this is the most valuable pasture status quantity to the farmer. The study was not aimed at devising any new methods or techniques for biomass prediction. Its primary intention was to quickly and cost-effectively explore potential benefits of pasture airborne remote sensing in the New Zealand farming context.

The study was done in collaboration with AgResearch Ltd. and Dexcel Ltd. Their staff prepared 65 test pasture plots, which were imaged in February 1999 using Charles Sturt University's Airborne Video System (ABVS) for two hours. The test plots, 3×3 metres in size, encompassed a range of different species, levels of grazing and nutritional supplement regimes (Appendix C.1). Sampling of the test plots started immediately at the end of imaging, and concluded the next day.

In order to derive useable data from the ABVS images of the test plots, we devised a procedure for their post-processing (Chapter 9). Its main stages were:

- Geometrical correction (Section 9.1)
- Radiometric correction (Section 9.2)

- Conversion of ABVS image pixel DN values to reflectance (Section 9.4)
- BRDF correction (Section 9.5)

In formulating the processing stages we took into account the charateristics of the ABVS imaging system (its cameras and image acquisition hardware), the properties of the targets (pasture plots) and the requirements of the end application (cost-effective pasture biomass prediction). A graphical user interface in MATLAB was created to simplify some of these tasks.

The geometrical correction removed the comb effect of an image by relatively shifting its odd and even frames (odd and even rows) by an integer number of pixels until the jaggedness of the across-track image features was minimized. The radiometric correction tried to compensate for the imaging system's imperfections related to the camera lenses and optical filters, and the physics and electronics of the CCD sensor. We note that the implemented procedure (Section 9.2), in the absence of a proper radiometric calibration, was highly speculative, and has certainly marred the results. The ABVS imaging system had never been used before in a quantitative investigation [David Lamb, priv. comm.], so that could explain the lack of proper radiometric calibration.

The BRDF correction dealt with the physics of canopy reflectance and allowed standardization of all the ABVS observations of the test plots to one illumination (solar zenith angle) and viewing geometry. The BRDF correction method of *Shepherd and Dymond* [1999] for AVHRR imagery, which employs the WAK canopy reflectance model [*Dymond et al.*, 2000], was adapted for use with our ABVS-acquired images. The WAK model parameters of our test pasture plots were determined by a model fitting procedure, which involved all the test plots with two or more observations. In the cases with more than two observations, we formed as many (9.3) and (9.4) pairs of equations as there were possible combinations.

ABVS image pixel DN values were converted to reflectance using two, 6×6 metres wide canvases, located near the test plots. In the absence of a proper

portable spectrometer, we designed, assembled and calibrated an *ad hoc* canvas reflectance measurement system (Section 8.5). Its reflectance measurements were used in the pixel DN conversion (Section 9.4). Since the canvas reflectance measurements were done in a laboratory environment and consisted of only the $0°/0°$ illumination-detector geometry, our converted reflectance certainly included an error associated with the non-Lambertian surface property of the canvases.

ABVS band-equivalent reflectances for each test plot were calculated after every image correction. Hence, we obtained three different reflectance data sets to use in biomass prediction. Due to different sampling methods (Section 8.2) for the AgResearch and Dexcel test plots we decided to consider three different biomass data sets as well: combined, AgResearch only (45 plots) and Dexcel only (20 plots). In total, we had nine combinations of reflectance and biomass data sets to analyze.

The biomass data was predicted (Chapter 10) with: a selection of vegetation indices (Section 7.3.4), and ABVS band-equivalent reflectance. The selection of vegetation indices did not include any which required the use of soil line data. Utilization of such indices would require coincident observations of bare soil. Since vegetation cover of New Zealand pastures is very high—the soil is practically completely covered—we judged that "soil line" vegetation indices are less likely to be used and hence did not include them in this study. The selected indices were: RVI, NDVI, IPVI, SAVI, MSAVI2 and GEMI. Since these vegetation indices were derived from the ABVS reflectance, three different vegetation index data sets, corresponding to the three levels of post-processing, were also generated.

The biomass was predicted with two types of equations. For the selected vegetation indices, we assumed a simple linear relationship with biomass (10.1). ABVS band-equivalent reflectance was utilized in multiple regression equations, i.e. linear combinations of ABVS bands.

The selected vegetation indices did not predict biomass very accurately for the three different data sets. The predictions were typically best for the AgResearch data set, and the worst predictions were always from the Dexcel biomass data set. We think this was mainly due to the entry of the Dexcel's DRC18 plot, by far the largest biomass reported. The AgResearch biomass set did not have it, and hence had the best predictions. The combined data set "diluted" the influence of the DRC18 entry by having the largest number of records (65 entries). However, the Dexcel set had the smallest number of records, twenty, allowing the DRC18 to influence the regression strongly.

ABVS band-equivalent reflectances predicted the biomass much better than the vegetation indices. These results seem to corroborate the findings of *Hanna et al.* [1999] and *Lin* [1999], who also observed that a linear combination of band-equivalent reflectances was superior to any vegetation index. These predictions also exhibited a steady improvement with the level of post-processing—something not observed with the vegetation indices.

However, we do not think this is due only to the compensation of the true BRDF effect. The sky on the day of imaging was overcast with thin stratus clouds. The Sun disk was visible, but the shadows on the ground were hardly noticeable. We think that the natural illumination on that day had a very strong diffuse component which certainly made the BRDF effect weaker than it would be for a clear sky conditions. The method we used for BRDF correction (Section 9.5) was based on a least-square fit [*Shepherd and Dymond*, 1999]. Thus, we conjecture that the fitting procedure did not only compensate the BRDF effect, but also inadvertently helped to improve the overall quality of the reflectance data.

The root mean square error (RMSE) of all prediction equations did not fall below 1000 kgDM/ha. We believe this is still far too high for an economically-viable remote sensing technology for pasture status monitoring. As probably the upper accuracy limit of such a technology, we cite [Mac Hanna, priv. comm.] the results of AgResearch test plot's biomass prediction using the

measurements of the three-channel Hanna radiometer (Section 8.3). A linear multiple regression equation involving all three radiometer's channels (green, red and near-infrared) yielded RMSE of 439.6 kgDM/ha, and R^2_{Adj} of 83.7%. It is important to note that the radiometer measurements corresponded precisely to every sampling plot (Section 8.2), and hence were better related to their biomass than our reflectance data derived from the ABVS imagery.

11.1 Suggestions for Future Work

Although the results of our study did not find that airborne multispectral remote sensing was readily available technique for pasture biomass measurement, the experience gained by those who took part was invaluable. We will list, in no particular order, some observations and recommendations for a future study, drawn from the participation in this project:

- Project participants involved in different segments of the project need to communicate between each other well in order to raise awareness of the important issues related to their own task and how it may affect the final project outcome.
- Records of important information about test plots need to be much more exhaustive to allow better discrimination of possible outliers in the data sets later.
- Biomass sampling protocol and measurement procedure should be the same for all the samples. Preferably, it should be performed by the same person to allow better statistical assessment of systematic errors.
- Instead of delineating test plots, a single object, easily distinguishable in all spectral bands, should be used. Sampling areas would uniquely be defined relative to this object. This should prevent pixel contamination and allow better alignment of the sampling areas and their corresponding pixels.

- Various land and sampling area features should be recorded using a high precision GPS systems (for example Differential Global Positioning System (DGPS)). Using such records during various quality assurance tests with acquired images can really help to improve the reliability of the data derived from such imagery.

- A portable spectroradiometer should be used on the day of imaging to record spectra of various land features (including test plots), as well as ground calibration targets.

- To improve image quality, especially to avoid the comb effect, progressive scan cameras should be used. The CCD readout in such cameras is sequential, thus the whole scene is captured in one snapshot—no frames, and no risk of frame mismatch (comb effect) when fast moving scenes are imaged.

- Megapixel CCD sensors are nowadays very affordable. Increasing the number of CCD pixels will allow airplanes to fly at higher altitudes for the same spatial resolution. Flying at higher altitudes provides better attitude control of the plane, and hence reduces pixel smearing.

- The imaging system's cameras should undergo a proper radiometric calibration to avoid data contamination caused by using questionable alternatives like in our study.

- Digital output cameras should be used, instead of analog as in our study. Digital output avoids the digital-to-analog and analog-to-digital conversion of CCD sensor pixel readouts of the analog cameras which effectively destroys the original CCD pixel information. The end result is much sharper image and a less ambiguous link between the amount of radiation impinging the CCD pixel and its digital number value stored in the computer memory.

We believe that fulfillment of any of the above suggestions would result in a much better set of data which would then permit a more objective assessment of the airborne multispectral remote sensing technique. The results of this study, as well as those of *Hanna et al.* [1999] and *Lin* [1999], indicate that an all-encompassing vegetation index will not work for New Zealand pastures. Using multispectral band reflectances is a more promising approach, and one that can potentially involve the use of alternatives to the regression-based methods, for example: neural networks, fuzzy logic estimators, expert-based systems, etc.

However, regardless of the quality of remotely-sensed data, the true success in predicting pasture status will come only when it is combined with other pasture-related information, such as: soil type, soil moisture, pasture species, pasture growth models, underground water flow, etc. Given the unique characteristics of the New Zealand climate and flora, it is highly unlikely that solutions derived for other parts of the world could be readily implemented here. This could create an excellent opportunity for furthering the basic science of vegetation remote sensing, while at the same time creating applications with a potential of adding significant value to the country's farming industry.

Appendix A

Additional DWVT Results

A.1 Graphs of the DWVT SST Residuals

The graphs in this section detail the relationship between the DWVT SST residuals, i.e. DWVT SST retrieval errors, versus channel-4 and -5 average atmospheric temperatures, total water vapour column and ground truth SST for the final DWVT atmospheric profiles. Any observed trend between the DWVT SST residuals and these variables would suggest some kind of inadequacy of the DWVT algorithm.

A.1.1 Graphs for the Hobart Radiosonde Site

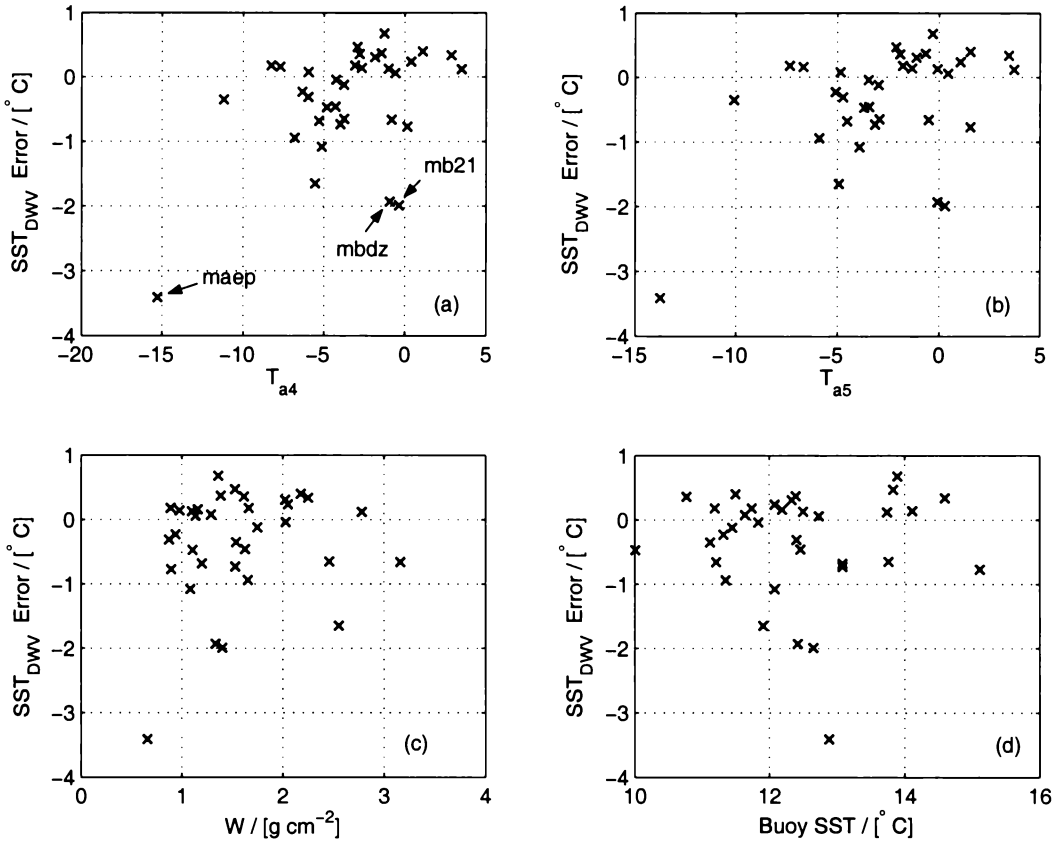

Figure A.1: DWVT SST residuals vs. channel-4 (a) and -5 (b) average atmospheric temperatures, total water vapour column (c) and ground truth SST (d) for the final DWVT atmospheric profiles. First-guess sondes were from Hobart; sonde selection mode was "5d-before". The passes with the three largest SST residuals are labelled in the (a) graph. No relationship can be observed between the SST residuals and the x-axis variables.

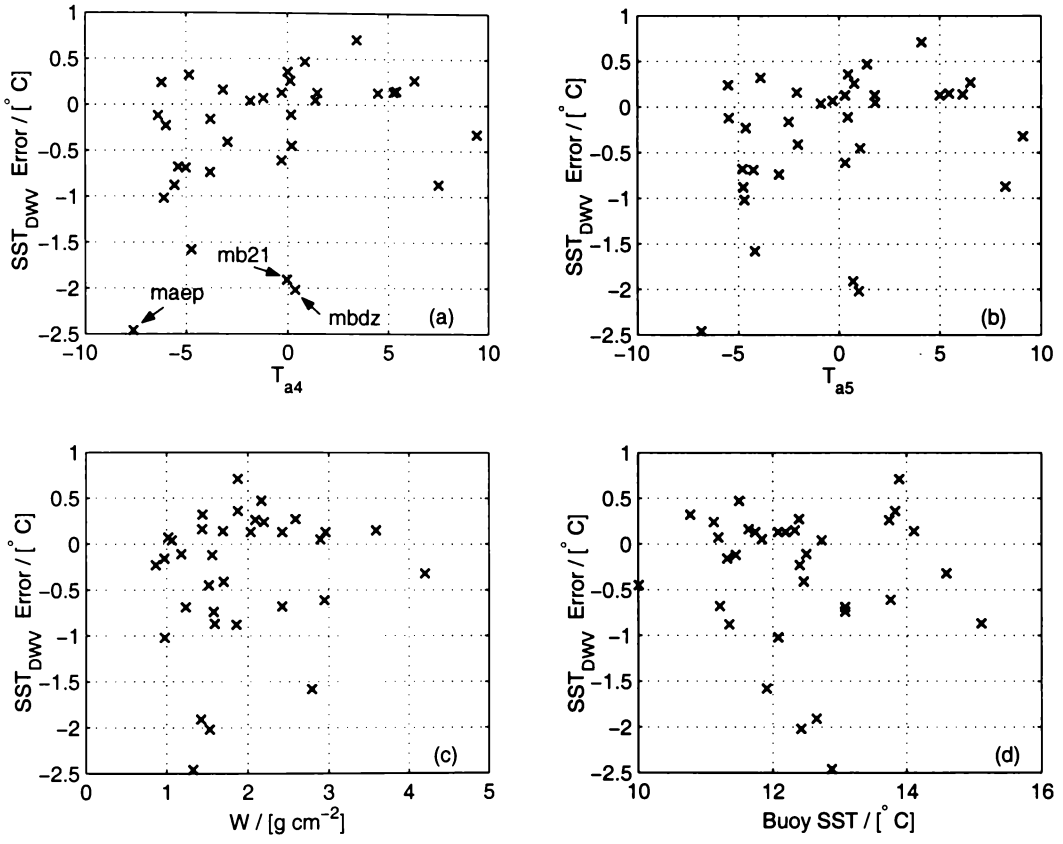

Figure A.2: DWVT SST residuals vs. channel-4 (a) and -5 (b) average atmospheric temperatures, total water vapour column (c) and ground truth SST (d) for the final DWVT atmospheric profiles. First-guess sondes were from Hobart; sonde selection mode was "closest". The passes with the three largest SST residuals are labelled in the (a) graph. No relationship can be observed between the SST residuals and the x-axis variables.

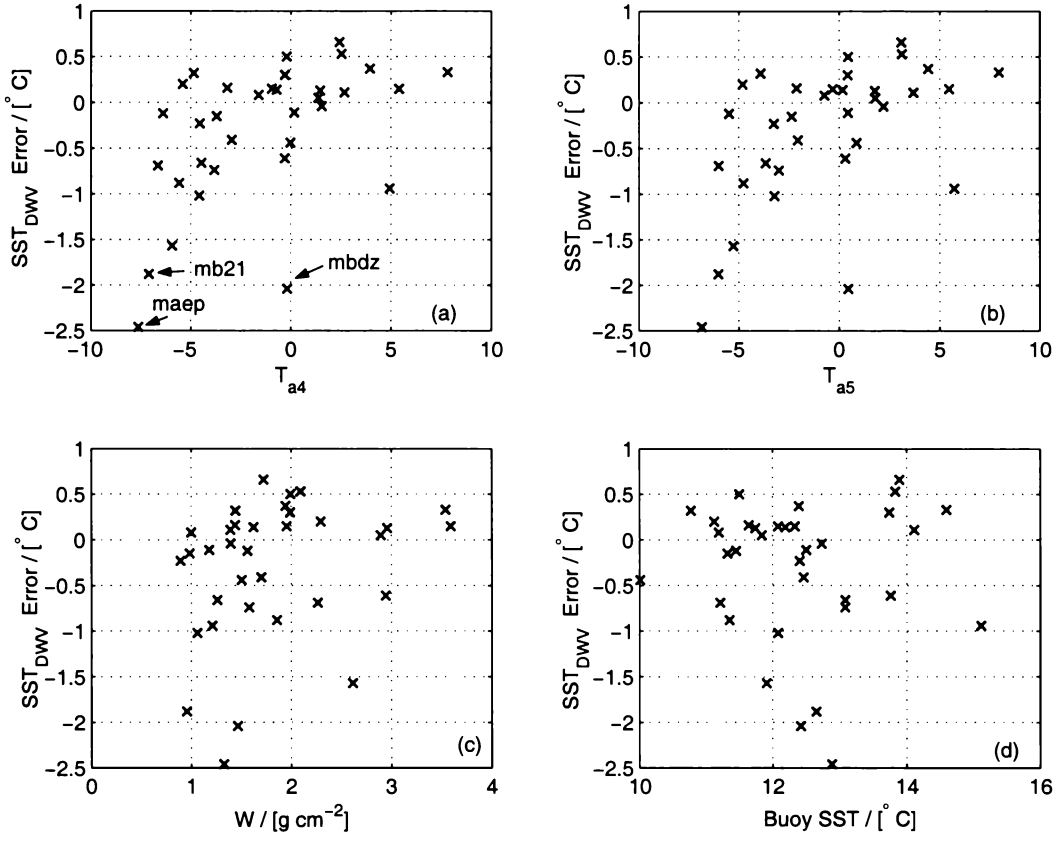

Figure A.3: DWVT SST residuals vs. channel-4 (a) and -5 (b) average atmospheric temperatures, total water vapour column (c) and ground truth SST (d) for the final DWVT atmospheric profiles. First-guess sondes were from Hobart; sonde selection mode was "night/day". The passes with the three largest SST residuals are labelled in the (a) graph. No relationship can be observed between the SST residuals and the x-axis variables.

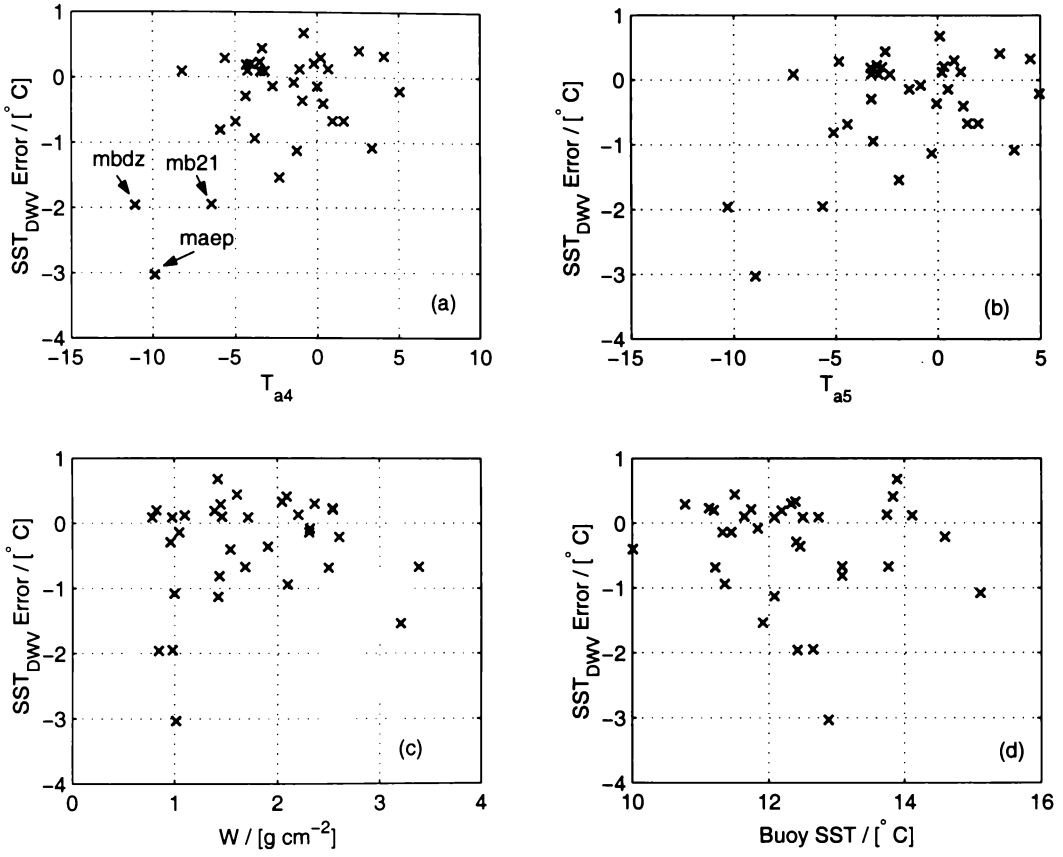

Figure A.4: DWVT SST residuals vs. channel-4 (a) and -5 (b) average atmospheric temperatures, total water vapour column (c) and ground truth SST (d) for the final DWVT atmospheric profiles. First-guess sondes were from Hobart; sonde selection mode was "5d-after". The passes with the three largest SST residuals are labelled in the (a) graph. No relationship can be observed between the SST residuals and the x-axis variables.

A.1.2 Graphs for the Mt. Gambier Radiosonde Site

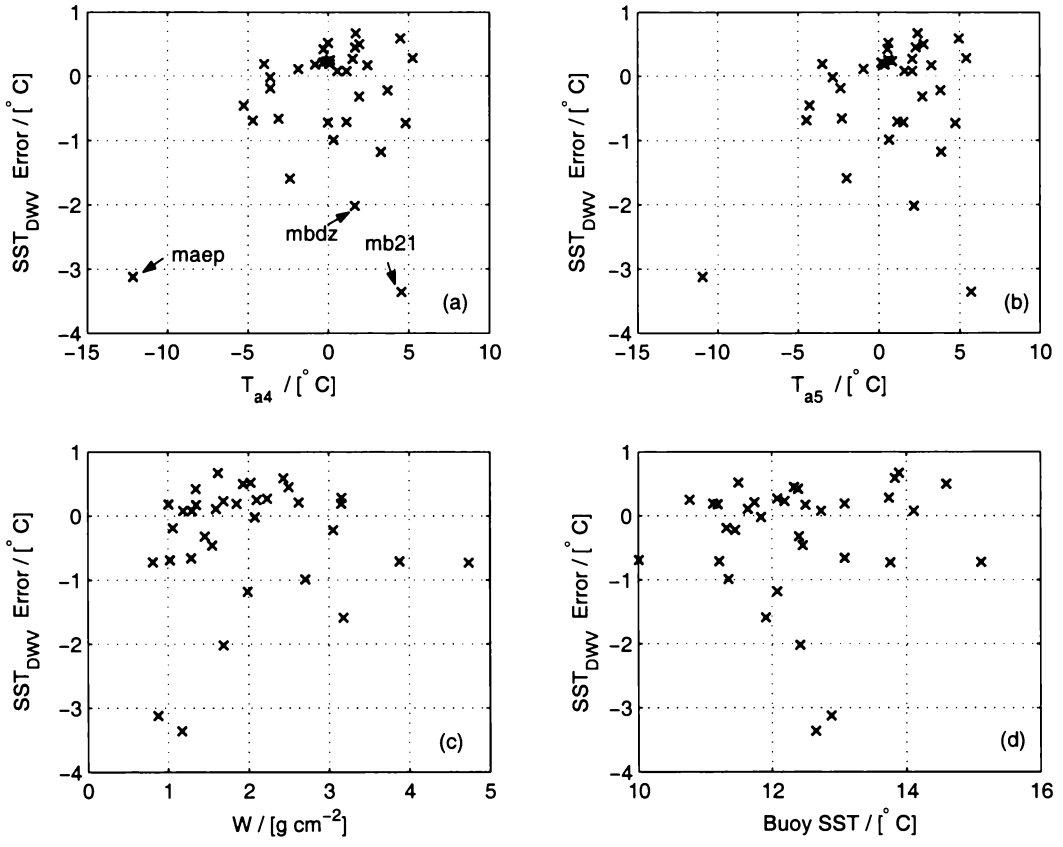

Figure A.5: DWVT SST residuals vs. channel-4 (a) and -5 (b) average atmospheric temperatures, total water vapour column (c) and ground truth SST (d) for the final DWVT atmospheric profiles. First-guess sondes were from Mt. Gambier; sonde selection mode was "5d-before". The passes with the three largest SST residuals are labelled in the (a) graph. No relationship can be observed between the SST residuals and the x-axis variables.

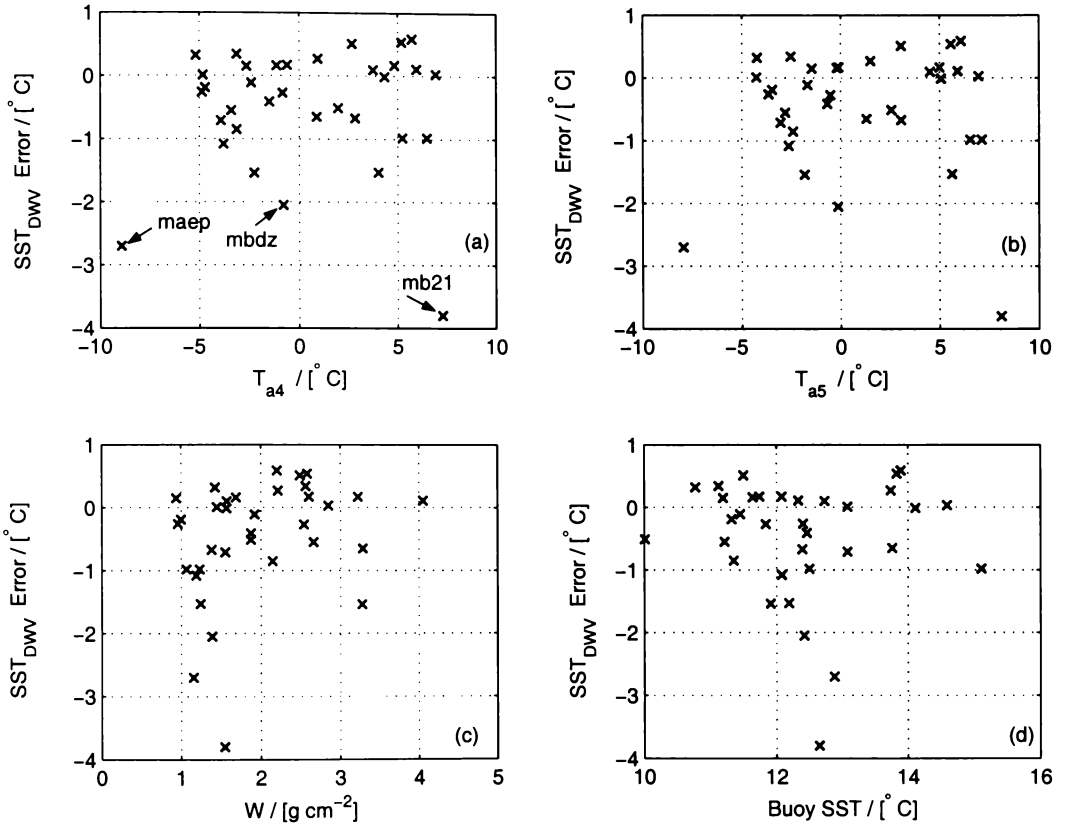

Figure A.6: DWVT SST residuals vs. channel-4 (a) and -5 (b) average atmospheric temperatures, total water vapour column (c) and ground truth SST (d) for the final DWVT atmospheric profiles. First-guess sondes were from Mt. Gambier; sonde selection mode was "closest". The passes with the three largest SST residuals are labelled in the (a) graph. No relationship can be observed between the SST residuals and the x-axis variables.

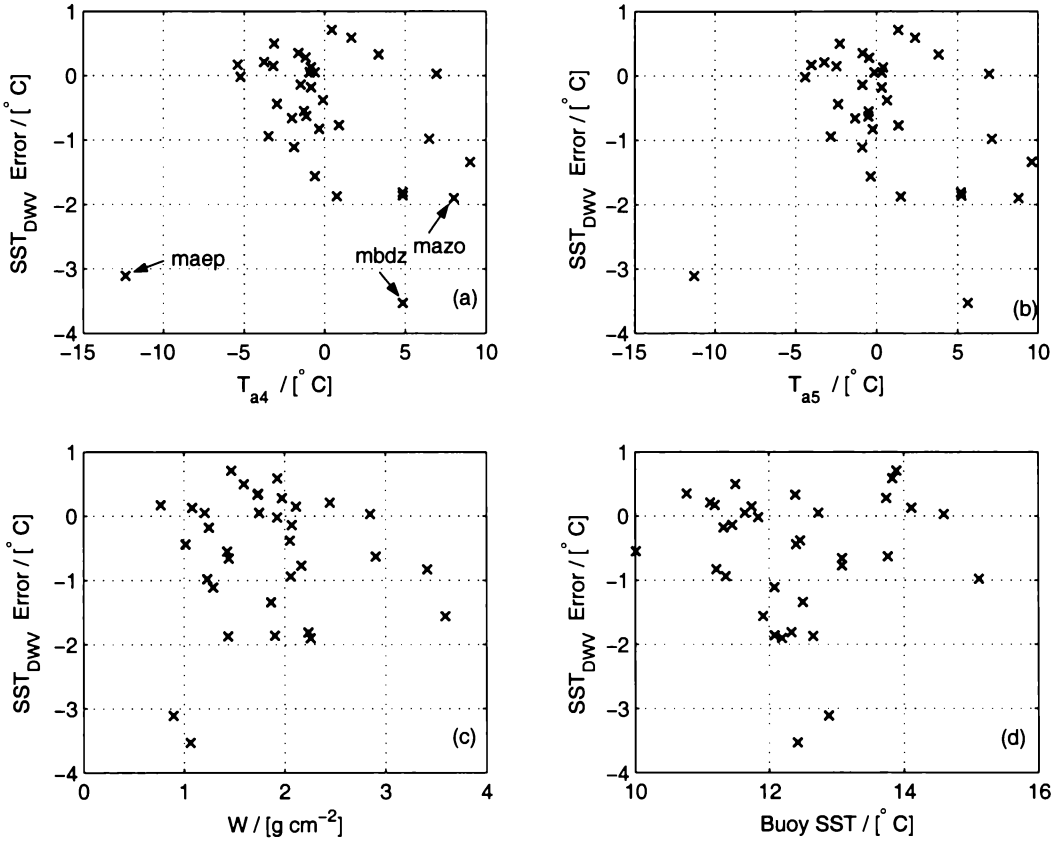

Figure A.7: DWVT SST residuals vs. channel-4 (a) and -5 (b) average atmospheric temperatures, total water vapour column (c) and ground truth SST (d) for the final DWVT atmospheric profiles. First-guess sondes were from Hobart; sonde selection mode was "5d-after". The passes with the three largest SST residuals are labelled in the (a) graph. No relationship can be observed between the SST residuals and the x-axis variables.

A.2 Complete TRSST Results

The following tables accompany the material in Section 4.7 on the comparison between the TRSST methods and the DWVT.

Table A.1: The complete results of the methods of H&M [*Harris and Mason*, 1992], Sob93 [*Sobrino et al.*, 1993] and Sob94 [*Sobrino et al.*, 1994] for the "5d-before" sondes. The value of R_{54} was calculated using LOWTRAN-7 from the first-guess atmospheric profiles from Hobart.

IFUT	R_{54}	H&M	Sob93	Sob94
m9jr	0.891631	-0.17	-0.27	-0.47
m9k5	0.925498	0.05	0.07	-0.09
m9kc	0.929905	-0.45	-0.54	-0.62
m9n9	0.832484	-1.82	-2.03	-2.35
m9na	0.786895	-0.29	-0.84	-1.15
m9vi	0.929635	-0.38	-0.46	-0.57
ma4c	0.923023	-1.64	-1.75	-1.89
ma4i	0.912282	-0.87	-0.86	-1.09
mabk	0.923307	-0.34	-0.33	-0.53
mabz	0.890589	-1.69	-1.63	-1.96
mac6	0.953386	-0.77	-0.74	-0.83
macc	0.927345	-0.87	-0.65	-0.97
macd	0.944236	-1.82	-1.64	-1.89
macq	0.921285	-2.86	-2.66	-3.00
macr	0.941221	-0.64	-0.57	-0.74
mad5	0.932714	-0.74	-0.82	-0.93
maeb	0.951564	-1.20	-1.05	-1.22
maep	0.951227	-1.86	-1.47	-1.83
maf3	0.936980	-1.47	-1.34	-1.55
mafh	0.937983	-1.29	-1.18	-1.38
mafw	0.927718	-1.03	-0.89	-1.15
mald	0.917793	-0.22	-0.41	-0.52
malk	0.942698	-0.84	-0.63	-0.89
mar9	0.936746	-0.26	-0.15	-0.36
mazo	0.949003	-0.57	-0.50	-0.63
mb11	0.909463	-0.52	-0.53	-0.75
mb1f	0.932506	-0.59	-0.48	-0.69
mb1n	0.941485	-0.29	-0.31	-0.41
mb21	0.934141	-2.32	-2.35	-2.49
mb2m	0.917122	-0.11	-0.18	-0.33
mb9o	0.939798	-0.96	-1.01	-1.14
mbdz	0.925159	-2.37	-2.44	-2.60
mbg5	0.884328	-1.18	-1.57	-1.68
mbgc	0.913625	-0.48	-0.47	-0.65
bias		-0.97	-0.96	-1.16
rms		0.73	0.70	0.73
Q		1.21	1.19	1.37

Table A.2: The complete results for the DWVT, H&M [*Harris and Mason*, 1992], Sob93 [*Sobrino et al.*, 1993] and Sob94 [*Sobrino et al.*, 1994] methods for the "5d-before" sondes. The value of R_{54} was calculated using LOWTRAN-7 from the final DWVT atmospheric profiles. The first-guess profiles came from Hobart.

IFUT	R_{54}	H&M	Sob93	Sob94	DWVT
m9jr	0.927387	-0.24	-0.17	-0.35	0.47
m9k5	0.927931	0.05	0.07	-0.08	0.68
m9kc	0.954824	-0.47	-0.45	-0.51	0.14
m9n9	0.880412	-1.96	-1.94	-2.25	-0.65
m9na	0.841710	-0.44	-0.69	-0.97	0.12
m9vi	0.940484	-0.39	-0.42	-0.52	0.06
ma4c	0.951235	-1.67	-1.65	-1.76	-1.08
ma4i	0.908569	-0.87	-0.87	-1.10	-0.12
mabk	0.912823	-0.32	-0.36	-0.57	0.36
mabz	0.824850	-1.50	-1.77	-2.11	-0.66
mac6	0.958017	-0.78	-0.72	-0.81	-0.31
macc	0.931934	-0.88	-0.64	-0.96	-0.35
macd	0.915106	-1.77	-1.71	-1.97	-0.94
macq	0.874994	-2.74	-2.73	-3.08	-1.65
macr	0.937674	-0.63	-0.58	-0.75	0.08
mad5	0.960447	-0.76	-0.72	-0.80	-0.23
maeb	0.935704	-1.17	-1.09	-1.27	-0.68
maep	0.972203	-1.92	-1.45	-1.80	-3.41
maf3	0.917972	-1.43	-1.39	-1.61	-0.73
mafh	0.922029	-1.26	-1.22	-1.43	-0.46
mafw	0.899921	-0.97	-0.95	-1.22	-0.04
mald	0.958341	-0.25	-0.25	-0.31	0.18
malk	0.923523	-0.80	-0.67	-0.94	0.18
mar9	0.873966	-0.15	-0.32	-0.57	0.40
mazo	0.955614	-0.57	-0.48	-0.61	0.16
mb11	0.883360	-0.47	-0.60	-0.84	0.24
mb1f	0.902723	-0.54	-0.56	-0.79	0.31
mb1n	0.944335	-0.29	-0.30	-0.39	0.13
mb21	0.922863	-2.30	-2.38	-2.54	-1.99
mb2m	0.931921	-0.13	-0.13	-0.27	0.37
mb9o	0.948329	-0.97	-0.98	-1.10	-0.47
mbdz	0.919250	-2.37	-2.46	-2.62	-1.93
mbg5	0.961415	-1.23	-1.25	-1.25	-0.77
mbgc	0.883763	-0.42	-0.55	-0.76	0.34
bias		-0.96	-0.95	-1.14	-0.36
rms		0.72	0.71	0.74	0.86
Q		1.20	1.19	1.37	0.93

Table A.3: The complete results for the methods of H&M [*Harris and Mason*, 1992], Sob93 [*Sobrino et al.*, 1993] and Sob94 [*Sobrino et al.*, 1994] for the "closest" sondes. The value of R_{54} was calculated using LOWTRAN-7 from the first-guess atmospheric profiles from Hobart.

IFUT	R_{54}	H&M	Sob93	Sob94
m9jr	0.949575	-0.27	-0.11	-0.28
m9k5	0.929422	0.05	0.08	-0.07
m9kc	0.912612	-0.44	-0.60	-0.71
m9n9	0.862116	-1.91	-1.97	-2.29
m9na	0.919575	-0.62	-0.51	-0.75
m9vi	0.943587	-0.40	-0.41	-0.50
ma4c	0.956644	-1.67	-1.63	-1.73
ma4i	0.950868	-0.94	-0.76	-0.97
mabk	0.938318	-0.36	-0.29	-0.48
mabz	0.919604	-1.76	-1.58	-1.90
mac6	0.955858	-0.77	-0.73	-0.82
macc	0.931137	-0.88	-0.64	-0.96
macd	0.934943	-1.81	-1.66	-1.92
macq	0.902254	-2.81	-2.69	-3.03
macr	0.934006	-0.63	-0.59	-0.76
mad5	0.949049	-0.75	-0.76	-0.86
maeb	0.955402	-1.20	-1.04	-1.21
maep	0.928273	-1.80	-1.50	-1.85
maf3	0.934140	-1.46	-1.35	-1.56
mafh	0.934846	-1.28	-1.19	-1.39
mafw	0.843693	-0.84	-1.09	-1.39
mald	0.976653	-0.26	-0.19	-0.22
malk	0.925267	-0.81	-0.67	-0.93
mar9	0.929295	-0.25	-0.17	-0.38
mazo	0.940060	-0.56	-0.53	-0.67
mb11	0.899913	-0.50	-0.56	-0.78
mb1f	0.910965	-0.55	-0.54	-0.76
mb1n	0.966528	-0.31	-0.23	-0.30
mb21	0.935692	-2.32	-2.34	-2.48
mb2m	0.936268	-0.14	-0.12	-0.26
mb9o	0.947950	-0.97	-0.98	-1.10
mbdz	0.901756	-2.35	-2.52	-2.70
mbg5	0.940090	-1.22	-1.33	-1.36
mbgc	0.879379	-0.41	-0.56	-0.77
bias		-0.98	-0.93	-1.12
rms		0.71	0.71	0.75
Q		1.21	1.18	1.35

Table A.4: The complete results for the DWVT, H&M [*Harris and Mason*, 1992], Sob93 [*Sobrino et al.*, 1993] and Sob94 [*Sobrino et al.*, 1994] methods for the "closest" sondes. The value of R_{54} was calculated using LOWTRAN-7 from the final DWVT atmospheric profiles. The first-guess profiles came from Hobart.

IFUT	R_{54}	H&M	Sob93	Sob94	DWVT
m9jr	0.915181	-0.21	-0.20	-0.39	0.36
m9k5	0.889919	0.11	-0.04	-0.22	0.71
m9kc	0.898522	-0.42	-0.65	-0.78	0.14
m9n9	0.839812	-1.84	-2.01	-2.33	-0.61
m9na	0.881042	-0.54	-0.60	-0.85	0.26
m9vi	0.949053	-0.40	-0.39	-0.48	0.04
ma4c	0.952974	-1.67	-1.64	-1.75	-1.02
ma4i	0.925061	-0.90	-0.82	-1.05	-0.12
mabk	0.927123	-0.35	-0.32	-0.52	0.32
mabz	0.885254	-1.67	-1.64	-1.97	-0.68
mac6	0.956859	-0.77	-0.73	-0.82	-0.23
macc	0.894953	-0.79	-0.71	-1.03	0.24
macd	0.907825	-1.75	-1.73	-1.99	-0.88
macq	0.866717	-2.72	-2.75	-3.10	-1.58
macr	0.921033	-0.61	-0.63	-0.81	0.16
mad5	0.949658	-0.75	-0.76	-0.85	-0.16
maeb	0.934699	-1.17	-1.09	-1.28	-0.69
maep	0.930803	-1.80	-1.50	-1.85	-2.46
maf3	0.917090	-1.43	-1.39	-1.61	-0.74
mafh	0.910755	-1.24	-1.25	-1.47	-0.41
mafw	0.827738	-0.80	-1.13	-1.44	0.05
mald	0.956236	-0.25	-0.26	-0.32	0.07
malk	0.832770	-0.59	-0.88	-1.19	0.13
mar9	0.874276	-0.15	-0.32	-0.57	0.47
mazo	0.854073	-0.44	-0.83	-1.05	0.13
mb11	0.895573	-0.49	-0.57	-0.79	0.13
mb1f	0.782128	-0.27	-0.92	-1.24	0.15
mb1n	0.949241	-0.30	-0.29	-0.37	-0.11
mb21	0.916603	-2.30	-2.41	-2.57	-1.91
mb2m	0.830083	0.02	-0.49	-0.73	0.27
mb9o	0.910525	-0.93	-1.12	-1.28	-0.45
mbdz	0.911862	-2.36	-2.49	-2.66	-2.02
mbg5	0.907370	-1.20	-1.46	-1.54	-0.87
mbgc	0.744537	-0.10	-1.02	-1.35	-0.32
bias		-0.91	-1.03	-1.24	-0.34
rms		0.74	0.68	0.71	0.75
Q		1.17	1.24	1.43	0.82

Table A.5: The complete results for the methods of H&M [*Harris and Mason*, 1992], Sob93 [*Sobrino et al.*, 1993] and Sob94 [*Sobrino et al.*, 1994] for the "night/day" sondes. The value of R_{54} was calculated using LOWTRAN-7 from the first-guess atmospheric profiles from Hobart.

IFUT	R_{54}	H&M	Sob93	Sob94
m9jr	0.919172	-0.22	-0.19	-0.38
m9k5	0.928434	0.05	0.07	-0.07
m9kc	0.930658	-0.45	-0.53	-0.62
m9n9	0.862116	-1.91	-1.97	-2.29
m9na	0.898919	-0.58	-0.56	-0.80
m9vi	0.956402	-0.41	-0.37	-0.45
ma4c	0.952739	-1.67	-1.64	-1.75
ma4i	0.950868	-0.94	-0.76	-0.97
mabk	0.938318	-0.36	-0.29	-0.48
mabz	0.933680	-1.79	-1.56	-1.88
mac6	0.950964	-0.77	-0.75	-0.84
macc	0.931137	-0.88	-0.64	-0.96
macd	0.937639	-1.81	-1.66	-1.91
macq	0.902254	-2.81	-2.69	-3.03
macr	0.932233	-0.62	-0.59	-0.77
mad5	0.949302	-0.75	-0.76	-0.85
maeb	0.955402	-1.20	-1.04	-1.21
maep	0.928273	-1.80	-1.50	-1.85
maf3	0.934140	-1.46	-1.35	-1.56
mafh	0.934846	-1.28	-1.19	-1.39
mafw	0.910210	-1.00	-0.93	-1.20
mald	0.976653	-0.26	-0.19	-0.22
malk	0.920886	-0.80	-0.68	-0.94
mar9	0.910353	-0.22	-0.22	-0.44
mazo	0.922051	-0.53	-0.59	-0.74
mb11	0.899913	-0.50	-0.56	-0.78
mb1f	0.910965	-0.55	-0.54	-0.76
mb1n	0.945469	-0.29	-0.30	-0.39
mb21	0.966664	-2.35	-2.24	-2.35
mb2m	0.914401	-0.11	-0.19	-0.35
mb9o	0.940950	-0.96	-1.00	-1.13
mbdz	0.894043	-2.34	-2.55	-2.74
mbg5	0.964844	-1.24	-1.23	-1.23
mbgc	0.917438	-0.48	-0.46	-0.64
bias		-0.98	-0.93	-1.12
rms		0.72	0.70	0.73
Q		1.22	1.16	1.34

Table A.6: The complete results for the DWVT, H&M [*Harris and Mason*, 1992], Sob93 [*Sobrino et al.*, 1993] and Sob94 [*Sobrino et al.*, 1994] methods for the "night/day" sondes. The value of R_{54} was calculated using LOWTRAN-7 from the final DWVT atmospheric profiles. The first-guess profiles came from Hobart.

IFUT	R_{54}	H&M	Sob93	Sob94	DWVT
m9jr	0.883636	-0.16	-0.29	-0.50	0.53
m9k5	0.903133	0.09	-0.00	-0.17	0.66
m9kc	0.928049	-0.45	-0.54	-0.63	0.11
m9n9	0.839812	-1.84	-2.01	-2.33	-0.61
m9na	0.883512	-0.54	-0.59	-0.85	0.30
m9vi	0.932455	-0.39	-0.45	-0.55	-0.04
ma4c	0.946721	-1.66	-1.66	-1.78	-1.02
ma4i	0.925061	-0.90	-0.82	-1.05	-0.12
mabk	0.927123	-0.35	-0.32	-0.52	0.32
mabz	0.895498	-1.70	-1.63	-1.95	-0.69
mac6	0.952071	-0.77	-0.74	-0.84	-0.23
macc	0.890229	-0.78	-0.71	-1.04	0.20
macd	0.907825	-1.75	-1.73	-1.99	-0.88
macq	0.878194	-2.75	-2.73	-3.07	-1.57
macr	0.921033	-0.61	-0.63	-0.81	0.16
mad5	0.948222	-0.75	-0.76	-0.86	-0.15
maeb	0.931042	-1.17	-1.10	-1.29	-0.66
maep	0.930803	-1.80	-1.50	-1.85	-2.46
maf3	0.917090	-1.43	-1.39	-1.61	-0.74
mafh	0.910755	-1.24	-1.25	-1.47	-0.41
mafw	0.827738	-0.80	-1.13	-1.44	0.05
mald	0.957969	-0.25	-0.26	-0.31	0.08
malk	0.832770	-0.59	-0.88	-1.19	0.13
mar9	0.886158	-0.17	-0.29	-0.53	0.50
mazo	0.922699	-0.53	-0.59	-0.74	0.14
mb11	0.901548	-0.50	-0.55	-0.77	0.15
mb1f	0.782128	-0.27	-0.92	-1.24	0.15
mb1n	0.949241	-0.30	-0.29	-0.37	-0.11
mb21	0.954291	-2.34	-2.28	-2.40	-1.88
mb2m	0.878603	-0.06	-0.31	-0.50	0.37
mb9o	0.912307	-0.94	-1.11	-1.27	-0.44
mbdz	0.917997	-2.37	-2.47	-2.63	-2.04
mbg5	0.944002	-1.22	-1.31	-1.34	-0.94
mbgc	0.779403	-0.19	-0.88	-1.18	0.33
bias		-0.92	-1.00	-1.21	-0.32
rms		0.73	0.68	0.71	0.77
Q		1.18	1.21	1.40	0.83

Table A.7: The complete results for the methods of H&M [*Harris and Mason*, 1992], Sob93 [*Sobrino et al.*, 1993] and Sob94 [*Sobrino et al.*, 1994] for the "5d-after" sondes. The value of R_{54} was calculated using LOWTRAN-7 from the first-guess atmospheric profiles from Hobart.

IFUT	R_{54}	H&M	Sob93	Sob94
m9jr	0.839011	-0.07	-0.42	-0.67
m9k5	0.907531	0.08	0.01	-0.15
m9kc	0.901236	-0.42	-0.64	-0.76
m9n9	0.879892	-1.96	-1.94	-2.25
m9na	0.904545	-0.59	-0.54	-0.79
m9vi	0.953752	-0.41	-0.38	-0.46
ma4c	0.902777	-1.62	-1.82	-1.98
ma4i	0.889152	-0.83	-0.92	-1.17
mabk	0.969747	-0.41	-0.20	-0.37
mabz	0.926357	-1.78	-1.57	-1.89
mac6	0.962810	-0.78	-0.71	-0.79
macc	0.942751	-0.91	-0.63	-0.94
macd	0.903963	-1.75	-1.74	-2.01
macq	0.896147	-2.80	-2.70	-3.04
macr	0.931075	-0.62	-0.60	-0.77
mad5	0.946491	-0.75	-0.77	-0.87
maeb	0.948086	-1.19	-1.06	-1.23
maep	0.953724	-1.87	-1.47	-1.82
maf3	0.911997	-1.42	-1.41	-1.63
mafh	0.914528	-1.25	-1.24	-1.46
mafw	0.914374	-1.01	-0.92	-1.19
mald	0.939245	-0.23	-0.33	-0.41
malk	0.885234	-0.72	-0.75	-1.04
mar9	0.911489	-0.22	-0.22	-0.44
mazo	0.956252	-0.58	-0.48	-0.60
mb11	0.914824	-0.52	-0.52	-0.73
mb1f	0.810134	-0.34	-0.83	-1.12
mb1n	0.930034	-0.28	-0.35	-0.46
mb21	0.929019	-2.31	-2.36	-2.51
mb2m	0.944441	-0.15	-0.09	-0.22
mb9o	0.919351	-0.94	-1.08	-1.23
mbdz	0.965013	-2.42	-2.31	-2.43
mbg5	0.932506	-1.22	-1.36	-1.40
mbgc	0.907115	-0.46	-0.48	-0.67
bias		-0.96	-0.97	-1.16
rms		0.73	0.69	0.72
Q		1.21	1.19	1.37

Table A.8: The complete results for the DWVT, H&M [*Harris and Mason*, 1992], Sob93 [*Sobrino et al.*, 1993] and Sob94 [*Sobrino et al.*, 1994] methods for the "5d-after" sondes. The value of R_{54} was calculated using LOWTRAN-7 from the final DWVT atmospheric profiles. The first-guess profiles came from Hobart.

IFUT	R_{54}	H&M	Sob93	Sob94	DWVT
m9jr	0.887532	-0.16	-0.28	-0.49	0.41
m9k5	0.925533	0.05	0.07	-0.09	0.68
m9kc	0.948817	-0.47	-0.47	-0.53	0.12
m9n9	0.808397	-1.74	-2.08	-2.41	-0.67
m9na	0.879883	-0.53	-0.60	-0.86	0.13
m9vi	0.966657	-0.42	-0.33	-0.40	0.09
ma4c	0.932991	-1.65	-1.71	-1.84	-1.13
ma4i	0.872767	-0.79	-0.96	-1.22	-0.14
mabk	0.933929	-0.36	-0.30	-0.49	0.29
mabz	0.881385	-1.66	-1.65	-1.98	-0.68
mac6	0.953552	-0.77	-0.74	-0.83	-0.29
macc	0.871829	-0.73	-0.75	-1.08	0.23
macd	0.895772	-1.73	-1.76	-2.03	-0.94
macq	0.832626	-2.61	-2.81	-3.17	-1.54
macr	0.929691	-0.62	-0.60	-0.78	0.10
mad5	0.942690	-0.74	-0.78	-0.89	-0.14
maeb	0.892335	-1.10	-1.21	-1.43	-0.67
maep	0.952370	-1.86	-1.47	-1.83	-3.03
maf3	0.930243	-1.46	-1.36	-1.57	-0.81
mafh	0.890424	-1.20	-1.31	-1.54	-0.36
mafw	0.873969	-0.91	-1.01	-1.30	-0.08
mald	0.961808	-0.25	-0.24	-0.29	0.20
malk	0.856984	-0.65	-0.82	-1.11	0.21
mar9	0.914411	-0.22	-0.21	-0.43	0.44
mazo	0.942507	-0.56	-0.52	-0.66	0.19
mb11	0.923061	-0.54	-0.49	-0.70	0.09
mb1f	0.883126	-0.50	-0.61	-0.85	0.30
mb1n	0.955274	-0.30	-0.26	-0.35	0.09
mb21	0.954780	-2.34	-2.28	-2.40	-1.95
mb2m	0.878498	-0.06	-0.31	-0.50	0.33
mb9o	0.905917	-0.93	-1.13	-1.30	-0.40
mbdz	0.965649	-2.42	-2.31	-2.43	-1.96
mbg5	0.962443	-1.23	-1.24	-1.25	-1.08
mbgc	0.880955	-0.41	-0.56	-0.77	-0.21
bias		-0.94	-0.97	-1.17	-0.36
rms		0.71	0.70	0.74	0.82
Q		1.17	1.20	1.38	0.89

A.3 Complete Set of Results for NESDIS SST Equations

Table A.9: Full set of SST retrieval errors for the selected test set of NESDIS operational algorithms (continues to Table A.10). SST retrieval was performed by applying the 34 (T_4, T_5) pairs of 1987 NOAA-9 brightness temperatures to each of the fixed-coefficient equations listed in Section 4.8. The method acronym and subscript identifies the equations used, thus $MCSST_9$ indicates multichannel SST using NOAA-9 equations (4.9) (night passes) and (4.10) (day passes). The NLSST equations were tested twice; once using the T_{guess} equations listed in Section 4.8.3 (e.g., $NLSST_{11}$), then a second time using NOAA-9 MCSST to provide the first guess (e.g., $NLSST_{11,9}$). Rank orders the methods based on the Q-statistic.

IFUT	$MCSST_9$	$MCSST_{11}$	$MCSST_{12}$	$MCSST_{14}$	$CPSST_{11}$	$NLSST_{11}$
m9jr	0.40	-0.28	-0.21	-0.86	-0.66	-0.54
m9k5	0.50	-0.18	-0.08	-0.74	-0.51	-0.35
m9kc	0.12	-0.78	-0.75	-0.99	-0.80	-0.48
m9n9	-0.84	-0.72	-1.29	-1.87	-1.74	-1.79
m9na	0.17	-0.42	-0.43	-1.11	-1.00	-0.96
m9vi	-0.17	-0.72	-0.66	-1.38	-1.08	-0.73
ma4c	-0.82	-1.96	-1.80	-2.19	-2.03	-1.61
ma4i	-0.11	-0.80	-0.71	-1.53	-1.45	-1.27
mabk	0.30	-0.44	-0.29	-1.13	-1.00	-0.73
mabz	-0.56	-0.67	-1.04	-1.81	-1.84	-1.82
mac6	-0.00	-0.89	-0.96	-1.35	-1.17	-0.81
macc	0.30	0.15	-0.19	-0.94	-0.96	-0.97
macd	-0.85	-1.46	-1.44	-2.29	-2.26	-2.09
macq	-1.53	-1.34	-1.95	-2.66	-2.70	-2.71
macr	-0.01	-0.76	-0.60	-1.40	-1.22	-0.95
mad5	-0.42	-1.09	-0.94	-1.75	-1.44	-0.99
maeb	-0.69	-1.40	-1.24	-2.06	-1.96	-1.76
maep	-0.81	-1.67	-1.46	-2.42	-2.67	-2.75
maf3	-0.78	-1.48	-1.37	-2.16	-2.07	-1.91
mafh	-0.51	-1.21	-1.12	-1.88	-1.74	-1.55
mafw	-0.06	-0.55	-0.63	-1.38	-1.32	-1.23
mald	-0.10	-0.57	-0.54	-1.32	-0.96	-0.47
malk	0.39	-0.76	-0.41	-0.74	-0.90	-0.76
mar9	0.45	-0.25	-0.14	-0.94	-0.83	-0.65
mazo	0.29	-0.99	-0.60	-0.91	-0.82	-0.49
mb11	0.16	-0.54	-0.44	-1.20	-1.07	-0.89
mb1f	0.28	-0.35	-0.34	-1.03	-0.87	-0.74
mb1n	0.42	-0.41	-0.52	-0.88	-0.69	-0.35
mb21	-1.43	-2.36	-2.44	-2.94	-2.79	-2.44
mb2m	0.27	-0.40	-0.28	-1.03	-0.80	-0.53
mb9o	-0.57	-1.29	-1.10	-2.00	-1.73	-1.21
mbdz	-2.06	-2.66	-2.54	-3.43	-3.23	-2.82
mbg5	-0.79	-1.44	-1.66	-1.83	-1.59	-1.19
mbgc	0.21	-0.44	-0.42	-1.00	-0.76	-0.67
bias	-0.26	-0.91	-0.90	-1.56	-1.43	-1.21
rms	0.64	0.63	0.64	0.67	0.70	0.72
Q	0.69	1.11	1.11	1.70	1.59	1.41
Rank	1	5	4	11	10	9

Table A.10: Full set of SST retrieval errors for the selected test set of NESDIS operational algorithms (continued from Table A.9). SST retrieval was performed by applying the 34 (T_4, T_5) pairs of 1987 NOAA-9 brightness temperatures to each of the fixed-coefficient equations listed in Section 4.8. The method acronym and subscript identifies the equations used, thus $MCSST_9$ indicates multichannel SST using NOAA-9 equations (4.9) (night passes) and (4.10) (day passes). The NLSST equations were tested twice; once using the T_{guess} equations listed in Section 4.8.3 (e.g., $NLSST_{11}$), then a second time using NOAA-9 MCSST to provide the first guess (e.g., $NLSST_{11,9}$). Rank orders the methods based on the Q-statistic.

IFUT	$NLSST_{11,9}$	$NLSST_{12}$	$NLSST_{12,9}$	$NLSST_{14}$	$NLSST_{14,9}$
m9jr	-0.48	0.13	0.17	-0.46	-0.37
m9k5	-0.29	0.35	0.38	-0.24	-0.17
m9kc	-0.43	0.19	0.22	-0.39	-0.35
m9n9	-1.72	-1.23	-1.19	-1.80	-1.70
m9na	-0.88	-0.27	-0.22	-0.90	-0.79
m9vi	-0.70	0.09	0.11	-0.53	-0.49
ma4c	-1.55	-0.73	-0.69	-1.49	-1.44
ma4i	-1.19	-0.37	-0.33	-1.09	-0.99
mabk	-0.66	0.20	0.24	-0.52	-0.44
mabz	-1.73	-1.01	-0.96	-1.71	-1.59
mac6	-0.75	0.02	0.06	-0.71	-0.66
macc	-0.88	-0.19	-0.15	-0.88	-0.76
macd	-2.00	-1.16	-1.11	-1.90	-1.79
macq	-2.63	-1.95	-1.91	-2.62	-2.51
macr	-0.89	-0.07	-0.03	-0.76	-0.68
mad5	-0.95	-0.05	-0.03	-0.74	-0.69
maeb	-1.69	-0.87	-0.83	-1.58	-1.49
maep	-2.62	-1.78	-1.70	-2.62	-2.45
maf3	-1.83	-1.05	-1.01	-1.75	-1.65
mafh	-1.48	-0.72	-0.68	-1.39	-1.30
mafw	-1.15	-0.43	-0.38	-1.11	-1.00
mald	-0.44	0.45	0.46	-0.21	-0.18
malk	-0.66	-0.09	-0.02	-0.66	-0.57
mar9	-0.58	0.21	0.26	-0.48	-0.39
mazo	-0.43	0.25	0.29	-0.39	-0.33
mb11	-0.82	-0.06	-0.02	-0.74	-0.65
mb1f	-0.66	0.01	0.05	-0.62	-0.53
mb1n	-0.29	0.45	0.49	-0.25	-0.20
mb21	-2.36	-1.49	-1.44	-2.33	-2.26
mb2m	-0.48	0.29	0.32	-0.35	-0.29
mb9o	-1.17	-0.15	-0.13	-0.91	-0.86
mbdz	-2.77	-1.80	-1.78	-2.55	-2.49
mbg5	-1.16	-0.53	-0.51	-1.09	-1.07
mbgc	-0.61	-0.07	-0.03	-0.62	-0.54
bias	-1.15	-0.40	-0.36	-1.07	-0.99
rms	0.71	0.69	0.68	0.72	0.71
Q	1.35	0.79	0.77	1.29	1.22
Rank	8	3	2	7	6

Appendix B

Additional SimWVT Results

B.1 Comparison Tables for SimWVT and DWVT

Tables containing detailed comparison between the SimWVT and DWVT SST results for both radiosonde sites and the different sonde selections are presented here. As a way of comparing the SimWVT and DWVT results, the tables have a column reporting relative change from the DWVT results in percentage for each pass. It is calculated as:

$$\text{Rel. Change} \;=\; 100 \cdot \left(\frac{|\text{SST}_{\text{Sim WVT}} - \text{SST}_{\text{Buoy}}|}{|\text{SST}_{\text{DWVT}} - \text{SST}_{\text{Buoy}}|} - 1 \right).$$

A negative relative change means the SimWVT reported a smaller absolute SST error than the DWVT for the same satellite pass. The passes are then ranked based on the relative improvement.

B.1.1 Comparison Tables of SimWVT and DWVT for the Hobart Sondes

Table B.1: SimWVT and DWVT SST errors for the "5d-before" sondes from Hobart. The passes are ranked according to the Relative Change column.

IFUT	SimWVT	DWVT	Rel. Change	Rank
m9jr	0.47	0.47	0.0%	14
m9k5	0.69	0.68	1.5%	17
m9kc	0.07	0.14	-50.0%	2
m9n9	-0.46	-0.65	-29.2%	3
m9na	0.22	0.12	83.3%	33
m9vi	0.11	0.06	83.3%	34
ma4c	-0.98	-1.08	-9.3%	9
ma4i	-0.13	-0.12	8.3%	20
mabk	0.35	0.36	-2.8%	13
mabz	-0.75	-0.66	13.6%	22
mac6	-0.30	-0.31	-3.2%	12
macc	0.01	-0.35	-97.1%	1
macd	-1.05	-0.94	11.7%	21
macq	-1.72	-1.65	4.2%	18
macr	0.08	0.08	0.0%	15
mad5	-0.20	-0.23	-13.0%	5
maeb	-0.86	-0.68	26.5%	28
maep	-3.15	-3.41	-7.6%	10
maf3	-1.11	-0.73	52.1%	31
mafh	-0.54	-0.46	17.4%	24
mafw	-0.07	-0.04	75.0%	32
mald	0.23	0.18	27.8%	29
malk	0.14	0.18	-22.2%	4
mar9	0.47	0.40	17.5%	25
mazo	0.14	0.16	-12.5%	7
mb11	0.28	0.24	16.7%	23
mb1f	0.27	0.31	-12.9%	6
mb1n	0.17	0.13	30.8%	30
mb21	-1.90	-1.99	-4.5%	11
mb2m	0.40	0.37	8.1%	19
mb9o	-0.42	-0.47	-10.6%	8
mbdz	-1.95	-1.93	1.0%	16
mbg5	-0.92	-0.77	19.5%	27
mbgc	0.40	0.34	17.6%	26
bias	-0.35	-0.36		
rms	0.85	0.86		
Q	0.92	0.93		

Table B.2: SimWVT and DWVT SST errors for the "closest" sondes from Hobart. The passes are ranked according to the Relative Change column.

IFUT	SimWVT	DWVT	Rel. Change	Rank
m9jr	0.29	0.36	-19.4%	3
m9k5	0.79	0.71	11.3%	21
m9kc	0.09	0.14	-35.7%	1
m9n9	-0.71	-0.61	16.4%	23
m9na	0.20	0.26	-23.1%	2
m9vi	0.04	0.04	0.0%	14
ma4c	-1.05	-1.02	2.9%	19
ma4i	-0.17	-0.12	41.7%	30
mabk	0.36	0.32	12.5%	22
mabz	-1.27	-0.68	86.8%	31
mac6	-0.22	-0.23	-4.3%	11
macc	0.22	0.24	-8.3%	8
macd	-1.21	-0.88	37.5%	27
macq	-1.91	-1.58	20.9%	25
macr	0.19	0.16	18.8%	24
mad5	-0.16	-0.16	0.0%	15
maeb	-0.70	-0.69	1.4%	18
maep	-2.47	-2.46	0.4%	17
maf3	-0.70	-0.74	-5.4%	10
mafh	-0.43	-0.41	4.9%	20
mafw	0.05	0.05	0.0%	16
mald	0.24	0.07	242.9%	34
malk	0.18	0.13	38.5%	28
mar9	0.39	0.47	-17.0%	5
mazo	0.16	0.13	23.1%	26
mb11	0.18	0.13	38.5%	29
mb1f	0.34	0.15	126.7%	33
mb1n	-0.09	-0.11	-18.2%	4
mb21	-1.84	-1.91	-3.7%	12
mb2m	0.56	0.27	107.4%	32
mb9o	-0.41	-0.45	-8.9%	7
mbdz	-1.90	-2.02	-5.9%	9
mbg5	-0.78	-0.87	-10.3%	6
mbgc	0.31	-0.32	-3.1%	13
bias	-0.34	-0.34		
rms	0.81	0.75		
Q	0.87	0.82		

Table B.3: SimWVT and DWVT SST errors for the "5d-after" sondes from Hobart. The passes are ranked according to the Relative Change column.

IFUT	SimWVT	DWVT	Rel. Change	Rank
m9jr	0.39	0.41	-4.9%	16
m9k5	0.73	0.68	7.4%	25
m9kc	0.23	0.12	91.7%	34
m9n9	-0.64	-0.67	-4.5%	18
m9na	0.17	0.13	30.8%	32
m9vi	0.03	0.09	-66.7%	1
ma4c	-0.95	-1.13	-15.9%	10
ma4i	-0.17	-0.14	21.4%	29
mabk	0.12	0.29	-58.6%	2
mabz	-0.75	-0.68	10.3%	26
mac6	-0.24	-0.29	-17.2%	9
macc	0.22	0.23	-4.3%	19
macd	-0.88	-0.94	-6.4%	15
macq	-1.60	-1.54	3.9%	23
macr	0.13	0.10	30.0%	31
mad5	-0.11	-0.14	-21.4%	8
maeb	-0.57	-0.67	-14.9%	12
maep	-2.81	-3.03	-7.3%	14
maf3	-0.83	-0.81	2.5%	21
mafh	-0.32	-0.36	-11.1%	13
mafw	0.05	-0.08	-37.5%	6
mald	0.17	0.20	-15.0%	11
malk	0.20	0.21	-4.8%	17
mar9	0.46	0.44	4.5%	24
mazo	0.14	0.19	-26.3%	7
mb11	0.04	0.09	-55.6%	3
mb1f	0.35	0.30	16.7%	28
mb1n	0.04	0.09	-55.6%	4
mb21	-1.96	-1.95	0.5%	20
mb2m	0.48	0.33	45.5%	33
mb9o	-0.23	-0.40	-42.5%	5
mbdz	-2.02	-1.96	3.1%	22
mbg5	-1.22	-1.08	13.0%	27
mbgc	-0.27	-0.21	28.6%	30
bias	-0.34	-0.36		
rms	0.81	0.82		
Q	0.87	0.89		

B.1.2 Comparison Tables of SimWVT and DWVT for the Mt. Gambier Sondes

Table B.4: SimWVT and DWVT SST errors for the "5d-before" sondes from Mt. Gambier. The passes are ranked according to the Relative Change column.

IFUT	SimWVT	DWVT	Rel. Change	Rank
m9jr	0.63	0.61	3.3%	24
m9k5	0.77	0.77	0.0%	19
m9kc	0.15	0.15	0.0%	20
m9n9	-0.56	-1.86	-69.9%	3
m9na	0.32	-2.64	-87.9%	1
m9vi	0.09	0.11	-18.2%	9
ma4c	-1.10	-1.18	-6.8%	13
ma4i	-0.14	-0.15	-6.7%	14
mabk	0.42	0.30	40.0%	33
mabz	-0.87	-0.71	22.5%	31
mac6	-0.22	-0.32	-31.3%	5
macc	0.05	0.21	-76.2%	2
macd	-0.89	-0.93	-4.3%	18
macq	-1.46	-1.61	-9.3%	11
macr	0.15	0.10	50.0%	34
mad5	-0.39	-0.35	11.4%	27
maeb	-0.63	-0.63	0.0%	21
maep	-2.35	-3.13	-24.9%	8
maf3	-0.78	-0.77	1.3%	22
mafh	-0.43	-0.46	-6.5%	15
mafw	-0.06	-0.08	-25.0%	7
mald	0.25	0.23	8.7%	26
malk	0.23	0.22	4.5%	25
mar9	0.53	0.52	1.9%	23
mazo	0.33	0.27	22.2%	30
mb11	0.32	0.27	18.5%	29
mb1f	0.17	0.25	-32.0%	4
mb1n	0.21	0.18	16.7%	28
mb21	-1.92	-2.02	-5.0%	17
mb2m	0.57	0.41	39.0%	32
mb9o	-0.31	-0.44	-29.5%	6
mbdz	-1.92	-2.12	-9.4%	10
mbg5	-0.73	-0.78	-6.4%	16
mbgc	0.30	0.33	-9.1%	12
bias	-0.27	-0.45		
rms	0.78	0.98		
Q	0.83	1.08		

Table B.5: SimWVT and DWVT SST errors for the "closest" sondes from Mt. Gambier. The passes are ranked according to the Relative Change column.

IFUT	SimWVT	DWVT	Rel. Change	Rank
m9jr	0.65	0.54	20.4%	27
m9k5	0.68	0.59	15.3%	24
m9kc	0.06	-0.01	500.0%	32
m9n9	-0.90	-0.65	38.5%	29
m9na	0.24	0.27	-11.1%	12
m9vi	0.18	0.10	80.0%	31
ma4c	-1.14	-1.08	5.6%	19
ma4i	-0.03	-0.11	-72.7%	4
mabk	0.38	0.32	18.8%	25
mabz	-0.63	-0.55	14.5%	23
mac6	-0.22	-0.26	-15.4%	9
macc	0.34	0.34	0.0%	17
macd	-0.82	-0.85	-3.5%	14
macq	-1.68	-1.54	9.1%	20
macr	0.13	0.16	-18.8%	8
mad5	-0.18	-0.19	-5.3%	13
maeb	-0.71	0.01	7000.0%	34
maep	-2.67	-2.70	-1.1%	16
maf3	-0.73	-0.71	2.8%	18
mafh	-0.54	-0.41	31.7%	28
mafw	-0.09	-0.27	-66.7%	5
mald	0.18	0.15	20.0%	26
malk	0.15	0.17	-11.8%	11
mar9	0.56	0.51	9.8%	21
mazo	0.29	-1.53	-81.0%	2
mb11	0.19	0.17	11.8%	22
mb1f	0.18	0.11	63.6%	30
mb1n	0.24	-0.98	-75.5%	3
mb21	-1.92	-3.80	-49.5%	6
mb2m	-0.01	-0.67	-98.5%	1
mb9o	-0.36	-0.51	-29.4%	7
mbdz	-2.00	-2.05	-2.4%	15
mbg5	-0.84	-0.98	-14.3%	10
mbgc	0.34	0.03	1033.3%	33
bias	-0.31	-0.48		
rms	0.81	0.96		
Q	0.87	1.07		

Table B.6: SimWVT and DWVT SST errors for the "5d-after" sondes from Mt. Gambier. The passes are ranked according to the Relative Change column.

IFUT	SimWVT	DWVT	Rel. Change	Rank
m9jr	0.59	0.59	0.0%	14
m9k5	0.71	0.72	-1.4%	13
m9kc	0.10	0.13	-23.1%	5
m9n9	-0.87	-0.59	47.5%	31
m9na	0.23	0.32	-28.1%	4
m9vi	0.15	0.13	15.4%	25
ma4c	-1.18	-1.15	2.6%	17
ma4i	0.04	-0.18	-77.8%	1
mabk	0.33	0.31	6.5%	21
mabz	-0.62	-0.65	-4.6%	11
mac6	-0.33	-0.33	0.0%	15
macc	0.23	0.22	4.5%	19
macd	-0.90	-0.96	-6.2%	10
macq	-1.66	-1.58	5.1%	20
macr	0.16	0.12	33.3%	29
mad5	-0.10	-0.16	-37.5%	2
maeb	-0.74	-0.69	7.2%	24
maep	-2.51	-2.89	-13.1%	8
maf3	-0.79	-0.74	6.8%	22
mafh	-0.47	-0.44	6.8%	23
mafw	-0.06	-0.02	200.0%	32
mald	0.25	0.18	38.9%	30
malk	0.15	0.18	-16.7%	6
mar9	0.55	0.47	17.0%	27
mazo	0.20	0.17	17.6%	28
mb11	0.17	0.25	-32.0%	3
mb1f	0.30	0.31	-3.2%	12
mb1n	-0.22	0.00	∞%	34
mb21	-2.25	-1.94	16.0%	26
mb2m	0.47	0.46	2.2%	16
mb9o	-0.74	-0.71	4.2%	18
mbdz	-2.04	-2.18	-6.4%	9
mbg5	-0.84	-0.98	-14.3%	7
mbgc	0.34	0.07	385.7%	33
bias	-0.33	-0.34		
rms	0.83	0.84		
Q	0.89	0.90		

B.2 Graphs of SimWVT SST Residuals

The graphs of this section depict the relationship between the SimWVT SST residuals (SimWVT SST errors) and a group of intrinsic variables most important to the SimWVT algorithm: channel-4 and -5 average atmospheric temperatures ($\overline{T}_{a4}$ and $\overline{T}_{a5}$), their difference from the first-guess profile values ($\Delta\overline{T}_{a4}$ and $\Delta\overline{T}_{a5}$), the total water vapour column for the final SimWVT profile (W), its difference from the first-guess profile value (ΔW), and buoy-measured ("ground truth") SST. Any observed trend between the SimWVT SST residuals and these variables would suggest some kind of inadequacy of the SimWVT algorithm.

B.2.1 SST Residual Graphs for the Hobart Sondes

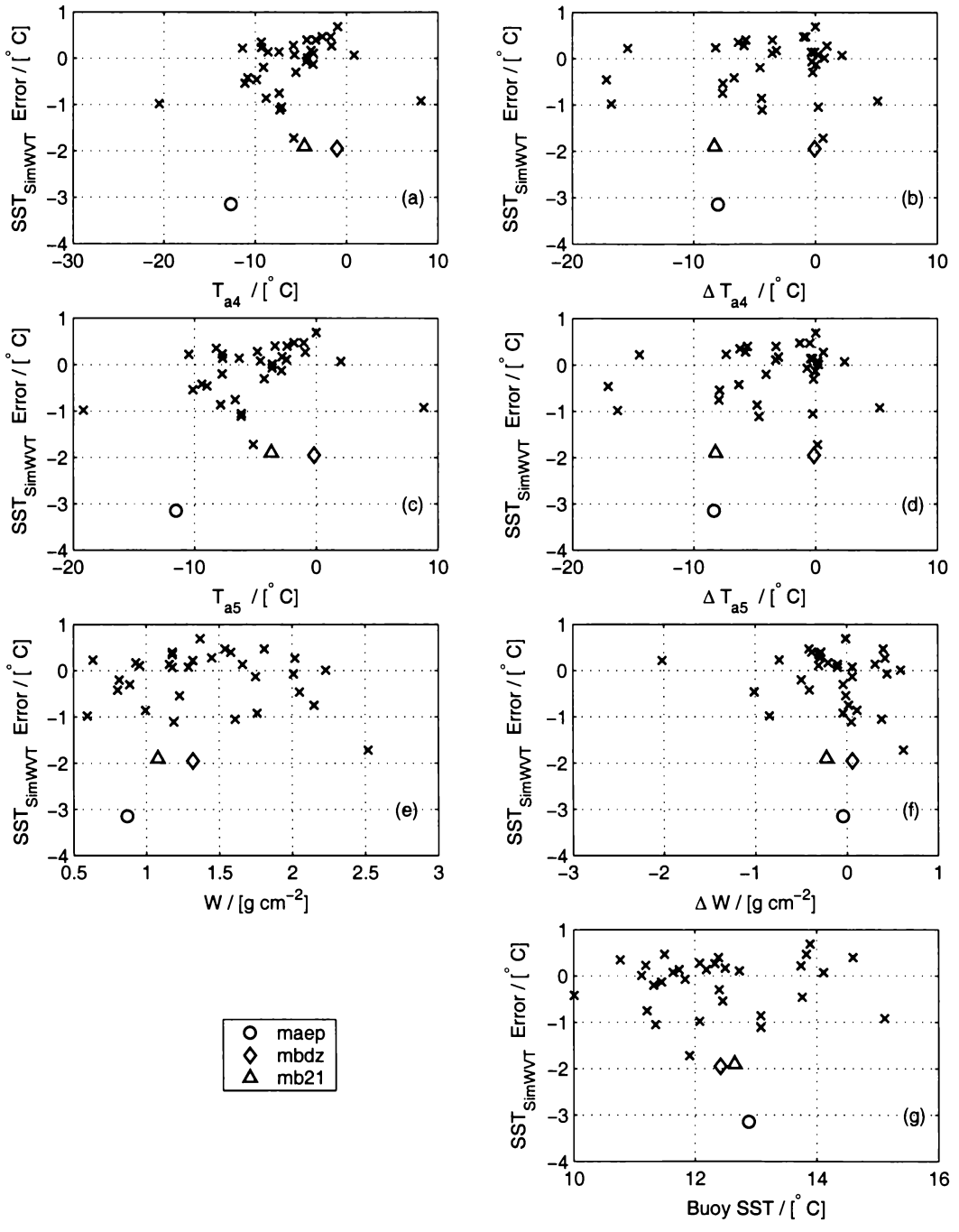

Figure B.1: SimWVT SST residuals vs. channel-4 (a) and -5 (c) average atmospheric temperatures, their difference from the first-guess profile values (b) and (d), the total water vapour column for the final SimWVT profile (e), its difference from the first-guess profile value (f), and buoy-measured SST (g). First-guess sondes were from Hobart; sonde selection mode was "5d-before". The satellite passes with the three largest SST residuals are labelled separately, in the descending order.

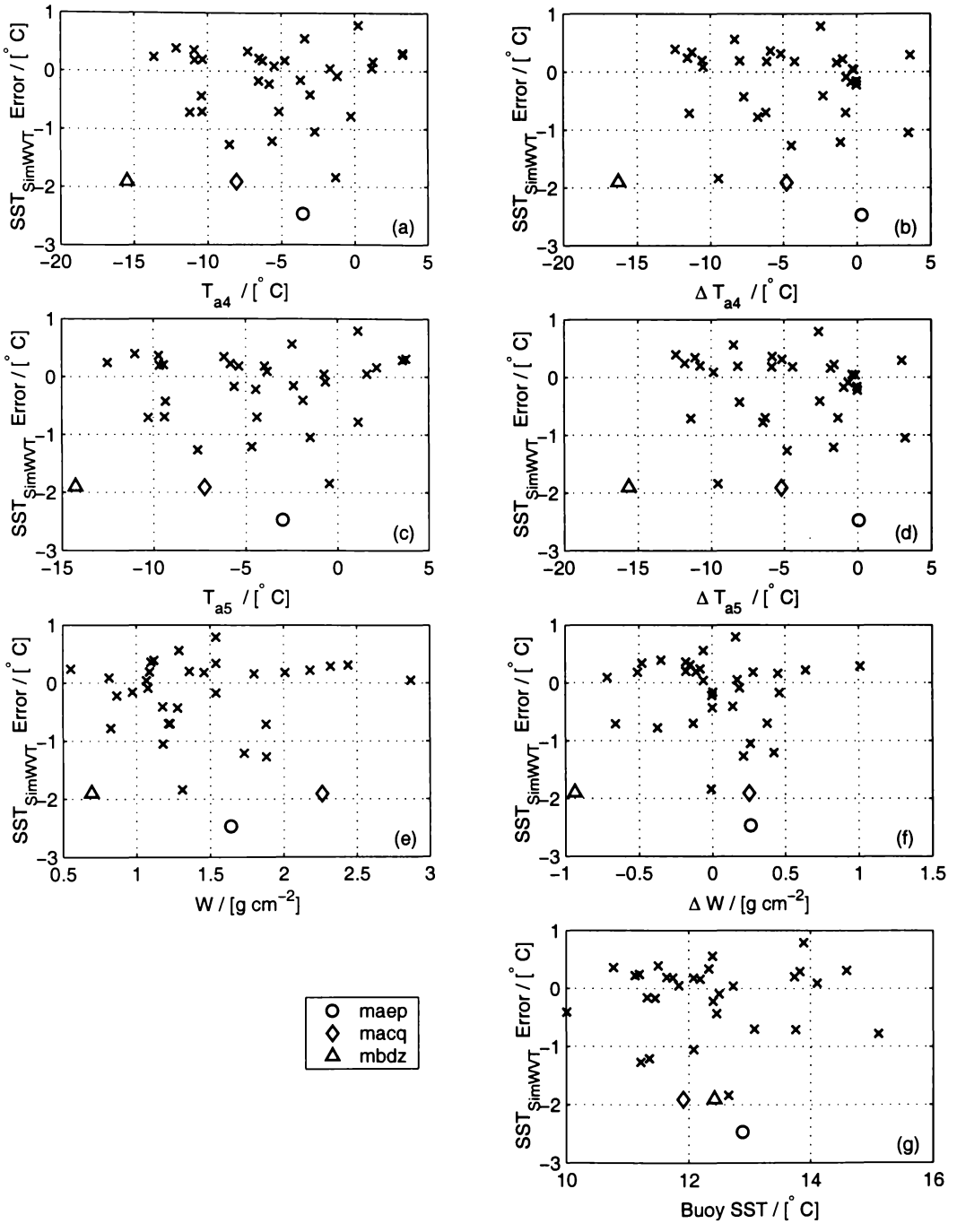

Figure B.2: SimWVT SST residuals vs. channel-4 (a) and -5 (c) average atmospheric temperatures, their difference from the first-guess profile values (b) and (d), the total water vapour column for the final SimWVT profile (e), its difference from the first-guess profile value (f), and buoy-measured SST (g). First-guess sondes were from Hobart; sonde selection mode was "closest". The satellite passes with the three largest SST residuals are labelled separately, in the descending order.

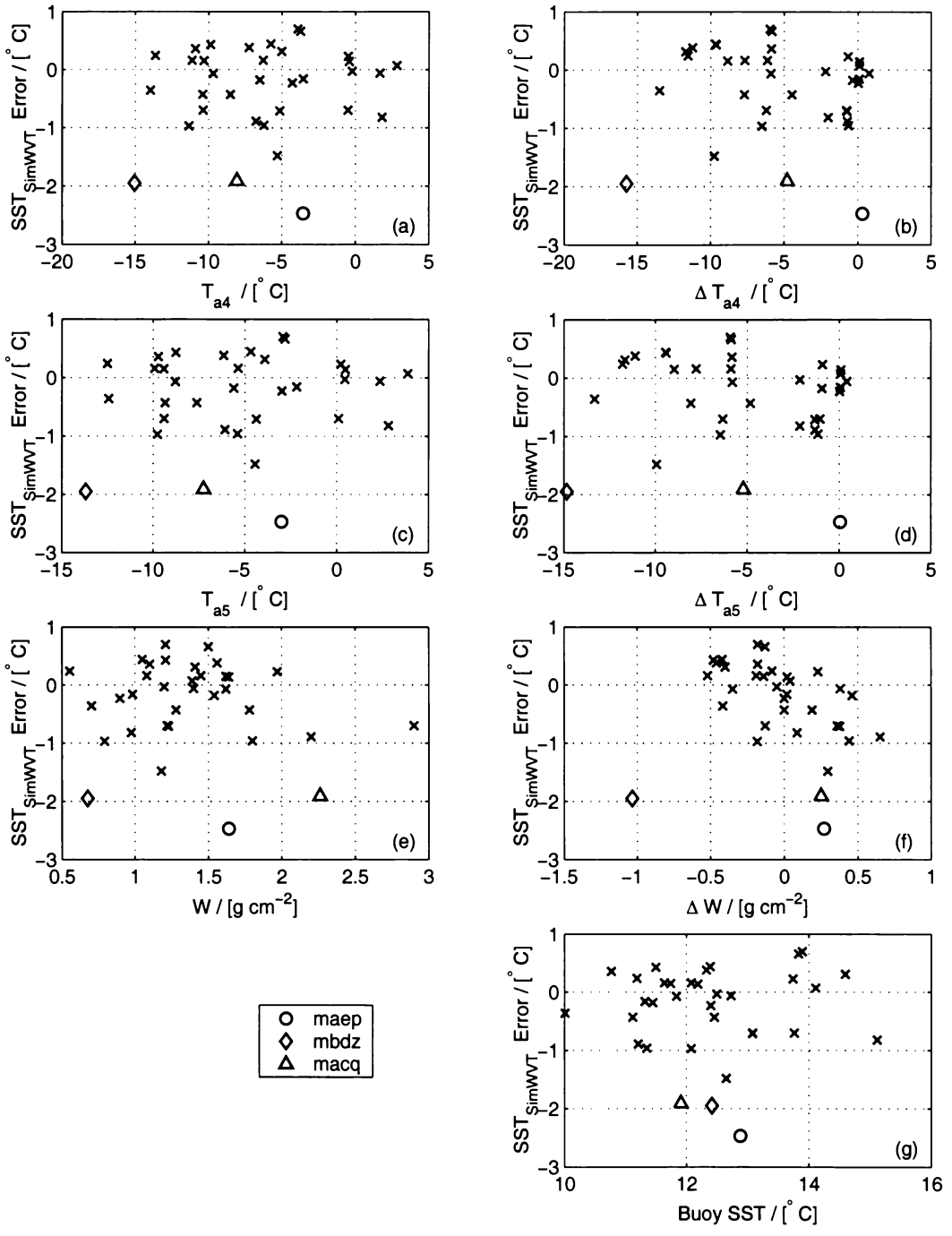

Figure B.3: SimWVT SST residuals vs. channel-4 (a) and -5 (c) average atmospheric temperatures, their difference from the first-guess profile values (b) and (d), the total water vapour column for the final SimWVT profile (e), its difference from the first-guess profile value (f), and buoy-measured SST (g). First-guess sondes were from Hobart; sonde selection mode was "night/day". The satellite passes with the three largest SST residuals are labelled separately, in the descending order.

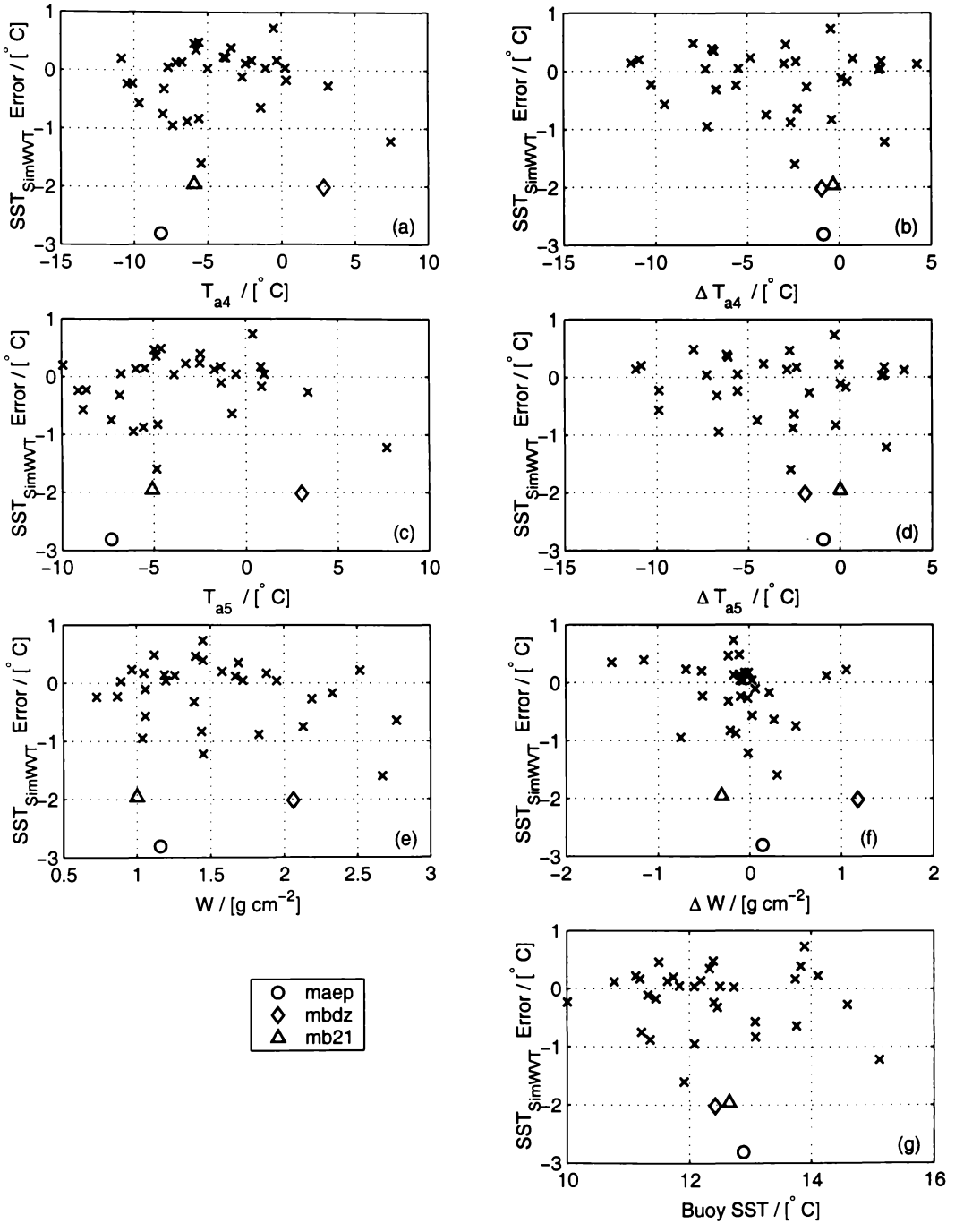

Figure B.4: SimWVT SST residuals vs. channel-4 (a) and -5 (c) average atmospheric temperatures, their difference from the first-guess profile values (b) and (d), the total water vapour column for the final SimWVT profile (e), its difference from the first-guess profile value (f), and buoy-measured SST (g). First-guess sondes were from Hobart; sonde selection mode was "5d-after". The satellite passes with the three largest SST residuals are labelled separately, in the descending order.

B.2.2 SST Residual Graphs for the Mt. Gambier Sondes

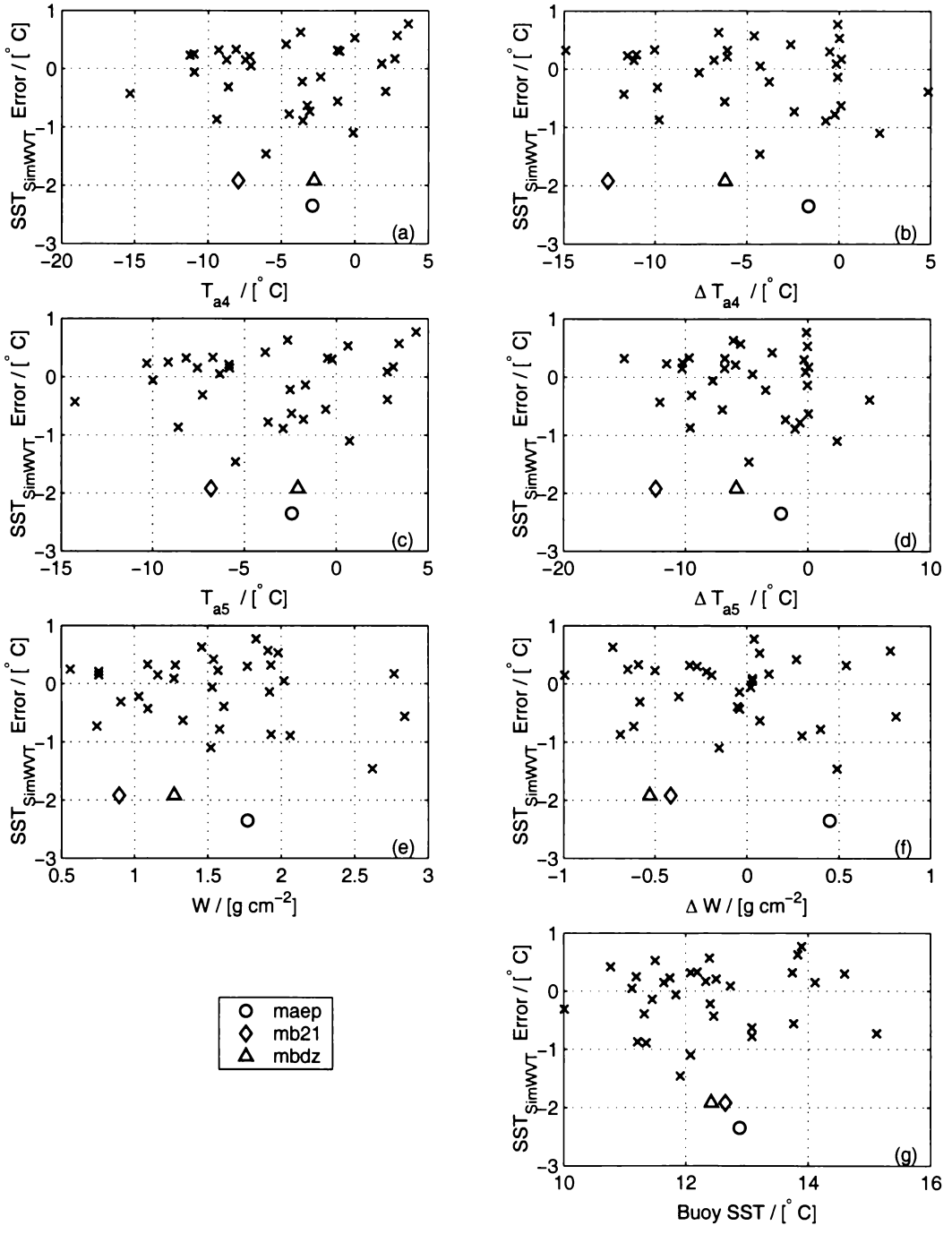

Figure B.5: SimWVT SST residuals vs. channel-4 (a) and -5 (c) average atmospheric temperatures, their difference from the first-guess profile values (b) and (d), the total water vapour column for the final SimWVT profile (e), its difference from the first-guess profile value (f), and buoy-measured SST (g). First-guess sondes were from Mt. Gambier; sonde selection mode was "5d-before". The satellite passes with the three largest SST residuals are labelled separately, in the descending order.

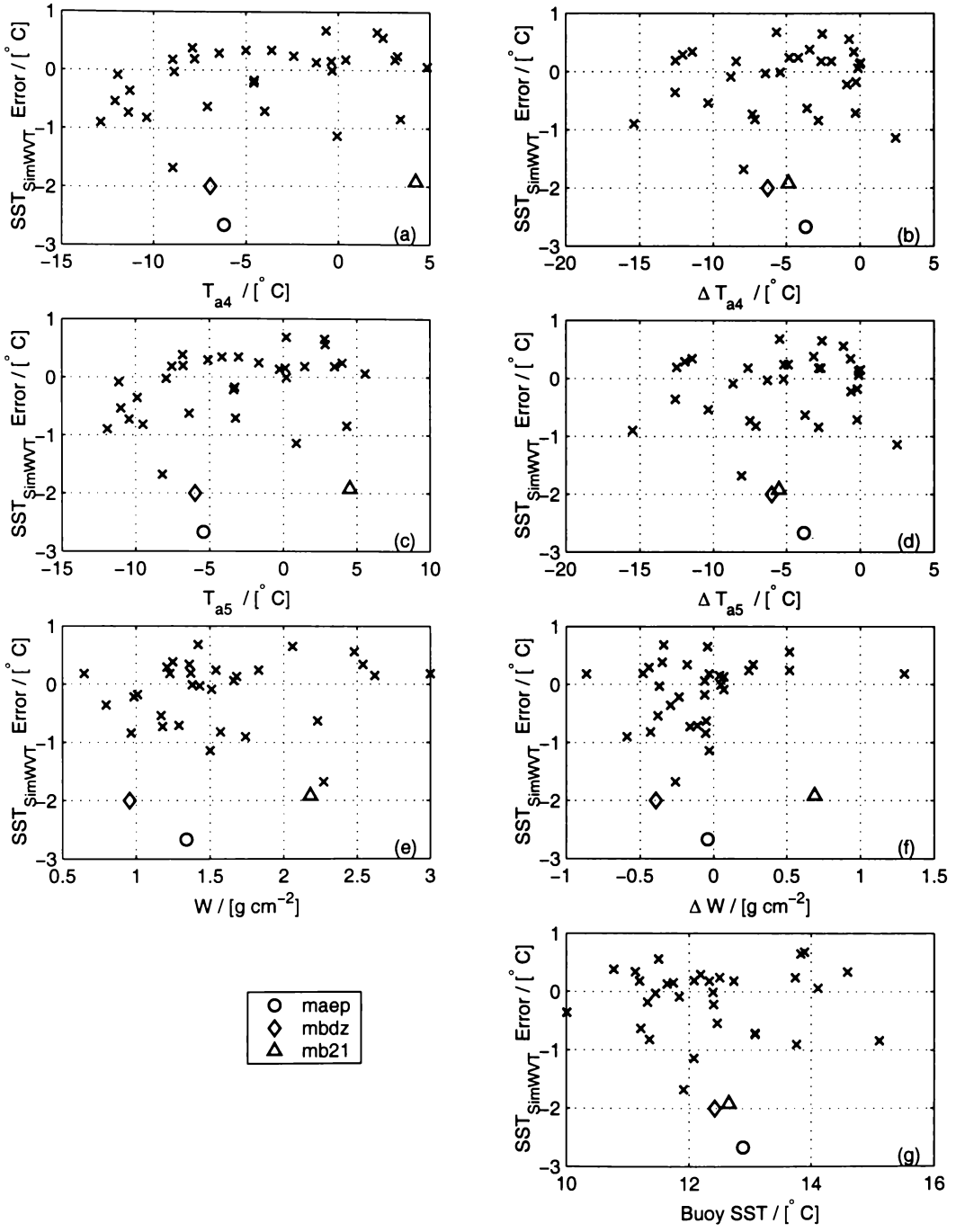

Figure B.6: SimWVT SST residuals vs. channel-4 (a) and -5 (c) average atmospheric temperatures, their difference from the first-guess profile values (b) and (d), the total water vapour column for the final SimWVT profile (e), its difference from the first-guess profile value (f), and buoy-measured SST (g). First-guess sondes were from Mt. Gambier; sonde selection mode was "closest". The satellite passes with the three largest SST residuals are labelled separately, in the descending order.

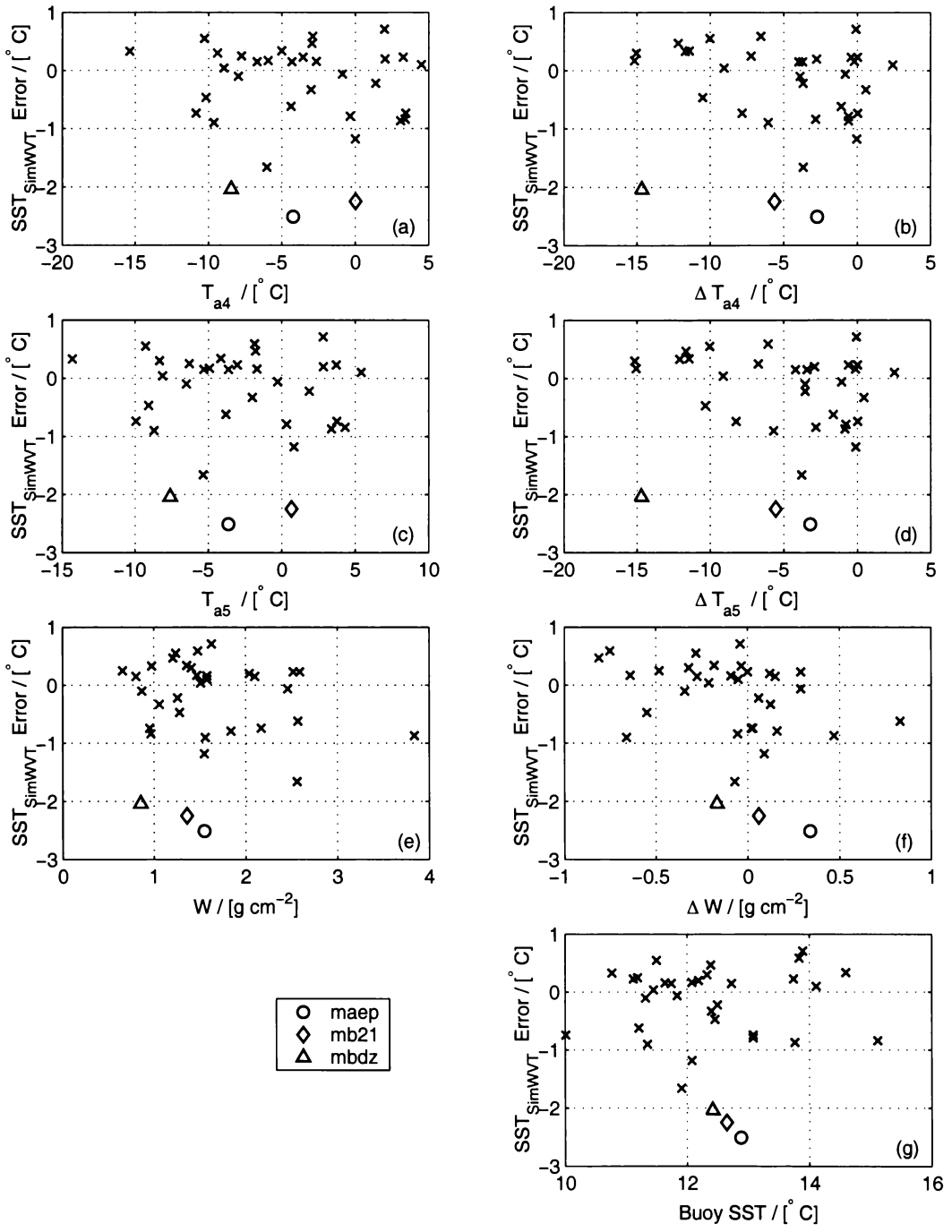

Figure B.7: SimWVT SST residuals vs. channel-4 (a) and -5 (c) average atmospheric temperatures, their difference from the first-guess profile values (b) and (d), the total water vapour column for the final SimWVT profile (e), its difference from the first-guess profile value (f), and buoy-measured SST (g). First-guess sondes were from Mt. Gambier; sonde selection mode was "5d-after". The satellite passes with the three largest SST residuals are labelled separately, in the descending order.

Appendix C

Accompanying Results for the Pasture Biomass Remote Sensing Study

C.1 Description of Test Plots

Descriptions of the test plots as received from AgResearch Ltd. and Dexcel Ltd. are given in the table below.

Table C.1: Description of the AgResearch and Dexcel test pasture plots.

Plot ID	Description
	AgResearch plots (prefix "P")
P01	Long rank dry grass
P02	Long rank dry grass
P03	Medium length dry grass (mowed)
P04	Medium length dry grass (mowed)
P05	Short dryland grass (mowed)

Table C.1: (continued)

Plot ID	Description
P06	Short dryland grass (mowed)
P07	Medium length, mowed, water+nitrogen
P08	Medium length, water+nitrogen
P09	Medium length, water+nitrogen
P10	Medium length, mowed, water+nitrogen
P11	Medium length, mowed, water+nitrogen
P12	Medium/short, water only
P13	Medium/short, mowed, water only
P14	Medium/short, mowed, water only
P15	Medium, mowed, water only
P16	Medium, mowed, water only
P17	Long, no grazing or mowing, water+nitrogen
P18	Long, no grazing or mowing, water+nitrogen
P19	Medium/short, mowed, water+nitrogen
P20	Medium, water+nitrogen
P21	Medium, water+nitrogen
P22	Medium/short, mowed, water+nitrogen
P23	Medium, water+nitrogen
P24	Medium/short, mowed, water+nitrogen
P25	Long rank and dry
P26	Long rank and dry
P27	Long rank and dry
P28	Very short hard graze (sheep)

Table C.1: (continued)

Plot ID	Description
P29	Very short hard graze (sheep)
P30	Irrigated, long and rank, ungrazed
P31	Irrigated, long and rank, ungrazed
P32	Irrigated, partial graze (cows)
P33	Irrigated, partial graze (cows)
P34	Irrigated, medium graze (cows)
P35	Irrigated, medium graze (cows)
P36	Irrigated, hard graze (cows)
P37	Irrigated, hard graze (cows)
P40	No irrigation, long and rank, ungrazed
P41	No irrigation, long and rank, ungrazed
P42	No irrigation, partial graze (cows)
P43	No irrigation, partial graze (cows)
P44	No irrigation, medium graze (cows)
P45	No irrigation, medium graze (cows)
P46	No irrigation, hard graze (cows)
P47	No irrigation, hard graze (cows)
	Dexcel plots (prefix "DRC")
DRC1	Irrigated, control
DRC2	Irrigated, Ryegrass/white clover
DRC3	Irrigated, turnip mix
DRC4	Irrigated, turnip mix/pasp.
DRC5	Irrigated, Canterbury

Table C.1: (continued)

Plot ID	Description
DRC6	Not irrigated, Ryegrass/white clover
DRC7	Not irrigated, Control
DRC8	Not irrigated, turnip mix/pasp.
DRC9	Not irrigated, turnip mix
DRC10	Not irrigated, Canterbury
DRC11	Irrigated, white clover
DRC12	Not irrigated, red clover
DRC13	Irrigated, lotus edge
DRC14	Irrigated, lotus
DRC15	Irrigated, ryegrass
DRC16	Not irrigated, ryegrass/white clover (low clover)
DRC17	Not irrigated, ryegrass/white clover (high clover)
DRC18	Not irrigated, good turnips
DRC19	Not irrigated, poor turnips
DRC20	Not irrigated, 100% chicory

C.2 Reported Biomass for the Pasture Test Plots

The measured biomass (ground truth) results for the AgResearch and Dexcel plots are shown in the table below. The data was supplied to us from the two organizations.

Table C.2: Measured biomass in kgDM/ha for the AgResearch test pasture plots. The results were given for each patch, "A" to "E". Five patches per plot. "P" prefix in patch IDs is assumed.

Patch ID	Total	Green Leaf	Green Stem	Non Green	Leg. Leaf	Leg. Stem	Inedible
1A	4234	968	142	3124	0	0	0
1B	4249	971	143	3135	0	0	0
1C	3600	823	121	2657	0	0	0
1D	4156	950	139	3066	0	0	0
1E	4295	982	144	3169	0	0	0
2A	4063	1521	580	1928	0	0	34
2B	3733	1398	533	1772	0	0	31
2C	2804	1050	400	1331	0	0	23
2D	2951	1105	421	1401	0	0	25
2E	3601	1348	514	1709	0	0	30
3A	2261	802	244	1069	0	0	146
3B	1858	772	114	764	133	75	0
3C	2776	1023	69	1416	134	125	9
3D	2238	871	230	1025	65	47	0
3E	2376	881	363	1132	0	0	0
4A	2305	1029	123	1152	0	0	0
4B	1908	852	102	954	0	0	0
4C	2033	908	109	1017	0	0	0
4D	2401	1072	128	1200	0	0	0
4E	2028	906	108	1014	0	0	0
5A	1299	643	54	255	140	135	72

Table C.2: (continued)

Patch ID	Total	Green Leaf	Green Stem	Non Green	Leg. Leaf	Leg. Stem	Inedible
5B	1496	741	62	294	161	155	83
5C	1651	817	68	324	178	171	91
5D	1755	869	73	345	189	182	97
5E	1663	823	69	327	179	172	92
6A	1196	608	214	314	0	0	60
6B	1695	932	239	524	0	0	0
6C	1202	701	98	387	0	0	15
6D	1871	1153	158	560	0	0	0
6E	2214	984	110	900	0	0	220
7A	2954	1955	482	369	107	40	0
7B	2492	1649	407	311	91	34	0
7C	3020	1999	493	377	110	41	0
7D	2333	1545	381	291	85	32	0
7E	2533	1677	414	316	92	34	0
8A	2501	1794	390	274	26	12	4
8B	2634	1890	411	288	28	13	4
8C	2691	1930	420	295	28	13	4
8D	2303	1652	359	252	24	11	4
8E	3064	2198	478	336	32	15	5
9A	3514	2424	414	407	13	7	250
9B	3596	2480	423	417	13	7	255
9C	3462	2388	408	401	13	6	246

Table C.2: (continued)

Patch ID	Total	Green Leaf	Green Stem	Non Green	Leg. Leaf	Leg. Stem	Inedible
9D	3338	2302	393	387	12	6	237
9E	2684	1851	316	311	10	5	191
10A	2107	1411	358	237	13	5	83
10B	3506	2349	595	394	21	9	138
10C	3035	2033	515	341	18	8	120
10D	2392	1602	406	269	14	6	94
10E	2757	1847	468	310	17	7	109
11A	3418	2476	649	279	4	3	8
11B	2948	2135	560	240	3	2	7
11C	2970	2151	564	242	3	2	7
11D	3350	2427	636	273	4	3	8
11E	2916	2112	553	238	3	2	7
12A	2924	1948	550	290	0	0	136
12B	2948	2050	578	168	0	0	152
12C	2742	1661	680	192	0	0	208
12D	2711	1293	402	637	0	0	380
12E	3153	2295	521	185	0	0	151
13A	1968	933	238	689	0	0	108
13B	1836	870	222	643	0	0	101
13C	2882	1366	349	1009	0	0	158
13D	2019	957	244	707	0	0	111
13E	2554	1210	309	894	0	0	140

Table C.2: (continued)

Patch ID	Total	Green Leaf	Green Stem	Non Green	Leg. Leaf	Leg. Stem	Inedible
14A	2135	1535	298	302	0	0	0
14B	1610	1041	193	330	0	0	46
14C	2364	1451	344	569	0	0	0
14D	1440	1082	105	196	39	18	0
14E	2059	1060	160	787	30	23	0
15A	2232	1276	181	776	0	0	0
15B	2716	1552	220	944	0	0	0
15C	2302	1316	186	800	0	0	0
15D	2741	1567	222	952	0	0	0
15E	2773	1585	225	964	0	0	0
16A	2457	897	426	1128	0	0	6
16B	1846	769	144	684	0	0	249
16C	1873	771	276	826	0	0	0
16D	2223	1007	166	1050	0	0	0
16E	1716	977	182	556	0	0	0
17A	6559	2822	1474	2263	0	0	0
17B	6711	3164	1424	2064	0	0	60
17C	6094	3058	1355	1574	51	56	0
17D	6262	2642	1240	2241	0	0	139
17E	5421	2383	599	2439	0	0	0
18A	5122	1965	685	2472	0	0	0
18B	6399	2455	855	3089	0	0	0

Table C.2: (continued)

Patch ID	Total	Green Leaf	Green Stem	Non Green	Leg. Leaf	Leg. Stem	Inedible
18C	7194	2760	962	3472	0	0	0
18D	5208	1998	696	2514	0	0	0
18E	5630	2160	753	2718	0	0	0
19A	3187	1622	557	744	155	110	0
19B	2435	1239	425	569	118	84	0
19C	2851	1451	498	666	138	98	0
19D	3048	1551	532	712	148	105	0
19E	3681	1873	643	859	179	127	0
20A	3765	2040	995	456	85	72	117
20B	4277	2317	1130	518	97	82	133
20C	4314	2337	1140	522	98	82	134
20D	3551	1924	938	430	80	68	111
20E	3442	1865	909	417	78	66	107
21A	3382	1615	652	544	140	82	349
21B	2596	1240	501	418	108	63	268
21C	3058	1460	590	492	127	74	315
21D	3052	1457	589	491	127	74	315
21E	3085	1473	595	496	128	75	318
22A	2608	1459	455	196	262	115	121
22B	2451	1169	263	455	402	163	0
22C	2562	1496	332	484	166	84	0
22D	1944	1229	380	100	149	74	12

Table C.2: (continued)

Patch ID	Total	Green Leaf	Green Stem	Non Green	Leg. Leaf	Leg. Stem	Inedible
22E	2403	1339	296	505	224	40	0
23A	2366	933	162	988	192	91	0
23B	2625	1713	524	309	59	20	0
23C	1782	937	104	531	143	67	0
23D	1821	872	166	609	109	46	18
23E	1948	1079	227	238	283	121	0
24A	2861	1366	482	589	213	176	35
24B	4240	2024	715	873	315	261	52
24C	3797	1812	640	782	282	234	47
24D	3711	1771	626	764	276	228	46
24E	3263	1557	550	672	242	201	40
25A	4574	1409	322	2819	15	9	0
25B	4622	1424	325	2848	15	9	0
25C	6234	1921	439	3842	20	12	0
25D	5615	1730	395	3460	18	11	0
25E	4441	1369	312	2737	14	9	0
26A	3526	951	591	1916	38	13	15
26B	5183	834	951	3398	0	0	0
26C	5428	827	1051	3551	0	0	0
26D	5878	1488	244	4069	43	34	0
26E	4136	1295	750	2068	17	6	0
27A	5413	1358	664	2743	0	0	648

Table C.2: (continued)

Patch ID	Total	Green Leaf	Green Stem	Non Green	Leg. Leaf	Leg. Stem	Inedible
27B	4264	1070	523	2161	0	0	510
27C	4357	1093	535	2208	0	0	521
27D	5041	1265	619	2555	0	0	603
27E	4198	1053	515	2127	0	0	502
28A	1572	359	94	1092	0	0	27
28B	1620	402	82	1102	19	16	0
28C	807	280	22	419	20	3	62
28D	619	196	33	281	62	47	0
28E	827	289	6	526	5	2	0
29A	1644	420	64	1111	33	15	0
29B	1529	391	60	1034	31	14	0
29C	928	237	36	627	19	8	0
29D	999	256	39	676	20	9	0
29E	1382	353	54	934	28	12	0
30A	6109	1592	1567	2950	0	0	0
30B	5335	1390	1369	2577	0	0	0
30C	4307	1122	1105	2080	0	0	0
30D	6117	1594	1569	2954	0	0	0
30E	5851	1524	1501	2826	0	0	0
31A	6068	2106	2871	1091	0	0	0
31B	6653	1915	2868	1870	0	0	0
31C	9449	1807	5050	2592	0	0	0

Table C.2: (continued)

Patch ID	Total	Green Leaf	Green Stem	Non Green	Leg. Leaf	Leg. Stem	Inedible
31D	7239	2190	2990	2058	0	0	0
31E	8788	1500	4036	3252	0	0	0
32A	4168	885	1808	1475	0	0	0
32B	6130	1302	2659	2169	0	0	0
32C	6226	1322	2701	2203	0	0	0
32D	5187	1102	2250	1835	0	0	0
32E	4689	996	2034	1659	0	0	0
33A	3643	1134	682	1828	0	0	0
33B	5620	1375	1542	2704	0	0	0
33C	3022	855	895	1272	0	0	0
33D	2865	579	976	1298	0	0	12
33E	3026	792	901	1333	0	0	0
34A	2188	329	404	1455	0	0	0
34B	3996	600	738	2658	0	0	0
34C	4163	626	769	2768	0	0	0
34D	2969	446	548	1974	0	0	0
34E	3762	565	695	2502	0	0	0
35A	2133	525	462	1146	0	0	0
35B	2179	251	511	1418	0	0	0
35C	2496	519	622	1355	0	0	0
35D	1882	327	382	1173	0	0	0
35E	1977	308	620	1049	0	0	0

Table C.2: (continued)

Patch ID	Total	Green Leaf	Green Stem	Non Green	Leg. Leaf	Leg. Stem	Inedible
36A	1983	123	52	1807	0	0	0
36B	1074	61	61	952	0	0	0
36C	1352	311	86	956	0	0	0
36D	882	96	12	774	0	0	0
36E	1686	111	74	1502	0	0	0
37A	1487	203	172	1073	0	0	39
37B	1039	142	121	750	0	0	27
37C	1905	260	221	1374	0	0	50
37D	2166	295	251	1563	0	0	56
37E	1662	227	193	1199	0	0	43
40A	2575	1431	466	679	0	0	0
40B	2888	1605	522	761	0	0	0
40C	3103	1724	561	818	0	0	0
40D	2234	1241	404	589	0	0	0
40E	2226	1237	403	587	0	0	0
41A	3525	1315	745	1370	0	0	94
41B	3233	919	941	946	0	0	427
41C	4026	1250	528	2079	83	86	0
41D	2487	1245	378	777	55	31	0
41E	6016	1071	163	4782	0	0	0
42A	2600	592	706	1166	82	54	0
42B	2700	685	407	1488	0	0	120

Table C.2: (continued)

Patch ID	Total	Green Leaf	Green Stem	Non Green	Leg. Leaf	Leg. Stem	Inedible
42C	1716	389	281	651	181	129	84
42D	1992	559	765	632	23	13	0
42E	2827	822	1173	832	0	0	0
43A	1484	460	596	386	17	15	10
43B	2346	728	942	610	27	23	16
43C	1244	386	500	323	14	12	9
43D	1665	516	669	433	19	16	12
43E	1554	482	624	404	18	15	11
44A	1726	473	949	303	0	0	0
44B	1799	528	334	937	0	0	0
44C	1439	687	406	346	0	0	0
44D	1118	320	174	570	11	44	0
44E	1096	385	403	308	0	0	0
45A	1473	448	309	454	129	133	0
45B	1804	549	378	555	158	163	0
45C	1996	608	418	615	175	181	0
45D	1764	537	370	543	155	160	0
45E	2066	629	433	636	181	187	0
46A	569	156	86	222	6	3	96
46B	503	138	76	196	5	3	85
46C	551	151	83	215	6	3	93
46D	743	203	112	290	8	4	125

Table C.2: (continued)

Patch ID	Total	Green Leaf	Green Stem	Non Green	Leg. Leaf	Leg. Stem	Inedible
46E	707	194	107	276	7	4	119
47A	466	129	45	278	0	0	13
47B	474	135	64	226	0	0	49
47C	756	110	43	574	4	1	24
47D	538	115	42	314	15	10	41
47E	601	170	76	317	28	10	0

Table C.3: Measured biomass in kgDM/ha for the Dexcel test pasture plots.

Plot ID	Biomass
DRC1	1628
DRC2	1341
DRC3	2397
DRC4	1555
DRC5	2788
DRC6	1395
DRC7	2059
DRC8	2491
DRC9	2552
DRC10	1646
DRC11	3688
DRC12	3610
DRC13	3999
DRC14	4140
DRC15	3081
DRC16	4082
DRC17	4690
DRC18	8447
DRC19	3354
DRC20	1530

C.3 Additional Graphs for Canvas Reflectance Measurements

Graphs of coefficients of variation of the spectrum curves for four reflectance standards and two ground calibration targets (Section 8.5) are shown below. The coefficient of variation of a set of observed values is the value that gives the proportion between the standard deviation and the arithmetic mean of the data. It is a relative measure of the spread of values in the data set. The smaller the value of the coefficient of variation, the tighter the spread of the data set values around their mean.

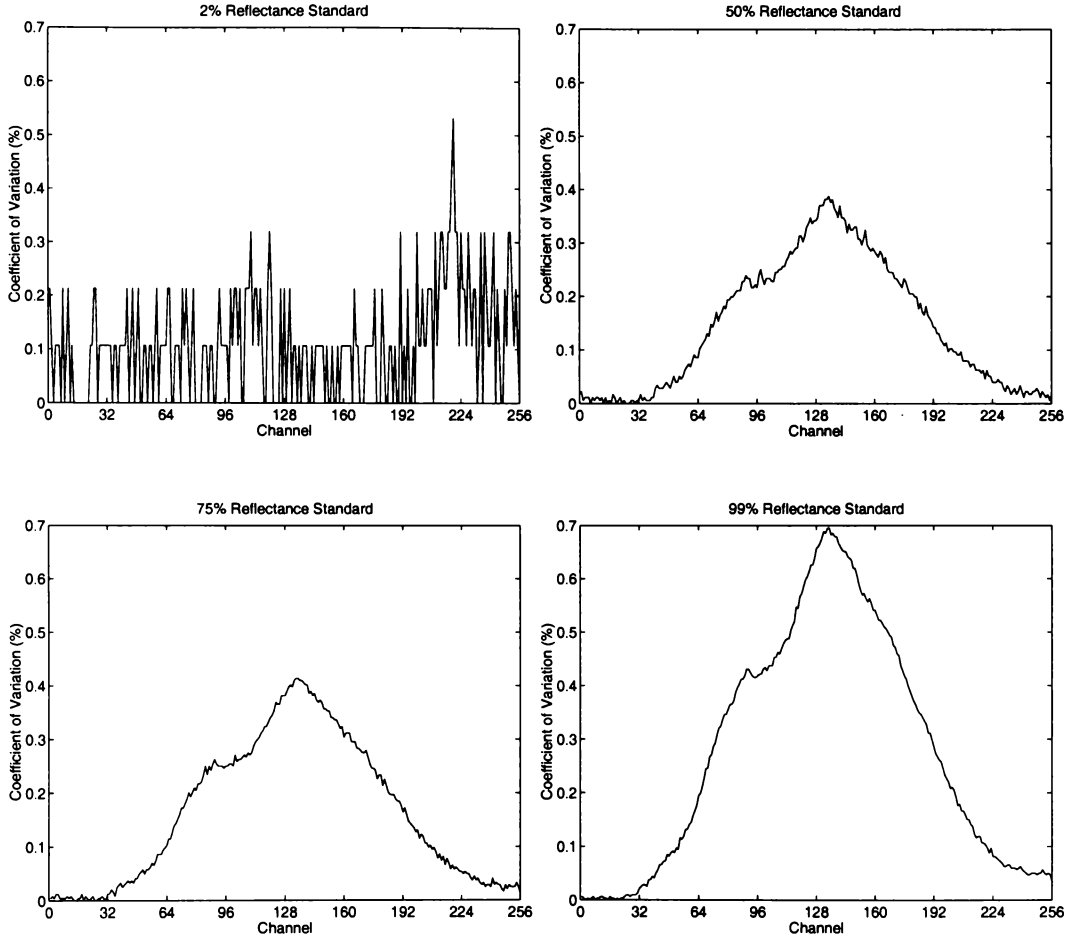

Figure C.1: Coefficients of variation for each spectrometer's channel and four reflectance calibration standards. The coefficients were derived using all available reflectance standards spectra. The values never exceed 0.7%, indicating very reliable measurements. They reduce with a decrease in reflectance, suggesting that the system noise is influenced by the magnitude of the signal as well. The results for the 2% reflectance standard show a typical digital quantization behaviour, caused probably by a low digital count readout, i.e. very close to the dark current measurements.

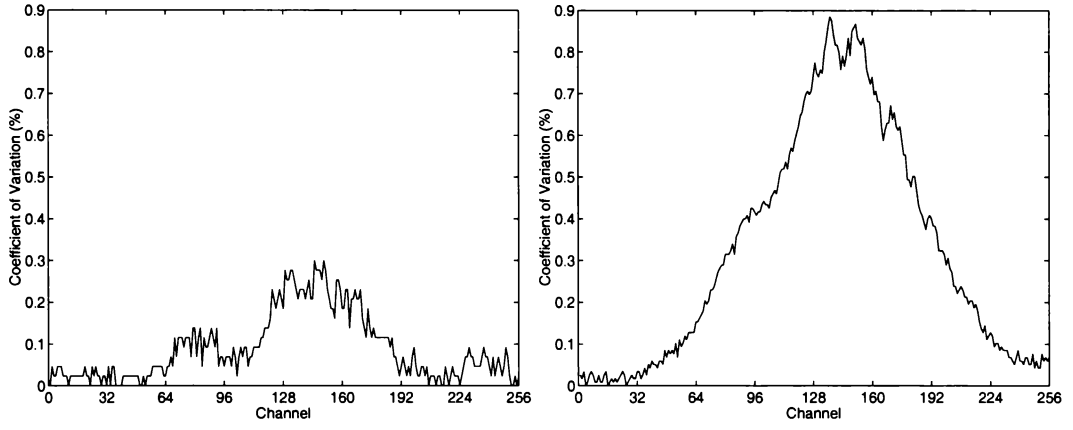

Figure C.2: Coefficients of variation for each spectrometer's channel for the two ground calibration canvases: Federation Green (left) and Dove Gray (right). The coefficients were derived using all available canvas spectrum measurements.

C.4 Images Produced for Radiometric Correction

C.4.1 "Typical" Images

The "typical" image for every ABVS band was produced by averaging all of the ABVS images of that band.

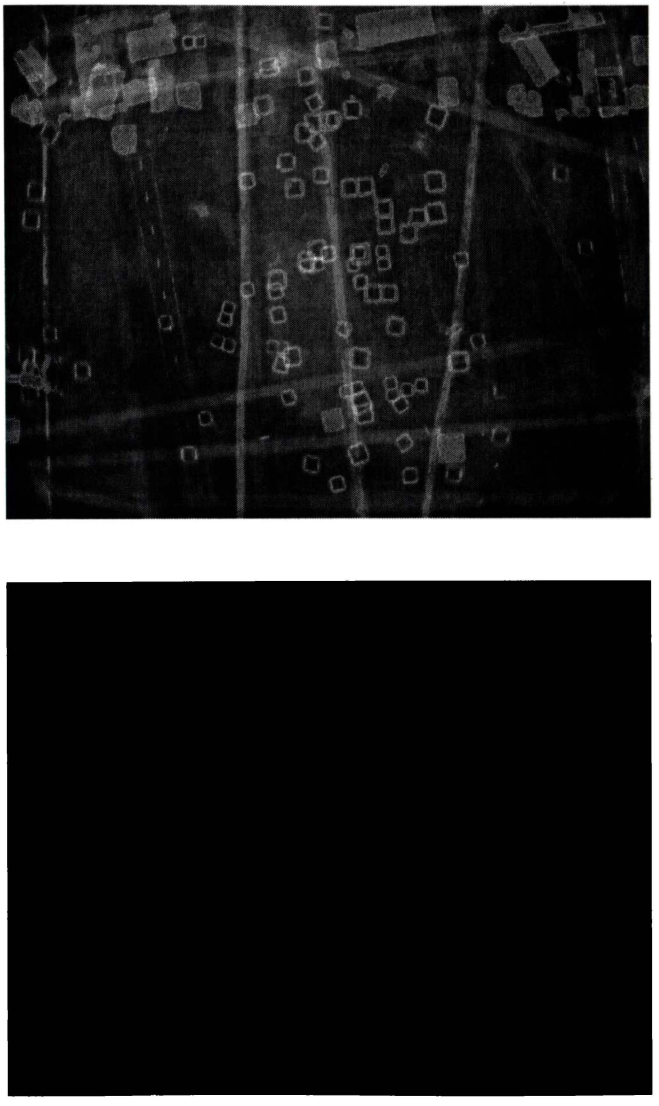

Figure C.3: "Typical" blue (top) and green (bottom) ABVS band images. Ground features—hay wrap, test plots, houses and roads—are more prominent in the "typical" blue band image.

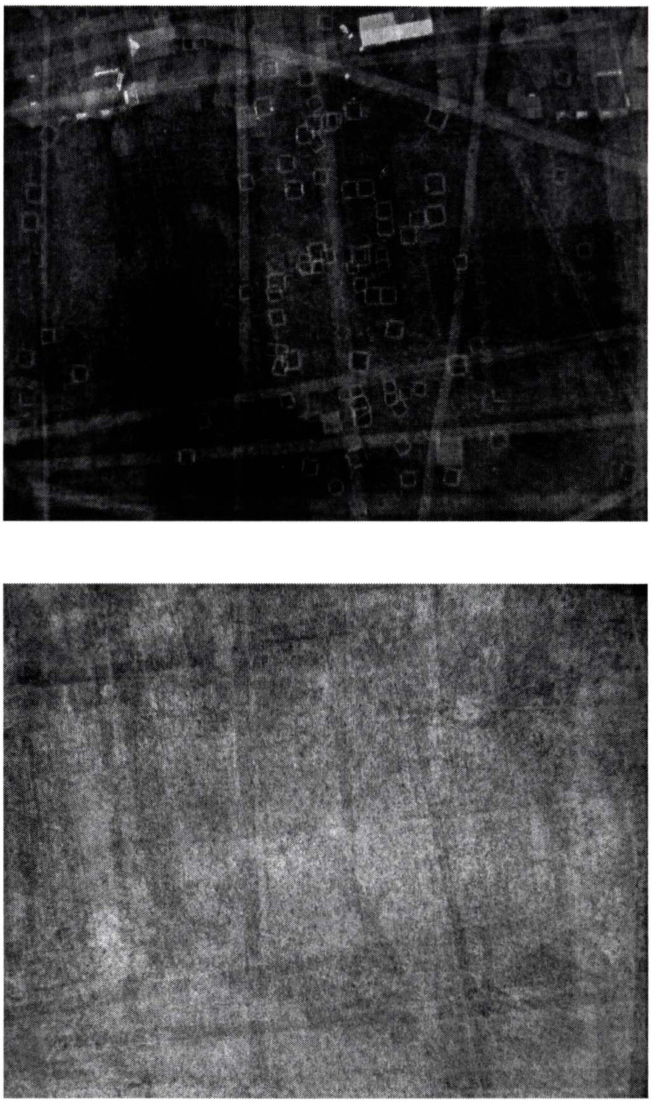

Figure C.4: "Typical" red (top) and near-infrared (bottom) ABVS band images. Ground features—hay wrap, test plots, houses and roads—are more prominent in the "typical" red band image.

C.4.2 Low-Pass Filtered "Typical" Band Images

Low-pass filtered "typical" images and the graphs associated with the low-pass filter design are shown here.

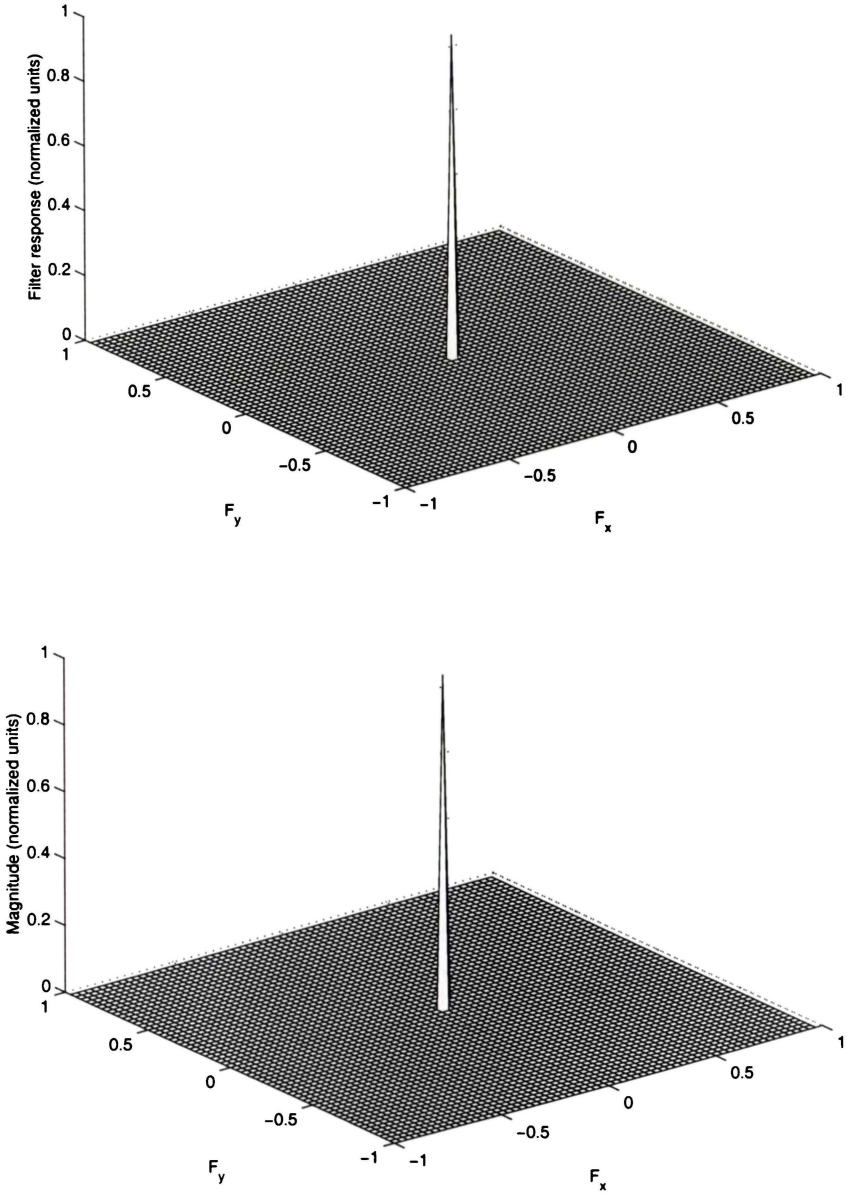

Figure C.5: Desired (top) and resulting (bottom) low-pass filter response. The resulting low-pass filter was implemented as an FIR filter, which response follows the desired as closely as possible in the least square sense. They appear very similar due to the small cut-off frequency.

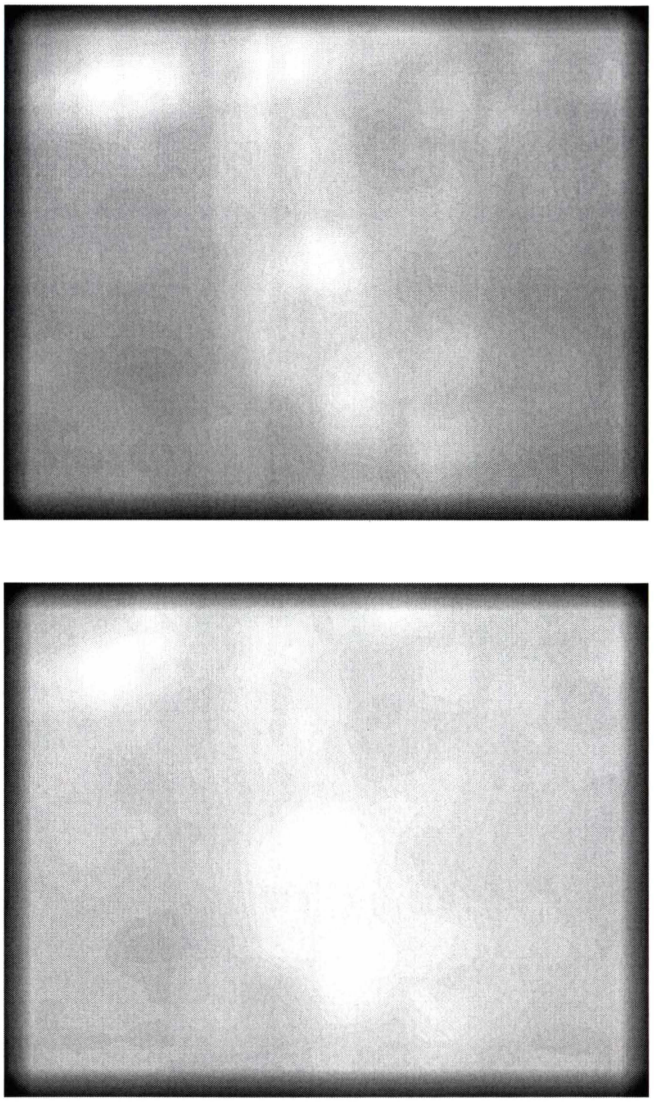

Figure C.6: Low-pass filtered "typical" blue (top) and green (bottom) ABVS band images. Ground features—hay wrap, test plots, houses and roads—are still slightly visible (white vertical stripes) in the blue band image. Image intensity is stretched as much as possible to show the differences across the images.

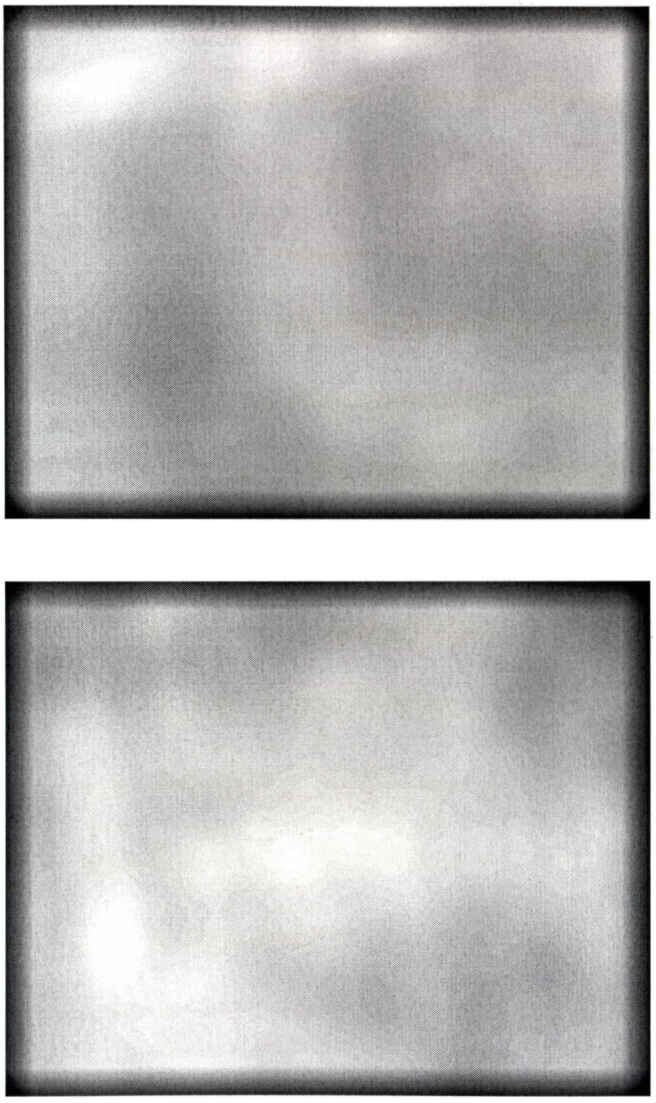

Figure C.7: Low-pass filtered "typical" red (top) and near-infrared (bottom) ABVS band images. No ground features are visible in the filtered images. Image intensity is stretched as much as possible to show the differences across the images.

C.4.3 Median-Filtered "Typical" Band Images

Median-filtered "typical" images, obtained by applying the median operation on a 41×49 pixels window centered on each pixel of the "typical" ABVS band images, are shown here.

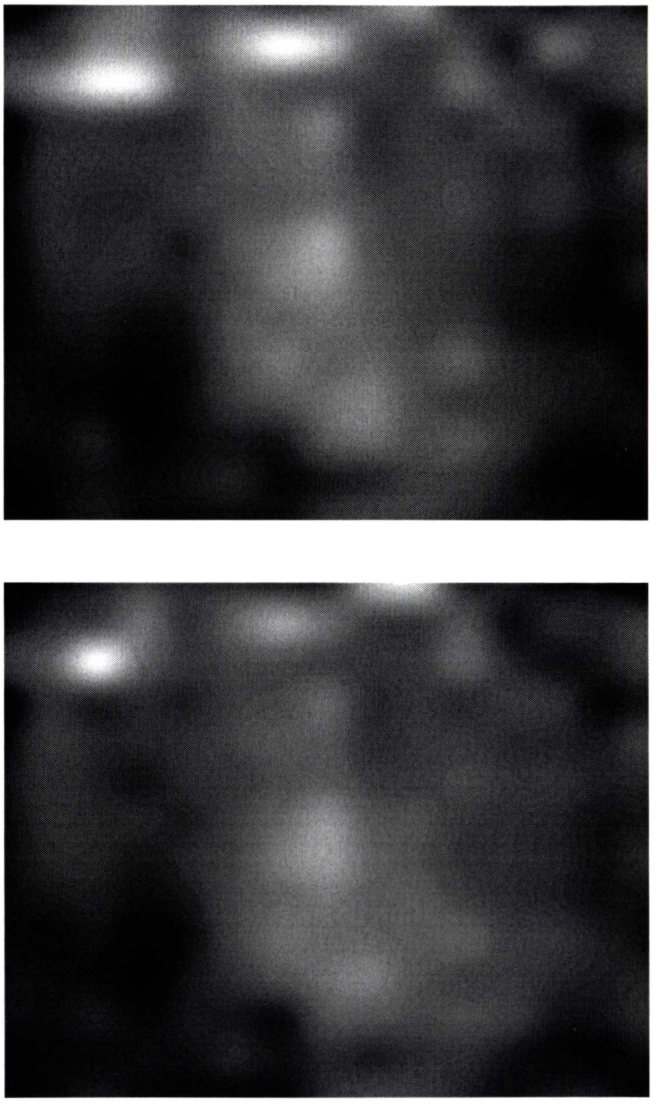

Figure C.8: Median-filtered"typical" blue (top) and green (bottom) ABVS band images. Ground features, such as house roofs, are still visible in both images, although heavily blurred. Image intensity is stretched as much as possible to show the differences across the images.

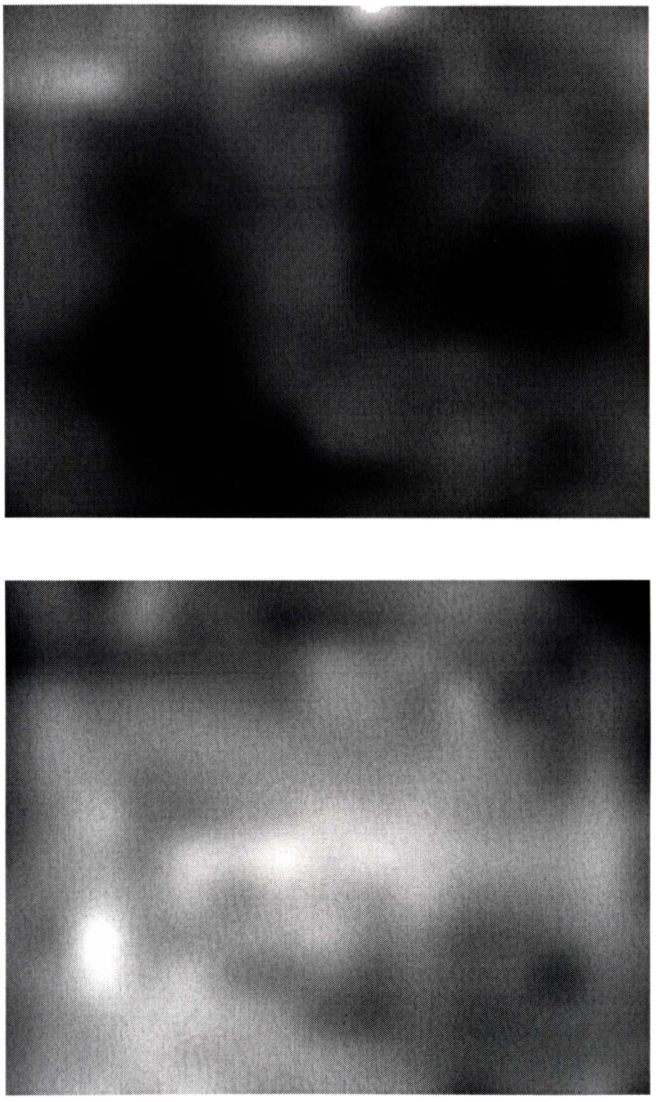

Figure C.9: Median-filtered "typical" red (top) and near-infrared (bottom) ABVS band images. Ground features, such as house roofs, are still visible in both images, although heavily blurred. Image intensity is stretched as much as possible to show the differences across the images.

C.5 Miscellaneous Graphs from Chapter 10

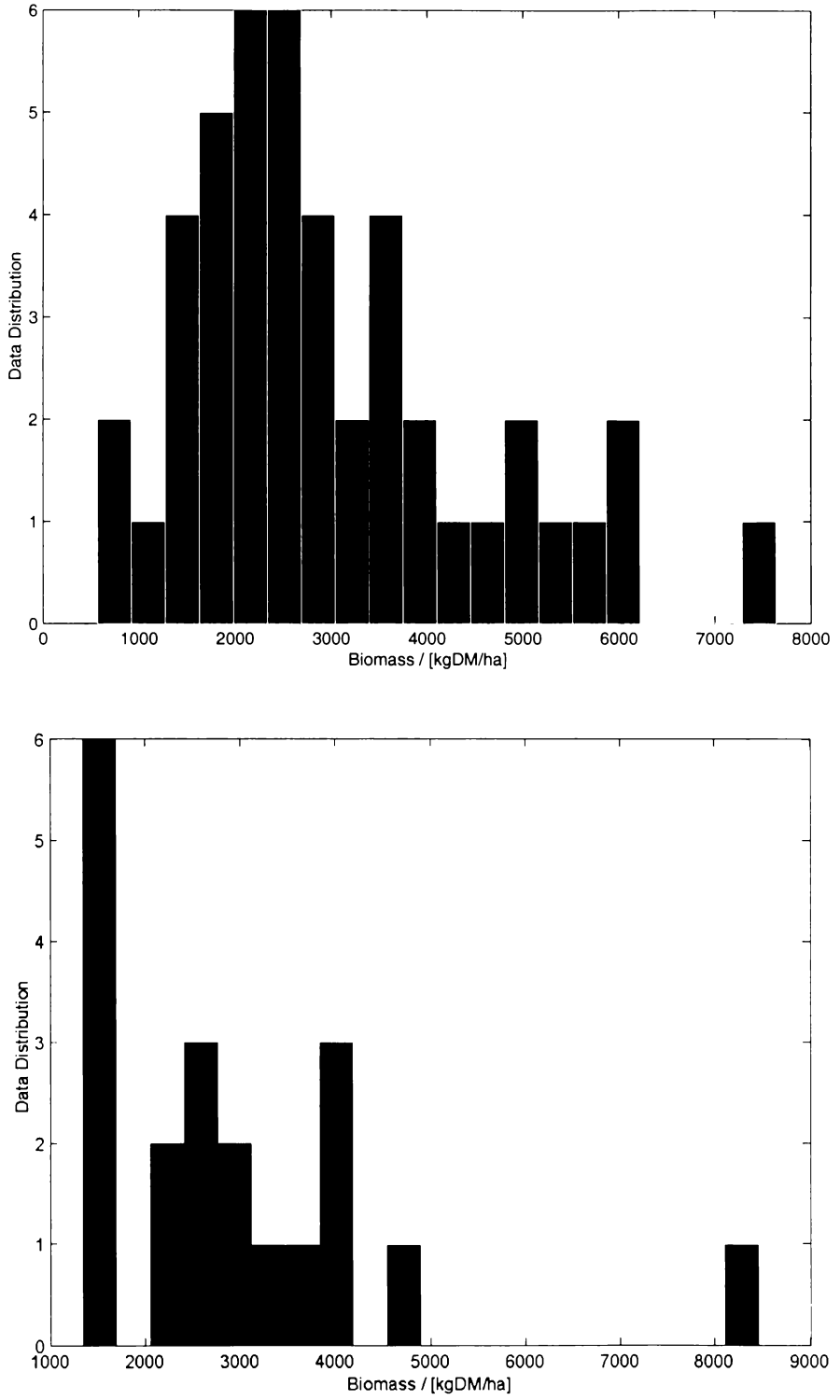

Figure C.10: Histograms of biomass values for the AgResearch (top) and Dexcel (bottom) test plots.

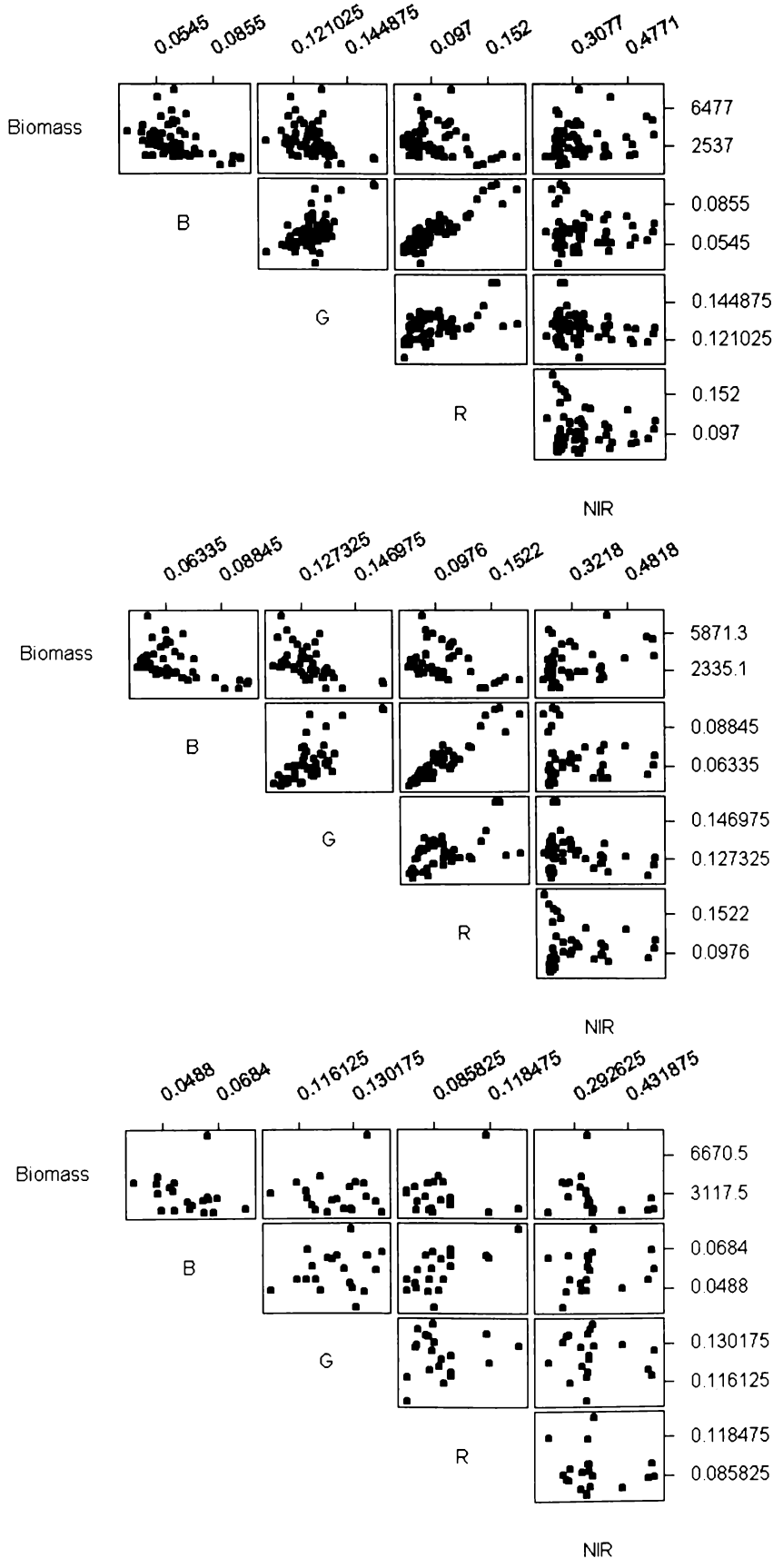

Figure C.11: Plot matrix of biomass and raw ABVS band reflectance for the complete (top), AgResearch (middle) and Dexcel (bottom) data sets. Biomass values are in kgDM/ha; reflectance values are dimensionless.

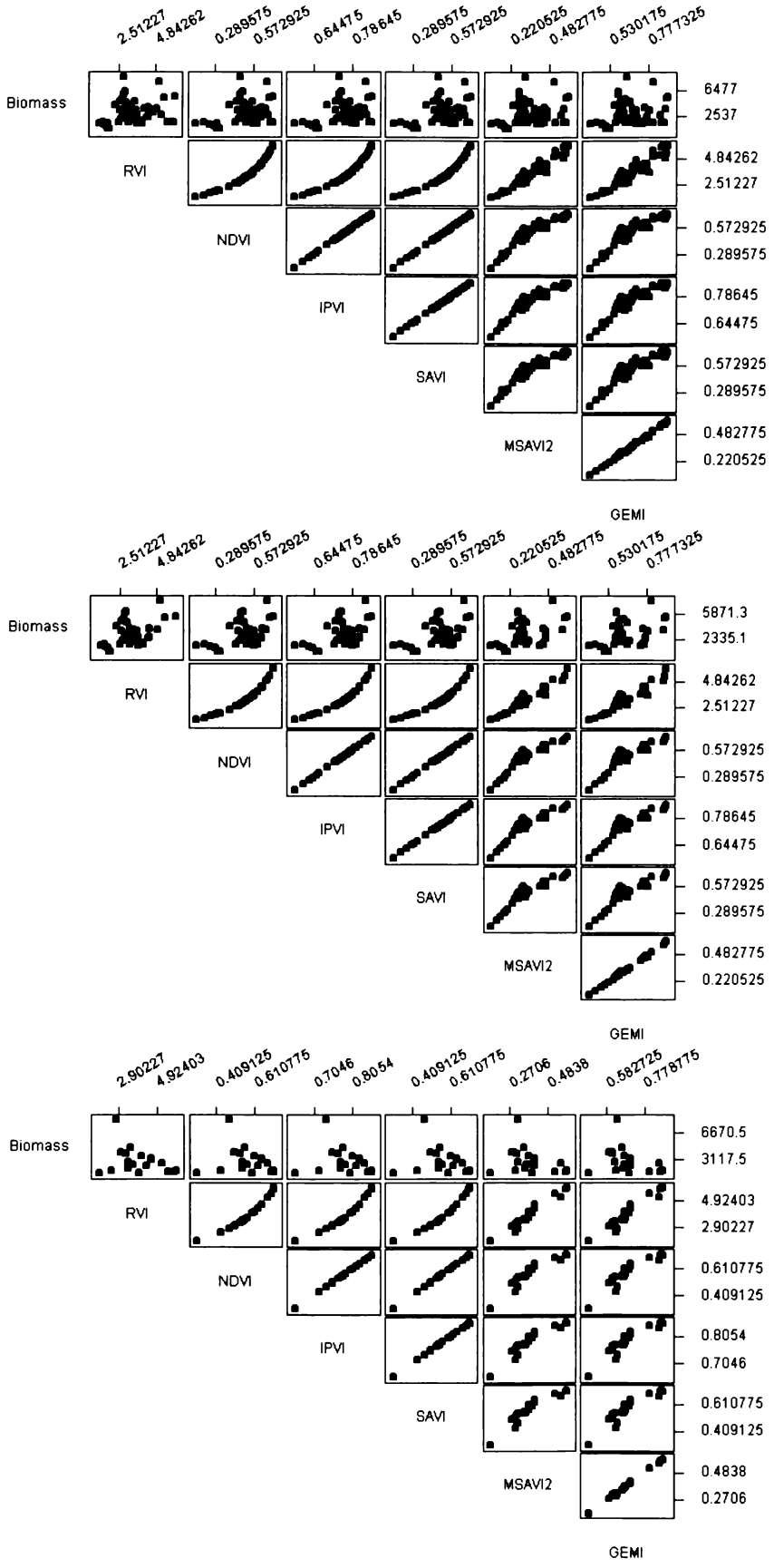

Figure C.12: Plot matrix of biomass and "raw" vegetation indices for the complete (top), AgResearch (middle) and Dexcel (bottom) data sets. Biomass values are in kgDM/ha; vegetation indices are dimensionless.

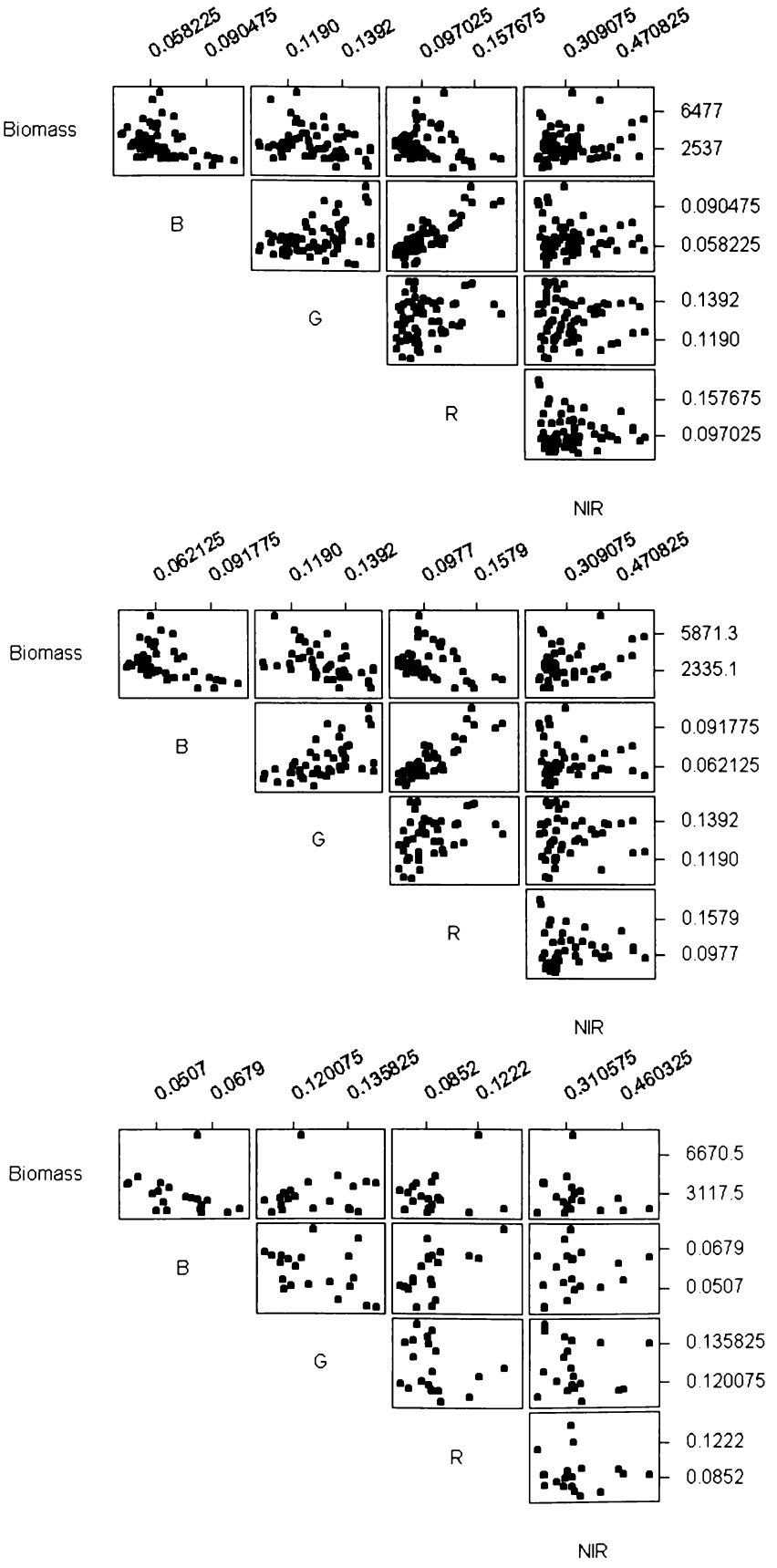

Figure C.13: Plot matrix of biomass and radiometrically-corrected (Section 9.2) ABVS band reflectance for the complete (top), AgResearch (middle) and Dexcel (bottom) data sets. Biomass values are in kgDM/ha; reflectance values are dimensionless.

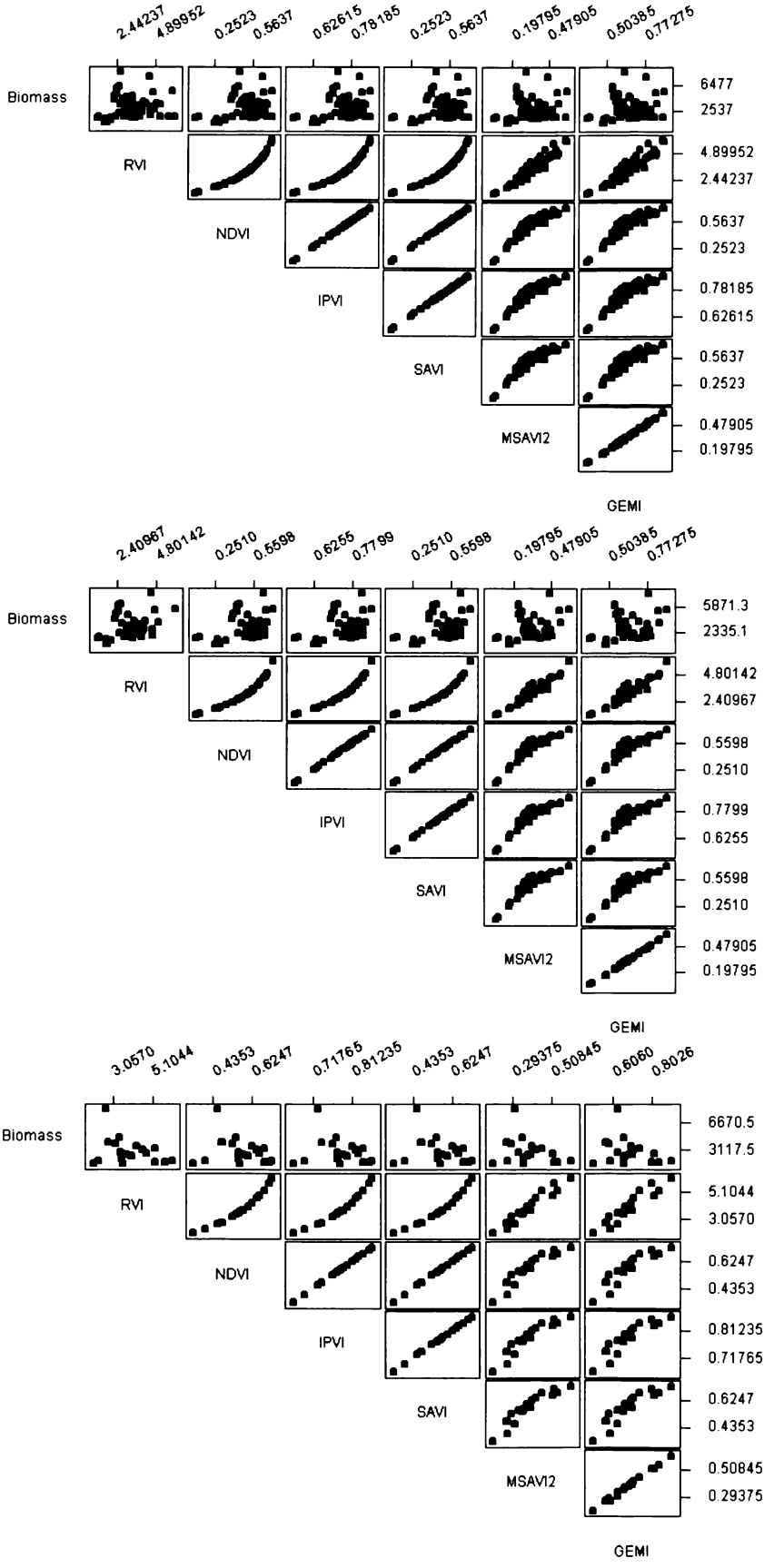

Figure C.14: Plot matrix of biomass and vegetation indices derived from the radiometrically-corrected ABVS reflectance for the complete (top), AgResearch (middle) and Dexcel (bottom) data sets. Biomass values are in kgDM/ha; vegetation indices are dimensionless.

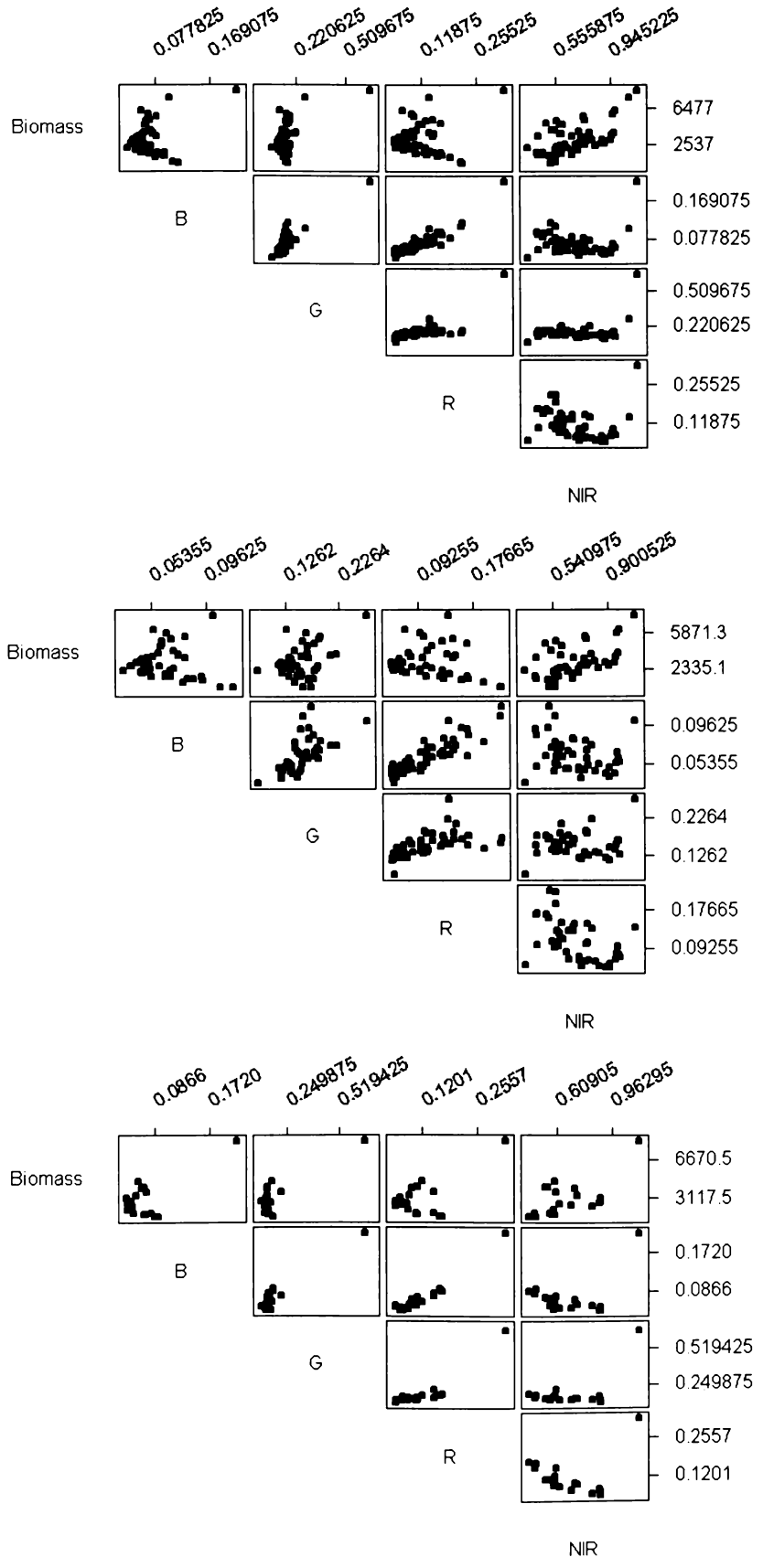

Figure C.15: Plot matrix of biomass and BRDF-corrected (Section 9.5) ABVS band reflectance for the complete (top), AgResearch (middle) and Dexcel (bottom) data sets. Biomass values are in kgDM/ha; reflectance values are dimensionless.

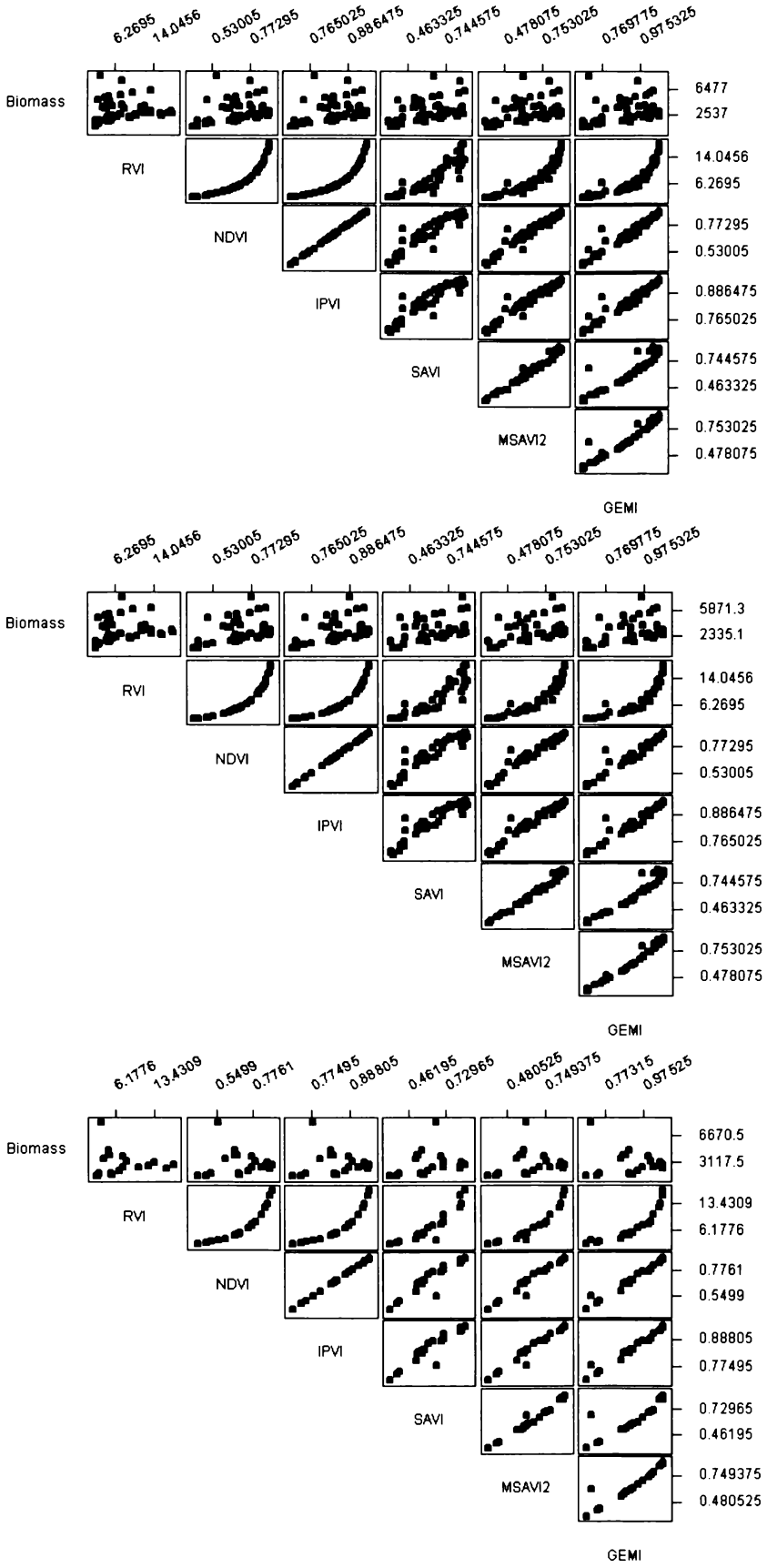

Figure C.16: Plot matrix of biomass and vegetation indices derived from the BRDF-corrected ABVS reflectance for the complete (top), AgResearch (middle) and Dexcel (bottom) data sets. Biomass values are in kgDM/ha; vegetation indices are dimensionless.

References

Anding, D. and R. Kauth. 'Estimation of sea surface temperature from space.' *Remote Sensing of Environment, vol. 1*: pp. 217–220 [1970].

Anding, D. and R. Kauth. 'Reply to the comment by G. A. Maul and M. Sidran.' *Remote Sensing of Environment, vol. 2*: pp. 171–173 [1972].

Asrar, G., editor. *Theory and Applications of Optical Remote Sensing.* Wiley Series in Remote Sensing. John Wiley & Sons [1989].

Baret, F. and G. Guyot. 'Potentials and limits of vegetation indices for LAI and APAR assessment.' *Remote Sens. of Environ., vol. 35*: pp. 161–173 [1991].

Baret, F., G. Guyot and D. Major. 'TSAVI: A vegetation index which minimizes soil brightness effects on LAI and APAR estimation.' In 'Twelveth Canadian Symposium on Remote Sensing and IGARSS'90,' IEEE [1989].

Barton, I. J. 'Transmission model and ground-truth investigation of satellite-derived sea surface temperatures.' *J. Clim. Appl. Meteorol., vol. 24*: pp. 508–516 [1985].

Barton, I. J. 'Satellite-derived sea surface temperatures: Current status.' *J. Geophys. Res., vol. 100*, no. C5: pp. 8,777–8,790 [1995].

Brutsaert, W. *Evaporation into the Atmosphere: Theory, History and Applications.* D. Reidel Publishing Company [1982].

Burns, S. P., D. Khelif, C. A. Friehe, P. Hignett, A. G. Williams, A. L. M. Grant, J. M. Hacker, D. E. Hagan, Y. L. Serra, D. P. Rogers, E. F. Bradley, R. A. Weller, C. W. Fairall, S. P. Anderson, C. A. Paulson and P. A. Coppin. 'Comparisons of aircraft, ship and buoy radiation and sst measurements from TOGA COARE.' *J. Geophys. Res., vol. 105*, no. D12: pp. 15,627–15,652 [2000].

Byers, H. R. *General Meteorology.* McGraw-Hill, third edn. [1959].

Campbell, J. B. *Introduction to Remote Sensing.* The Guilford Press, 2nd edn. [1996].

Chahine, M. T. 'Inverse problems in radiative transfer: Determination of atmospheric parameters.' *Journal of the Atmospheric Sciences, vol. 27*: pp. 960–967 [1970].

Chen, J. M. and J. Cihlar. 'A hotspot function in a simple bidirectional reflectance model for satellite applications.' *J. Geophys. Res., vol. 102*, no. D22: pp. 25,907–25,913 [1997].

Clevers, J. G. P. W. 'The derivation of a simplified reflectance model for the estimation of leaf area index.' *Remote Sens. of Environ., vol. 35*: pp. 53–70 [1988].

Collins, W. 'Remote sensing of crop type and maturity.' *Photogrammetric Engineering and Remote Sensing, vol. 44*: pp. 43–55 [1978].

Crippen, R. E. 'Calculating the vegetation index faster.' *Remote Sens. of Environ., vol. 34*: pp. 71–73 [1990].

Czajkowski, K. P., S. N. Goward and H. Ouaidrari. 'Impact of AVHRR filter functions on surface temperature estimation from the split window approach.' *Int. J. Remote Sens., vol. 19*, no. 10: pp. 2007–2012 [1998].

Dickinson, R. E. 'Land surface processes and climate-surface albedos and energy balance.' *Adv. Geophys., vol. 25*: p. 305 [1983].

Dymond, J. R., J. D. Shepherd and J. Qi. 'A simple physical model of vegetation reflectance for standardising optical satellite imagery.' *Remote Sens. of Environ., vol. 75*: pp. 350–359 [2000].

Emery, W. J., Y. Yu, G. A. Wick, P. Schlüessel and R. W. Reynolds. 'Correcting infrared satellite estimates of sea surface temperature for atmospheric water vapor attenuation.' *J. Geophys. Res., vol. 99*, no. C3: pp. 5,219–5,236 [1994].

Eyre, J. R. 'On systematic errors in satellite sounding products and their climatological mean values.' *Quarterly Journal of the Royal Meteorological Society, vol. 113*: pp. 279–292 [1987].

Eyre, J. R. 'Inversion of cloudy satellite soundings radiances by nonlinear optimal estimation I: Theory and simulation for TOVS.' *Quarterly Journal of the Royal Meteorological Society, vol. 115*: pp. 1001–1026 [1989].

Flores, A., J. Vilà-Guerau de Arellano, L. P. Gradinarsky and A. Rius. 'Tomography of the lower troposphere using a small dense network of GPS receivers.' *IEEE Trans. Geosci. Remote Sensing, vol. 39*, no. 2: pp. 439–447 [2001].

Gobron, N., B. Pinty, M. M. Verstraete and Y. Govaerts. 'A semidiscrete model for the scattering of light by vegetation.' *J. Geophys. Res., vol. 102*, no. D8: pp. 9431–9446 [1997].

Hanna, M. M., D. A. Steyn-Ross and M. Steyn-Ross. 'Estimating biomass for New Zealand pasture using optical remote sensing techniques.' *Geocarto International, vol. 14*, no. 3: pp. 89–94 [1999].

Hapke, B. 'Bidirectional reflectance spectroscopy 1. theory.' *J. Geophys. Res., vol. 86*: pp. 3039–3054 [1981].

Harris, A. R. and I. M. Mason. 'An extension to the split-window technique giving improved atmospheric correction and total water vapour.' *Int. J. Remote Sens., vol. 13*, no. 5: pp. 881–892 [1992].

Hepplewhite, C. L. 'Remote observation of the sea surface and atmosphere: The oceanic skin effect.' *Int. J. Remote Sens., vol. 10*, no. 4 & 5: pp. 801–810 [1989].

Holst, G. C. *CCD Arrays, Cameras and Displays.* J C D Publishing [1998].

Huete, A. R. 'A soil-adjusted vegetation index (SAVI).' *Remote Sens. of Environ., vol. 25*: pp. 295–309 [1988].

Jedlovec, G. J. 'Precipitable water estimation from high-resolution split window radiance measurements.' *J. Appl. Meteor., vol. 29*: pp. 863–877 [1990].

Jordan, C. F. 'Derivation of leaf area index from quality of light on the forest floor.' *Ecology, vol. 50*: pp. 663–666 [1969].

Kleespies, T. J. and L. M. McMillin. 'Retrieval of precipitable water from observations in the split window over varying surface temperatures.' *J. Appl. Meteorol., vol. 29*: pp. 851–862 [1990].

Kneizys, F. X., E. P. Shettle, L. W. Abreu, J. H. Chetwynd, G. P. Anderson, W. O. Gallery, J. E. A. Selby and S. A. Clough. *Users Guide to LOWTRAN-7.* Tech. Rep. AFGL-TR-88-0177, Opt./Infrared Technol. Div., U.S. Air Force Geophys. Lab., Hanscom Air Force Base, Massachusetts [1988].

Kriegler, F. J., W. A. Malila, R. F. Nalepka and W. Richardson. 'Preprocessing transformations and their effects on multispectral recognition.' In 'Proceedings of the Sixth International Symposium on Remote Sensing of Environment,' pp. 97–131. University of Michigan, Ann Arbor, MI [1969].

Kuusk, A. 'A computer-efficient plant canopy reflectance model.' *Computers & Geosciences, vol. 22*, no. 2: pp. 149–163 [1996].

Lillesand, T. M. and R. W. Kiefer. *Remote Sensing and Image Interpretation.* John Wiley & Sons, Inc., 3rd edn. [1994].

Lim, J. S. *Two-Dimensional Signal and Image Processing.* Prentice Hall, Englewood Cliffs, NJ [1990].

Lin, T. *Estimating Pasture Biomass from Multiband Reflectance Measurements.* Master's thesis, University of Waikato [1999].

Liou, K.-N. *An Introduction to Atmopsheric Radiation*, vol. 26 of *International Geophysics Series.* Academic Press [1980].

List, R. *Smithsonian Meteorological Tables.* The Smithsonian Institute, Washington D.C., 6th rev. ed. edn. [1968].

Maul, G. A. and M. Sidran. 'Comment on "Estimation of sea surface temperature from space" by D. Anding and R. Kauth.' *Remote Sensing of Environment, vol. 2*: pp. 165–169 [1972].

May, D. A. *Global and Regional Comparative Performance of Linear and Nonlinear Satellite Multichannel Sea Surface Temperature Algorithms.* Tech. Rep. NRL/MR/7240-93-7049, Naval Research Laboratory, Washington D.C. [1993].

McClain, E. P. 'Global sea surface temperatures and cloud clearing for aerosol optical depth estimate.' *Int. J. Remote Sens., vol. 10*, no. 4 & 5: pp. 763–769 [1989].

McMillin, L. M. *A Method of Determining Surface Temperatures from Measurements of Spectral Radiance at Two Wavelengths.* Ph.D. thesis, Iowa State University [1971].

McMillin, L. M. 'Estimation of sea surface temperatures from two infrared window measurements with different absorption.' *J. Geophys. Res., vol. 80*, no. 36: pp. 5113–5117 [1975].

McMillin, L. M. and D. S. Crosby. 'Theory and validation of the multiple window sea surface temperature technique.' *J. Geophys. Res., vol. 89*: pp. 3655–3661 [1984].

Meador, W. E. and W. R. Weaver. 'Two-stream approximations to radiative transfer in planetary atmospheres: A unified description of existing methods and a new improvement.' *J. Atmos. Sci., vol. 37*: p. 630 [1980].

Merchant, C. J., A. R. Harris, M. J. Murray and A. M. Závody. 'Toward the elimination of bias in satellite retrievals of sea surface temperature 1. theory, modelling and interalgorithm comparison.' *J. Geophys. Res., vol. 104*, no. C10: pp. 23,565–23,578 [1999].

Michalsky, J. J. 'The astronomical almanac's algorithm for approximate solar position.' *Solar Energy, vol. 40*: pp. 227–235 [1988].

Ohtani, R. and I. Naito. 'Comparisons of GPS-derived precipitable water vapors with radiosonde observations in japan.' *J. Geophys. Res., vol. 105*, no. D22: pp. 26,917–26,929 [2000].

Osborne, B. J. *Atmospheric Properties and SST Retrieval from AVHRR.* Master's thesis, University of Waikato [1995].

Otterman, J., T. Brakke and A. Marshak. 'Scattering by Lambertian-leaves canopy: Dependence on leaf-area projections.' *Int. J. Remote Sens., vol. 16*, no. 6: pp. 1107–1125 [1995].

Pinty, B. and M. M. Verstraete. 'GEMI: A non-linear index to monitor global vegetation from satellites.' *Vegetation, vol. 101*: pp. 15–20 [1991].

Prabhakara, C., G. Dalu and V. G. Kunde. 'Estimation of sea surface temperature from remote sensing in the 11- to 13-μm window region.' *J. Geophys. Res., vol. 79*, no. 33: pp. 5039–5044 [1974].

Press, W. H., S. A. Teukolsky, W. T. Vetterling and B. P. Flannery. *Numerical Recipes in C: The Art of Scientific Computing.* Cambridge University Press, 2nd edn. [1992].

Purevdorj, T., R. Tateishi, T. Ishiyama and Y. Honda. 'Relationships between percent vegetation cover and vegetation indices.' *Int. J. Remote Sens., vol. 19*, no. 18: pp. 3519–3535 [1998].

Qi, J., A. Chehbouni, A. R. Huete and Y. H. Kerr. 'Modified soil adjusted vegetation index (MSAVI).' *Remote Sens. of Environ., vol. 48*: pp. 119–126 [1994].

Qiu, J. 'An improved model of surface BRDF-atmospheric coupled radiation.' *IEEE Trans. Geosci. Remote Sensing, vol. 39*, no. 1: pp. 181–187 [2001].

Richards, J. M. 'Simple expression for the saturation vapour pressure of water in the range -50 °*c* to 140 °*c*.' *Brit. J. Appl. Phys., vol. 4*: pp. L15–L18 [1971].

Richardson, A. J. and C. L. Wiegand. 'Distinguishing vegetation from soil background information.' *Photogramm. Engin. and Remote Sens., vol. 43*: pp. 1541–1552 [1977].

Rodgers, C. D. 'Retrieval of atmospheric temperature and composition from remote measurements of thermal radiation.' *Reviews of Geophysics and Space Physics, vol. 14*, no. 4: pp. 609–624 [1976].

Roujean, J. 'A parametric hot spot model for optical remote sensing applications.' *Remote Sens. Environ., vol. 71*: pp. 197–206 [2000].

Roujean, J., M. Leroy and P. Deschamps. 'A bidirectional reflectance model of the earth's surface for the correction of remote sensing data.' *J. Geophys. Res., vol. 97*, no. D18: pp. 20,455–20,468 [1992].

Rouse, J. W., R. H. Haas, J. A. Schell and D. W. Deering. 'Monitoring vegetation systems in the Great Plains with ERTS.' In 'Third ERTS Symposium, NASA SP-351,' vol. 1, pp. 309–317 [1973].

Saunders, P. M. 'Aerial measurements of sea surface temperature in the infrared.' *J. Geophys. Res., vol. 72*, no. 16: pp. 4109–4117 [1967].

Schanda, E. *Physical Fundamentals of Remote Sensing.* Springer-Verlag [1986].

Schlüessel, P., W. J. Emery, H. Gassl and T. Mammien. 'On the bulk skin temperature difference and its impact on satellite remote sensing of SST.' *J. Geophys. Res., vol. 95*, no. C8: pp. 13,341–13,356 [1990].

Sellers, P. J. 'Canopy reflectance, photosynthesis and transpiration.' *Int. J. Remote Sens., vol. 6*: p. 1335 [1985].

Shepherd, J. D. *Comparative Study of Sea Surface Temperature Retrievals from AVHRR.* Master's thesis, University of Waikato [1993].

Shepherd, J. D. and J. R. Dymond. 'BRDF correction of vegetation in AVHRR imagery.' *Preprint* [1999].

Smith, G. M. and E. J. Milton. 'The use of the empirical line method to calibrate remotely sensed data to reflectance.' *Int. J. Remote Sens., vol. 20*, no. 13: pp. 2653–2662 [1999].

Smith, P. *The Dynamic Water-Vapour Algorithm for SST Retrievals.* Master's thesis, University of Waikato [1993].

Smith, W. L. 'Iterative solution of the radiative transfer equation for temperature and absorbing gas profile of an atmosphere.' *Applied Optics, vol. 9*: pp. 1993–1999 [1970].

Sobrino, J. A., Z.-L. Li and M. P. Stoll. 'Impact of the atmospheric transmittance and total water vapour content in the algorithms for estimating satellite sea surface temperatures.' *IEEE Trans. Geosci. Remote Sensing, vol. 31*, no. 5: pp. 946–952 [1993].

Sobrino, J. A., Z.-L. Li, M. P. Stoll and F. Becker. 'Improvements in the split-window technique for land surface temperature determination.' *IEEE Trans. Geosci. Remote Sensing, vol. 32*, no. 2: pp. 243–253 [1994].

Steyn-Ross, D. A., M. Steyn-Ross and S. Clift. 'Radiance calibration for advanced very high resolution radiometer infrared channels.' *J. Geophys. Res., vol. 97*, no. C4: pp. 5551–5568 [1992].

Steyn-Ross, M. L., D. A. Steyn-Ross, P. J. Smith, J. D. Shepherd, J. Reid and P. Tildesley. 'Water vapour correction method for advanced very high resolution radiometer data.' *J. Geophys. Res., vol. 98*, no. C12: pp. 22,817–22,826 [1993].

Verstraete, M. M., B. Pinty and R. E. Dickinson. 'A physical model of the bidirectional reflectance of vegetation canopies 1. theory.' *J. Geophys. Res., vol. 95*, no. D8: pp. 11,575–11,765 [1990].

Wallace, J. M. and P. V. Hobbs. *Atmospheric Science: An Introductory Survey.* Academic Press [1977].

Walton, C. C. 'Nonlinear multichannel algorithms for estimating sea surface temperature with avhrr data.' *J. App. Meteorology, vol. 24*: pp. 501–507 [1988].

Walton, C. C., E. P. McClain and J. F. Saper. 'Recent changes in satellite-based multi-channel sea surface temperature algorithms.' *Marine Technology Society* [1990].

Walton, C. C., W. G. Pichel and J. F. Saper. 'The development and operational application of nonlinear algorithms for the measurement of sea surface temperatures with the noaa polar-orbiting environmental satellites.' *J. Geophys. Res., vol. 103*, no. C12: pp. 27,999–28,012 [1998].

Wanner, W., X. Li and A. H. Strahler. 'On the derivation of kernel-driven models of bidirectional reflectance.' *J. Geophys. Res., vol. 100*, no. D10: pp. 21,077–21,089 [1995].

Yu, Y. and I. J. Barton. 'A non-regression-coefficients method of sea surface temperature retrieval from space.' *Int. J. Remote Sens., vol. 15*, no. 6: pp. 1189–1206 [1994].